Towards Understanding Differential Ion Mobility and its Applications in Analytical and Medicinal Chemistry

by

Christian Ieritano

A thesis

presented to the University of Waterloo

in fulfillment of the

thesis requirement for the degree of

Doctor of Philosophy

in

Chemistry

Waterloo, Ontario, Canada, 2023

Examining Committee Membership

The following served on the Examining Committee for this thesis. The decision of the Examining Committee is by majority vote.

External Member	Prof. Erin S. Baker Associate Professor Department of Chemistry University of North Carolina at Chapel Hill Chapel Hill, North Carolina, United States.
Internal Member	Prof. J. Larry Campbell Adjunct Professor Department of Chemistry University of Waterloo, Waterloo ON, Canada.
Internal Member	Prof. Richard A. Marta Materials & Nanosciences Continuing Lecturer International Department of Chemistry University of Waterloo, Waterloo ON, Canada.
Internal-External Member	Prof. Brian Kendall Associate Professor, Canada Research Chair (Tier II) Department of Earth and Environmental Sciences University of Waterloo, Waterloo ON, Canada.
Supervisor	Prof. W. Scott Hopkins Associate Professor Department of Chemistry University of Waterloo, Waterloo ON, Canada.

Author's Declaration

This thesis consists of material all of which I authored or co-authored: see the Statement of Contributions included in the thesis. This is a true copy of the thesis, including any required final revisions as accepted by my examiners. I understand that my thesis may be made electronically available to the public.

Statement of Contributions

The contents of this thesis have been compiled from my published manuscripts, a list of which is provided in **Appendix A**. Each chapter contains the work of myself and several researchers, whose contributions are summarized below.

Chapters 1 and 6:

The information in **Chapters 1** and **6** is reproduced from the publication cited below. This work was co-written by myself and Prof. W. Scott Hopkins as part of an invited perspective article submitted to PCCP. The first draft of the perspective article was written by myself, with extensive intellectual input from Prof. Hopkins. Both chapters are adapted with permission from the Royal Society of Chemistry (see citation).

> **(Citation)** Ieritano, C., Hopkins, W. S. The hitchhiker's guide to dynamic ion–solvent clustering: applications in differential ion mobility spectrometry. *Phys. Chem. Chem. Phys.* **2022**. 24, 20594 – 20615.

Chapters 2.1 and 2.4:

Chapter 2.1 is adapted with permission from the Royal Society of Chemistry (see citation).

> **(Citation)** Ieritano, C., Hopkins, W. S. The hitchhiker's guide to dynamic ion–solvent clustering: applications in differential ion mobility spectrometry. *Phys. Chem. Chem. Phys.* **2022**. 24, 20594 – 20615.

Chapter 2.2:

Chapter 2.2 is adapted with permission from the Royal Society of Chemistry (see citation below). This work was conceptualized and written by myself with guidance from Prof. Hopkins. The construction of the DMS-MS database of SV/CV pairs was a collaborative effort, with equal

contributions from myself and Prof. Campbell. Prof. Hopkins was responsible for creating the machine learning code.

> **(Citation)** Ieritano, C., Campbell, J. L., Hopkins, W. S. Predicting Differential Ion Mobility Behaviour *in silico* using Machine Learning. *Analyst.* **2021**. 146 (*15*), 4737 – 4743.

Chapter 2.3:

Chapter 2.3 is adapted with permission from the American Chemical Society (see citation below). This work was conceptualized by myself and Prof. Hopkins. I spearheaded the construction of the DMS-MS database of SV/CV pairs, with assistance from Dr. Jeff Crouse, Zack Bowman, Dr. Nour Mashmoushi, and Prof. Campbell. I also conducted CCS calculations, with assistance from Zack Bowman, Dr. Mashmoushi, Paige Crossley, and Benjamin P. Friebe. Coding and optimization of the machine learning framework was performed with equal contribution from Arthur Lee, Dr. Crouse, and Prof. Hopkins. The manuscript pertaining to Chapter 2.3 was written by myself with input from Prof. Hopkins.

> **(Citation)** Ieritano, C., Lee, A., Crouse, J., Bowman, Z., Mashmoushi, N., Crossley, P. M., Friebe, B. P., Campbell, J. L., Hopkins, W. S. Determining Collision Cross Sections from Differential Ion Mobility. *Anal. Chem.* **2021**. 93 (*25*), 8937 – 8944.

Chapter 2.4:

Chapter 2.4 is adapted with permission from the Royal Society of Chemistry (see citation). This work was co-written by myself and Prof. W. Scott Hopkins, with experimental and computational data being acquired by myself and Prof. Campbell.

> **(Citation)** Ieritano, C., Hopkins, W. S. The hitchhiker's guide to dynamic ion–solvent clustering: applications in differential ion mobility spectrometry. *Phys. Chem. Chem. Phys.* **2022**. 24, 20594 – 20615.

Chapter 3:

Chapter 3 is adapted with permission from the American Chemical Society (see citation below). This work was conceptualized and written by myself under the supervision of Prof. Hopkins. The DMS-MS data for the MP1 peptide was obtained through equal contributions from myself and Daniel Rickert. The systematic sampling of cluster surfaces algorithm, which was used to sample the geometries of microsolvated ions, was conceptualized and coded by Dr. Joshua Featherstone. Molecular dynamics simulations were carried out by Prof. John F. Honek with all other calculations, including CCS evaluations, being performed by myself. Intellectual contributions, alongside edits to the final version of the manuscript, were made by Prof. Larry J. Campbell, Dr. Yves Le Blanc, and Dr. Bradley B. Schneider.

> **(Citation)** Ieritano, C., Rickert, D., Featherstone, J., Honek, J. F., Campbell, J. L., Le Blanc, J. C. Y., Schneider, B. B., Hopkins, W. S. The Charge-State and Structural Stability of Peptides Conferred by Microsolvating Environments in Differential Mobility Spectrometry. *J. Am. Soc. Mass Spectrom.* **2021**. 32 (*4*), 956 – 968. ***Cover Article.***

Chapter 4:

Chapter 4 is adapted with permission from Wiley (see citation). The phenomenon of protonation-induced chirality was identified by me from DMS data of Verapamil and Norverapamil presented by Dr. Yves Le Blanc and Dr. Bradley B. Schneider. Subsequent DMS-MS and TWIMS experiments on other compounds susceptible to protonation-induced chirality were conducted by myself with assistance from Justine Bissonnette. First-principles modeling of the DMS behaviour of Verapamil was conducted by Dr. Alexander Haack. The manuscript was written by myself, with intellectual contributions from Prof. Hopkins.

> **(Citation)** Ieritano, C., Le Blanc, J. C. Y., Schneider, B. B., Bissonnette, J. R., Haack, A., Hopkins, W. S. Protonation-Induced Chirality Drives Separation by Differential Ion Mobility Spectrometry. *Angew. Chem. Int. Ed.* **2022**. 61 (9), e202116794. *Frontispiece*.

Chapter 5:

Chapter 5 is adapted with permission from the American Chemical Society (see citation below). This work was conceptualized and written by myself. Patrick Thomas assisted with the DMS-MS experiments, while Prof. W. Scott Hopkins oversaw the project and provided intellectual contributions.

> **(Citation)** Ieritano, C., Thomas, P, Hopkins, W. S. Argentination: A Silver Bullet for Cannabinoid Analysis by Differential Mobility Spectrometry. *Anal. Chem.* **2023**. 93 (22), 8668 – 8678.

Chapter 6:

Chapter 6 is adapted with permission from the Royal Society of Chemistry (see citations below). The conceptualization and parameterization of MobCal-MPI was done by myself. Dr. Crouse parallelized the MobCal Fortran code to create MobCal-MPI from the work of the Kim group, who modified the original MobCal code (Shvartsburg *et al.* and Campuzano *et al.*). I created the GUI that accompanies MobCal-MPI, wrote its manual, and the manuscript under the supervision of Prof. Hopkins and Prof. Campbell. Subsequently, Dr. Haack implemented two-temperature theory (2TT) and the respective empirical corrections. Dr. Alexander Haack coded these changes into MobCal-MPI 2.0, and I parameterized the updated version. The manuscript for MobCal-MPI 2.0 was co-written by myself and Dr. Alexander Haack under the supervision of Prof. W. Scott Hopkins.

> **(Citation)** Ieritano, C., Crouse, J., Campbell, J. L., Hopkins, W. S. A Parallelized Molecular Collision Cross Section Package with Optimized Accuracy and Efficiency. *Analyst* **2019**, *144* (5), 1660–1670.
>
> **(Citation)** Haack, A.,* Ieritano, C.,* Hopkins, W. S. MobCal-MPI 2.0: An Accurate and Parallelized Package for Calculating Field-Dependent Collision Cross Sections and Ion Mobilities. *Analyst* **2023**. 148, 3257 – 3273. *equal contribution
>
> **(Citation)** Ieritano, C., Hopkins, W. S. The hitchhiker's guide to dynamic ion–solvent clustering: applications in differential ion mobility spectrometry. *Phys. Chem. Chem. Phys.* **2022**. 24, 20594 – 20615.

Abstract

This PhD thesis, titled "Towards Understanding Differential Ion Mobility Spectrometry and its Applications in Analytical and Medicinal Chemistry," encompasses a broad effort to understand the principles that underpin differential mobility spectrometry (DMS), and how the DMS technique can be employed within the analytical and medicinal facets of chemistry. Specifically, this work highlights the components of the ion-neutral interaction potential that are pertinent to rationalize an ion's DMS behaviour and how such information can be modelled using *in silico* and machine-learning approaches. Understanding the nature of ion-neutral interactions is especially important when DMS experiments are conducted in microsolvating environments (*i.e.,* those in which the carrier gas is seeded with small amounts of a volatile solvent vapour), as components of the interaction potential can be used to predict molecular properties that are routinely screened during drug discovery. In the **Chapter 1**, we introduce the ion-solvent interactions that are intrinsic to DMS experiments and how microsolvation can impact an ion's mobility. We specifically emphasize the significance of ion solvent clusters and how the waveform used in DMS separations fosters a dynamic solvation environment. Because field-induced heating is modulated such that an analyte undergoes many cycles of solvent condensation and evaporation at charge-dense regions of the analyte, DMS effectively samples interactions that may resemble the dynamics of solvation within the analyte's primary solvation shell. In this regard, DMS can be utilized to probe characteristics of a molecule related to its insipient solvation, which, when used in conjunction with quantum-chemical calculations and/or machine learning algorithms, affords accurate predictions of that molecule's physicochemical properties.

In addition to the information regarding an analyte's physicochemical properties that can be gleaned from DMS measurements in microsolvating environments (**Chapter 2**), ion microsolvation can help alleviate complications related to field-induced heating. This phenomenon is explored in **Chapter 3**, where microsolvation was found to stabilize analytes through the formation of localized ion-solvent clusters. In particular, the chapter explores the DMS behaviour of the MP1 peptide,

which, when exposed to a microsolvation partner, underwent chemical transformations that reduced the observed charge state of MP1 from $[MP1 + 3H]^{3+}$ to $[MP1 + 2H]^{2+}$, and shielded protonated MP1 from fragmentation induced by collisional activation within the DMS cell. This behaviour suggests that microsolvation provides analytes with a solvent "air-bag," which could play a role in retaining native-like ion configurations during DMS separations that operate well above the low-field limit.

Chapter 4, titled Protonation-Induced Chirality Drives Separation by DMS, explores a fascinating phenomenon that can be probed by DMS. In short, chiral species possessing a permanent stereocenter and a prochiral, tertiary amine can form two diastereomers upon protonation during electrospray ionization. The resulting diastereomers exhibit distinct conformations that are resolvable by DMS, constituting the first measurement of this behaviour in the gas phase. Protonation-induced chirality appears to be a general phenomenon, as *N*-protonation at the tertiary amino moiety of 13 chiral compounds that contained a prochiral, tertiary amine moiety. The analytical utility of DMS is further exemplified in **Chapter 5**, where DMS and tandem mass spectrometry (MS) were used to distinguish a set of seven cannabinoids. Detection of analytes as argentinated species (*i.e.,* $[M + Ag]^+$ adducts) also led to the discovery that argentination promotes distinct fragmentation patterns for each cannabinoid, enabling their partial distinction by tandem-MS. By adding DMS to the tandem-MS workflow, each cannabinoid was resolved in a pure N_2 DMS environment, allowing for accurate assessment of cannabinoid levels within commercial products with excellent accuracy and limits of detection/quantitation.

In addition to the analytical utility provided by DMS and the other ion mobility spectrometry (IMS) techniques, IMS-based separation prior to mass spectrometry has become an invaluable tool in the structural elucidation of gas phase ions and in the characterization of complex mixtures. Application of ion mobility to structural studies requires an accurate methodology to bridge theoretical modelling of chemical structure with experimental determination of an ion's collision cross section (CCS). **Chapter 6** discusses the software package MobCal-MPI, which was developed

to calculate CCSs efficiently and accurately at arbitrary field strengths via the trajectory method, including those accessed during DMS experiments. While significant progress has been made towards modelling the phenomenon of differential mobility, there are still several properties that have yet to be captured by *in silico* models. This thesis concludes with **Chapter 7**, which outlines unresolved issues in the field and suggests several directions in which future research endeavours can be directed.

Acknowledgements

While I can't possibly do justice to everyone who has contributed to my academic journey within the limited space here, I am compelled to acknowledge some of the most important individuals. Foremost among them is my brilliant supervisor, Prof. W. Scott Hopkins, who has been a guiding force in my scientific career since he took me under his wing as an eager undergraduate in 2014. Scott's mentorship has provided me with opportunities that my 19-year-old self could only dream of, including playing with lasers, delving into the crazy world of high-performance computing architecture, and not getting upset that I used around 200 years of computing time within my first six months in the group. Many lessons have been learned since then, and I'm glad we've laughed about it over beers, shared other great stories, and vibed over some stellar tunes. Thank you for being an amazing supervisor and making my graduate school journey truly memorable. I can't wait to see everything that we will accomplish with the establishment of WaterFEL.

Next, I would like to express my heartfelt appreciation to my esteemed committee members and highlight their invaluable contributions. First and foremost, I owe a debt of gratitude to Prof. Terry McMahon; his guidance and support have been invaluable to me, not only in shaping my understanding of gas phase ion chemistry, but also in inspiring me to approach science with humility, openness, and a willingness to learn. Terry's love for road bikes and Friday afternoon "meetings," which were rarely related to science, were a beacon of light during the challenging times of the COVID-19 pandemic – I will always treasure our interactions and the wisdom you have imparted to me. Prof. Larry Campbell (together with Scott) deserves an equally large amount of gratitude as he was the one who ignited my passion for differential mobility and the abundance of information that can be extracted from the technique. His guidance also taught me everything I know about the SelexION DMS platform, as well as the tricks to troubleshoot its numerous annoying problems, which proved to be a lifesaver on many occasions when I broke the cardinal rule of "no new experiments on Fridays." I would also like to thank Prof. Rick Marta, who was the first professor I ever had since starting my undergraduate career in 2012 and has been a wonderful friend and role-

model ever since. Rick's mentorship style is one that I admire greatly, and one which I strive to emulate in my own interactions with others. Rick has a way of making even the most complex topics accessible and understandable, and his ability to break down concepts into manageable pieces has been instrumental in my academic success. On the topic of great mentors, I would like to express my gratitude to Prof. Erin Baker for her invaluable support and guidance. Despite your busy schedule leading her own research group and engaging in numerous leadership roles within the mass spectrometry community, you agreed to serve on my examining committee and offered valuable insights and feedback that have greatly shaped this research. Even outside of formal events, you have always been approachable and willing to share your expertise, made time to chat with me during conferences and answer my questions without hesitation or judgment. Your generosity and kindness have meant the world to me as a growing scientist, and I am truly grateful for her contributions to my academic journey. Finally, I would like to thank Prof. Brian Kendall; your input and the time you have taken out of your schedule to serve on my examining committee is truly appreciated.

Several other faculty members deserve recognition, as most of my successes can be attributed to the knowledge that I have acquired by being mentored by some of the most exceptional scientists around the world. Our entire Organic department laid the foundation of the knowledge I colloquially refer to as chemical intuition. Of particular note is Prof. Monica Barra, Prof. Scott Taylor, Prof. Mike Chong, Prof. Graham Murphy, and Prof. Eric Fillion – thank you all for teaching me what I know; I wouldn't be half the scientist that I am now without your guidance. I am particularly grateful to Prof. Betsy Daub, whose metabolism lectures were not only insightful, but also entertaining and the inspiration for naming the first Keats Way kitten.

I would like to extend an equally large portion of gratitude to several current and past Hopkins lab members, including Dr. Josh Featherstone, Dr. Jeff Crouse, Dan Rickert, Dr. Steve Walker, Zack Bowman, Arthur Lee, Dr. Patrick Carr, Dr. Luke Melo, Dr. Geoff Sinclair, Dr. Moaraj Hasan, Dr. Mike Lecours, Dr. Emir Nazdrajic, Chris Ryan, and Shannon Lemmens. The work presented in

this thesis would not have been possible without the help of this army of exceptionally intelligent individuals. A few lab members and collaborators deserve special recognition, the first of which is Dr. Alexander Haack, whose willingness to help others no matter how busy he was is a trait few possess, and one which I aspire to have. I'll always value our friendship and collective taste in beer and music. Dr. Neville Coughlan deserves equal recognition, as he is one of the most intelligent and humble people I have encountered throughout my academic career. Thank you for teaching me about the wonderful (but also terrible) world of OPOs, and for fueling my love of beer with your delicious home brew. You have been, and always will be missed in the Hopkins lab, and I hope our paths cross again soon. Last and certainly not least is the person who kept our lab functioning throughout most of the tenure in the Hopkins group. Dr. Nour Mashmoushi, your contributions to the lab deserve a lot more recognition than you have received during your tenure here. Not only did you spearhead the maintenance and upkeep of our instruments, but you also did so much work behind the scenes and never asked for recognition. You are one of the most selfless people I have ever known, and I regret not getting to know how awesome of a person you are earlier in my degree – you and Henry are so fun to chat with, and I wish you nothing but the best for the remainder of your career.

Of course, none of this research would have been possible without the generous support from our SCIEX collaborators: Dr. Yves Le Blanc, Dr. Brad Schneider, and Dr. Mircea Guna. Their expertise in mass spectrometry instrumentation and their willingness to discuss results and provide support for our instruments (for free, too!) were invaluable to the success of my research. I couldn't have accomplished as much as I have throughout my time as a graduate student without these experts in my corner, and words cannot express how thankful I am for their contributions.

Throughout my tenure at UW, I have also had the privilege of mentoring several students, including Lynne Murdoch, Ben Friebe, Louis Nguyen, and Brad Howie, who all deserve recognition for their hard work. Justine Bissonnette and Patrick Thomas deserve special recognition for being two of the hardest-working undergraduate students I've had the pleasure of working with. Not only

is their work ethic stellar, but they are also wonderful individuals who have enriched my experience in the Hopkins group. I am grateful for the opportunity to mentor and work alongside such talented students, and I hope we continue to stay in touch.

Then of course, there is my family, who have been nothing but supportive throughout my entire academic journey despite rarely understanding what I am talking about. To my dad, Frank Ieritano, thank you for being such an amazing father. You raised me to be curious, to question everything, and to strive for excellence in everything I do. Your hard-working mentality has been a guiding force for me ever since I was a kid (albeit an annoying one), and I will always be grateful for your tireless efforts to help me achieve my goals. To my mom, Cathy Ieritano, thank you for being such a great role-model to me. Your kindness, compassion, and hard-working personality helped shape the person I am today. From teaching me how to live independently, you have equipped me with the tools I need to succeed in life, although I don't think I will never be able to fold clothes as good as you can. To my brother, Frankie Ieritano, and my sister-in-law, Christina Ieritano, thank you both for being such great role models and someone to whom I could always look up to. Your unwavering encouragement has been invaluable to me, and I cannot thank you enough for everything you've done. I particularly appreciate the time we've spent together playing games. Those moments of relaxation and fun have been a welcome respite from the stress and demands of academia. Your willingness to engage in these activities with me, even when you may have had other things to do, has meant the world to me. I am incredibly fortunate to have had such a loving and supportive family by my side throughout my PhD; I love you all more than words can express.

I am also grateful to my other families who were instrumental in helping me maintain my sanity throughout grad school. First and foremost, a heartfelt shout-out goes to the Old School RuneScape crew: Dr. Joshua Featherstone, Dr. Braden Kralt, Mark Zanon, Dr. Mike Lecours, Yaroslav Gorban, Zack Bowman, Molly Forward, and Hunter Hughes. We spent many (though some might say *too* many) hours playing this game, reliving our childhoods, clicking the same trees, and progressing in an otherwise meaningless world, but holy heck was it ever fun. From the thrill of living vicariously

through Brado's RNG to the hilarious moments of our notorious dry streaks at raids, our adventures brought us together and created bonds that I will always treasure. Thank you for being there for me, and for making grad school a little more bearable.

Next, I would like to thank the UW Cycling Club and my cycling friends (especially Lily Southcott) for their camaraderie and the stories, beers, and ice cream we've shared over the years on our rides. I would also like to apologize to any of my cycling friends who have unfortunate enough to be downwind of me after consumption of said ice cream, as my body doesn't handle milk sugars well. Then of course, there is the core group of humans who have been a part of my academic journey since the beginning, whose names in no particular order are Dalia Naser, Rafael Mirabel, Ryan Moreira, Ryan Garner, Jen Aguiar, and Will Nippard. It speaks volumes that we've remained friends since meeting you all in 2015, even after several heated bouts of Monopoly, Mario Party, and Mary-o Kart. Dalia, Raf, and Ryan (a.k.a. the Keats Way goon squad) each deserve their own special shout outs, as you three have been my rock throughout my academic journey, always there to lend an ear or provide a much-needed distraction from the stresses of grad school. Whether we were enjoying a game night, or just hanging out on the couch, you all have made my grad school experience so much better. Dalia, thank you for being such an amazing friend. You have stuck by my side through countless puzzle adventures (even when I intentionally moved the pieces around to mess with you), and you have never once given up on me. You deserve a medal for tolerating my nonsense, which I know can be a bit much at times; your unwavering loyalty and dedication to our friendship means the world to me, and I hope there is much more House/Hell's Kitten/Top Scallop in our future. Raf, you and I have been through it all together, from epic battles in Dungeons & Dragons to unravelling the layers of Mario Party, N64 Style. It sucked when you were the first of the Keats Way crew to graduate, as the house just wasn't the same without you. Nevertheless, I am so proud of everything you've accomplished and the life you and Alex are building in Toronto - you'll always be one of my best friends. Ryan, where do I even begin? You are one of the smartest and hardest-working people I know, and your drive and determination have always inspired me to be better. Ever since we met in second year, I knew that you were going places. And now, as a post-

doc, you have already accomplished so much and are well on your way to achieving even more (probably more than anyone else I know). I miss having you around, but I am so excited to see where your journey takes you next. I can't wait for you to be back in the country so we can share stories, beers, and most importantly, the 2022 Ieritano Estates vintage.

I would like to give a special shout-out to my animal companions, as I don't think I could have survived a PhD without them. Betsy Jones Keats, James Francis Keats, and the newest addition, Freya Jean Margaret, were there for me during the good days and the bad, offering unwavering love and support when I needed it most. Unfortunately, we had to say goodbye to Francis recently, and while it breaks my heart to think about him, I know he's watching over us from the great cat tree in the sky. I am forever grateful for the joy and comfort these animals have brought into my life, and I can't imagine going through my PhD journey without them.

Francis (left) and Betsy (right)

Freya Jean Margaret

Dedication

This thesis is dedicated to my friends, family, and kittens, whose collective support kept me sane throughout the arduous journey of doing a PhD in Chemistry.

Table of Contents

List of Figures

List of Tables

List of Equations

List of Abbreviations

2TT	Two-temperature theory
ACE	Acetone
AgOAc	Silver acetate
AIA	Agriculture improvement act
Arg	Arginine
ATD	Arrival time distribution
B3LYP	DFT functional of Becke, Lee Yang, and Parr
BH	Basin hopping
BSA	Bovine serum albumin
CAD	Collision gas pressure
CBC	Cannabichromene
CBD	Cannabidiol
CBG	Cannabigerol
CBN	Cannabinol
CCS	Collision cross section
CCSD(T)	Coupled cluster singles, doubles, and perturbative triples
CI	Confidence interval
CID	Collision induced dissociation
CoM	Center/centre of mass
CREST	Conformer-Rotamer Ensemble Sampling Tool
CV	Compensation Voltage
CXP	Collision cell exit potential
DEA	Drug enforcement administration
DFT	Density Functional Theory
DFTB	Density functional based Tight Binding
DIMS	Differential Ion Mobility Spectrometry
DLPNO-CCSD(T)	Domain-based local pair natural orbital CCSD(T)
DMO	DMS offset potential
DMS	Differential Mobility Spectrometry
DMSO	Dimethyl sulfoxide
DP	Declustering potential
DR	DMS resolving gas
DT	DMS heater setting. Note that DT > T_{bath}

DTIMS	Drift-tube ion mobility spectrometry
EHSS	Elastic hard sphere scattering
EP	Entrance potential
ESI	Electrospray ionization
FAIMS	Field-asymmetric waveform ion mobility spectrometry
FWHM	Full-width half-maximum
GPB	Gas phase basicity
HF	Hartree Fock
His	Histidine
HPC	High-performance computing
IID	Ion-induced dipole
imp	Number of impact parameters sampled during each itn cycle by MobCal-MPI
IMS	Ion mobility spectrometry
inp	Number of relative velocities sampled during each itn cycle by MobCal-MPI
IPA	Isopropyl alcohol
IQ	Ion-quadrupole
itn	Number of cycles of mobility calculations employed by MobCal-MPI
LC	Liquid chromatography
LIT	Linear ion trap
LOD	Limit of detection
LOQ	Limit of quantitation
Lys	Lysine
m/z	Mass to charge ratio
mAb	Monoclonal antibody
MAE	Mean absolute error
MAPE	Mean absolute percent error
MC	Monte-Carlo
MD	Molecular dynamics
MeCN	Acetonitrile
MK	Merz–Singh–Kollman
ML	Machine learning
MP1	Polybia-MP1; IDWKKLLDAAKQIL-NH2
MP2	Second-order Møller–Plesset perturbation theory
MQ	Methylquinoline
MQOH	Methylquinolin-8-ol

MRM	Multiple reaction monitoring
MS	Mass spectrometry
NVE	Number of particles, volume, and energy
NVT	Number of particles, volume, and temperature
PA	Proton affinity or projection approximation
PES	Potential energy surface
PM7	Parameterized model 7
ppb	Parts per billion (ng/mL)
ppm	Parts per million (µg/mL)
psi	Pounds per square inch
RFR	Random forest regression
RMSD	Root mean square deviation
RMSE	Root mean square error
RRCK	Ralph Russ Canine Kidney
SSCS	Systematic sampling of cluster surfaces
SV	Separation voltage
$SV@CV_{min}$	The SV in which the CV reaches a minimum of a Type B dispersion curve
SV_{pp}	Separation Voltage (peak-to-peak) - used interchangeably with SV
SY	Survival yield
Tbath	Bath-gas temperature
Td	Townsend; unit for reduced field strength. 1 Td = 10^{-21} V $\cdot$ m^2
Teff	Effective temperature
THC	Tetrahydrocannabinol
TM	Trajectory method
TMAO	Trimethylamine-N-Oxide
TWIMS	Travelling wave ion mobility spectrometry
UFF	Universal forcefield
vdW	van derWaals
ΔG_{ass}	Gibbs energy of association

Quote

...yes idealism, yes the dignity of pure research, yes the pursuit of truth in all its forms, but there comes a point I'm afraid where you begin to suspect that the entire multidimensional infinity of the Universe is almost certainly being run by a bunch of maniacs.

Douglas Adams, The Hitchhiker's Guide to the Galaxy

Chapter 1

A primer on microsolvation and its influence on ion mobility

1.1 The importance of ion-solvent clusters

The investigation of gas-phase clusters continues to garner attention amongst global academic community, with their appeal driven by the diverse range of physicochemical properties they exhibit.[1–3] As one might expect, the term "cluster" encompasses a vast range of chemical entities, prompting researchers to focus their efforts on a specific type of cluster (*e.g.*, metal clusters, carbon clusters), which is typically motivated by an interest in a particular property and/or application (*e.g.*, optical, magnetic, catalytic).[4–8] Our group is interested in small molecules and molecular ions within dynamic microsolvation environments, whereby a small number of solvent ligands continually condense and evaporate from a central analyte. Heteromolecular ion-solvent clusters, or more appropriately "microsolvated" ions, can be viewed as a model for insipient solvation[9] and may provide insight into the chemistry occurring within, for example, atmospheric water droplets.[10] Depending on number of solvent ligands contained within the cluster, the physicochemical properties of the microsolvated analyte can be akin to those of the condensed phase or to the properties of the gas phase species.[11–15] For example, in cases where the gas phase and condensed phase analyte structures differ, the degree of microsolvation can dictate whether the gas phase or condensed phase favoured isomer will be present in the experimental ensemble.[16–18] The number of solvent ligands required to transition between the preferred gas and condensed phase isomers depends on the analyte. In fact, there is no "back-of-the-envelope" method that can estimate this quantity, or the number of solvent ligands required to observe the onset of different condensed phase properties (*e.g.*, electronic or vibrational spectra,[19–24] molecular conformation,[15,25,26] and chemical reactivity).[27]

To discern the cluster sizes at which structural transitions occur, one can study microsolvated clusters with mass spectrometry (MS) such that specific cluster sizes can be selected by their mass to charge ratio (m/z) and probed individually (*e.g.*, with trapped ion spectroscopy).[17] Because MS is insensitive to cluster geometry, supplementary characterization by ion mobility spectrometry (IMS) is often used in tandem with MS to provide information about the cluster's geometric configuration.[25,28–32] Thus, researchers can interrogate mass-selected microsolvated species to monitor the evolution of an analyte's geometric structure as it is sequentially solvated.

Drift-tube IMS (DTIMS) can provide information about a microsolvated cluster's geometry by monitoring its size dependent drift time through the IMS cell.[33,34] In a traditional DTIMS experiment, a charged analyte is pulsed into an inert collision environment under the influence of a weak electric field. The velocity of the ion through the drift cell (v_D) depends on the mobility of the ion through the specific gas (K) and the strength of the electric field (E) applied, as described by **Eq. 1.1**.

$$v_D = KE \qquad \textbf{Eq. 1.1}$$

If the electric field strength is sufficiently low (< 10 Td; 1 Td $= 10^{-21}$ V $\cdot$ m^2), then the ion's velocity responds linearly to changes in the electric field. Since DTIMS experiments are performed near or below this low-field limit, one can determine the mobility of an ion from its measured velocity,[35] which can then be related to its geometric structure via the Mason-Schamp relation by **Eq. 1.2**,[36,37]

$$K = \frac{\sqrt{18\pi}}{16}\sqrt{\frac{1}{m_{ion}}+\frac{1}{m_{gas}}}\frac{ze}{\sqrt{k_B T}}\frac{1}{\Omega}\frac{1}{N} \qquad \textbf{Eq. 1.2}$$

where m_{ion} is the ion molecular mass, m_{gas} is the molecular mass of the buffer gas, z is the charge of the ion (*e.g.*, +2), e is the elementary charge, k_B is the Boltzmann constant, T is the temperature, N is the number density of the gas, and Ω is the ion-neutral collision cross section (CCS). The ion's CCS represents the orientationally averaged collision area of the analyte with the buffer gas that fills the drift cell. To determine molecular geometry, the experimentally measured CCS is compared to the CCSs calculated for candidate structures, the latter of which are typically conducted via

quantum chemical calculations. The subsequent determination of CCSs generally requires simulation of the collisions between the ion and the neutral collision partner,[38] which is discussed in detail in **Chapter 6**.

By performing IMS-MS characterizations of mass-selected microsolvated clusters, one can infer how the geometry of a microsolvated analyte evolves with the degree of solvation. For example, the Russell group measured the mobilities of microsolvated diaminoalkanes with varying alkyl chain lengths.[26] They found that when a specific number of water molecules were coordinated to the doubly-charged analyte, an abrupt structural transition occurred that corresponds to the transition point between the preferred gas phase and condensed phase configurations. Although studies such as this provide remarkable insight regarding gas phase ion structure, it is unclear as to whether these microsolvated systems are good models of bulk solvation. In the condensed phase, the primary solvation shell is dynamic – the number and configuration of the solvent ligands within the primary solvation shell is never fixed. Thus, in addition to studying steady-state fixed-geometry species, it is beneficial to investigate microsolvated clusters whose composition and geometry varies temporally.

The study of the temporal evolution of microsolvated species is possible with differential mobility spectrometry (DMS), an IMS technique that employs time-dependent electric fields that can be used to drive dynamic ion microsolvation.[39–42] During the high-field portion of the applied waveform, field-induced acceleration of the ion results in high-energy collisions between the ion and background gas, which increases its effective temperature (T_{eff}) via collisional excitation. Conversely, collisional cooling lowers the internal energy of the ion as the electric field transitions from the high-field to the low-field portion of the waveform. If solvent vapour is seeded into the DMS carrier gas, modulating the ion's temperature with the dynamic electric field can drive cycles of evaporation and condensation of the neutral solvent moieties around the analyte. One can take advantage of this phenomenon in two ways. First, because species with the same m/z but different geometries have different interaction strengths with solvent molecules, slight differences in ion-solvent clustering propensities can be leveraged to enhance mobility-driven gas phase separations.[43–50] Second, if the

field-induced heating is modulated such that an analyte undergoes many cycles of solvent condensation and evaporation, one effectively samples the ion-solvent interaction potential of the analyte. Since solvent clustering in DMS tends to occur near sites of high partial charge on the analyte, it may mimic the dynamics of solvation in the primary solvent shell of the condensed phase.[51] Although it is unclear how closely the dynamic DMS clustering environment resembles the condensed phase, we have demonstrated that the clustering behaviour observed in the DMS device correlates with other gas phase and condensed phase physicochemical properties, the details of which are provided in **Chapter 2**.[51,52]

The study of the temporal evolution of microsolvated species is possible with differential mobility spectrometry (DMS), an IMS technique that employs time-dependent electric fields that can be used to drive dynamic ion microsolvation.[39–42] During the high-field portion of the applied waveform, field-induced acceleration of the ion results in high-energy collisions between the ion and background gas, which increases its effective temperature (T_{eff}) via collisional excitation. Conversely, collisional cooling lowers the internal energy of the ion as the electric field transitions from the high-field to the low-field portion of the waveform. If solvent vapour is seeded into the DMS carrier gas, modulating the ion's temperature with the dynamic electric field can drive cycles of evaporation and condensation of the neutral solvent moieties around the analyte. One can take advantage of this phenomenon in two ways. First, because species with the same m/z but different geometries have different interaction strengths with solvent molecules, slight differences in ion-solvent clustering propensities can be leveraged to enhance mobility-driven gas phase separations.[43–50] Second, if the field-induced heating is modulated such that an analyte undergoes many cycles of solvent condensation and evaporation, one effectively samples the ion-solvent interaction potential of the analyte. Since solvent clustering in DMS tends to occur near sites of high partial charge on the analyte, it may mimic the dynamics of solvation in the primary solvent shell of the solution phase.[51] Although it is unclear how closely the dynamic DMS clustering environment resembles the solution phase, our group demonstrated that the clustering behaviour observed in the DMS device correlates with other gas-phase and solution-phase physicochemical properties.[51,52] Accordingly, the focus of

my doctoral dissertation revolves around the continued development of DMS as a tool to screen the physicochemical properties of analytes that are of use in the drug design process. Concurrently, this investigation aims to uncover the core principles that drive chemical separations using DMS, thereby amplifying its effectiveness as a tool within the realms of analytical and medicinal chemistry.

1.2 The fundamentals of DMS

DMS,[40–43] which is also referred to as high-field asymmetric waveform ion mobility spectrometry (*i.e.*, FAIMS)[53] and differential ion mobility spectrometry (*i.e.*, DIMS),[54] is a powerful analytical tool capable of resolving enantiomeric,[43] regioisomeric,[44,45,49] tautomeric,[46,50] and structurally similar[47,48] analytes prior to characterization with methods such as tandem MS. The principles of DMS are similar to those of traditional IMS technologies (*e.g.,* DTIMS, travelling wave IMS)[55,56] in that ions are distinguished based on mass, charge, and geometric structure. However, the chemical and physical phenomena that underpin DMS take advantage of the non-linear dependence of ion mobility on the electric field when field-strengths *exceed* the low-field limit. As per **Eq. 1.1**, an ion's drift is velocity is directly proportional to the strength of the electric field (E).[36,57] A linear dependence of drift velocity with field strength is only observed in the low-field limit, where any increase to the ion's T_{eff} (and hence, its drift velocity) is negligible compared to the drift velocity of the ion at the temperature of the experiment (typically 298 K). Operating above the low-field limit promotes collisional activation of the ion, causing its T_{eff} to increase. At which point, the ion's drift velocity no longer changes linearly with respect to the applied electric field, the nature of which is described by **Eq. 1.3**, where $\alpha(E)$ is the fractional change of an ion's high- field mobility, $K(E)$, with respect to its low-field mobility, $K(0)$. $\alpha(E)$ is often expressed as an even-numbered power series whereby alpha coefficients weight the applied electric field (see **Eq. 1.4**), which is usually described in terms of the reduced field strength (*i.e.,* E/N).[58–60]

$$K\left(\frac{E}{N}\right) = K(0)\left[1 + \alpha\left(\frac{E}{N}\right)\right] \quad \textbf{Eq. 1.3}$$

$$K(E) = K(0)\left[1 + a_2\left(\frac{E}{N}\right)^2 + a_4\left(\frac{E}{N}\right)^4 + a_6\left(\frac{E}{N}\right)^6 + \cdots\right] \quad \textbf{Eq. 1.4}$$

Consider the waveform shown in **Figure 1.1A**. The waveform is a sum of two sinusoids, one at 3 MHz and the other at 6 MHz,[39] phase-shifted by 90 degrees such that high-field and low-field components are created; the high-field element comprises one-third of the duty cycle and the low-field elements comprises the remaining two-thirds. Although the high- and low-field components have equivalent but opposite areas, a differential mobility exists because the ion's mobility during the high-field portion of the DMS waveform is not linearly proportional to its mobility during the low-field portion. High- and low-field mobilities that are not linearly proportional induce unequal displacements orthogonal to the transmission axis, resulting in migration of the ion from a stable trajectory. As a gas flow carries the entrained ions through the DMS cell, the asymmetric waveform (known as the separation voltage, SV) causes ions to migrate continually off-axis in a zig-zag light pattern (**Figure 1.1B**, black trace). Ions can be steered back onto the transmission axis by application of a static compensation voltage (CV), which offsets the SV such that the integral over a single duty-cycle is no longer zero (**Figure 1.1B**, red trace). Ions will be transmitted through the DMS device when the applied CV causes the ions to travel the *same* distance away from and then back to the transmission axis over the course of the SV duty cycle.

The CV required to transmit an ion of a given m/z and molecular geometry will depend on the magnitude of the SV and the conditions within the DMS cell (*i.e.*, temperature, pressure, gas composition). One can garner insight into the ion-neutral interaction potential by monitoring how the CV changes as a function of SV in a specific DMS environment. For weakly interacting collision environments (*i.e.*, those dominated by hard sphere collisions), the ion's mobility diminishes as the strength of the electric field increases due to the rising apparent viscosity of the gas, which intensifies with higher field strengths.[61] In this case, the ion requires increasingly positive CVs to be transmitted through the DMS device as the amplitude of the SV increases. Practitioners refer to this as Type C

behaviour (**Figure 1.2**),[62] which corresponds to increasingly negative values of the $\alpha(E)$ parameter (see **Eq. 1.3**).

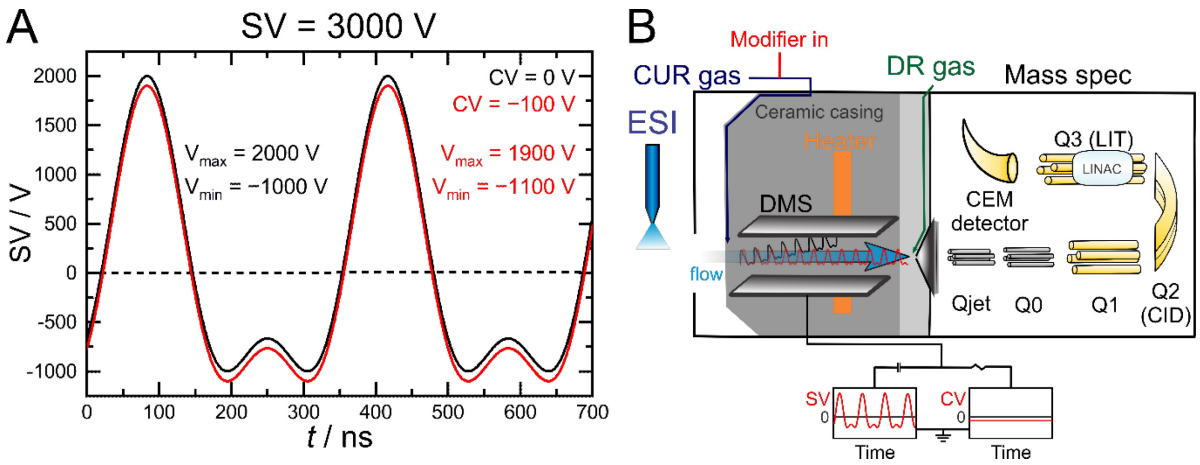

Figure 1.1. (**A**) The SV waveform applied across the planar electrodes of the differential mobility spectrometer. The black trace shows the waveform for SV = 3000 V and CV = 0 V, and the red trace shows the waveform for SV = 3000 and CV = −100 V. (**B**) A schematic diagram of the planar DMS cell and QTRAP 5500 hybrid linear ion trap (LIT)/triple-quadrupole mass spectrometer. The black and red traces indicate representative ion trajectories when the voltages shown in panel A are applied to the planar electrodes; application of the correct CV steers the ion through the DMS cell and towards the detector.

Seeding the DMS carrier gas with a low partial pressure of a polar solvent vapour alters the collision environment with respect to the apparent viscosity experienced by the analyte ions, and can lead to dynamic ion microsolvation.[42,63] As the SV waveform transitions from the high-field to the low-field component, ions in the DMS cell decelerate following collisions with the carrier gas. This collisional cooling promotes cluster formation through ion microsolvation, which leads to an effective increase in the ion CCS. Consequently, ion-solvent clustering causes an apparent decrease in ion mobility under the low-field condition. As the SV transitions back to the high-field condition, the ion-solvent cluster accelerates and experiences relatively energetic collisions with the carrier gas. These collisions impart significant internal energy to the cluster, which increases its T_{eff}. Heating of the cluster during the high field component promotes desolvation, resulting in a reduction of apparent CCS and an increase in ion mobility. Thus, clustering environments exhibit *positive values*

of $\alpha(E)$ and induce off-axis migration of the ions in the direction opposite to that experienced under hard-sphere scattering conditions.

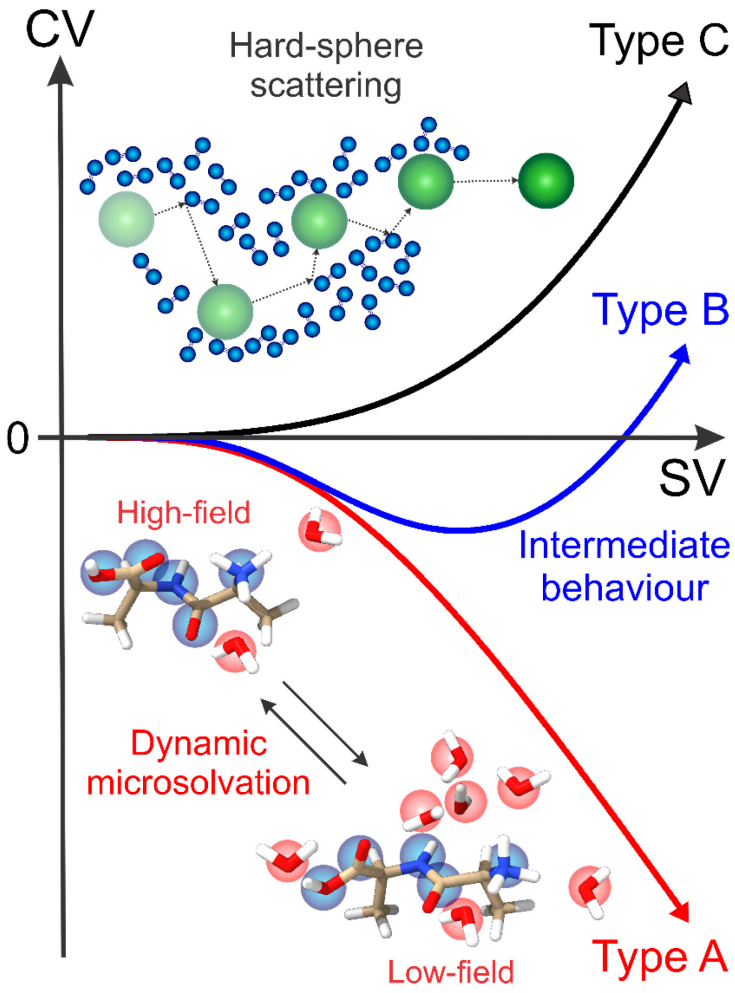

Figure 1.2. Dispersion plots reveal the nature of the ion-neutral interactions occurring within the DMS cell. The three most common behaviours are strong dynamic clustering (Type A; red), weak dynamic clustering (Type B; blue), and hard sphere scattering (Type C; black).

If dynamic clustering processes persist throughout all SVs, the CV required for optimal ion transmission decreases with increasing SV. This is known as Type A behaviour and is indicative of a strongly clustering environment. In some cases, enough energy can be imparted to the ion at a particular SV such that ion-solvent cluster formation is inhibited during the low-field condition. In

this situation, the CV required for optimal ion transmission decreases with increasing SV until a threshold SV is reached, leading to a CV minimum. At SVs beyond the CV minimum, CVs become increasingly positive since ion-solvent clustering becomes disfavoured thermodynamically. Practitioners refer to this intermediate "switching" behaviour as Type B.

Intermolecular interactions between the analyte molecules and the collision gas dictate whether Type A, B, or C behaviour will be observed. In DMS environments composed of a weakly interacting gas (*e.g.*, N_2), analyte dispersion curves are typically Type C in nature.[39,62] Notable exceptions tend to occur for smaller analytes that contain localized and unprotected charge sites (*e.g.*, *N*-protonated propylamine), which can interact with N_2 via relatively strong charge/induced-dipole and charge/quadrupole interactions.[64] When the N_2 environment is modified with solvent vapour, analyte species can experience additional charge/dipole interactions and hydrogen bonding interactions with the solvent modifier. One can approximate the relative strength of these ion-solvent interactions based on the solvent molecule's dipole moment. However, care should be exercised since additional solvent-solvent interactions and differences in ion-solvent cluster geometries can subvert this correlation. For example, consider the DMS behaviour of tetramethylammonium.[63] When the N_2 collision environment is doped with 1.5% (v/v) of a polar, protic modifier (*e.g.*, H_2O, MeOH, *i*PrOH), Type B clustering behaviour is observed. Doping the DMS carrier gas with polar, aprotic modifiers such as acetone (ACE) or acetonitrile (MeCN) results in Type A behaviour, which indicates a stronger clustering interaction between the analyte and solvent molecule. However, the observed clustering propensity of N_2 < H_2O < MeOH < *i*PrOH < MeCN < ACE does not strictly follow the solvent dipole moment trend of m_{N_2} (0.0 D) < m_{IPA} (1.66 D) < m_{MeOH} (1.69 D) < m_{H_2O} (1.81 D) < m_{ACE} (2.91 D) < m_{MeCN} (3.92 D). The origin of this discrepancy stems from differences in the ion-neutral interaction potentials for the various solvent systems. In other words, the analyte's affinity for one microsolvation partner versus another depends on the number of solvent molecules that can accrete onto the analyte, the geometries of the nascent ion-solvent clusters, and how strongly the solvent molecules bind to the accretion sites. Understanding how dissimilar clustering

behaviours translate into unique DMS behaviours requires atomistic insight of the microsolvated ion, which can be ascertained through quantum-chemical calculations.

1.3 Computing cluster structures, energies, and thermochemistry

Modelling differential ion mobility requires the consideration of: (1) the geometries, relative energies, and populations of the ion-solvent clusters present during a DMS experiment, and (2) how the field-dependent mobility of each solvent cluster affects the mobility of the microsolvated ensemble. Ion-solvent cluster geometries can be determined by taking "snapshots" from molecular dynamics (MD) simulations, wherein the number of particles, volume, and energy (NVE) of the system is fixed. However, obtaining accurate energies and thermochemistry for each MD snapshot requires high-level quantum chemical calculations since MD energies do not adequately capture the thermochemistry of the cluster. These quantum chemical calculations can be prohibitively expensive depending on the size of the system; even for small, tractable molecular clusters, the associated potential energy surface (PES) can be of high dimensionality. To address this challenge, we use targeted methods to map low energy regions of the PES. PES mapping is typically performed using a basin hopping (BH) or the systematic sampling of cluster surfaces (SSCS)[65–68] algorithm to identify candidate low energy cluster structures,[69–71] which are subsequently refined using higher levels of theory (**Figure 1.3**).

Upon mapping the cluster PES, candidate isomers can be sorted based on energetics and geometry to identify unique cluster structure.[72] For the cluster systems and sizes that we study, typically fewer than 100 unique candidate cluster structures are refined using low-level electronic structure theories such as Density Functional based Tight Binding (DFTB)[73,74] or the semi-empirical parameterized model 7 (PM7).[75] These methods approximate the Hartree-Fock (HF) formalism,[76] where certain 2-electron Hamiltonians are either omitted or replaced by a set of parameters identified for analogous systems. Although the cluster geometries predicted by DFTB and PM7 are similar to those predicted by higher level *ab initio* theory, the electronic energies and thermochemical corrections require further refinement. Density Functional Theory (DFT)[76] calculations provide the

necessary improvement to molecular geometries, electronic energies, and thermochemical data such that microsolvated cluster populations can be determined with sufficient accuracy.[64,77,78] When appropriate DFT functionals are used (*i.e.,* hybrid/long-range corrected functionals or those that contain empirical dispersion corrections), benchmarking suggests that the resulting DFT energies and thermochemical data can be used to accurately reproduce experimentally measured binding energies, vibrational spectra, and reaction barriers.[79–83] We direct readers to reference 83 for guidance on selecting a DFT functional for a specific chemical purpose. We typically employ the ωB97X-D3BJ/Def2-TZVPP level of theory when performing DFT calculations to determine vibrational frequencies and/or relative isomer populations. Using this level of DFT theory, one can also accurately map the cluster electrostatic potential to determine atomic partial charges, which are required for CCS calculations (see **Chapter 6**).

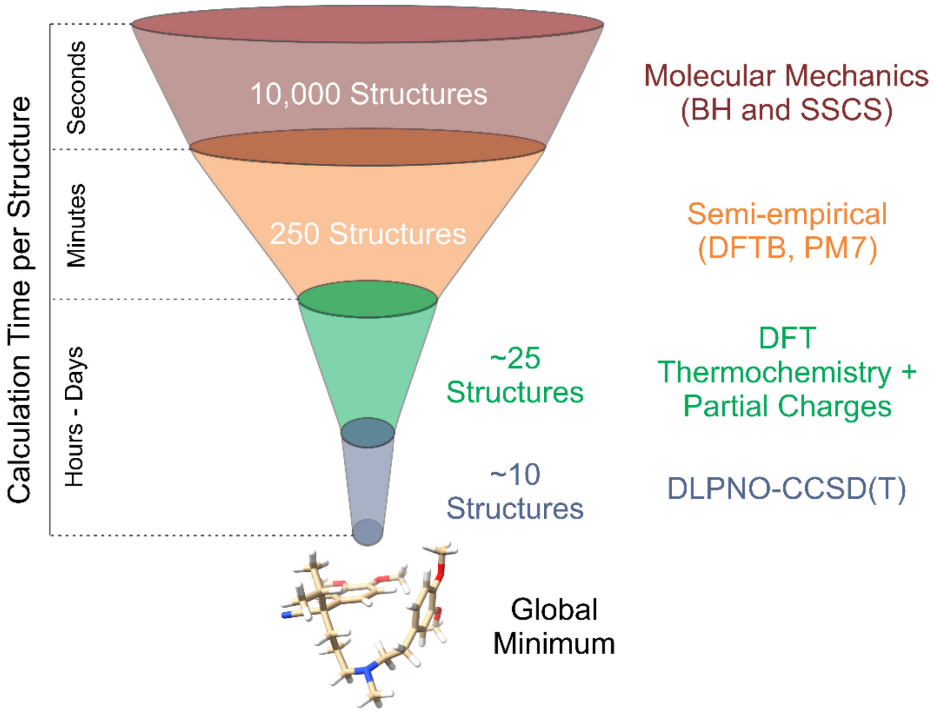

Figure 1.3. The process of calculating cluster geometries, relative energies, and thermochemistry requires refinement using progressively higher levels of quantum-chemical theory.

It is worth noting that the thermochemistry computed using DFT methods relies on harmonic vibrational frequencies, which can fail to accurately capture ion-solvent interactions in highly anharmonic systems (*e.g.*, hydrogen-bonded clusters).[84–86] This situation can become increasingly problematic as the size of the microsolvated cluster increases. In principle, one can circumvent this issue by computing anharmonic vibrational partition functions, but this comes at a high computational cost. Since most hybrid DFT functionals are parametrized to yield good thermochemistry with the harmonic approximation,[83] this considerable computational cost is not justified. Calculation accuracy can be improved by combining DFT-computed harmonic thermochemistry with electronic energies calculated at the coupled cluster level of theory, which is the "gold-standard" for computational accuracy. However, the N^7 scaling of coupled cluster methods also imposes a substantial computational cost and, depending on available computational resources, may be impractical for some chemical systems (*e.g.*, those with more than *ca.* 150 electrons). Much of the computational cost for CCSD(T) calculations (*i.e.*, coupled cluster singles, doubles, and perturbative triples) stems from computing electron-electron correlations for *every* electron-electron pairing in the molecule. One can therefore reduce calculation times (and achieve relatively accurate results) by considering only local electron correlations. The domain-based local pair natural orbital (DLPNO) coupled cluster methods implemented in the ORCA software package achieves comparable accuracy to CCSD(T) (< 5 kJ mol^{-1}),[87–90] but scales linearly with the number of electrons in the system.[91–93] Thus, DLPNO-CCSD(T) energies combined with DFT thermochemistry yield accurate and efficient calculations of ion-solvent cluster thermochemistry, facilitating their usage in understanding an analyte's DMS behaviour and, by association, using DMS to predict the physicochemical properties of the ion embedded within the ion-solvent cluster.

Chapter 2

Correlating DMS behaviour with molecular properties

2.1 Direct correlations between an analyte's DMS behaviour and its condensed phase properties

To this point, we have established that an ion's DMS behaviour is governed by the interaction potential between the ion and its collision partner(s). For example, Type A and B behaviours are usually observed when DMS experiments are performed in an environment conducive to forming a microsolvated cluster. However, Type A/B classifications do not adequately describe the strength of the ion-neutral interactions, which means that an ion's clustering propensity cannot be assessed quantitatively. So how can we show the correlation between clustering propensity and a dispersion curve? Recall that Type B DMS behaviour exhibits a characteristic minimum CV as the SV increases ($SV@CV_{min}$). This minimum can be thought of as the point where the heating supplied to the analyte under the high field condition begins to overcome the ion cooling and clustering processes that occur during the low field condition. Simply put, the $SV@CV_{min}$ can be viewed as the field condition under which dynamic ion-solvent clustering and declustering processes are most prominent. It stands to reason that the $SV@CV_{min}$ for an ion should correlate with an analyte's affinity for the solvent modifier, which can be represented by the calculated binding energy between an ion and a single solvent ligand (*e.g.,* ΔG_{ass}; see **Eq. 3.6** in **Chapter 3.7**). However, this correlation method requires the observation of a minimum in the dispersion curve, which precludes Type A ions. One can circumvent this limitation by realizing that Type A curves are the early portion of Type B curves, where the $SV@CV_{min}$ occurs at a SV greater than the highest SV that can be achieved experimentally. As such, one can extrapolate the $SV@CV_{min}$ of a Type A dispersion curve by fitting the existing data to a function and finding its minimum. Since dispersion curves resemble a skewed Gaussian distribution that has been reflected along the x-axis, our group devised a function that

mimics this qualitative observation. The empirical function is shown in **Eq. 2.1**, where a, b, c, and d are fit parameters.

$$CV = \left(\frac{1}{d}\right)\left[(a - SV)\,exp\left(-\frac{(a - SV)}{b + [(c)(SV)]}\right)\right] \qquad \textbf{Eq. 2.1}$$

Figure 2.1A shows the calculated single-solvent binding energies (zero-point energy corrected) for clusters containing single solvent molecules plotted against the SV@CV_{min} values for a variety of Type A and B analytes. Calculated ion-solvent binding energies (zero-point corrected) were collated from several previously published works using the CCSD(T)/6-311++G(d,p)//B3LYP-D3/6-311++G(d,p) level of theory.[51,52,63,94] The data show a clear correlation between ion DMS behaviour and affinity for solvent modifiers in several modified collision environments (*i.e.*, N_2 seeded with 1.5 mol% of H_2O, MeOH, IPA, MeCN, or acetone). First, we note that all the tetraalkylammonium species in the dataset lie on the red dashed (bottom) trend line shown in **Figure 2.1A**. Since solvent molecules predominantly interact with the tetraalkylammonium species via charge-dipole interactions, we expect that other molecules interacting with the solvent through charge-dipole interactions will also lie near this trendline. Linear regression indicates that measuring the SV@CV_{min} of these species enables prediction of the respective ion-solvent binding energies to within 2.6 kJ mol^{-1}. Also observed is an analogous trend for protonated 2-methylquinoline (2MQ) and 2-methylquinolin-8-ol (2MQOH) derivatives,[51,52] for which quantum chemical calculations show that solvent molecules interact with the analyte via hydrogen bonding at the charge site. Linear regression of this data series yields an error of 7.1 kJ mol^{-1}, a value that is somewhat inflated owing to three outliers (8-nitro-2MQ, 8-amino-2MQ, and 7-Cl-2-MQ-8-OH). The calculations indicate that these outliers exhibit electronic and steric interactions that differ somewhat from the other quinoline species, which in turn disproportionately impact the analyte's affinity the solvent ligands.[51,52] Removing these outliers decreases the error to 2.9 kJ mol^{-1}, similar to that observed for the tetraalkylammonium species. In the case of tri-, di-, and mono-alkylammonium ions, we observed that ion-solvent binding energies and SV@CV_{min} values increase as steric hinderance around the charge site is reduced. As one might expect, these species lie between the charge-dipole and hydrogen

bonding trendlines on the correlation plot since solvent accretion occurs through hydrogen-bonding interactions at the charge site, which becomes increasingly de-shielded as the number of alkyl substituent decreases.

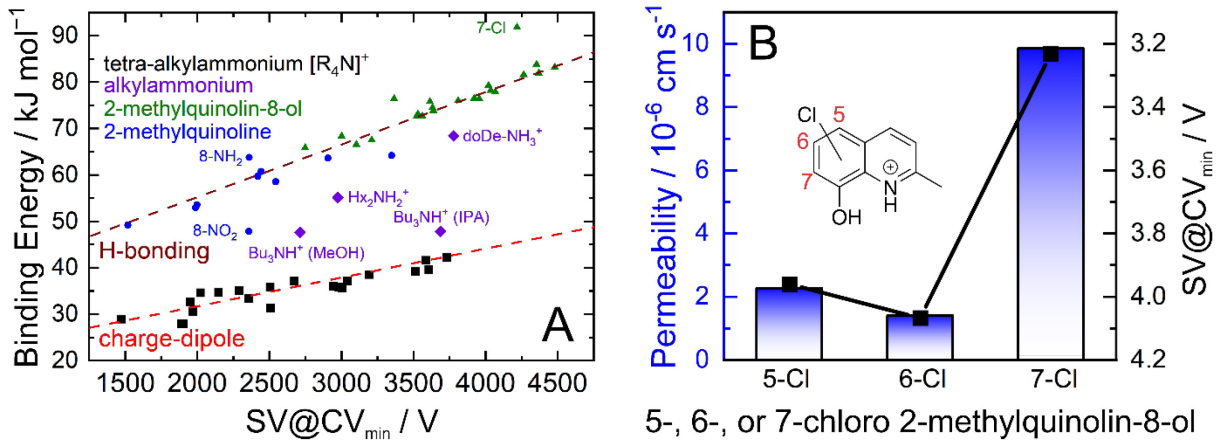

Figure 2.1. (**A**) Zero-point corrected binding energies for single solvent clusters of tetraalkylammonium (black), alkylammonium (purple), 2-methylquinolinium (blue), and 2-methylquinolin-8-ol ions (green). Clusters bound by charge-dipole interactions are highlighted with the bright red dashed trendline towards the bottom of the panel. Clusters bound by single hydrogen bonds are highlighted by the maroon dashed line near the top of the panel. Clusters bound by hindered hydrogen bonds are scattered between the two dashed trendlines. Binding energies are calculated at the CCSD(T)/6-311++G(d,p)//B3LYP-D3/6-311++G(d,p) level of theory. (**B**) The RRCK passive cell permeability (blue bars) and SV@CV$_{min}$ (black points) for three positional isomers of chloro-2-methylquinolin-8-ol.

Having identified correlations between DMS-measured clustering behaviour and ion-solvent binding energies, we explored the possibility of correlation with other molecular physicochemical properties related to the analyte's interaction with solvent.[51,95,96] Indeed, when investigating a series of 2-methylquinolin-8-ol derivatives, strong correlations were discerned between an analyte's DMS behaviour and its condensed phase properties such as pK$_A$, pK$_B$, and passive cell permeability.[51] **Figure 2.1B** shows the measured *in vitro* passive cell permeability for 5-, 6-, and 7-substituted chloro-2-methylquinolin-8-ol overlayed with the measured SV@CV$_{min}$ for the protonated analytes in

a MeOH-modified DMS environment. Passive cell permeabilities were measured using the Ralph Russ canine kidney (RRCK) cell-based assay.[97] This strong correlation suggests that the subtle structural differences between the quinoline isomers influences their respective solvent binding energies, which in turn affects their ability to navigate biological barriers. In other words, species that are more water soluble (*i.e.*, more strongly clustering) are less likely to shed their aqueous solvation shell in favour of the hydrophobic environment of a lipid bilayer, thus slowing transport across the cell membrane and reducing the rate of passive diffusion into a cell.

Of course, ion-solvent clustering in the DMS environment is not constrained to a single solvent ligand, which raises the question of why bulk-phase properties should correlate so well with DMS dynamic clustering behaviour. To answer this, we must consider how the population of the microsolvated ensemble changes throughout the SV duty cycle. At the SV@CV_{min}, modelling shows that protonated 3-bromoquinoline clusters with one solvent ligand are populated for most of the duty cycle (see **Figure 4C** in reference 64). Protonated 3-bromoquinoline has only one hydrogen bond donor and the first solvent molecule binds to this site of strongest interaction as the analyte is sequentially solvated.[52] Since this site is the position at which incipient solvation is thought to initiate, the single-solvent cluster can be considered the "most important" species for the solvation process. Although this scenario seems to explain our observations for small molecule systems, the situation is more complicated for larger molecules with multiple solvent accretion sites. Addressing a wide variety of molecular types and sizes requires treatment with machine learning (ML) to correlate DMS behaviour with condensed phase properties.

2.2 Employing ML to predict an ion's DMS behaviour *in silico*

Using DMS for molecular property determination is a desirable prospect given that data acquisition is automated, rapid, and requires only nanograms of material. These attributes suggest that DMS could be used during pre-clinical drug screening, where the physicochemical properties of

thousands of compounds need to be assessed with high throughput.[98,99] However, the SV@CV_{min} correlation methodology that we developed within **Chapter 2.1** is not entirely satisfactory, as Type C analytes do not exhibit a characteristic SV@CV_{min}. Moreover, extrapolation of the SV@CV_{min} for Type A ions can be inaccurate if an insufficient portion of the analyte's dispersion curve has been sampled (*i.e.*, if the SV@CV_{min} is too far beyond the highest SV accessible by the instrument). Further still, correlations between molecular properties and SV@CV_{min} can only be made for analytes within the same molecular class (*e.g.*, the tetraalkylammoniums *or* the quinolines in **Figure 2.1B**). These limitations of the SV@CV_{min} correlation method diminish the potential value of DMS as a tool for property determination, as an ideal method would be one that can treat all types of dispersion curves.

Recall that the field-dependent mobility of an ion is encoded within the compensation voltage (CV) required for transmission through the DMS cell, as the CV is related to the alpha function,[39] and by association, the ion's CCS. Based on this first-principles consideration, mapping the field-dependent mobility should be feasible using only the intrinsic properties associated with the ion's mobility (*i.e.*, mass and CCS). Haack and coworkers made a first step in this regard by reproducing the DMS behaviour of the tetramethylammonium[77] and tricarbastannatrane ($[N(CH_2CH_2CH_2)_3Sn]^+$)[78] cations using only temperature dependent CCS calculations in the free molecular regime. Given the reasonable accuracy of this approach, we hypothesized that dispersion plots could be generated *in silico* using ML models trained only with CCS and m/z as inputs. This follows the absence of a closed-form expression that can relate the ion-neutral interaction potential with the ion's field-dependent mobility. Using ML to complete this connection would enable predictions of dispersion plots using only intrinsic ion properties that are accessible via CCS libraries[100–107] or calculation packages.[108–110] The ability to model the CV required for analyte transmission would be of tremendous utility for method development within the various 'omics realms, where the CV space exhibited by the desired analytes could be mapped prior to data acquisition with minimal effort. However, broadly applicable predictions of an ion's DMS behaviour necessitate the use of a calibration set spanning several chemical classes, CCSs, and m/z ratios. As

a first step in our endeavour to map DMS behaviour in general, we report on the ML-based *in silico* generation of dispersion plots in an N_2 environment for a compendium containing 409 molecular cations.

2.2.1 Database curation

For the ML-based methodology to be applicable across several chemical classes, the compounds present in the database must be: (1) chemically diverse and (2) have consistent, reproducible CCSs against which to calibrate. To this end, we have generated a library consisting of 409 compounds that include a series of 2-methylquinoline derivatives,[52] 2-methylquinolin-8-ol derivatives,[51] previously characterized small drug molecules and acrylamides,[96] pesticides,[111] and a wide variety of biomolecules (*e.g.*, amino acids, small molecule xenobiotics, and nucleobases).[112]

Curation of experimentally measured CCSs for all 409 analytes used in this study would have been preferable, especially given the exceptional interlaboratory agreement of CCSs acquired using the DTIMS platform.[113] However, several of the molecules studied have yet to be characterized by linear IMS and the instrumentation to perform experimental CCS measurements for these species was not at our disposal. In principle, one could retrain our ML models using experimental CCSs should those measurements come available. We instead opted to train the ML models using CCSs calculated by MobCal-MPI to maintain internal consistency rather than select CCSs from the various libraries present in the literature,[100–107] as experimental CCSs for the same compounds determined by DTIMS and TWIMS can exhibit deviations of up to 6%.[114] MobCal-MPI has been shown to calculate CCSs in N_2 with a root mean square deviation (RMSD) of 2.2% for geometries generated at the B3LYP-D3/6-31++G(d,p) level of theory,[115] and should serve as a viable alternative until experimental CCSs become available. The m/z and CCS distributions of the compounds studied here are shown in **Figure 2.2**, which span the range of 76 – 540 Da and 110.8 Å^2 – 235.7 Å^2, respectively.

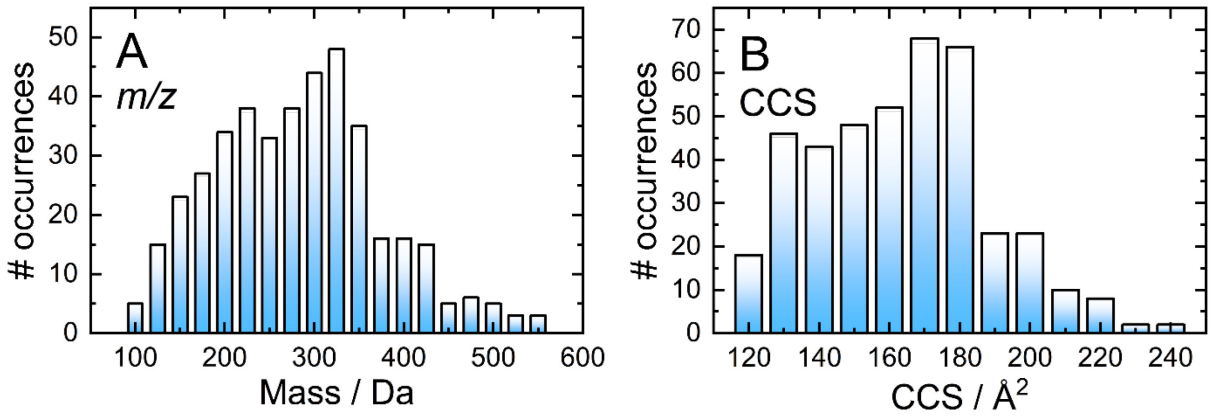

Figure 2.2. **(A)** m/z and **(B)** CCS distributions of the 409 species examined in this study. m/z values are binned in groups with a 25 Da range and CCS values are binned in groups with a 10 Å^2 range.

2.2.2 Experimental details

A planar SelexION differential mobility spectrometer with a 1 mm gap-height (SCIEX, Canada) was mounted in the atmospheric region between the sampling orifice of a QTRAP 5500 hybrid triple quadrupole linear ion trap mass spectrometer and a Turbospray electrospray ionization (ESI) source (SCIEX). This instrumental setup has been described extensively in the literature and is shown in **Figure 1.1B**.[39,41,42]

All data acquisition was acquired by direct infusion of the analyte mixtures into the ESI source. Analytes were solubilized in either a 50:50 MeOH:H_2O or MeCN:H_2O solvent mixture, both of which contained 0.1% formic acid. Analyte mixtures contained 10 ng mL^{-1} of each species and were infused into the ESI source operating in positive mode at a flow rate of 10 µL min^{-1}. The ESI probe was set to 5500 V and ambient temperature. A nebulizing gas pressure of 30 psi and an auxiliary gas pressure of 10 psi was introduced to the ESI source to aid in desolvation. N_2 was used as source gas, the curtain gas in the DMS cell (20 psi), and as the collision gas (*ca.* 7 mTorr) for data acquisition in multiple reaction monitoring (MRM) mode. The following settings were employed in Analyst 1.7 for the ion optics: entrance potential (EP) of 10 V, collision cell exit potential (CXP) of 15 V,

declustering potential (DP) of 100 V, DMS offset potential (DMO) of −3 V, and a collision gas (CAD) setting of low (2 psi).

DMS experiments to map ion differential mobility were conducted using a heater setting of 150 °C, which corresponded to a bath gas temperature of 100 °C.[77,116] DMS measurements consisted of stepping the SV from 1500 V to 3000 V in 500 V increments and in 250 V increments thereafter up to SV = 4000 V. At each SV, the ion current was monitored as the CV was scanned from −10 V to 30 V in increments of 0.1 V to produce an ionogram. Each ionogram is fit with a Gaussian distribution, for which the centroid is taken as the CV that corresponds to maximum ion transmission. The CV required for maximum ion transmission at a particular SV was recorded for each ion. The m/z of the parent ion and the CV required for elution at SV = 1500, 2000, 2500, 3000, 3250, 3500, 3750, and 4000 V were collated and used as the inputs for training the ML model.

2.2.3 Computational details and CCS calculations

The ions considered in this study were either protonated molecules (*i.e.*, $[M + H]^+$) or those with permanent positive charges (*e.g.*, quaternary ammonium groups). For the protonated species, all possible protonation sites for each molecule were explored computationally. In cases where protonation sites or molecular conformations could not be easily assigned by inspection, the PES of the molecular ion was mapped using a custom-written BH script that was interfaced with Gaussian 16 (Version C.01).[117] For BH searches,[65–67,86,118] ions were modelled with the Universal Force Field (UFF),[70] which used partial charges for a 'guess structure' calculated at the B3LYP-D3/6-31+G(d,p) level of theory[119,120119,120] according to the Merz–Singh–Kollman (MK) partition scheme.[121,122] At each step of the BH algorithm, all rotatable dihedral angles were randomly distorted by $-10° \leq \Phi \leq 10°$. In total, 5000 to 20000 structures were sampled depending on the size of the ion in question (larger species required more sampling). Typically, the BH routine would identify 5 – 100 low-energy conformers for each molecular cation. Candidate structures were then carried forward for pre-optimization at the semi-empirical PM7 level of theory and subsequently sorted based on cosine similarities.[75,123] For details on cosine similarities, see reference 72. Unique conformers within

50 kJ mol^{-1} of the PM7 global minimum were then treated at the B3LYP-D3/6-31++G(d,p) level of theory. Normal mode analyses were conducted to verify that each structure corresponded to a minimum on the PES. These calculations were also used to estimate the gas phase thermochemical quantities (enthalpy, entropy, and Gibbs energy) for each species.

The MobCal-MPI code, a tool that was developed as part of my PhD work (see **Chapter 6**), was used to calculate ion-neutral CCSs in N_2 (Ω_{N_2}). All CCS calculations involved 10 complete cycles of mobility calculations that used 48 points of velocity integration and 512 points of impact parameter integration. Calculated Ω_{N2} values are reported as average values with standard deviations ($< 1.5\%$) assessed from the 10 cycles of calculation. For ions exhibiting multiple low-energy conformations or prototropic isomers, a Boltzmann-weighted CCS is reported based on the standard Gibbs corrected energies ($T = 298.15$ K) as determined by DFT. The ML source-code, which employs the Random Forest Regression model as implemented in the Python Sci-kit Learn package, and associated benchmarking data is available on the Hopkins Laboratory GitHub repository (https://github.com/HopkinsLaboratory).

2.2.4 Results and discussion

The field-dependent nature of the interaction potential between the analyte and DMS carrier is an important metric to consider when modelling an ion's field-dependent mobility. Qualitative insights in this regard can be inferred from the analyte's dispersion curve (*i.e.*, plots of the CV required for optimal ion transmission as a function of SV).[42,124] For example, three dispersion curves from the 409 molecules evaluated in this study are shown in **Figure 2.3A**; these represent the most common behaviours observed in DMS experiments. In a dry N_2 environment, dispersion curves are predominantly Type C in nature, whereby the ion-neutral interaction potential results in a hard-sphere scattering event upon collision. Type C ions are characterized by increasingly positive CV shifts for optimal ion transmission as the SV increases (*e.g.*, protonated atenolol; black curve). As the molecular weight of the ion decreases or charge sites become "exposed," the interactions between the analyte and carrier gas become stronger and, rather than hard-sphere behaviour, analytes exhibit

behaviour associated with dynamic clustering. The clustering phenomenon can manifest in one of two ways depending on the binding strength of the adduct formed. Type B behaviour is characterized by CVs that initially decrease with increasing SV before reaching a minimum, upon which CVs trend towards more positive values. This is interpreted as arising from weak clustering interactions under low-field conditions, which are eventually overcome at high-field. Dimetridazole (blue trace) is a representative Type B ion that exhibits weak ion-neutral interactions with the carrier gas due to greater charge density within the analyte. Cluster formation can be long-lived in cases when the ion's charge is highly localized, resulting in Type A dispersion curves. In a dry N_2 environment, Type A behaviour is only observed in rare cares for low molecular weight ions and is characterized by continually decreasing CV shifts as the SV increases (*e.g.*, **Figure 2.3A**; glycine, red trace).

The range of CVs adopted by the 409 cations are shown in **Figure 2.2B**. At low SVs, the CVs of Type A, B, and C ions are similar. However, differential mobilities become more pronounced at higher SVs due to the field-dependence of ion mobility. At SV = 4000 V, the optimum CV for ion elution ranges from −26 V for glycine to +20 V for atenolol. Untargeted analysis would necessitate sampling this entire window to ensure adequate coverage of the chemical space even though most ions are Type C and elute within the CV = 0 – 15 V window (**Figure 2.3C**). As it stands, there are no "rules" for predicting an ion's DMS behaviour, which presents a significant challenge for coupling DMS-MS to some front-end interfaces (*e.g.*, LC). Introduction of the desired analytes to the DMS cell within a short time window precludes a full scan of the CV range, necessitating predictive technologies to facilitate method development in tandem separation workflows the incorporate DMS.

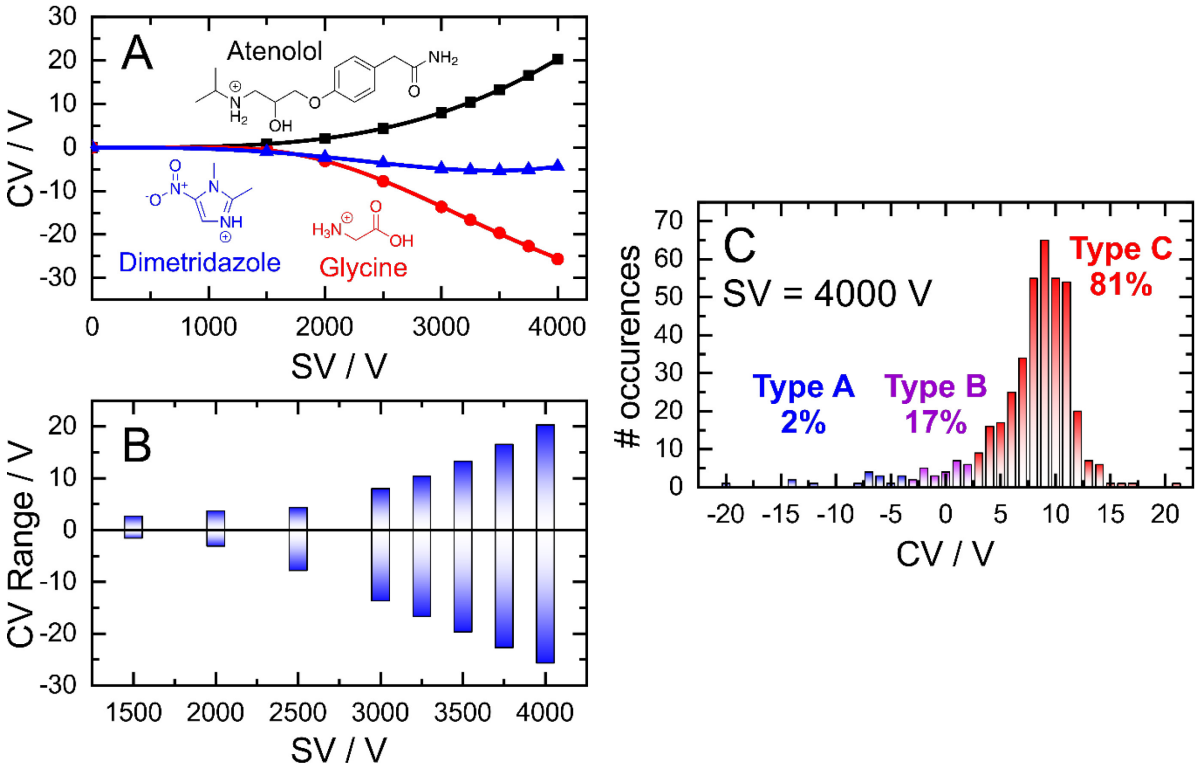

Figure 2.3. (**A**) Dispersion curves for protonated atenolol (black squares), protonated dimetridazole (blue triangles), and protonated L-glycine (red circles). (**B**) The range of CV values for given SV values for the 409 molecules in our dataset and their distributions (**C**) at SV = 4000 V according to their Type A (blue), B (purple) or C (red).

Modelling the dispersion curves (*i.e.*, the DMS behaviour) of an ion requires metrics that capture the ion-neutral interaction potential. This is especially important in the case of the dataset used here, where 331 ions exhibit Type C behaviour but only 72 and 6 ionic species exhibit Type B and A behaviours, respectively. The interaction potential is heavily influenced by the charge density and conformation of the ion, both of which can be reasonably captured through the ion's m/z and CCS.[77,78] However, the broad distributions of m/z and CCS within this dataset (*cf.* **Figure 2.2**) requires an ML framework to incorporate these properties in the prediction of an ion's differential mobility.[96] One must also be cognisant of bias, variance, and overfitting in the chosen ML model, all of which contribute to poor predictive capabilities for systems outside of the training set. Random Forest Regression (RFR), an unbiased decision-tree-based model, has demonstrated low variance

and low susceptibility to overfitting.[125,126] The resistance to overfitting stems from the law of large numbers, which states that the average obtained from many trials will become closer to the expected (real) value as more trials are performed. As such, we employed a RFR algorithm to create a predictive model for DMS dispersion curve data utilizing 200 randomized decision trees as implemented in the scikit-learn Python package. To train the RFR framework, our DMS-MS database was randomly split into a training set and an "out-of-the-bag" external validation set using only analyte m/z and CCSs as inputs.

The mean absolute error (MAE) of the RFR predictions, averaged across 100 randomized training/validation set splits, is plotted as a function of training set size (*i.e.*, a learning curve) for SV = 4000 V in **Figure 2.4A**. Since the CV window occupied by the analytes is largest at SV = 4000 V, the associated MAE can be thought of as the upper limit of error for the RFR model. Training the RFR model using 95% of the database at SV = 4000 V predicts the corresponding CV with a MAE of 2.4 V. This is an encouraging result considering the relatively small size of the dataset and the limited number of parameters used in the ML framework. Excitingly, the MAEs associated with CV predictions typically lie within the full-width half-maximum (FWHM) range of a DMS peak (±1.5 V). It is also worth noting that the unguided learning curve shown in the top panel of **Figure 2.4A** does not plateau at large training set sizes. This implies that more accurate predictions using the unguided approach are to be expected as the DMS-MS dataset expands with the addition of information for more analytes.

Recalling that the proportion of Type A, B, and C ions within the database are 2%, 17%, and 81%, respectively, it is necessary to investigate the accuracy of model predictions for each different DMS behaviour. If a validation set is disproportionately composed of Type A or B ions, which have a relatively low representation in the data set, the MAE for the data set can be especially high. Conversely, if the validation set is entirely composed of Type C ions, the associated MAE will be low and not representative of the global accuracy. To ensure adequate validation, we performed an additional 1000 randomized trials using a 95:5 partition of the dataset for training/validation. The

deviations of calculated versus experimental CV values at SV = 4000 V are shown as a boxplot in **Figure 2.4B** according to their classification as a Type A, B, or C ions. For the unguided ML model (*i.e.*, just using m/z and CCS as input), dispersion curve predictions for Type A, B, or C ions exhibit average errors of –7.9, –2.3, and 0.6 V, respectively. The low errors for Type C ions from the out-of-the-bag external validation set demonstrates that the ML model is accurate to within the day-to-day variance in SV/CV pairs (typically the peak's FWHM).

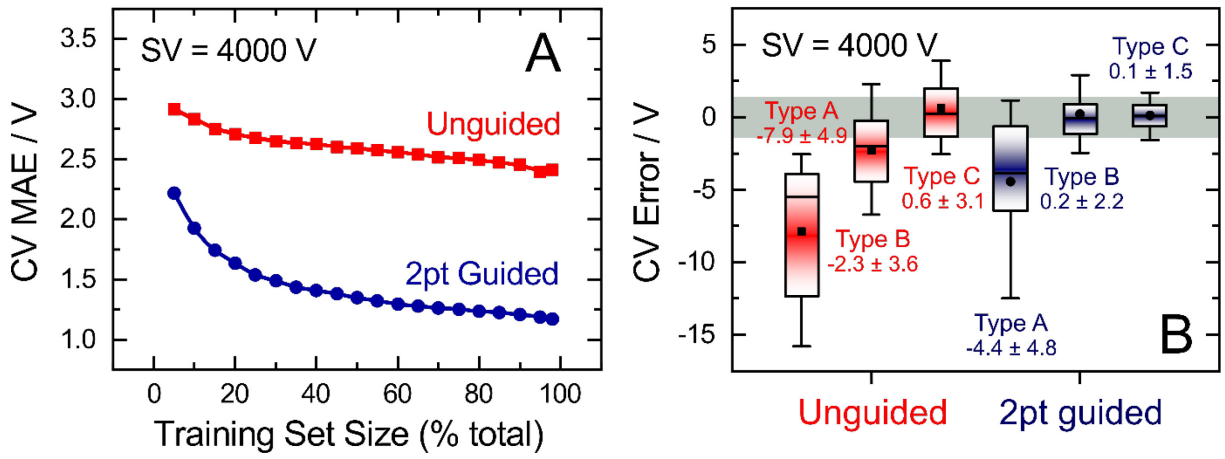

Figure 2.4. (**A**) Learning curve depicting the mean absolute error (MAE) for CV predictions as a function of training set size with inputs of m/z and CCS (unguided; red) and including CV values at SV = 1500, 2000 V (guided; blue). (**B**) Boxplot of CV error according to dispersion plot type for 1000 predictions at SV = 4000 using a randomized 95:5 training/validation split. The mean and median are shown as a black circle/square and solid black line, respectively. Boxes correspond to the 25th and 75th percentile; whiskers extend to the 10th and 90th percentile. The mean CV error and one standard deviation are shown as text. The green highlighted region corresponds to the typical FWHM of a peak in a DMS ionogram (± 1.5 V).

While predictions of Type C curves lie within the typical FHWM of the associated ionogram peak, the predictions for Type A and B ions are consistently at more positive CV values than those observed experimentally. Given that a general methodology for the prediction of all dispersion curves is desired, a guided ML approach was introduced. It should be noted that the RFR-predicted Type

A and B dispersion curves only deviate appreciably from experiment at SV > 2000 V. Therefore, we hypothesized that a "guided" ML model supplemented with CV values measured at SV = 1500 and 2000 V would provide the curvature required to capture Type A and B behaviour. Indeed, this was the case as demonstrated by the two-point guided learning curve and the distribution of errors. Although this procedure had only a marginal improvement on Type C curve predictions (average error 0.1 V), the overall predictive capability when all species were considered improved by a factor of two (**Figure 2.4A**; 1.2 V MAE for guided model). This improvement stems from the considerable error reduction in predictions of Type A and B behaviour, which exhibit average errors of −4.4 V and 0.2 V, respectively, for the guided model (see **Figure 2.4B**).

The success of the ML-approach in predicting an ion's DMS behaviour is further exemplified by analysis of the experimental and predicted dispersion curves. **Figure 2.5** shows three representative Type A, B, and C dispersion plots taken from a single validation set. The Type C behaviour of flufenoxuron is captured almost exactly by both the guided and unguided RFR approach, which is true for nearly all Type C ions in this study. Although the unguided ML model captures the shape of the Type A and B dispersion curves, the predicted CV values are *ca.* 2 V more positive at the high SV region of the curves. This shift to more positive CV values is consistently observed for predictions of the other Type A and B ions, likely arising from their under-representation in the training set (and thus positive skewing due to over-representation of Type C). The 2-point guided approach substantially improves predictions of Type B ions (*e.g.*, niacin) and, in some instances, produced a near exact prediction of Type A dispersion curves (*e.g.*, sarcosine).

2.3 Reverse engineering the ML-approach to predict an ion's low-field CCS from DMS data

The same ML-driven approach can be used to "reverse engineer" DMS dispersion curves such that CCS can be predicted. To begin the process of obtaining CCS values from the DMS workflow,

one must first evaluate the data that can be probed during a DMS-MS experiment. These include the parameters required for the ion swarm to successfully traverse the DMS device, but specifically those that relate to the $\alpha(E)$ as per **Eq. 1.3**, and hence, the zero-field CCS. Monitoring the SV/CV pairs required for the elution of a specific parent ion as a function of field strength provides a direct measure of that ion's differential mobility since the CV is directly related to $\alpha(E)$.[39] Plotting the requisite CV as a function of SV generates a dispersion plot, which provides direct insight into the ion's field-dependent mobility.

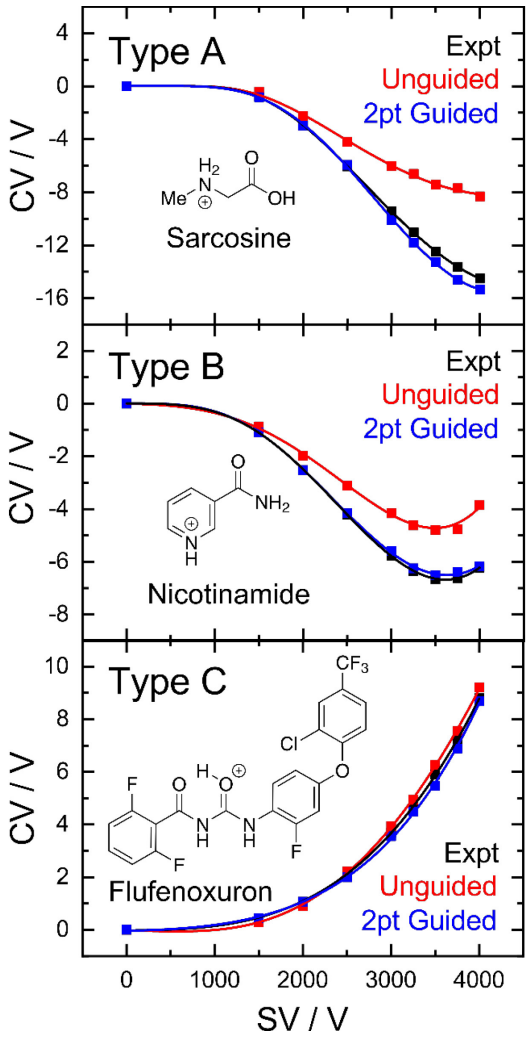

Figure 2.5. Experimental (black), unguided ML (red) and 2-point guided ML (blue) dispersion curves for (**top**) sarcosine, (**middle**) nicotinamide, and (**bottom**) flufenoxuron. The validation data was generated from a randomized 95:5 training/validation data split.

It follows then that isobaric species exhibiting dissimilar CCSs and/or disparate interaction strengths with the collision gas will exhibit unique differential mobilities that can be resolved by DMS. To ensure that ML modelling could capture subtle differences between isobaric species with different CCSs, 67 different groups of isobaric species (≥ 2 isomers per group) were included in this study. Representative Type B and C dispersion plots for these isobaric species are shown in **Figure 2.6**. **Figure 2.6A** shows the dispersion curves for the smallest isobaric set, choline (black curve) and protonated 4-aminobutyric acid (*i.e.*, GABA; red curve), both of which have m/z 104. **Figure 2.6B** shows the dispersion curves for one of the larger isobaric sets, protonated Clethodim (black curve) and Buscopan (red curve), both of which have m/z 360.

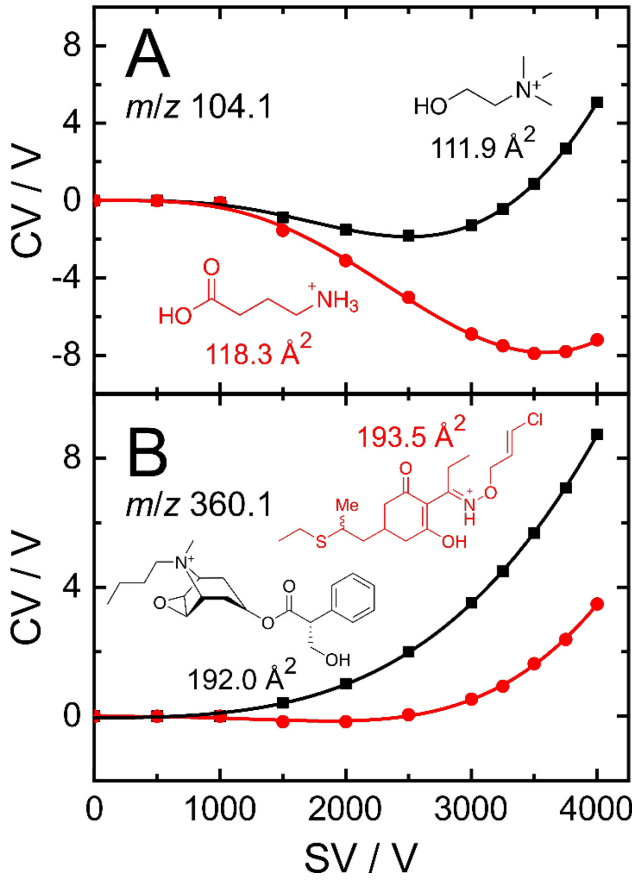

Figure 2.6. Dispersion plots of **(A)** choline (black squares) and protonated 4-aminobutyric acid (red circles), both of which have m/z 104.1, and **(B)** protonated Buscopan (black squares) and Clethodim (red circles) (both m/z 360.1).

In general, the species with the smaller CCS of the isobaric pair exhibits the more positive CV shift at a given SV. To rationalize this behaviour, recall that DMS probes the differential ion mobility under high and low electric field strengths. Isobaric species that are similar with respect to chemical class (*e.g.*, small flexible organic compounds) and charge type (*e.g.*, quaternary permanent charge) will exhibit similar differential mobilities owing to similarities in their field-dependent mobilities, and by association, their CCS. In contrast, isobaric species that are dissimilar with regard to molecular class (*e.g.*, large and flexible versus compact and rigid) or charge state will exhibit dissimilar differential mobilities. The nature of the charge site is the key differentiator in **Figure 2.6A**, where choline (111.9 $Å^2$) and GABA (118.3 $Å^2$) contain quaternary and primary amino moieties, respectively. The extensive shielding of the charge in choline mitigates the formation of clusters with N_2, which results in a reduced ion-neutral CCS and greater tendency for hard-sphere scattering interactions with the carrier gas relative to GABA. As the ion increases in size, charge dilution favours a shift to Type C hard-sphere interactions, but this is not always the case. Buscopan (192.0 $Å^2$) and Clethodim (193.5 $Å^2$) exhibit similar CCSs but dissimilar charge sites. Buscopan exhibits Type C behaviour, as was the case with the quaternary amine containing choline. On the other hand, Clethodim, whose charge is localized on the *O*-alkyl oxime, exhibits weak Type B behaviour. Connecting this qualitative behaviour of an ion's dispersion plot to its CCS requires the use of some empirical function. We are unaware of any current chemical theory or closed functional form that can correlate the specific DMS behaviour of an ion to its zero-field CCS. However, the fact that a trend exists between an ion's differential and zero-field mobility suggests that one can employ ML to "empirically" measure CCS from DMS behaviour.

RFR models were tested to determine which supervised ML methodology could best correlate an ion's differential mobility to its CCS.[125] Selection and training of the ML models involved finding a compromise between minimizing bias, variance, and overfitting. Bias in a model is associated with preselecting a functional description of the data whereas variance is associated with the agreement of the ML output between trials depending on how the data are partitioned between validation and training sets. RFR is an unbiased decision-tree based learner that typically yields low variance and

exhibits low susceptibility to overfitting,[125,126] which would lead to poor model applicability outside the range of inputs used for training. For our RFR model, we employed 200 randomized decision trees as implemented in the scikit-learn Python package to predict CCS from DMS-MS data by taking the average CCS determined by the "forest". To ensure low variance of the model, the DMS-MS database was randomly split into a model training set and an "out-of-the-bag" external validation set, which was subsequently utilized to assess model accuracy and overfitting. As a further test of variance, the RFR model was trained and validated 80 times using different seed integers to initialize the random forest and to split the database into randomized training and validation sets.

Figure 2.7 shows the learning curve (*i.e.*, error reduction as a function of training set size) for the RFR-based CCS calibration. The mean absolute percent error (MAPE) of the external validation set reaches *ca.* 2.6% at a training set size corresponding to 97% of the total dataset (396 molecules). In other words, the RFR model can use DMS-MS data for unknown biological/organic species to determine CCS to an accuracy of 2.63% on average. Note that an effectively linear increase in the accuracy of the ML predictions begins once the training set size reaches 85%. Based on this trend, we anticipate that inclusion of more compounds in the training set will continue to reduce the MAPE towards the $< 2\%$ limit expected for empirical CCS calibration procedures using TWIMS.[107,127,128] We hypothesized that introducing chemical class labels as ML learning features should further improve prediction accuracy, even though m/z and DMS dispersion curve data already correlate strongly with molecular CCS. By introducing a ClassyFire superclass label and re-training the RFR model, the MAPE is slightly reduced to *ca.* 2.57%, approaching the 2.2% root mean square deviation (RMSD) limit imposed by the MobCal-MPI methodology.[115] We expect that additional classification labels, such as intrinsic size parameters, will greatly improve the accuracy of the ML framework as other biologically relevant compounds are added to the training set (*e.g.*, peptides, lipids, and carbohydrates). However, we did not pursue this further in this initial study given the application to untargeted analyses, for which the identity of the analytes is not known.

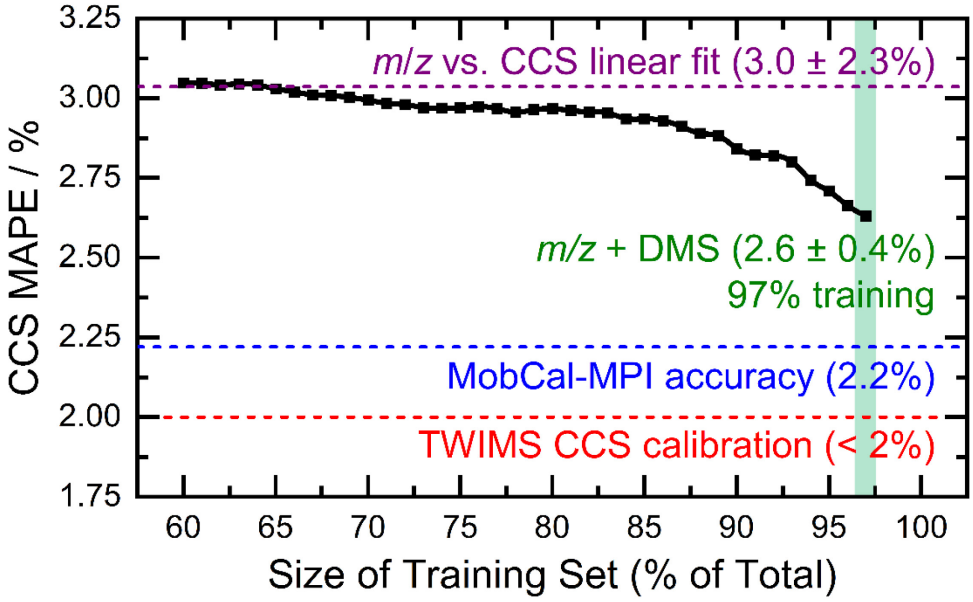

Figure 2.7. Mean absolute percent error (MAPE) for the RFR-based CCS predictions as a function of randomly selected training/validation splits (black line). Each data point is the average of 80 randomized trials. The purple dashed line indicates the MAPE for a linear regression model of m/z versus CCS for the dataset. The blue dashed line indicates the error limit associated with MobCal-MPI CCS calculations. The red dashed line shows the error expected for CCSs determined from calibrated TWIMS measurements.

Figure 2.7 additionally depicts the error associated with calculation of CCS using a functional fit of CCS versus m/z. For $m/z < 700$ Da, this correlation is best captured by a linear function between CCS and m/z rather than the square-root dependence defined by the Mason-Schamp relationship (**Eq. 1.2**). Calculation of CCSs using the linear fit returns predictions with a MAPE of 3.0 ± 2.3 %, indicating a substantial spread of errors compared to RFR. The improved accuracy and precision of the RFR-based CCS calibration becomes immediately obvious from **Figure 2.8**, which shows correlation plots for predicted versus target CCS values as determined by linear fit (**Figure 2.8A**) and for four training/validation sets the RFR model (**Figure 2.8B**). Although the RFR model is resistant to overfitting,[125,126] note that the training set is slightly overfit as evidenced by the lower MAPE (1.1%) compared to the MAPE from the out-of-the-bag external validation set (2.6%).

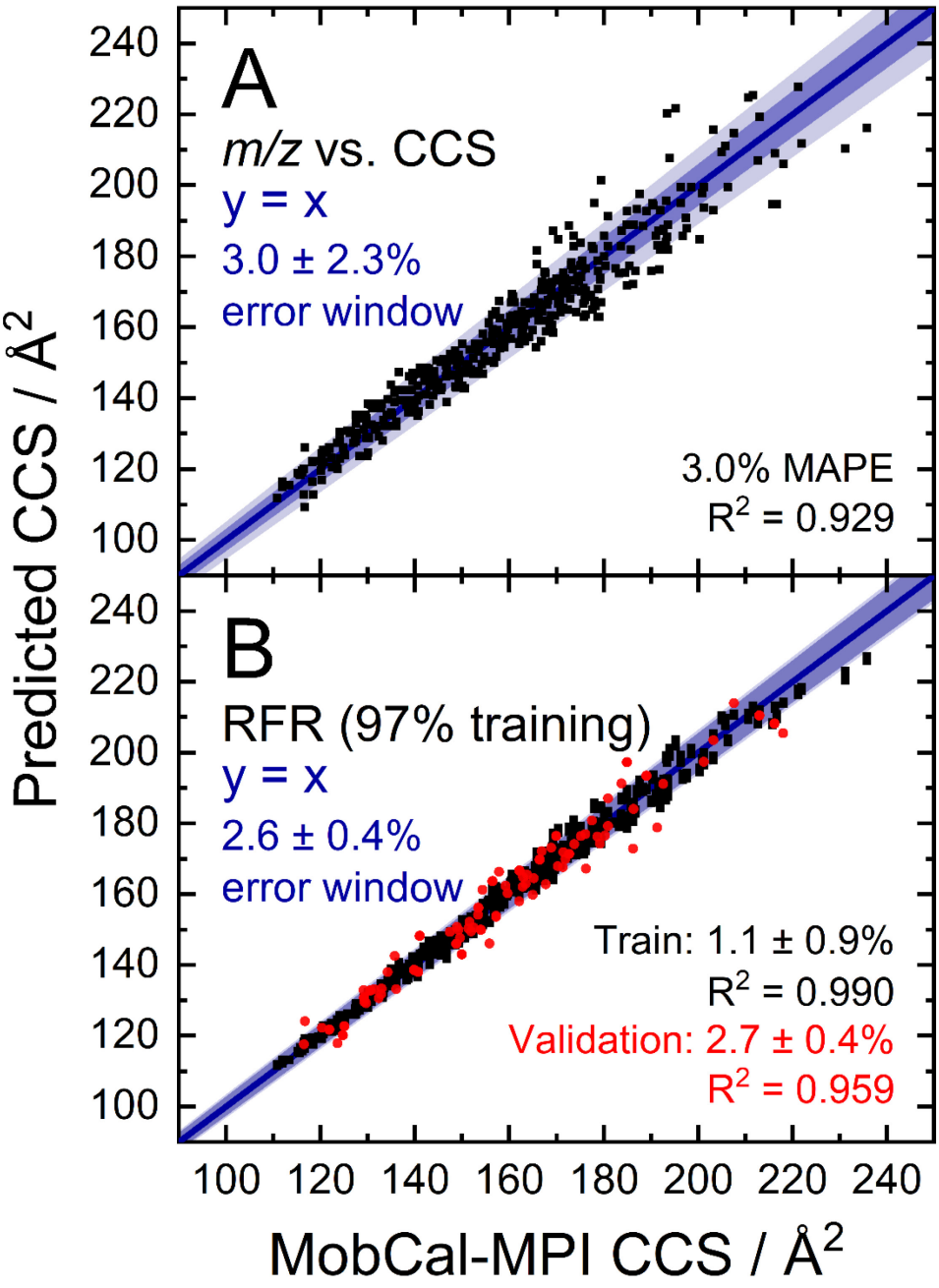

Figure 2.8. Correlation plots showing (**A**) CCSs determined using a linear fit of MobCal-MPI CCS versus m/z and (**B**) using the RFR ML model (97% training set) with m/z and DMS data as inputs. For (**B**), black squares show the data from four randomly generated training sets and red circles show data of the four associated external validation sets. The solid blue line corresponds to y = x and fit errors are displayed as bands with dark blue portion corresponding to the fit accuracy (MAPE) and transparent blue corresponding the fit precision (MAPE $\pm$ σ_{MAPE}).

The isomeric species in the database facilitate an additional means of assessing the accuracy of the RFR model. Whereas isomeric species cannot be distinguished within the linear fit model (since m/z is identical for all species within the group), DMS behaviour can be used as a distinguishing feature. As mentioned earlier, there are 67 groups of isomers in our DMS-MS database; 24 of these groups have three or more members. In examining the predicted CCS values for the members of these groups, we find that the MAPE = 1.0% and that the relative ordering of member CCS values across the group was correct in 81 % of cases (55 of 67 isomer pairs). These findings demonstrate the ability of the ML model to capture subtle structural differences that impact an ion's differential mobility. We expect that one could improve the accuracy of the ML model by including additional molecular descriptors (*e.g.*, molecular class, dipole moment, Morgan fingerprint, etc.). This improvement was demonstrated by Stienstra and coworkers in 2023,[129] but doing so required prior knowledge of the analyte's identity rather than relying on the observables available on the DMS-MS platform.

2.4 DMS measurements in a microsolvating environments facilitate prediction of molecular properties

Coupling ML with DMS experiments in a microsolvating environment enables predictions of an ion's condensed phase properties. In a microsolvating environment, ion trajectories are determined by m/z, CCS, and how the effective CCS of an analyte changes due to solvent accretion and dissociation as driven by the time-dependent electric field. For the ML model predictions of water solubility (*i.e.*, Log S) shown in **Figure 2.9**, DMS data recorded for a non-interacting environment (*e.g.*, pure N_2) and for a clustering environment (*e.g.*, 1.5 % MeOH in N_2) were employed as features along with m/z and computed CCS. The data set is comprised of 334 analytes and, rather than record data at low SV where ion trajectories are poorly distinguished from one another, measurements were taken in ΔSV = 500 V increments from 1500 V to 3000 V, then in ΔSV = 250 V increments to 4000 V. Water solubilities were calculated using OPERA, a chemoinformatic

tool that can use SMILES codes to estimate molecular physicochemical properties (*i.e.,* water solubility).[130] Clearly, it would be preferable to demonstrate ML model performance using experimentally measured values, but these values were not available for the molecules in our data set.

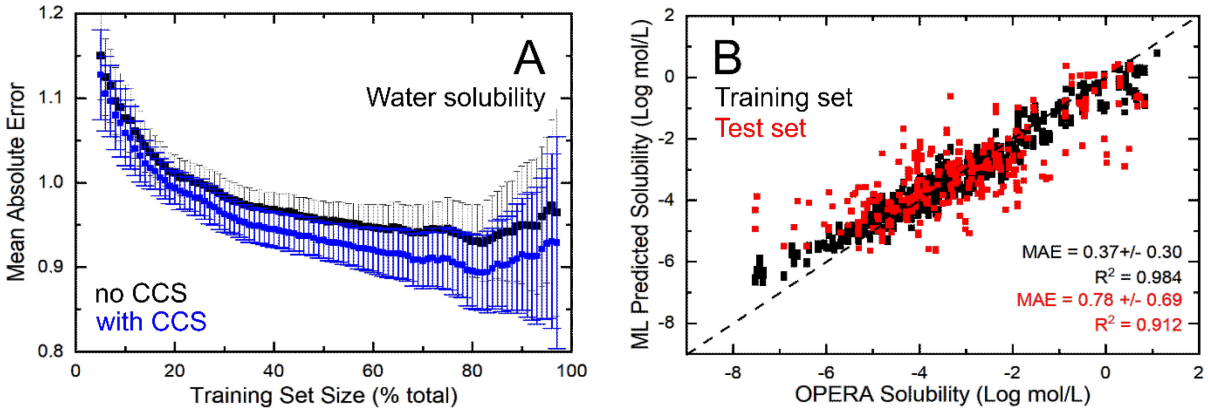

Figure 2.9. (**A**) Out-of-the-bag test set error as a function of train:test split for the Random Forest Regression model of water solubility. Black data points show errors when CCS is not included as a training feature and blue data points show errors when CCS is included. Error bars indicate model precision and show the standard deviation for 100 randomized train:test splits. (**B**) The correlation between OPERA-calculated and ML-predicted water solubility for 334 analytes from 11 chemical classes for an 80:20 train:test split (i.e., 267 training instances, 67 test instances). Training set (black points) and test set (red points) data indicate that log S can be determined for unknown analytes with an error of 0.78 log mol/L. Five randomly selected train:test splits are plotted.

Figure 2.9A shows the mean absolute error of the test set as a function of train:test split. The error bars represent the standard deviation of 100 randomized train:test splits and serve as an indication of model precision. As expected, the accuracy of the ML predictions improves as the size of the training set increases. We observe a slight increase in mean absolute error and significant decrease in model precision when the training set size exceeds 80% of the total data set. This is a consequence of the relatively small size of the dataset; as the size of the test set approaches zero, the degrees of freedom for the error assessment goes to zero, resulting in increased error and higher

variance. We expect that model errors will continue to decrease as the size of the data set increases. The bottom panel of **Figure 2.9B** shows the correlation between the ML-predicted water solubility and those computed by the OPERA software package for an 80:20 train:test split (*i.e.*, 267 training instances, 67 test instances). The weakest correlation occurs in the "wings" of the Log S distribution. At (log S) $< 10^{-6}$ Log mol/L, ML-predicted values tend to be higher than OPERA-computed values and at (log S) > 1 Log mol/L, the ML-predicted values tend to be lower. This bias towards under forecasting high solubility and over forecasting low solubility is a consequence of regression towards the mean of the dataset, which is a phenomenon commonly observed in predictive statistical models.

Considering that the ML framework was trained using (log S) values computed by OPERA, one might question the utility DMS-MS measurements to predict solubilities if the same information can be determined from the molecules SMILES string. The answer this comes down to the accuracy and precision in which DMS-based measurements can predict a molecule's solubility relative to OPERA. For example, the expected error of the OPERA solubility prediction can range between 1 - 2 units of log mol/L. For the OPERA Log S model, we find that ML predictions are accurate to within 0.78 log mol/L across nine orders of magnitude. If we consider only (log S) values between 1×10^{-6} log mol/L and 1×10^{0} log mol/L, the error is 0.32 log mol/L. We also demonstrated the usefulness of DMS to predict experimentally measured properties in 2019, where we used a similar ML training methodology on a smaller dataset (113 compounds) to model CCS, pK_A, pK_B, hydrophobicity (log D), passive cell permeability, and polar surface area.[96] Whether one can further improve model accuracy by including additional computed molecular descriptors (*e.g.*, number of H-bond donors and acceptors) is an interesting question, and one that has been addressed in a recent publication by our group (currently in peer review). Nevertheless, the dynamic solvation processes that occur within a microsolvating DMS environment offer more than just insights into the physicochemical properties of an analyte. The solvation/desolvation cycles induced by the oscillating SV waveform fosters a gas phase environment that reminisces the primary solvation shell of the analyte, which may help preserve the condensed phase structures of ions in a "harsh" gas phase environment; this potential is discussed extensively in the subsequent chapter.

Chapter 3

Experimental consequences of dynamic ion solvation

This chapter contains supplementary material that can be found within **Appendix B**.

3.1 Introduction

Ion mobility spectrometry (IMS) has emerged as one of the most versatile methods for separating ions prior to mass spectrometric detection.[47,131–135] In addition to its analytical capabilities, IMS can be used to discern the relationship between the gas phase structure of ions and their respective mobilities. When IMS is utilized in combination with native mass spectrometry,[136] there is considerable potential for studying condensed phase structures of biological targets in the gas phase. The majority of the work in native ion mobility has been focused on low-field ion mobility techniques and/or has employed settings that minimize ion activation, since the use of electric fields above the so-called 'low-field limit' can confound the interpretation of ion mobility data.[136–142] Distortion of ion structure has been observed in travelling-wave IMS (TWIMS), an analog of drift-tube IMS (DTIMS) that uses non-uniform drift fields surpassing the low-field limit,[33,60] where more elongated structures of proteins were detected in TWIMS compared to those using DTIMS.[143,144]

Preservation of condensed phase structures becomes even more problematic when high-field ion mobility techniques, such as DMS, are used.[39,41,42,58] In DMS, ions are subjected to an oscillating electric field applied between two planar electrodes (separation field), which consists of a low-field and high-field component. Owing to the dependence of ion mobility on electric field strength, ions are spatially resolved through their differential mobility incurred during the low and high field portions of the separation field. The differential mobility of an ion is encoded in a secondary, constant voltage (denoted the compensation voltage, CV) required to transmit the ion through the DMS device. To achieve this spatial resolution of ions in DMS, the strength of the separation field (10 – 250 Td; 1 Td = 10^{-21} V $\cdot$ m^2) must surpass E/N ratios that define the low-field limit

(*ca.* 2 – 10 Td)[58,59] and is likely to induce significant ion heating. However, recent assessments indicate that effective ion temperatures (T_{eff}) experienced in DMS[116,145,146] and TWIMS[143,147] in an N_2 environment are comparable, presumably due to the disparate operating pressures of DMS (ambient) compared to TWIMS (0.025 – 3 mbar). Given the capability of TWIMS to conduct analyses of biomolecules in their native configurations,[148–153] native analyses may be possible with DMS given the similar T_{eff}.

Preservation of native ion conformations within the DMS environment is more likely when the carrier gas is seeded with chemical modifiers.[44,45,48,51,52,94,154–157] Modifiers are selected to have non-covalent interactions with the analytes; these are typically low molecular weight alcohols, ketones, esters, ethers, or hydrocarbons. In the case of polar modifiers, the modifier-analyte interaction potential is predominantly composed of contributions from hydrogen bonding, ion-dipole, and/or ion-quadrupole interactions. As a result of the non-covalent nature of the interaction potential between the analyte and modifier molecules, the separation voltage (SV), which is analogous to the separation field, will drive cycles of microsolvation during the low-field portion and desolvation during the high-field portion of the waveform due to field-induced heating. Dynamic microsolvation cycles are hypothesized to shield ions from internal fragmentation caused by collisional activation during the high-field portion of the SV cycle (*i.e.*, field-heating).[77] In other words, microsolvated ions are equipped with an "air-bag" that can dissipate internal energy through boiling off solvent molecules from sites of accretion (*i.e.,* sites of localized solvent clustering).

Peptide and protein ions are interesting targets to investigate the suspected stabilization conferred by microsolvation. Assuming generation by electrospray ionization (ESI) in positive mode, the analyte would undergo dynamic microsolvation cycles at sites of protonation in a solvent-modified DMS environment, which includes the N-terminus and/or the side chains of the basic amino acids lysine (Lys), histidine (His), and arginine (Arg).[158] Accretion of solvent molecules onto charge sites are complemented by a net increase in ion-neutral collision cross section (CCS), which would cause a reduction in T_{eff} stimulated by a decrease in ion mobility.[37,59,60] In the absence of a

microsolvating partner or a native ionization setup, the ESI process would effectively desolvate the protein.[159] Thus, any protonated residue would be forced to stabilize itself through formation of intramolecular hydrogen bonds with the nearest acceptor site, likely with carbonyl moieties present on the peptide backbone. This would cause distortion and elongation of the peptide as the folding landscape of the system is perturbed to accommodate disruption of the backbone geometry.[160] In a microsolvating environment, trace solvent vapour can locally solvate protonation sites, preventing backbone collapse and potentially preserve the ion's native-like configuration. This was demonstrated in TWIMS, where analysis of cytochrome *c* and ubiquitin using crown-ether as the microsolvating partner resulted in observation of native-like structures compared to the desolvated ion.[30] Based on this success, microsolvation of protonated residues through formation of ion-solvent clusters suggests that seeding the DMS cell with solvent vapour might be appropriate for conducting native experiments when coupled to native ionization techniques. This hypothesis is supported by several studies conducted by the Cooper group, who have utilized field-asymmetric waveform IMS (FAIMS),[58,161] an analog of DMS that uses cylindrical electrodes, to study a series of intact proteins assemblies containing post-translational modifications up to 147 kDa.[162–164]

To examine the role that microsolvation plays in stabilizing biologically relevant ions during DMS analysis, the microsolvation propensity of common DMS modifiers towards lysine residues is investigated. However, since structural information cannot by directly obtained from DMS measurements, the focus of this study concerns only the impact that microsolvation has on biomolecule stability and charge state. Solvent clusters of H_2O, MeOH, EtOH, *i*PrOH (IPA), MeCN, and acetone (ACE), as well as their affinity towards protonated *n*-propyl amine ($[PrNH_3]^+$), a mimic of the Lys side chain and N-terminus, were assessed using computational chemistry. Clustering thermochemistry in these systems was used to explain the enhanced stabilization of two small tripeptides GGG and AAA, as well as the disordered, Lys-rich peptide Polybia-MP1 (MP1; IDWKKLLDAAKQIL-NH_2) in solvent-modified DMS environments. Circular dichroism studies of MP1 indicate a disordered structure in both pure and Tris-buffered water (pH = 7.5); helical motifs in the condensed phase structure of MP1 emerge in the presence of 2-trifluoroethanol,

detergents, and phospholipids.[165] As a result, the propensity of MP1 towards microsolvation is expected to be considerable.

3.2 Experimental details

A SelexION differential mobility spectrometer was mounted in the atmospheric region of a QTRAP 5500 mass spectrometer (SCIEX, Concord, Ontario, Canada) between the sampling orifice and ESI source. This instrument has been extensively described in literature and is shown in **Figure S3-1**.[39,41,42]

MP1 was synthesized by NovoPro Bioscience (Shanghai, China). GGG and AAA were purchased from Sigma-Aldrich (Oakville, Ontario, Canada). All peptides were used without further purification and diluted to working concentrations of *ca.* 0.2 μM in MeOH/H_2O (1:1) with 0.1% formic acid. Although these ESI conditions do not support native ionization, it should be noted that the peptides chosen for this study are intrinsically disordered in the condensed phase.

Analyte solutions were infused into the ESI source at 15 μL min^{-1}. The ESI probe (TurboV, SCIEX, Canada) was operated at 5500 V with the source heater off; a nebulizing gas pressure of 30 psi and an auxiliary gas pressure of 10 psi were used to aid in desolvation. Electrosprayed ions were carried into the DMS cell with the carrier gas. N_2 was used as both the carrier gas (20 psi) and as the collision gas (*ca.* 9 mTorr) for sample acquisition in MRM mode. Seeding the carrier gas with chemical modifiers was accomplished by infusing liquid reagent into the carrier gas at a concentration of 1.5 mol % using an Agilent 1100 series LC pump.

The planar DMS cell (1 mm gap height) was held at one of three fixed temperatures pertaining to the experiment of interest. We previously assessed the temperature of ions in the DMS cell and found that the DMS heater settings of 150 °C, 225 °C, and 300 °C correspond to bath gas temperatures (T_{bath}) of 100 °C, 150 °C, and 177 °C (373 K, 423 K, 450 K), respectively.[116] DMS experiments involved incremental stepping of the SV from 0 to 4500 V at each of the three T_{bath}

settings. At each SV, ion intensity was monitored as the CV was scanned from −5 V to 30 V in increments of 0.1 V to produce an ionogram. SVs are reported as reduced field strengths (E/N) in Td (1 Td = 10^{-21} V · m^2). The resulting ionograms were integrated using the IntelliQuant package in Analyst 1.6.3. Unless stated otherwise, all DMS experiments were conducted with the following settings for the ion optics: declustering potential (DP) of 100 V; entrance potential (EP) of 10 V; collision cell exit potential (CXP) of 15 V.

3.3 Computational details

A common assumption of protonated peptides generated using ESI is that positive charges primarily reside on basic residues.[158] For MP1, sites of protonation are possible at the *N*-terminus, Lys-4, Lys-5, or Lys-11. We hypothesize that a model of microsolvated *n*-propyl amine can be used to model the thermodynamics of cluster formation around the Lys side chain while also serving as a proof-of-concept model for the *N*-terminus. Previous work showing that microsolvation of peptide side chains promotes the stabilization of native structures suggests it to be unlikely that a microsolvated side chain will interact with the peptide backbone.[30] Thus, in microsolvating DMS environments, it is a reasonable approximation to treat solvent cluster accretion on protonated side chains in an isolated manner.

Modelling clustering thermochemistry using molecular dynamics (MD) simulations, where the number of particles, volume, and temperature (NVT) of the system is fixed would be ideal. However, obtaining thermochemistry using a high level of electronic structure theory from even a handful of MD snapshots of a short peptide (*ca.* 5 residues) would be prohibitively expensive. Thus, computational microsolvation studies of $[PrNH_3]^+$ were conducted using the systematic sampling of cluster surfaces (SSCS) algorithm that is interfaced with Gaussian 16 C.01.[117] The workflow of the SSCS algorithm is shown in **Figure S3-2**. Briefly, SSCS builds candidate structures in a microsolvating environment guided by the interaction potential between the analyte and solvent.

Electronic partial charges are used to describe the interaction potential, as determined using the Merz-Singh-Kollmann partition scheme,[121,122] and evaluated at the ωB97X-D/6-311++G(d,p) level of theory.[166] The interaction potential between the protonated analyte and solvent molecule is sampled by generating a sphere of points within a 10 Å radius of the charged analyte. Each point in this sphere represents a position to sample the ion-solvent interaction potential. Points are then pruned from the sphere if the distance to a charge centre is greater than 4.0 Å, as the strength of intermolecular interactions (*e.g.,* hydrogen bonding) diminishes at longer distances. Charge centres are arbitrarily defined as the atoms whose partial charge lies within 10 % of the most positive and most negative atom on the charged analyte.

After pruning the points in the sphere, a series of molecular rotations are performed to orient solvent molecules in directions that facilitate hydrogen bonding or charge-dipole interactions. Unique minima, as identified by universal forcefield (UFF) energies and cosine similarities,[70,72] are optimized at the PM7 level of theory.[75] To further explore the microsolvation propensity, solvent ligands in the PM7 minima are randomly translated by 2 Å in increments of 0.25 Å and randomly rotated about their centres of mass by $-25° \leq \theta \leq 25°$. Unique minima, again identified by UFF energies and cosine similarities, are optimized at the PM7 level of theory. All PM7 minima comprise isomers in the population of the singly solvated analyte. Each minimum serves as the input for the next round of calculations to determine microsolvated geometries of clusters containing two solvent ligands; the process is repeated until a user-specified number of solvent ligands is reached. In this way, candidate structures for $[PrNH_3 \cdot \cdot \cdot (Solv)_n]^+$, $[(Solv)_n + H]^+$, and $[(Solv)_n]^0$ up to $n = 8$ (Solv = H_2O, MeOH, EtOH), $n = 7$ (Solv = IPA), or $n = 5$, (Solv = ACE, MeCN) were generated. The respective values of n were chosen based on computational limitations. Aprotic clusters were capped at $n = 5$ due to the lack of hydrogen bond donors in the solvent ligand, which will impact the ability of $[PrNH_3]^+$ to accommodate additional solvent molecules that directly participate in ion-solvent bonding.

Unique structures identified by the SSCS routine were pre-optimized at the HF/6-31g level of theory and subsequently sorted based on cosine similarities. Unique structures from the HF pre-optimization were fully optimized at the ωB97X-D/6-311++G(d,p) level of theory. Normal mode analyses were conducted to verify that each isomer corresponded to a minimum on the PES and to calculate isomer thermochemistry, for which the ωB97X-D functional has demonstrated superiority compared to other functionals available in Gaussian.[83] In total, the optimized geometry and thermochemistry for over 2000 unique ion-solvent clusters were calculated. The size of the isomer pool limited our ability to analyze electronic energies and thermochemistry across different DFT functionals and basis sets. As such, we supplemented ωB97X-D optimized geometries and thermochemistry with single-point energy calculations conducted at the MP2(full)/6-311++G(d,p) level of theory. Thermochemical quantities were determined by combining MP2 single point electronic energies on ωB97X-D minima with ωB97X-D thermochemistry, which are reported as the MP2(full)/6-311++G(d,p)//ωB97X-D/6-311++G(d,p) level of theory. Due to computational limitations, all calculations involving IPA were performed at the MP2(full)/6-31+G(d,p)//ωB97X-D/6-31+G(d,p) level of theory. Molecular graphics were generated using the UCSF ChimeraX package.[167]

3.4 Solvent modified DMS environments promote the stability of peptides

To investigate the stabilizing effects of solvent-modified DMS environments, the survival yields (SYs) of the tripeptides $[GGG + H]^+$ and $[AAA + H]^+$ were evaluated at various separation field strengths using the highest bath gas temperature accessible (T_{bath} = 450 K). Comparisons of the stability of $[GGG + H]^+$ and $[AAA + H]^+$ are shown in **Figure 3.1**, where DMS experiments were conducted in pure N_2 and N_2 seeded with 1.5 mol % MeOH or MeCN. SYs are calculated as the fraction of total peak area corresponding to the intact parent ($A_{[M+H]^+}$) compared to the total peak area of the detectable parent and fragment ($A_{[Frag+H]^+}$) species as defined in **Eq. 3.1**.

$$SY = \frac{A_{[M+H]^+}}{A_{[M+H]^+} + \sum_i A_{[Frag_i+H]^+}} \qquad \textbf{Eq. 3.1}$$

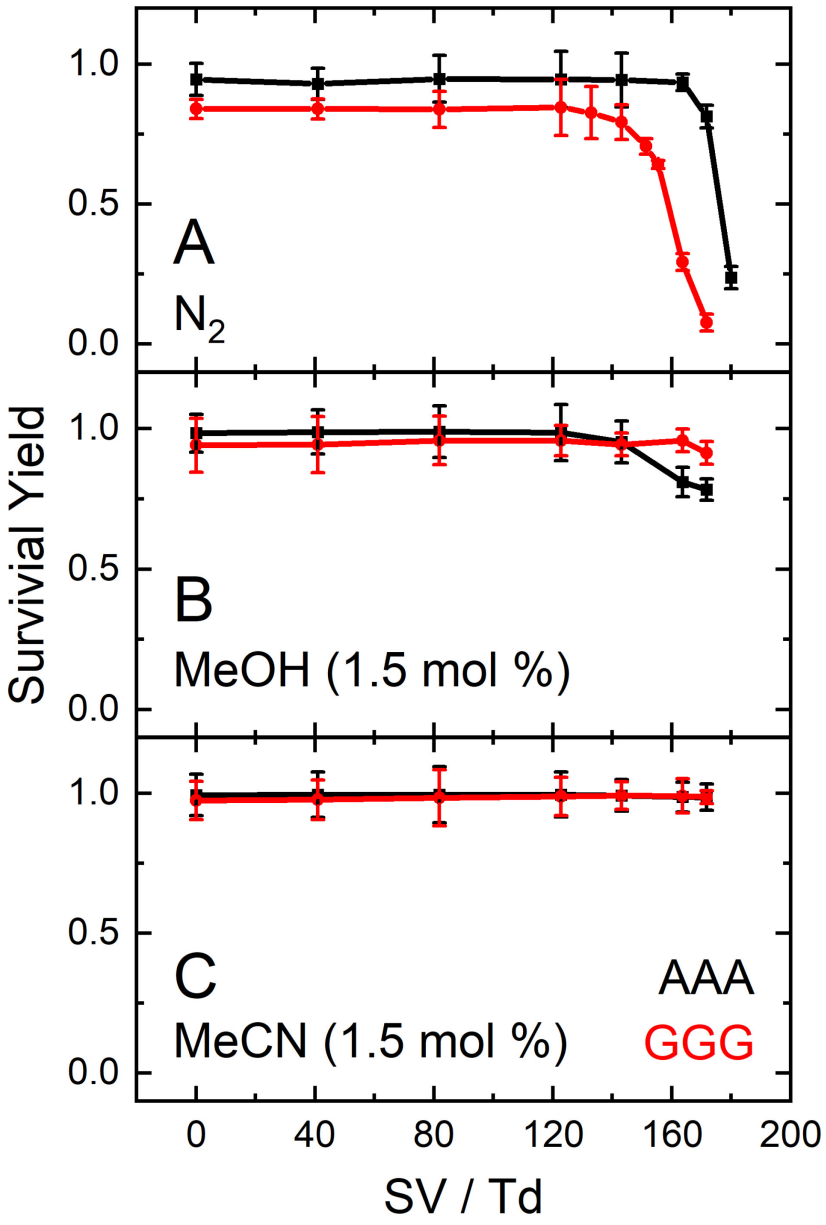

Figure 3.1. Survival yields of the tripeptides [GGG + H]$^+$ (red trace) and [AAA + H]$^+$ (black trace) following activation by the separation field in N_2 (**A**) and N_2 seeded with 1.5 mol% MeOH (**B**) and MeCN (**C**). SYs in panel C are calculated from peak areas of [M + H]$^+$ and [M + H + MeCN]$^+$. T_{bath} = 450 K.

Significant depletion of the parent ion was observed as the field strength surpassed 140 Td in pure N_2 DMS environments. For $[GGG + H]^+$, the onset of dissociation began at SV = 143 Td, whereas $[AAA + H]^+$ started to show depletion at 172 Td. The earlier onset of dissociation for $[GGG + H]^+$ corresponds to its higher T_{eff} as predicted by two-temperature theory (*vide infra*), as there are fewer internal degrees of freedom into which the ion can partition energy. Intuitively, fragmentation of the parent ions should correspond to an increase in population of fragments originating from the parent peptide. However, this was not observed in the ionograms of $[GGG + H]^+$ and $[AAA + H]^+$ (**Figure S3-3**), where an increase in intensity of the $[GGG + H]^+$ and $[AAA + H]^+$ signals between SV = 0 – 123 Td was met with a sharp decrease in parent ion intensity as the SV surpassed 123 Td without a corresponding increase in fragment ion intensity. To rationalize the lack of fragment signal, the potential disparity in differential ion mobility between the parent and fragment ions must be considered. For small molecules such as $[GGG + H]^+$ and $[AAA + H]^+$, the differences between the differential mobility of the parent and fragment ions in modified DMS environments is expected to be substantial. This behaviour has been observed in other systems, namely in the differential mobilities of parent and fragment ions of proton-bound ketone dimers and chemical warfare agents.[146,168] Detection of the corresponding fragment ion depends on the timepoint when it forms within the DMS cell, as it requires the parent ion to be on an initially stable trajectory. If the differential mobility of the fragment ion is disparate at the CV required for parent transmission, the fragment will be lost via upon its formation due to a mismatch in CV required for transmission through the DMS cell. Thus, comparing relative signal intensities between parent and fragment ions is not always possible.[169] Normalizing peak areas to the sum of all ions (**Figure S3-4**) allows for visualization of some characteristic peptide fragments, although the fragments are still comparatively weak.

Analysis of **Figure 3.1B** and **Figure 3.1C** indicate that the population of the parent ion was essentially unchanged in a microsolvating environment, which is in stark contrast to the rapid decrease in SY of the parent observed in pure N_2. In effect, ion microsolvation produces a solvent 'air-bag,' sheltering the parent species from activation by high energy collisions induced by the SV

waveform. Modifier-induced stabilization of the parent species was accompanied by a greater transmission of the parent ions of $[AAA + H]^+$ and $[GGG + H]^+$ at high SV, as evidenced by comparing peak areas in N_2, MeOH, and MeCN (**Figures S3-3** and **S3-4**). Only minor depletions of $[AAA + H]^+$ and $[GGG + H]^+$ were observed in MeOH modified environments compared to N_2, which is likely a consequence of proton transport from the *N* to the *C*-terminus through the microsolvated hydrogen-bond network,[170,171] resulting in the production of H_2O and CO via fragmentation at the C-terminus. No substantial depletion of the parent ions was observed when MeCN, an aprotic species, was used as the chemical modifier. In fact, doping the carrier gas with MeCN enables detection of $[M + H + MeCN]^+$ adducts of the tripeptides. This observation further supports the postulate that modified DMS environments are conducive to the formation of stable, non-covalent complexes that mitigate ion activation by the SV waveform.

The shielding effect of ion microsolvation can play a vital role in the growing field of DMS-based proteomics,[133,162,172–174] where SV-induced fragmentation can mask targets of biological importance. Qualifying the stabilizing effects afforded by ion microsolvation towards collisional activation by the separation field could enhance sequence coverage when implemented into proteomics workflows. Up-front CID, which encompasses any ion fragmentation stimulated by the separation field and during the atmosphere-to-vacuum transfer process, is suggested to be responsible for up to 60% of non-tryptic peptides in standard protein digests.[175,176] To assess the potential of microsolvation to alleviate complications associated with up-front CID, we conducted an additional study using the DP to mimic up-front CID effects on the tripeptides $[GGG + H]^+$ and $[AAA + H\ ]^+$ (**Figure S3-5**). For these experiments, the DMS was operated in transmission mode (SV = 0 Td) with T_{bath} = 450 K. In a pure N_2 environment, ion intensity depleted to 50 % of its original intensity at approximately DP = 135 V for both tripeptides. Doping the carrier gas with either MeOH or MeCN prevented fragmentation of the parent ion up to DP = 300 V, the highest DP setting for the instrument. The protection of peptides afforded by microsolvation suggests that conducting DMS experiments with solvent-modified environments will result in enhanced sequence coverage. This postulate is validated by Seale and coworkers, where analysis of tryptic digests of bovine serum

albumin (BSA) and a monoclonal antibody (mAb) in a microsolvating environment reduced the number of spectra required to achieve sequence coverage by 40 % compared to pure N_2.[177]

The stability afforded by microsolvation is also applicable to peptides larger than $[GGG + H]^+$ and $[AAA + H]^+$. The intensities of MP1 in its various charge states and detectable solvent adducts were monitored while ramping the DP from 0 to 300 V in Q1 mode (**Figure 3.2**). Ion signals corresponding to $[MP1 + 2H]^{2+}$ and $[MP1 + 3H]^{3+}$ were detected, whereas the $[MP1 + H]^+$ species was not observed. In a pure N_2 environment, the $[MP1 + 3H]^{3+}$ signal (**Figure 3.2A**; black trace) exhibited significant depletion beginning at DP = 150 V until it reached zero intensity at DP = 265 V. Seeding the carrier gas with MeCN precluded any fragmentation by up-front CID, as signal intensities of $[MP1 + 2H]^{2+}$, $[MP1 + 3H]^{3+}$, and a MeCN adduct, $[M + 3H + MeCN]^{3+}$, were maintained at all DPs sampled. Detection of the exceptionally stable $[M + 3H + MeCN]^{3+}$ adduct indicated that the species survived transit through the DMS cell, expansion into the vacuum region, and transit through the mass spectrometer. The fragile adducts $[M + 4H + n\text{MeCN}]^{4+}$ ($n = 1 - 3$) were also detected (**Figure S3-6**), which exhibited uniform signal intensity at all DP values sampled. Given that $[MP1 + 4H]^+$ species were not detected in a pure N_2 DMS environments, side-chain microsolvation is presumed to confer significant protection from the separation field. Significant differences in ion population were observed upon introduction of protic modifiers into the DMS cell. No ion-solvent adducts were detected in MeOH microsolvation environments. In fact, the only ion signal observed corresponded to $[MP1 + 2H]^{2+}$ (**Figure 3.2C**). The detection of higher charge states in pure N_2 DMS environments and those seeded with aprotic modifiers suggests that proton transfer is occurring from the analyte to the protic solvent modifier. The proton transfer is ascribed to the proclivity of protic solvents to form extended hydrogen bond networks, whose GPB increases with cluster size.[178–181]

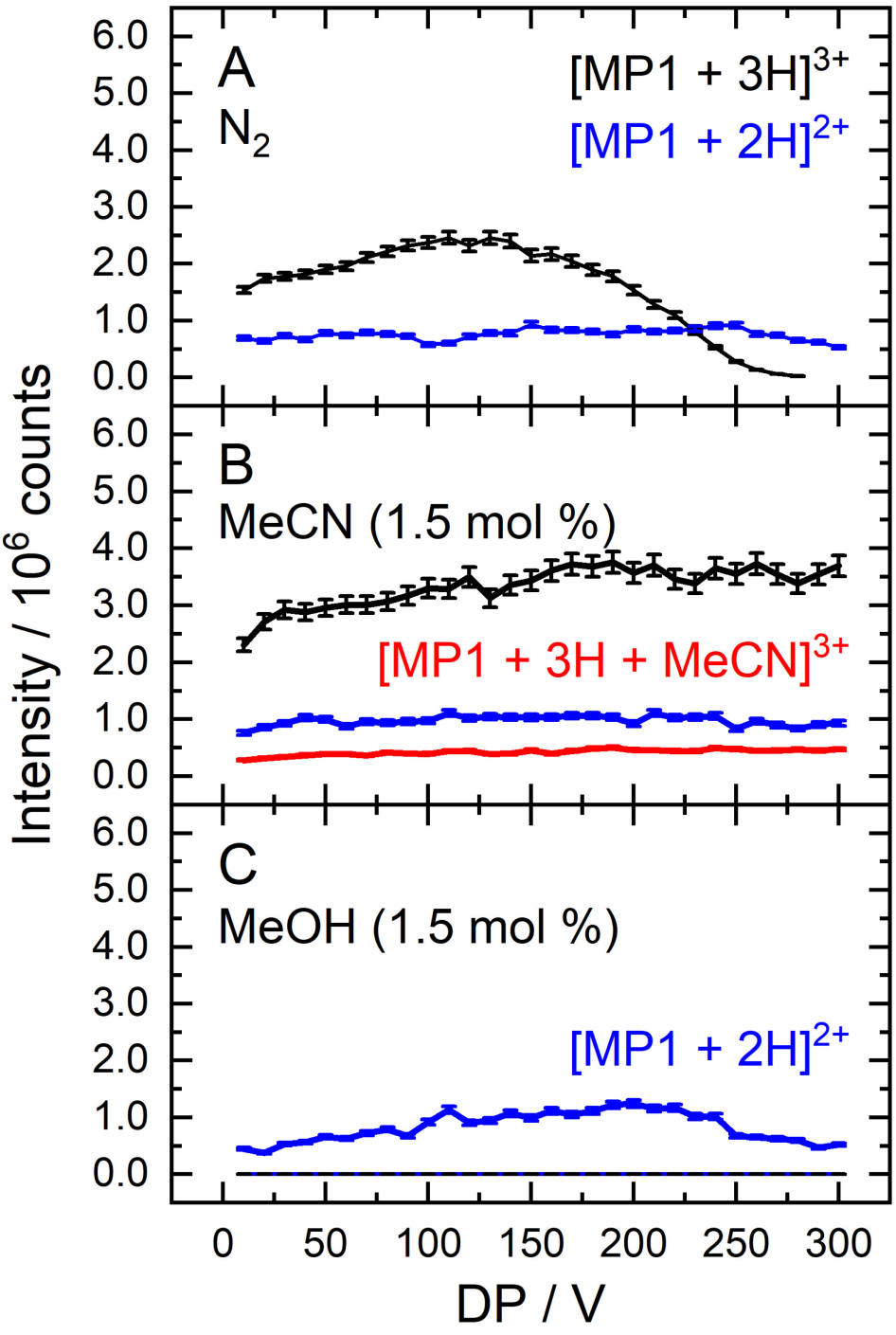

Figure 3.2. Stability of MP1 towards up-front CID induced by application of a declustering potential in pure N_2 (**A**), and in N_2 seeded with 1.5 mol% of MeOH (**B**) and MeCN (**C**). Charge states and adducts are colour coded as follows: $[MP1 + 3H]^{3+}$ (black); $[MP1 + 3H + MeCN]^{3+}$ (red); $[MP1 + 2H]^{2+}$ (blue). $T_{bath} = 450$ K.

3.5 Microsolvation-induced charge reduction in modified DMS environments

The observation of charge-depletion via proton scavenging and the implication of microsolvation mediating this process was further explored by monitoring the shift in the population of MP1 protonation states as a function of ion activation. The distribution of ion charge states is expected to depend on the GPB of the solvent modifier and the ion's effective temperature, which governs the size of the microsolvated adduct. Analysis of population-weighted charge, as defined in **Eq. 3.2**, allows for such a comparison,

$$z_{avg} = \frac{\sum_i^N (z_i)(P_i)}{\sum_i^N (P_i)} \qquad \textbf{Eq. 3.2}$$

where N is the number of charge states experimentally observed, z_i is the charge of the i^{th} charge state, and P_i is the area of the ionogram corresponding to the i^{th} charge state. To investigate the effect of bath gas temperature and field-induced heating on charge state, population-weighted charges were evaluated as a function of increasing SV at the three standard DMS temperature settings (T_{bath} = 373, 423, and 450 K). **Figure 3.3** shows the charge evolution for MP1 as a function of the bath gas temperature and SV (*i.e.*, field-induced heating) in N_2 and in N_2 environments doped with protic (H_2O, MeOH, EtOH, and IPA) and aprotic (ACE, MeCN) modifiers at a fixed modifier concentration of 1.5 mol %. It should be noted that population-weighted charge, as determined by **Eq. 3.2**, will additionally depend on the ionization voltage, sample infusion rate, and concentration of both the analyte and solvent modifier.

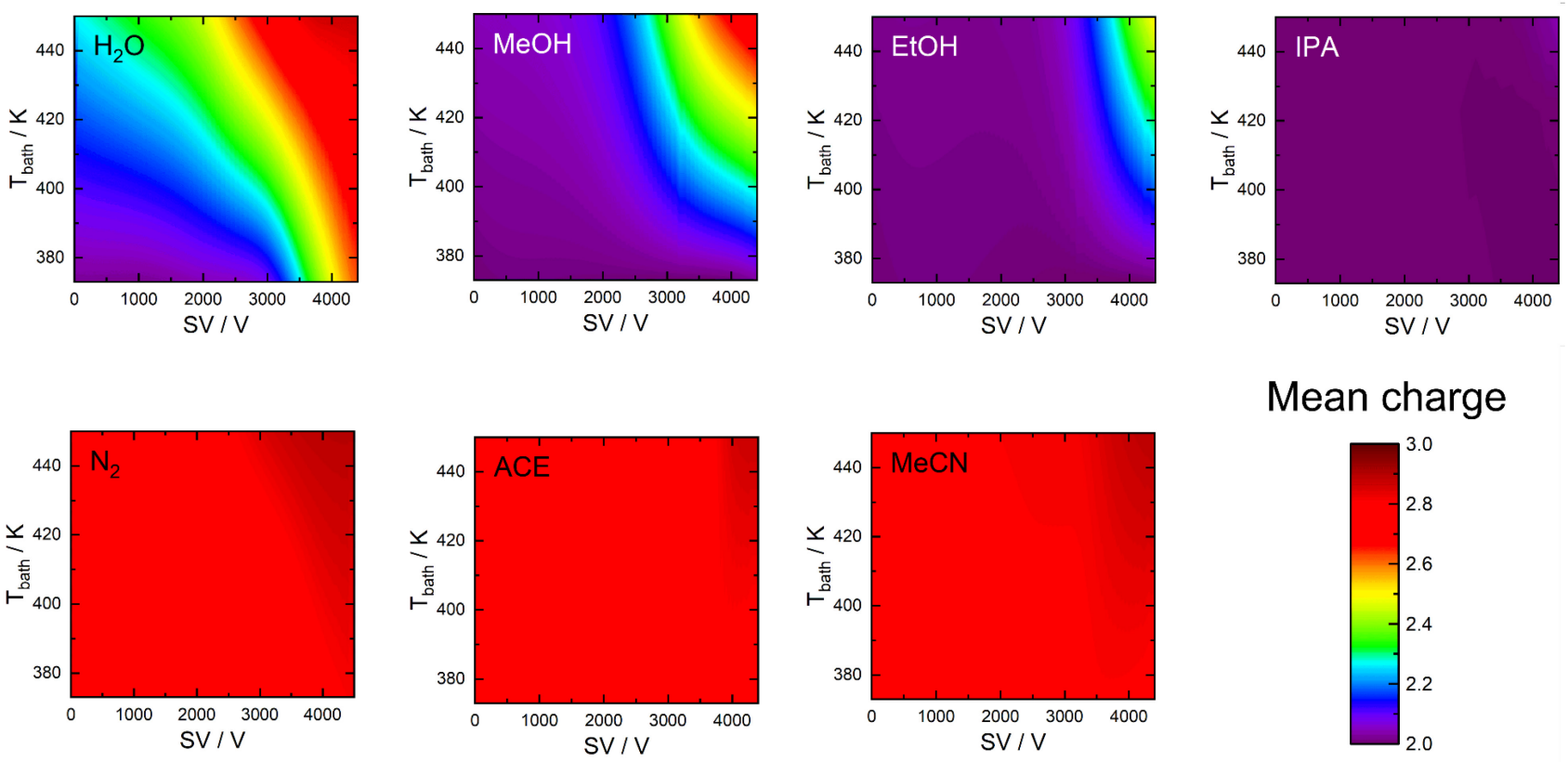

Figure 3.3. Evolution of the mean charge state adopted by MP1 as a function of the separation field and bath gas temperature in DMS environments consisting of N_2 and N_2 doped with 1.5 mol% of H_2O, MeOH, EtOH, IPA, ACE, or MeCN. SV corresponds to the peak-to-peak potential applied across a planar DMS cell with a 1 mm gap.

Introduction of protic modifiers into the DMS cell caused near quantitative depletion of the $[MP1 + 3H]^{3+}$ signal and shifted the gas phase population to $[MP1 + 2H]^{2+}$. Interestingly, activation of the analyte through increasing the SV or T_{bath} in environments seeded with H_2O, MeOH, and EtOH yielded increasing populations of $[MP1 + 3H]^{3+}$ and concurrent depletion of $[MP1 + 2H]^{2+}$ signal intensity (**Figure S3-7**). Appearance of the $[MP1 + 3H]^{3+}$ species at high SV and T_{bath} is a direct consequence of the analyte's reduced propensity for microsolvation as T_{eff} increases, where decreasing the number of solvent ligands in an ion-solvent cluster reduced the effective GPB of the associated solvent cluster. This suggests that proton transfer was occurring through the solvent hydrogen-bond network, which directly contrasts the mechanism of proton transfer with conventional charge reducing agents (e.g., imidazole, sulfolane, DMSO, TMAO).[182–184] Traditional reagents function more efficiently as the energy between analyte/modifier collisions increase.[185] However, in this study, reactivity is associated with the effective GPB of the solvent cluster, where the favourability of charge-transfer process depends on the cluster size. We hypothesize that a stepwise accretion mechanism followed by proton transfer through the hydrogen-bond network and dissociation of the protonated solvent cluster is responsible for proton abstraction, similar to the mechanism proposed by Thinius *et al.*[186,187] In short, more energetic collisions facilitate charge-retention rather than proton transfer since collisional activation reduces the size of the microsolvated cluster.

In pure N_2 DMS environments, gas phase populations favour the $[MP1 + 3H]^{3+}$ protomer over $[MP1 + 2H]^{2+}$. Addition of either MeCN or ACE also favours the $[MP1 + 3H]^{3+}$ protomer and gives rise to additional signals in the mass spectrum corresponding to clusters of the form $[MP1 + 3H + n(Solv)]^{3+}$ (Solv = MeCN, ACE; $n = 1, 2$) and $[MP1 + 4H + n(Solv)]^{4+}$ (Solv = MeCN, ACE; $n = 1 – 3$). Given that the $[MP1 + 4H]^{4+}$ species was not observed in pure N_2, the microsolvating environment was presumed to confer additional stability to this higher charge state species. Detection of fragile charge states was accompanied by an increase in peak area of all ions by a factor of approximately two in DMS environments seeded with aprotic modifiers compared to pure N_2. No charge reduction was observed in DMS environments seeded with aprotic modifiers,

which is consistent with observations made by Seale et al.[177] and Thinius et al.[186] This appears counterintuitive if one considers the enhanced GPB of the free molecules of ACE (782 kJ mol^{-1}) and MeCN (748 kJ mol^{-1}) relative to EtOH (746 kJ mol^{-1}),[188] which depleted the $[MP1 + 3H]^{3+}$ species under most experimental conditions. To explore the observed charge reduction observed with protic modifiers and the stabilization afforded by aprotic modifiers, the thermochemistry of cluster formation and feasibility of proton transfer pathways was evaluated using computational chemistry.

3.6 Gas phase basicity and proton affinity of solvent clusters

The geometries of gas phase solvent clusters have been reported in the literature alongside a systematic evaluation of their physicochemical properties.[178–181] Specifically, these studies show that the GPB of solvent clusters increase with cluster size, as extended hydrogen bonding networks and/or additional intermolecular interactions can stabilize the positive charge more effectively. Assuming that the protonation sites lie on basic residues of a protein, the GPB of the Lys side chain, (represented by $PrNH_2$; 884 kJ mol^{-1}) is greater than that of individual molecules of IPA and MeCN (763 and 748 kJ mol^{-1}, respectively).[188] This simple comparison suggests that individual solvent molecules should not be able to remove the charge from proteins via proton transfer. Thus, the charge transfer is likely occurring through the microsolvation hydrogen-bond network.

The GPB and proton affinity (PA) of various solvent clusters were calculated using the computational workflow described in **Chapter 3.3** to generate 'microsolvated' structures of neutral and protonated solvent cores. The GPB and PA are defined as the change in Gibbs energy and enthalpy, respectively, for the protonation of a neutral species (*i.e.,* $[B_n] + H^+ \rightarrow [B_n + H]^+$). Calculation of GPB uses weighted Gibbs energies (G_n) described in **Eq. 3.3**, and PA uses the weighted enthalpies (H_n) defined below in **Eq. 3.4**, respectively.

$$\left(G_n(T)\right) = \sum_k \left(\rho_n^{(k)}(T)\right)\left(G_n^{(k)}(T)\right) \qquad \textbf{Eq. 3.3}$$

$$\left(H_n(T)\right) = \sum_k \left(\rho_n^{(k)}(T)\right)\left(H_n^{(k)}(T)\right) \qquad \textbf{Eq. 3.4}$$

Using the Gibbs energies evaluated at a series of temperatures, the population (ρ) for the k^{th} isomer of cluster size n in a canonical ensemble can be evaluated as a function of ion temperature (T) as per **Eq. 3.5**:

$$\rho_n^{(k)}(T) = \frac{exp\left[\left(G_n^{(k)}(T)\right)(RT)^{-1}\right]}{\sum_k exp\left[\left(G_n^{(k)}(T)\right)(RT)^{-1}\right]} \qquad \textbf{Eq. 3.5}$$

where R is the gas constant and $G_n^{(k)}(T)$ is the Gibbs energy of the k^{th} isomer of the cluster consisting of n solvent molecules at temperature T in kJ mol^{-1}. The total Gibbs energy of the microsolvated cluster of size n, G_n, is the sum of the Gibbs energy of the k^{th} isomer weighted by its relative population, $\rho_n^{(k)}$, at temperature T. It should be noted that, for the calculation of PA, $\rho_n^{(k)}$ is evaluated using $H_n^{(k)}(T)$ in place of $G_n^{(k)}(T)$. GPB and PA values for solvent clusters as a function of size and temperature are shown in **Figures S3-8** through **S3-13**. Calculated GPB and PA values of the monomeric solvents at the MP2(full)/6-311++G(d,p)//ωB97X-D/6-311++G(d,p) level of theory agree to within 4 kJ mol^{-1} of values determined experimentally.[188] Furthermore, calculated PAs of H_2O and MeOH clusters up to $n = 8$ (**Table S3-1**) correlate well with experimental values (1.7 % RMSD), suggesting that the theoretical method employed for this study is appropriate and provides a starting point to evaluate the relative uncertainty in our Boltzmann weighting of ensemble energies.

3.7 Thermochemical consequences of microsolvated ions

A description of the microsolvated clusters determined from the computational approach can be found in **Supplementary Section S3-1**. Over a residence time of ~7 ms in the DMS cell, where collisions occur in the nanosecond regime, a canonical ensemble consisting of all isomers of each cluster size is likely to be established. Accordingly, the thermochemistry of an ensemble of structures

is required to yield a coarse estimate of cluster populations. Using the population weighted Gibbs energies in **Eq. 3.3** approximately accounts for the variety of microsolvated structures that can be populated during an ion's transit through the DMS cell. This treatment is necessary as the timescale of DMS separations ensures that all degrees are freedom are equilibrated.[189] Appropriately, $G_n(T)$ is then used to evaluate the stability of a microsolvated species consisting of the analyte ion and n solvent molecules compared to the bare ion and n free solvent molecules (**Eq. 3.6**). We refer to this quantity as the Gibbs energy of association ($\Delta G_{ass,n}(T)$; $[PrNH_3]^+ + n\text{Solv} \rightarrow [PrNH_2 + H + n(\text{Solv})]^+$), where $G_0(T)$ is the weighted Gibbs energy of each isomer of $[PrNH_3]^+$, $G_{solv}(T)$ is the Gibbs energy of the neutral, monomeric solvent, and $G_n(T)$ is the weighted Gibbs energy of each isomer of $[PrNH_2 + H + n(\text{Solv})]^+$).

$$\big(\Delta G_{ass,n}(T)\big) = G_0(T) + (n)\big(G_{solv}(T)\big) - G_n(T) \qquad \textbf{Eq. 3.6}$$

Figure 3.4 shows $\Delta G_{ass,n}$ calculated for each cluster size at 450 K, which corresponds to operation of the DMS cell at an intermediate temperature with additional contributions from field heating. MeOH and MeCN are used as model systems for protic and aprotic clustering thermochemistry, respectively. In both cases, microsolvation of $[PrNH_3]^+$ with n solvent molecules is spontaneous with respect to formation from the bare ion. It should be noted that microsolvated clusters containing protic modifiers are less thermodynamically stable compared to those comprised of aprotic modifiers for the cluster sizes studied here. Calculations of cluster thermochemistry are performed at 1 atm (the approximate pressure inside the DMS cell) with an additional scaling factor (0.95 ± 0.05) applied to vibrational frequencies. In this way, errors on the relative populations can be generated in tandem with the propagation of error from the Boltzmann weighting method (*ca.* 1.7 %).

In the case of MeOH, $\Delta G_{ass} = -33.2 \pm 4.3$, -49.2 ± 7.8, and -55.1 ± 10.6 kJ mol^{-1} for $n = 1$, 2, and 3, respectively. MeCN microsolvation yields significantly more thermodynamically stable ion-solvent clusters, as $\Delta G_{ass} = -47.5 \pm 5.1$, -88.2 ± 10.0, and -109.4 ± 14.9 kJ mol^{-1} for $n = 1$, 2, and 3, respectively. The same disparity in microsolvated cluster stability can be seen between the

other protic and aprotic microsolvation partners investigated in this study (**Figure S3-14**). The difference in cluster stability stems from the physicochemical properties microsolvating partner, where the dipole moment, and hence the ion-dipole interaction, of aprotic solvents is generally greater than protic solvents. Nevertheless, protic species can accommodate large cluster sizes through expansion of the ion-solvent hydrogen bond network, whereas aprotic species are limited by the number of available hydrogen bond donors on the analyte. At $n = 3$, each H-bond donor from the $[PrNH_3]^+$ core coordinates to a single MeCN molecule. Additional MeCN molecules must bind through a shared proton motif with the $[PrNH_3]^+$ core, or with other MeCN molecules in head-to-tail or stacked motifs (see **Supplementary Section S3-1**). Thus, stabilization of the $[PrNH_2 + H + n(MeCN]^+$ is maximized at $n = 3$ at 450 K, as subsequent MeCN binding occurs through less stabilizing motifs that do not incorporate hydrogen bonding.

Consequently, it is expected that a variety of protic and aprotic ion-solvent cluster sizes will be present in the gas phase ensemble for a specific T_{eff} (assuming thermodynamic equilibrium). By evaluating ΔG_{ass} at various ion temperatures, the relative populations of each cluster size (N_n) as a function of T_{eff} can be calculated using **Eq. 3.7**, where $\Delta G_{rel_{ass,n}}$ is the Gibbs energy of formation of the cluster size n relative to the lowest energy cluster ($\Delta G_{rel_{ass,n}} = \Delta G_{ass,n} - min(\Delta G_{ass,n})$). It should be noted that relative populations are pressure dependent and sensitive to the vibrational contribution to Gibbs energy.

$$N_n(T) = \frac{exp\left(-\frac{\left(\Delta G_{rel_{ass,n}}(T)\right)}{(RT)}\right)}{\sum_n exp\left(-\frac{\left(\Delta G_{rel_{ass,n}}(T)\right)}{(RT)}\right)} \qquad \textbf{Eq. 3.7}$$

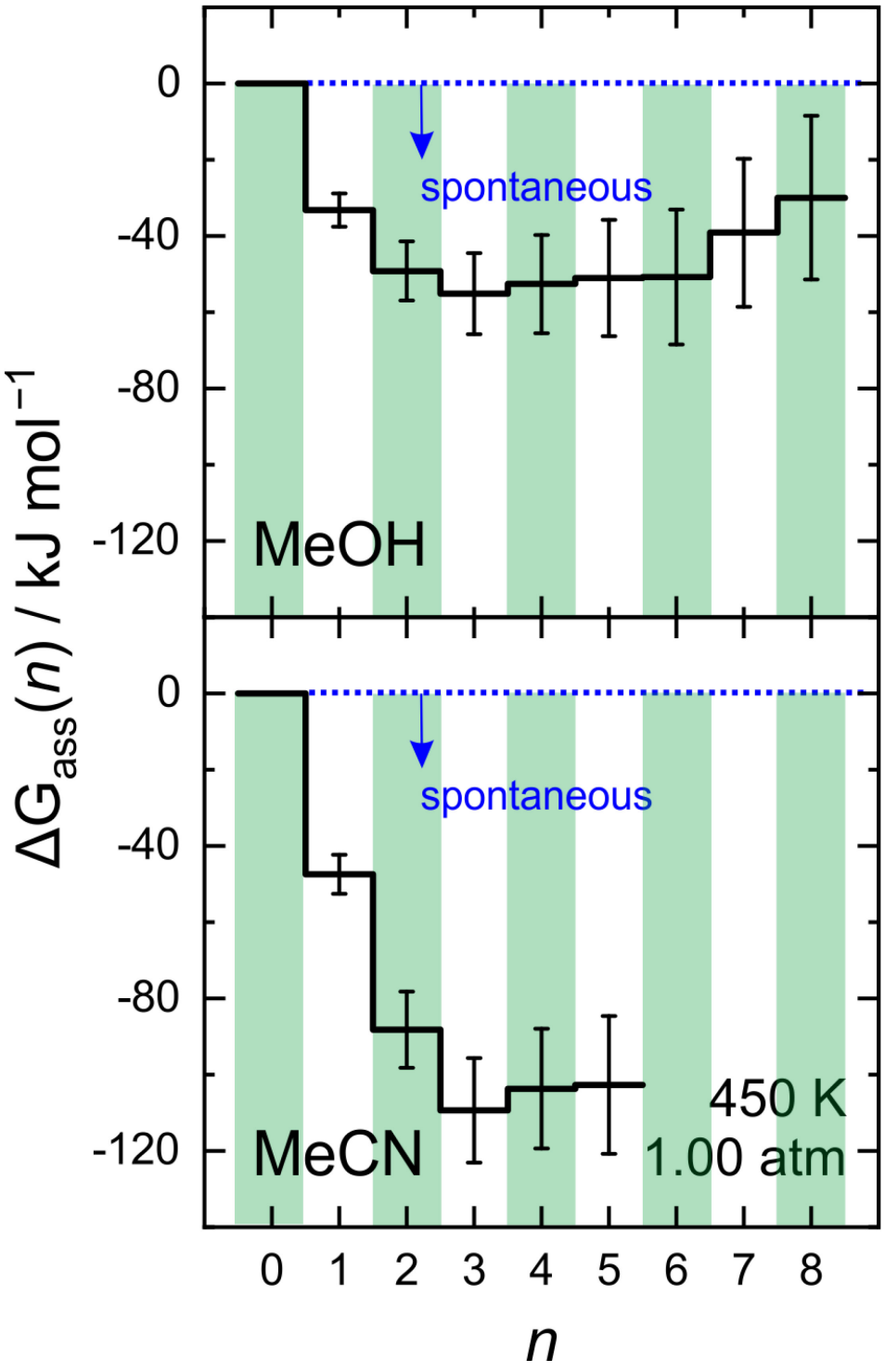

Figure 3.4. Gibbs energy of association (ΔG_{ass}) for each cluster size of MeOH and MeCN coordinated to $[PrNH_3]^+$. Values are calculated at 450 K and 1.00 atm. Error bars correspond to evaluation of ΔG_{ass} using scaling factors of 0.95 ± 0.05 for vibrational frequencies ($\pm 2\sigma$) and propagation of error (1.7 % RMSD) from the Boltzmann weighting method.

Relative populations for $[PrNH_2 + H + n(Solv)]^+$ (Solv = MeOH and MeCN) are shown in **Figure 3.5**. For the lowest temperature accessible (T_{bath} = 373 K, SV = 0 Td), $[PrNH_3]^+$ populations favour a microsolvated state consisting of four to eight MeOH molecules and three to five MeCN molecules. As T_{eff} increases beyond 450 K, entropic factors (*i.e.*, $T\Delta S_{ass}$) begin to take precedence over the intermolecular interactions (ΔH_{ass}) that regulate microsolvated structures (**Figures S3-15**). At T_{eff} = 500 K, microsolvated clusters composed of two to four MeOH molecules or three MeCN molecules dominate the gas phase ensemble. The stability of the MeCN microsolvated states is apparent, as the gas phase ensemble consists of $[PrNH_3]^+$ solvated by at least two MeCN ligands at all temperatures sampled. This supports the detection of MeCN adducts of MP1 reported in **Chapter 3.4** and, as the bare $[PrNH_3]^+$ ion only becomes populated at $T_{eff} > 850$ K. Notably, the desolvated ion becomes populated at $T_{eff} > 650$ K when MeOH is the microsolvating partner, highlighting the enhanced stability of ion-solvent clusters containing aprotic species. Microsolvated populations for the other solvent species investigated are available in **Figure S3-16**, which shows the same qualitative trends corresponding to their protic or aprotic nature.

It should be noted that **Eq. 3.7** does not account for the concentration of solvent modifier present in the DMS cell. Clearly, if the solvent concentration is zero, the population of the microsolvated cluster must also be zero. Beyond this fundamental caveat, its inclusion is necessary as the populations of microsolvated ions are directly related to the collision frequency between the analyte and chemical modifier, which determines the equilibrium constant for cluster formation. However, observations in this study suggest that the degree of microsolvation is underestimated by the modifications to Eq. 3.7 proposed in literature.[77,190] This underestimation is discussed extensively in **Supplementary Section S3-2**, alongside the complications associated with calculating thermochemistry using harmonic vibrational frequencies in systems dominated by hydrogen bonding. The overestimation of ion-solvent cluster populations by excluding the dependence of solvent concentration in **Eq. 3.7** should, to some degree, cancel the underestimation of ion-solvent

cluster size imposed by inclusion of the solvent concentration term. Thus, the stabilizing effects conferred by microsolvation reported in the subsequent section are based on ion-solvent cluster populations generated from **Eq. 3.7**.

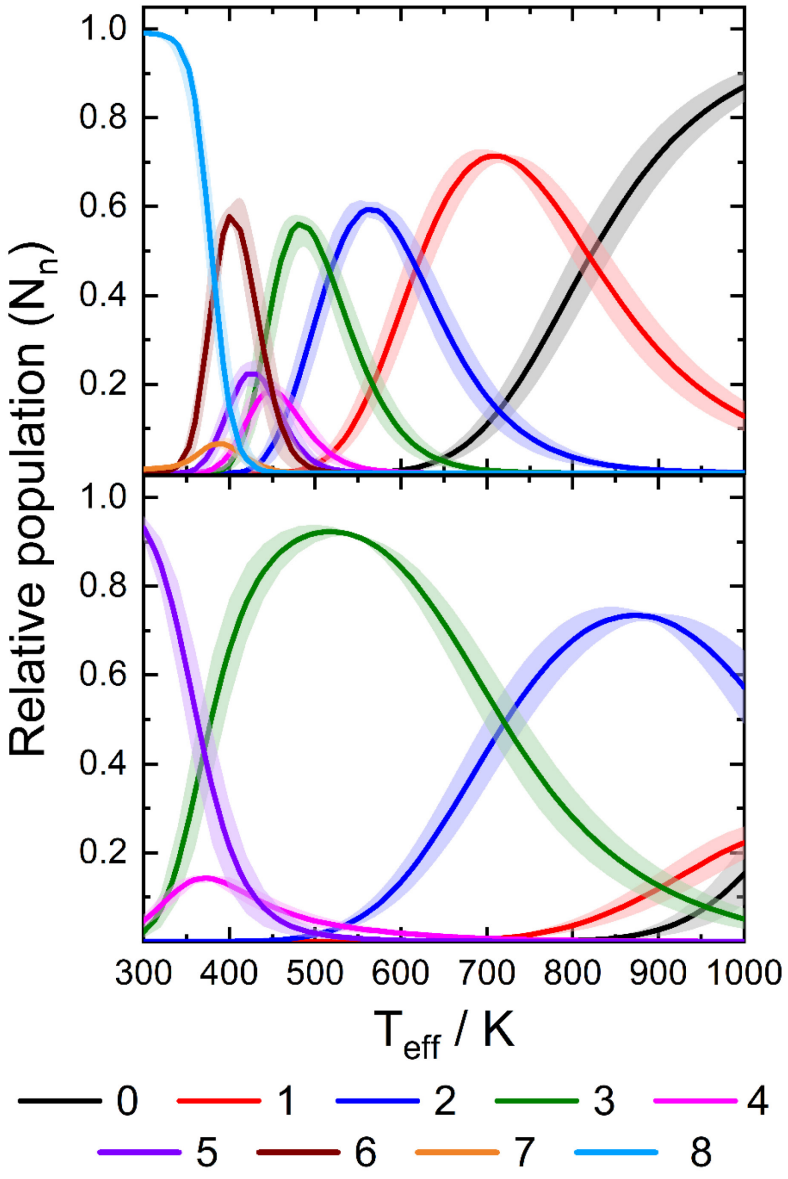

Figure 3.5. Relative populations (N_n) of microsolvated clusters of $[PrNH_3]^+$ with n MeOH (top) or MeCN (bottom) molecules as function of effective ion temperature. Error bars correspond to evaluation of ΔG_{ass} using scaling factors of 0.95 ± 0.05 for vibrational frequencies ($\pm 2\sigma$) and propagation of error (1.7 % RMSD) from the Boltzmann weighting.

3.8 The stabilizing effects conferred by ion microsolvation

Analyzing microsolvated ion populations provides critical insight into the dynamic ion-solvent clustering processes that occur in solvent-modified DMS environments. In this regard, T_{eff} is almost entirely responsible for dictating how many solvent molecules adhere to the analyte in the presence of a microsolvation partner. Incorporation of microsolvated cluster populations into the two-temperature theory approach (**Eq. 3.8**) allows for the evaluation of reductions in T_{eff} incurred upon ion microsolvation, which states that ion temperature is the sum of the bath gas temperature (T_{bath}) and heating due to the separation field (T_{field}).[58,59,77,116]

$$T_{eff} = T_{bath} + T_{field} \approx T_{bath} + \frac{M}{3k_b}(KE)^2 \qquad \textbf{Eq. 3.8}$$

In **Eq. 3.8**, M is the mass of the bath gas, K is the ion mobility, and E is the electric field strength. Predictions of T_{eff} using the two-temperature theory approach correlate well with experimentally determined T_{eff} for a suite of benzylpyridinium 'thermometer' ions evaluated under the most harsh conditions possible in our DMS system ($T_{bath} = 450$ K, $T_{field} = 276$ Td).[116] However, for the two-temperature theory approach to apply to microsolvated species, a modification that accounts for: 1) the increase in apparent mass and CCS of the microsolvated cluster due to solvent accretion, and 2) the decrease in temperature associated with solvent binding and evaporation would need to be incorporated. Both features are unfortunately difficult to integrate accurately, as the oscillating separation field creates a dynamic environment in which ion-solvent cluster populations of a finite size are transient. Moreover, the decrease in temperature associated with the evaporation processes driven by the constantly changing electric field are not known. Modelling this requires quantifying the amount of energy that goes into breaking the ion-solvent interaction and the momentum transfer between the ion-solvent cluster fragment and the solvent molecule(s) liberated during dissociation (*viz.* the partition function). Consequently, *ab initio* determinations of enthalpy changes upon evaporation of solvent from a microsolvated cluster cannot easily be converted into a relative decrease in temperature. This process is further complicated by the fact that evaporation

of solvent may occur through an unknown number of neutral solvent molecules (*i.e.,* how many neutrals are ejected from the solvent cluster as the ion core heats?) and the unknown partitioning of energy between linear momentum and internal energy of the evaporating solvent species.

Nevertheless, a crude model can be proposed using the clustering thermochemistry presented in **Chapter 3.7** combined with molecular dynamics (MD) to assess the accessibility of the protonation site(s). Details concerning this modification can be found in **Supplementary Section S3-3**. The modified two-temperature approach was conducted for each peptide and charge state employed in this study; representative examples for $[GGG + H]^+$, $[AAA + H]^+$, and $[MP1 + 3H]^{3+}$ are shown in **Figure 3.6** for select solvent modifiers at $T_{bath} = 450$ K. Plots for the remaining peptides and solvent modifiers are shown in **Figure S3-17**. The high degree of microsolvation observed at most DMS temperatures (*cf.* **Figure 3.5**) translates to significantly cooler ion temperatures in modified DMS environments, especially for smaller peptides. For example, at SV = 184 Td, two-temperature theory predicts an effective temperature of 607 K for $[GGG + H]^+$ in N_2 compared to 556 K in a MeOH modified environment. Cooling effects diminish as the ion increases in size because the ion can partition energy into a larger number of internal degrees of freedom. The tripeptide $[AAA + H]^+$, which differs from $[GGG + H]^+$ by three methyl groups, experiences a decrease in T_{eff} of 37 K in a DMS environment seeded with MeOH ($T_{eff} = 547$ K) compared to pure N_2 ($T_{eff} = 573$ K). The significantly larger $[MP1 + 3H]^{3+}$, which contains three protonated amine residues, experiences a reduction in T_{eff} of 21 K under the same conditions. The most drastic reductions in T_{eff} predicted by the two-temperature theory approach are observed when MeCN is the microsolvating partner. $[GGG + H]^+$, $[AAA + H]^+$, and $[MP1 + 3H]^{3+}$ are predicted to experience reductions in T_{eff} of 86, 62, and 38 K, respectively, compared to pure N_2 evaluations at SV = 184 Td.

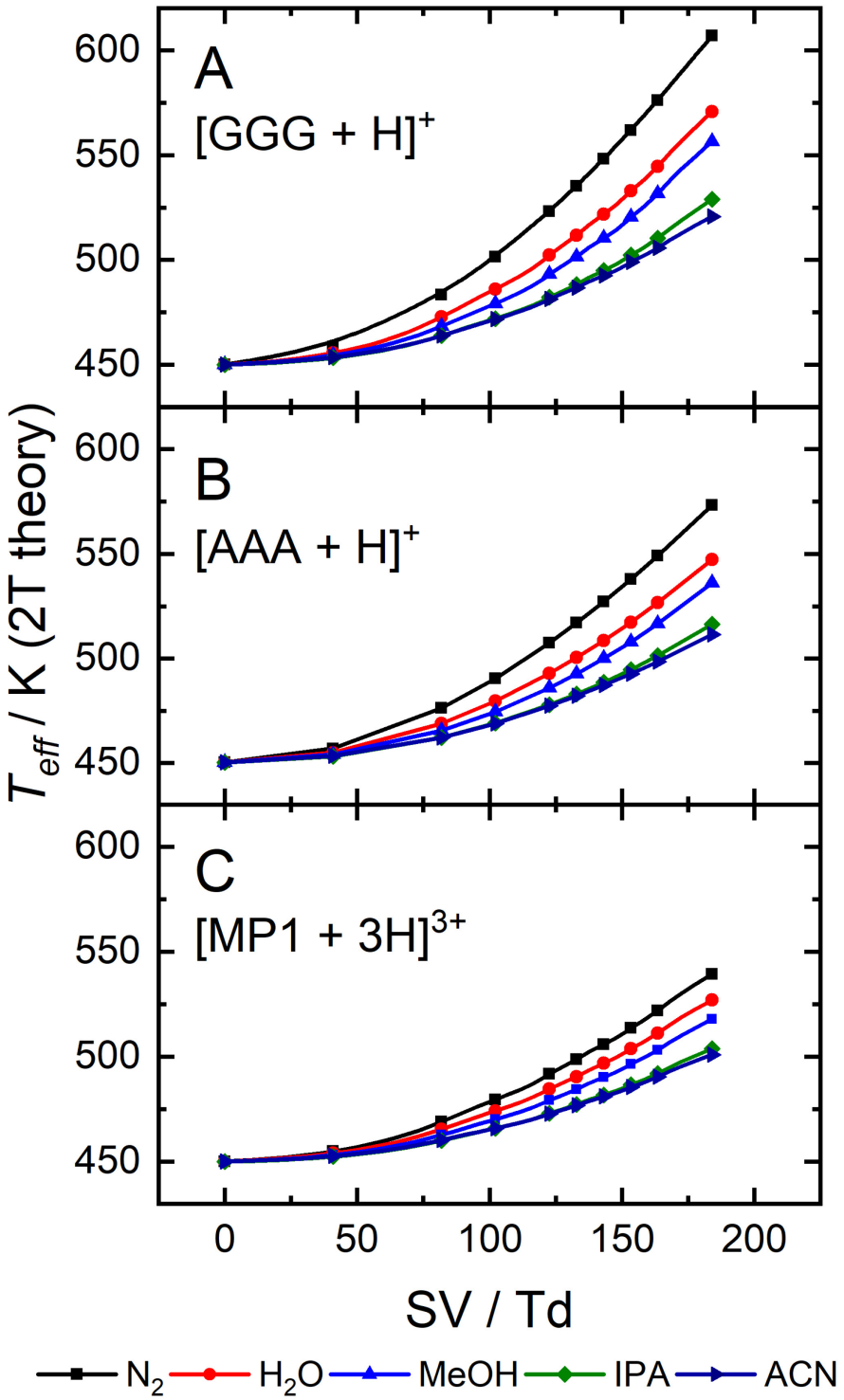

Figure 3.6. Evaluation of T_{eff} at various separation field strengths using a modified two-temperature theory approach to account for microsolvation (T_{bath} = 450 K).

Overall, the clustering propensity of $[PrNH_3]^+$ towards common DMS solvent modifiers results in a cascade of complementary effects that reduce T_{eff}. Clustering with solvent increases the ion's apparent mass and CCS, which introduces additional states in which to partition internal energy. Microsolvation also shields the analyte's charge sites from field-heating through stabilization of charge density and field-driven evaporative cooling processes. This stabilization is best achieved by aprotic solvent due to the enhanced clustering propensity relative to protic modifiers, where decreases of T_{eff} when MeCN is the microsolvating partner are nearly 2-fold greater compared to MeOH. Cooler ion temperatures favour formation of comparatively large solvent networks at sites of protonation. In the case of protic solvent modifiers, ion microsolvation can result in proton transfer through the ion-solvent hydrogen bond network if the GPB of the accreted solvent cluster exceeds that of the analyte. In instances of analyte charge reduction, T_{eff} is also reduced due to the proportionality of ion temperature with the square of ion mobility.

3.9 Conclusions

Stabilization of protonated analytes in microsolvating environments can be observed experimentally when ions are subjected to collisional activation by the separation field used in DMS. Monitoring the parent ions of the fragile tripeptides $[GGG + H]^+$ and $[AAA + H]^+$ indicated that both species are sheltered from the separation field in DMS environments seeded with volatile solvent vapour. Stabilizing effects are also observed for MP1, a 14-residue peptide containing three Lys residues. However, due to the enhanced GPB of solvent clusters compared to the free molecule, proton abstraction from the $[MP1 + 3H]^{3+}$ protomer to yield $[MP1 + 2H]^{2+}$ was observed in the presence of protic modifiers. Conducting DMS experiments in environments seeded with aprotic modifiers enabled detection of fragile $[MP1 + 4H + n(Solv)]^{4+}$ (Solv = MeCN; $n = 1 - 3$) species, which was not observed in a pure N_2 environment. This disparity between charge states observed in the presence of protic and aprotic modifiers stems from the nature of the microsolvated cluster formed, as aprotic species cannot form hydrogen-bonded solvent networks around the site of

protonation. Thus, proton transfers to aprotic modifiers cannot occur through conventional Grotthuss mechanisms or through direct transfer, as this barrier is accompanied by an energetically inaccessible structural rearrangement.[187]

Experimental observations are complemented with computational models of the microsolvation propensity of $[PrNH_3]^+$ clusters towards common protic and aprotic modifiers (H_2O, MeOH, EtOH, IPA, ACE, and MeCN) used in DMS. Clusters with protic modifiers are dominated by hydrogen bonding networks when $n > 3$, whereas aprotic modifier cluster geometries are limited to interaction with the protonated amine through direct coordination of the free protons ($n = 3$). The degree of microsolvation (*i.e.*, the number of solvent molecules bound to the protonation site) is largely dependent on entropic effects, which is evidenced through modelling populations of the microsolvated clusters. Increases in T_{eff} translate to a reduction in the number of solvent ligands attached to the corresponding ion-solvent cluster. However, the nature of the solvent also dictates the degree of microsolvation for the ion, as aprotic modifiers form more stable clusters compared to protic solvents for small cluster sizes.

Calculations of T_{eff} using ion-solvent cluster populations illustrates the stabilizing effects conferred by microsolvation in modified DMS environments. The greatest degree of ion cooling occurs when MeCN is used as the microsolvating partner, which complements both the calculated stability of MeCN clusters and the experimental detection of solvent adducts of the form $[GGG + H + MeCN]^+$, $[AAA + H + MeCN]^+$, $[MP1 + 3H + n(MeCN)]^{3+}$ ($n = 1, 2$), and $[MP1 + 4H + n(MeCN)]^{4+}$ ($n = 1, 2, 3$). Reductions in T_{eff}, prompted by formation of ion-solvent clusters, favours greater degrees of ion microsolvation through formation of large solvent networks, particularly in the case of protic modifiers. If the GPB of the solvent cluster exceeds that of the analyte, it is possible that the hydrogen-bonded solvent network can abstract a proton from the analyte and dissociate to form a protonated solvent cluster. Regardless of whether proton abstraction occurs, doping the carrier gas with volatile solvent causes a net reduction in T_{eff}. If the charge is retained on the analyte, solvent aggregation at charge sites leads to a decrease in T_{eff} through an

increase in ion-neutral CCS while also providing an avenue for ions to dissipate internal energy through evaporation of solvent. In effect, microsolvation creates a sort of "air-bag" that shelters ions from collisional activation by the separation field (*i.e.*, field-heating).

Theoretically, native ion conformations may also be preserved under high SV and high T_{bath} conditions in solvent modified DMS environments. Consider a multiply protonated peptide produced by ESI. In the condensed phase, protonated side-chain residues would protrude away from the protein core due to the extensive solvation afforded in bulk solution. During the ESI process, the transition to the gas phase removes the solvent blanket, forcing the 'naked' charges to stabilize themselves through hydrogen-bonding with carbonyl moieties present on the peptide backbone.[160] This would result in collapse of peptide secondary and tertiary structure, which would trigger a cascade of unfolding events that would ultimately result in disruption of the ion's native configuration. Backbone collapse could be prevented in a microsolvating environment, as trace solvent vapour can confer stability at protonation sites through localized solvation. This has been demonstrated in TWIMS studies of proteins, where capping protonation sites with crown ethers preserved native-like conformations of cytochrome *c* and ubiquitin.[30,32] Of course, this assumes that any ESI solvent that evaporates away during ionization is instantaneously replaced by a microsolvation partner. In our instrumental setup, solvent modifier is doped directly into the curtain gas, which flows into the DMS cell from the outer edges of the electrodes. Due to the carrier gas being introduced above atmospheric pressure, there is also some backflow of the doped carrier gas into in the ionization region. It stands to reason then that employing the stabilizing effects afforded by microsolvation in tandem with and native ionization techniques might enable native analyses in this high-field mobility regime inherent to DMS/FAIMS, as any depleted solvent can be replaced by the dopant solvent vapour during ESI droplet evaporation.

Chapter 4

Protonation-induced chirality drives separation by DMS

This chapter contains supplementary material that can be found within **Appendix C**.

4.1 *N*-protonated Verapamil exhibits two features in a DMS ionogram

The enhanced separation space afforded by DMS as either a standalone technique or coupled to LC has provided the resolution necessary for drug-monitoring workflows,[47,191–197] which can be especially challenging when isobaric metabolites are present. Upon devising a DMS-based separation workflow for a series of anti-arrhythmic drugs (**Figure S4-1** and **Supplementary Section S4-1**), we noticed that the calcium channel blocker Verapamil and its primary metabolite Norverapamil exhibited inconsistent behaviour. The structures of the two chiral compounds differ only by the presence or absence of a methyl group at the amino moiety (**Figure 4.1**). Based on their comparable structures, one might expect that the DMS behaviour of Verapamil ($[M + H]^+$; m/z 455.29) and Norverapamil ($[M + H]^+$; m/z 441.27 Da) would be similar. Much to our surprise, the ionogram of Verapamil exhibited two, baseline resolved features of equal intensity (**Figure 4.2A**), whereas Norverapamil (**Figure 4.3A**) and other analogous compounds (**Figure S4-2**) exhibited only a single peak.

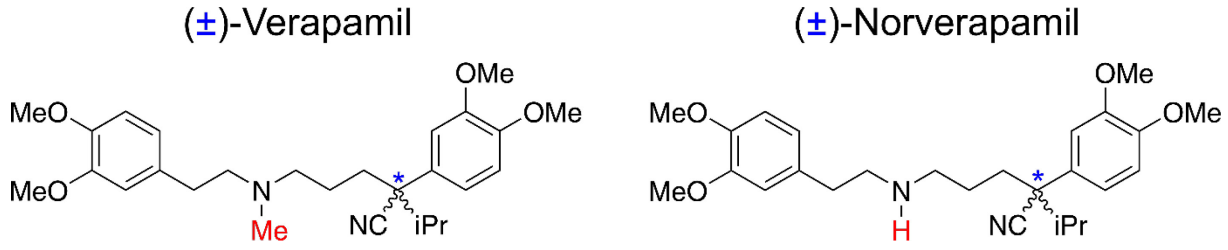

Figure 4.1. The structures of (±)-Verapamil and (±)-Norverapamil. Stereocenters are denoted with an asterisk.

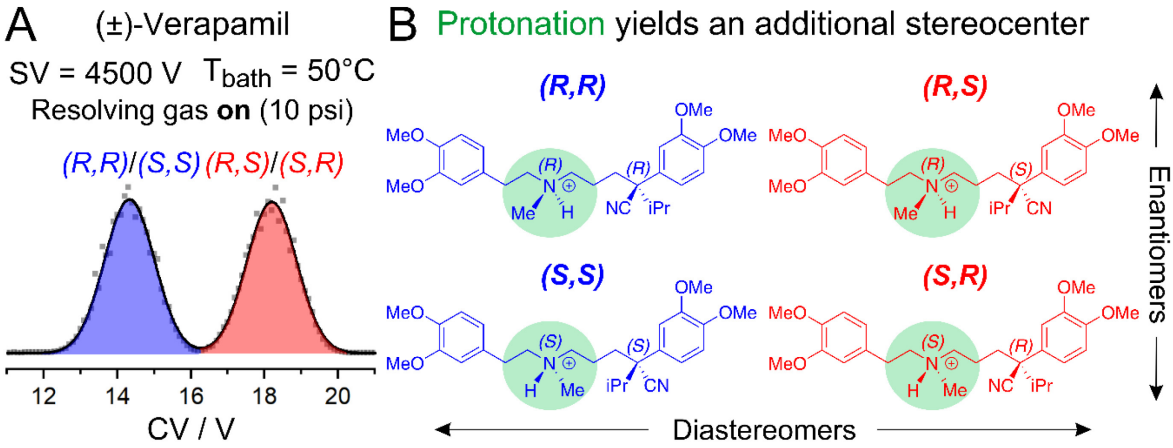

Figure 4.2. (**A**) DMS ionogram and (**B**) stereoisomers of *N*-protonated (±)-Verapamil obtained in N_2 at SV = 4500 V and T_{bath} = 50 °C with the resolving gas on (N_2; 10 psi).

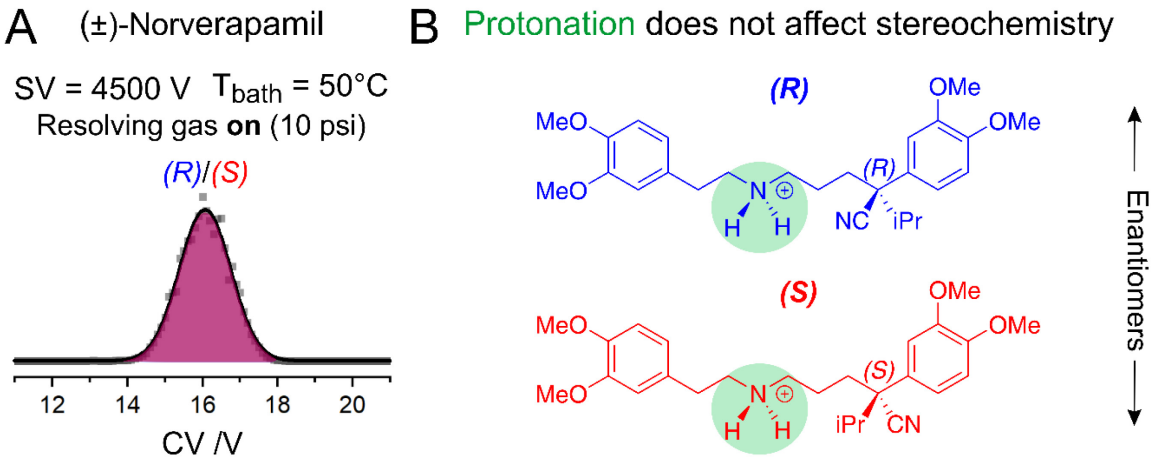

Figure 4.3. (**A**) DMS ionogram and (**B**) stereoisomers of *N*-protonated (±)-Norverapamil obtained in N_2 at SV = 4500 V and T_{bath} = 50 °C with the resolving gas on (N_2; 10 psi).

We initially thought that the species present in Verapamil's ionogram originated from the two enantiomeric forms comprising the racemate. However, this was not possible since enantiomer separation by DMS requires chiral derivatization prior to analysis.[157,198–200] We then hypothesized that the separation was caused by protonation at differing gas phase basic sites (*i.e.*, prototropic isomers), which have been resolved by DMS in the past.[46,50,201,202] In the case of Verapamil, the

energies of the prototropic isomers were higher in energy by at least 110 kJ mol^{-1} relative to the isomers that were protonated at the tertiary amine (**Figure S4-3**). Even if kinetic trapping was occurring, it is unlikely that these high-energy species would be present in the gas phase ensemble. Moreover, if the multiple signals for Verapamil were associated with prototropic isomers, analogous behaviour would have also been observed for Norverapamil.

Knowing that protonation was likely occurring at the amino moieties, we envisioned something truly out-of-the-box: chirality induced by protonation. Tertiary amines are achiral due to rapid inversion about the nitrogen centre.[203,204] However, protonation of Verapamil at the tertiary amine (hereafter called *N*-protonated Verapamil) during electrospray ionization (ESI) yields a quaternary amine with four unique substituents, which introduces an additional chiral centre. In the condensed phase at acidic pH prior to ESI (50:50 H_2O/MeOH with 0.1% HCOOH), this proton is dynamically exchanged with the protic solvent, creating an equilibrium between tertiary and quaternary nitrogen configurations. Upon desolvation of *N*-protonated Verapamil during the ESI process, nitrogen inversion is not possible since there is no mechanism to remove the proton and regenerate the tertiary centre (**Figure S4-4**). In other words, the stereochemical configuration of a protonated, quaternary amine is locked in the gas phase.

Bearing this in mind, the gas phase ensemble of *N*-protonated (±)-Verapamil consists of four possible stereoisomers: (R,R), (S,S), (R,S), or (S,R) (**Figure 4.2B**). Note that the R or S nomenclature denotes the stereochemical configuration at the quaternary nitrogen and permanent stereocenter, respectively. The set of four stereoisomers contains two enantiomeric pairs (*i.e.,* mirror images that differ in the absolute configuration of every stereocenter); (R,R) is the mirror image of (S,S), and (R,S) is the mirror image of (S,R). The stereochemical relationship between $(R,R)/(S,S)$ and $(R,S)/(S,R)$ is diastereomeric, meaning that they differ in the configuration of at least one, but not all, stereocenters. Since diastereomers exhibit unique physicochemical properties, it is possible that the two peaks observed in the DMS data can be ascribed to protonation-induced chirality. Because protonation does not introduce a second chiral center for

Norverapamil, diastereomeric pairs are not formed and only a single feature is observed since the resulting enantiomers cannot be resolved in the achiral DMS environment (**Figure 4.3B**).

To further test our hypothesis that the resulting diastereomers of *N*-protonated Verapamil exhibit unique ion mobilities, we characterized the arrival time distribution (ATD) of Verapamil using travelling wave IMS (TWIMS; **Figure 4.4**). An ion's ATD adopts a single Gaussian distribution if the gas phase ensemble consists of a single structural/stereochemical configuration. If the ATD is unimodal, the full-width half-max (FWHM) will be influenced by the conformational flexibility of the analyte. In other words, the FWHM of the ATD of a rigid ion will be smaller than that of a flexible ion of similar mass. Interestingly, the FWHM of the Verapamil ATD was reproducibly broader than the ATD of Norverapamil at several TWIMS wave height and wave speed combinations (see **Table S3-3**), suggesting that protonation-induced diastereomers are nearly coeluting.

To explore the possibility of coeluting diastereomers, two Gaussian distributions with a FWHM equal to that of Norverapamil were fit to Verapamil's ATD. The centroids of each Gaussian distribution were converted to a collision cross section (CCS) using a procedure outlined in the **Supplementary Section S4-2**. One can determine ion structure by comparing the experimental CCS to those generated by a computational model for computed low-energy structures. These computations require conformational mapping of the ion's potential energy landscape followed by high-level quantum chemical calculations, usually at the density functional level of theory (DFT).[65,67,117,118] Details of the CCS calculation protocol employed in this study are outlined in **Supplementary Section S4-3**.[110,115]

The agreement between the calculated and experimental CCSs supports the hypothesis that Verapamil's ATD consists of two diastereomers. The CCSs of the (R,R) and (S,S)-Verapamil enantiomers were calculated to be 209.2 and 210.3 Å^2, respectively. The average value of 209.7 Å^2 agrees well with the experimental CCS for the larger Verapamil diastereomer, 212.3 Å^2. The CCSs for (R,S) and (S,R)-Verapamil were calculated to be 205.8 and 205.4 Å^2. The average value of

205.6 Å^2 agrees well with the experimental CCS of 208.4 Å^2, which differs from $(R,R)/(S,S)$-Verapamil's CCS as per the Z-test ($\sigma_{CCS} < 1.7$ Å^2). Conversely, the calculated CCS of (R)-Norverapamil (205.3 ± 1.3 Å^2) is indistinguishable from (S)-Norverapamil (205.5 ± 1.3 Å^2), both of which agree with the experimental value (206.6 Å^2).

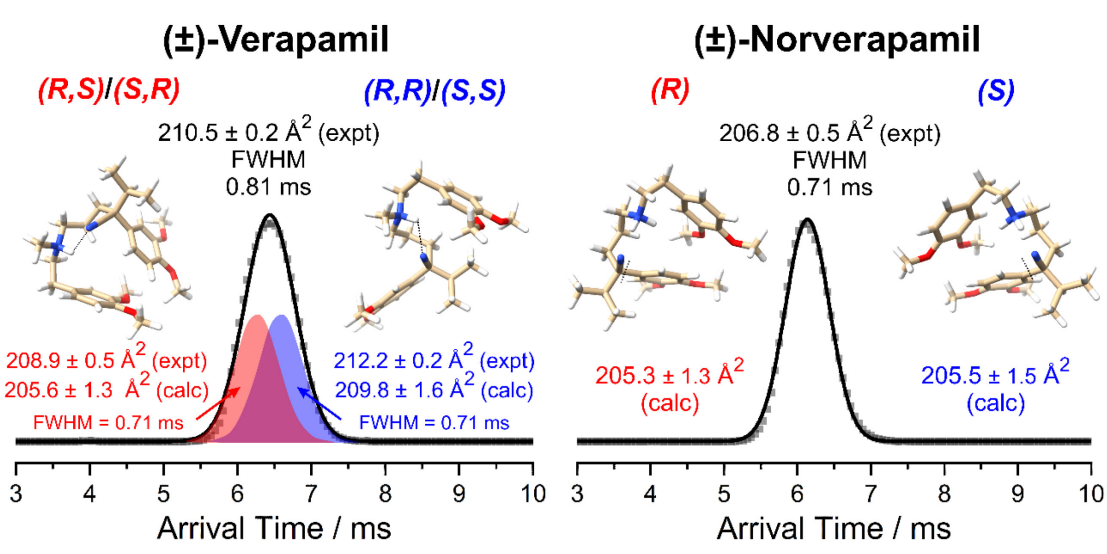

Figure 4.4. ATDs of *N*-protonated (±)-Verapamil (top) and (±)-Norverapamil (bottom) ATD datapoints (transparent squares) are fit with a Gaussian distribution (black line). Two additional Gaussian distributions are fit to the ATD of (±)-Verapamil with a constrained FWHM of 0.71 ms (the FWHM of the (±)-Norverapamil ATD). Experimental CCSs are determined from the centroid of the ATD and compared to calculated CCSs from DFT models.

Further evidence to support protonation induced chirality as the separation mechanism can be ascertained by modelling the DMS behaviour of Verapamil and Norverapamil.[77,78] The modelling protocol employs first-principles IMS theory,[36] which incorporates the temperature-dependent CCS of each conformation present in the gas phase ensemble. A comparison of the experimental and simulated dispersion curves (*i.e.*, a plot of the CV required for ion elution as a function of SV) for *N*-protonated Verapamil and Norverapamil is shown in **Figures S4-5** and **S4-6**, respectively. Full details of the *in silico* modelling procedure are provided in **Supplementary Section S4-4**.

Simulating DMS behaviour qualitatively reproduces the separability of $(R,R)/(S,S)$-Verapamil from $(R,S)/(S,R)$-Verapamil and lack of separation for $(\pm)$-Norverapamil. Moreover, the relative CV shifts determined for each diastereomeric pair enables assignment of each peak in Verapamil's ionogram to the corresponding stereoisomers (*cf.* **Figure 4.2A**). It is interesting that the DMS modelling captures the diminishing resolution of Verapamil's diastereomers at elevated bath gas temperatures. To highlight this result, experimental and simulated ionograms of *N*-protonated Verapamil are shown in **Figure 4.5**. Simulated ionograms were generated using two Gaussians with centroids determined by the predicted CV and FWHMs that match the experimental peak. For ease of visualization, simulated ionograms are shifted such that the lower CV species overlaps with the lowest CV experimental peak.

With compelling evidence to support protonation-induced chirality as the separation mechanism, we postulated that this phenomenon could be observed in analogous chemical systems. In theory, only two criteria need to be met for *N*-protonation to produce diastereomers: 1) the molecules must contain at least one permanent stereocenter, and 2) protonation must occur only on a tertiary amino moiety containing three unique substituents. To test this hypothesis, we measured the DMS behaviour of the metabolite pairs Selegiline/Norselegiline, Rotigotine/Dethienylethyl Rotigotine (*i.e.*, Rotigotine Impurity B), and *N*-methyl proline/proline. Within these pairs, *N*-protonation yields an additional stereocenter at the *N*-methylated amino moiety of the parent molecule but does not affect chirality in the metabolite. **Figure 4.6** shows that the *N*-methylated metabolites exhibit dual features in their ionograms, albeit at different relative intensities compared to Verapamil. The relative intensities of these two peaks should be equal since chirality is introduced to the nitrogen centre, which is racemized in the condensed phase prior to ESI. Differences in peak intensities can likely be attributed to the differing intermolecular interactions occurring within each diastereomer, which can either stabilize or destabilize the molecule. For example, the presence or absence of intramolecular hydrogen bonding between the protonated amine and carboxylic acid in *N*-methyl proline yields substantial differences in the relative stabilities of the diastereomers, and hence, their population in the gas phase ensemble. Differences in peak intensity are also possible if

1) nitrogen inversion in the condensed phase is slow (*i.e.,* steric hindrance) or 2) if the more stable condensed phase diastereomer gets kinetically trapped during the droplet evaporation portion of ESI.

To further test the protonation-induced chirality hypothesis, we performed DMS measurements on six additional molecules (**Figure S4-7**) and three Verapamil-like molecules (**Figure S4-8**). Separation of the *N*-protonated diastereomers was achieved for all but one species (Ibutilide), suggesting that a third prerequisite must be met to observe protonation-induced chirality. Since Ibutilide contains several rotatable dihedral angles, its conformational flexibility likely masks differences in the differential mobility between two protonation-induced diastereomers, precluding their total resolution. This interpretation is consistent with the diminishing resolution observed for Verapamil as the bath gas temperature increases (*cf.* **Figure 4.5**). Increasing the bath gas temperature imparts more energy into the analyte, which can break the intramolecular interactions that give rise to the unique differential mobilities of each diastereomer. Experimental conditions then must be 'cool' enough to preserve the structural motifs that facilitate separation. Given the increasing usage and resolution of ion mobility instrumentation,[205–208] practitioners should be aware that protonation-induced chirality is a general phenomenon that can impact their experimental outcomes by introducing additional peaks that would otherwise not be expected.

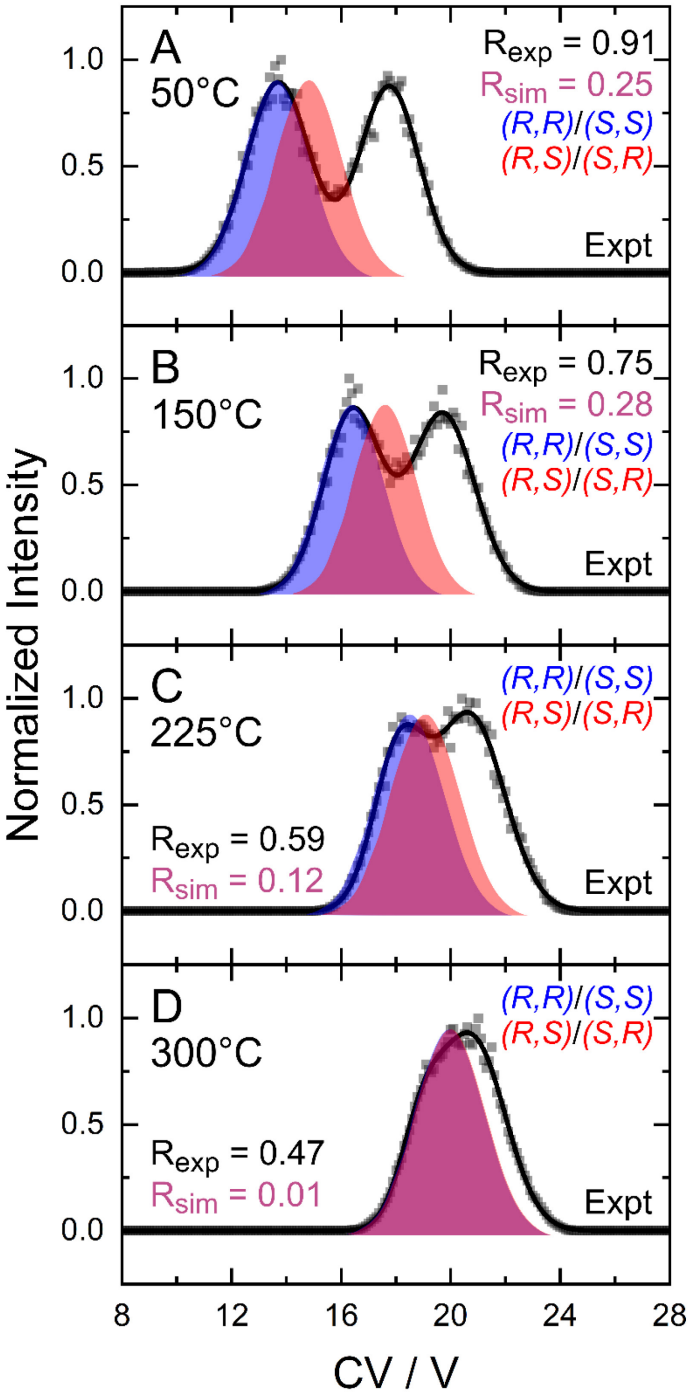

Figure 4.5. Experimental (black) and simulated ionograms of *N*-protonated (R, R) and (S, S)-Verapamil (blue) and (R, S) and (S, R)-Verapamil (red) at SV = 4500 V in N_2. Ionograms were acquired at DMS cell temperatures of (**A**) 50 °C, (**B**) 150 °C , (**C**) 225 °C, and (**D**) 300 °C. Peak resolution in the experimental (R_{exp}) and simulated (R_{sim}) ionograms are provided.

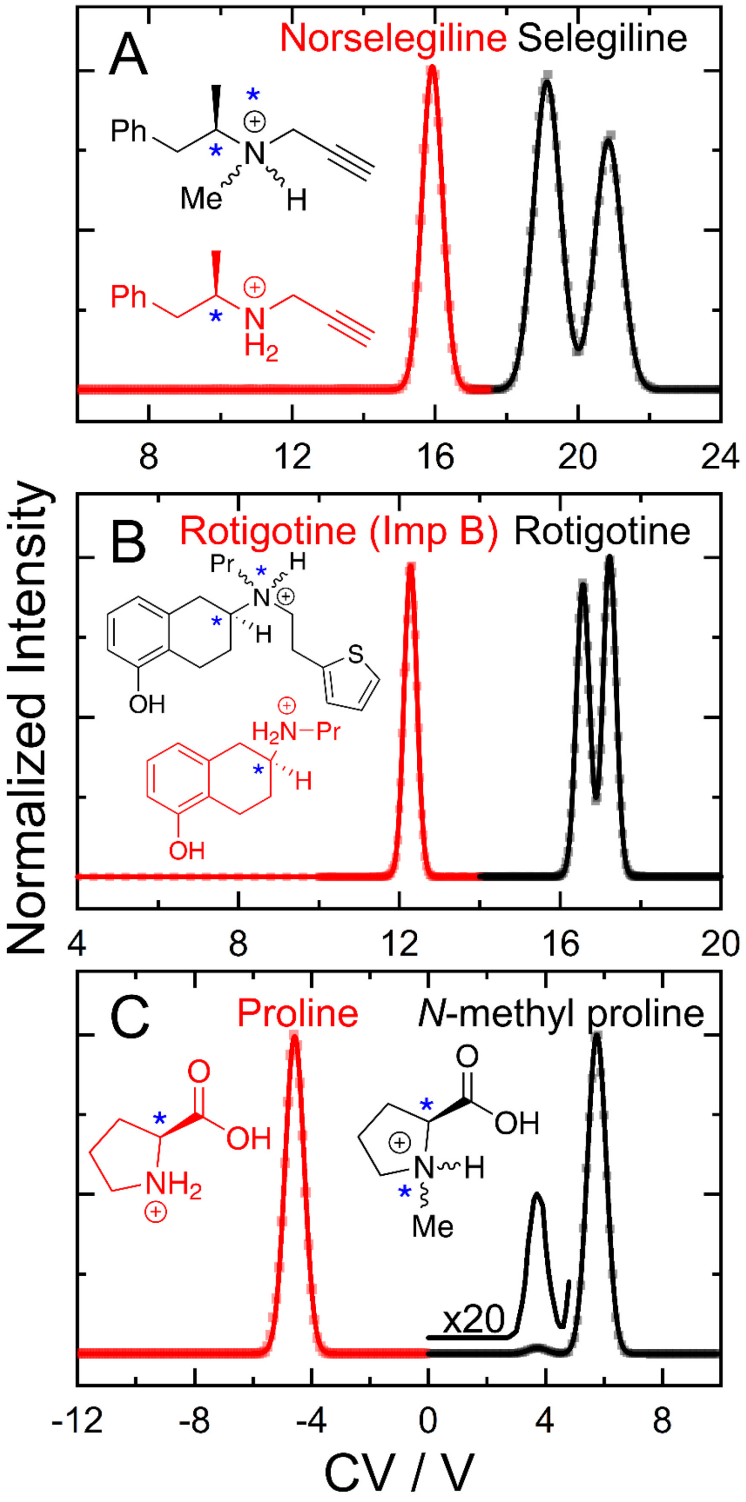

Figure 4.6. DMS ionograms of (**A**) Selegiline/Norselegiline, (**B**) Rotigotine/Rotigotine Impurity B, and (**C**) *N*-methyl proline/proline at SV = 4500 V and T_{bath} = 150 °C. Stereocenters are denoted by a blue asterisk.

Chapter 5

Argentination: a silver bullet for cannabinoid analysis by DMS-MS²

This chapter contains supplementary material that can be found within **Appendix D**.

5.1 Introduction

With recreational cannabis becoming legalized in more parts of the world, governing bodies are implementing new regulations for products by which commercial growers must abide.[209,210] For example, cannabis products sold in Canada must state the quantity of Δ^9-tetrahydrocannabinol (THC) and cannabidiol (CBD) contained within the product either as purchased (*e.g.,* edibles) or once activated by combustion (dried cannabis). This information is important for quality control purposes and is invaluable to the consumer,[211] especially to new users who may be unaware of their tolerance for a particular cannabinoid. Recreational cannabis users often seek the "high" associated with Δ^9-THC, whose psychotropic effects stem from its ability to act as a partial agonist to the cannabinoid receptors found within the brain.[212,213] Normally, the brain's cannabinoid receptors are stimulated by anandamide, a fatty acid neurotransmitter that is endogenous to humans.[214] Since these receptors are located in areas of the brain that regulate muscle coordination and memory, stimulation by THC disrupts regular communication pathways, leading to cannabis' well-known psychoactive effects.

In contrast to Δ^9-THC, CBD is negative allosteric modulator of cannabinoid receptors,[215] decreasing the response induced from chemical stimuli. Some clinical work has demonstrated that CBDs behaviour can be used in the treatment of neurodegenerative disease,[216,217] although its popularity amongst the public is a result of anecdotal reports claiming its effectiveness for treating anxiety and other related conditions. Because of the proliferation of anecdotal evidence, recreational use of CBD products has increased, particularly in the United States where the passing of the

Agriculture Improvement Act (AIA) in 2018 effectively legalized the cannabinoid.[218] Known informally as the 'Farm Act,' the AIA distinguished hemp from marijuana, removing it from the DEA schedule of controlled substances. The amended AIA states that hemp is "the plant *Cannabis sativa* L. and any part of that plant, including the seeds thereof and all derivatives, extracts, cannabinoids, isomers, acids, salts, and salts of isomers, whether growing or not, with a Δ^9-THC concentration of not more than 0.3 percent on a dry weight basis." As a result, CBD sourced and isolated directly from hemp is legal if the total content of Δ^9-THC within the cannabis plant is below 0.3 %. Once enacted, a significant increase in the production of hemp and marketing of CBD products was anticipated,[219] and naturally led to the increased usage of cannabis and its legalization within certain states.[220,221] However, the AIA's compliance requirement only considers the Δ^9-THC content of hemp, so CBD and its derivatives have been granted protection under the AIA's interpretation. This situation has opened legal loopholes because CBD can be chemically transformed into several isomers of Δ^9-THC by heating under acidic conditions.[222–225] One of the more notable isomers is Δ^8-THC,[226] a psychoactive cannabinoid whose synthesis from CBD was first reported in the 1940s and has since been refined to improve its selectivity.[227–229] Since Δ^8-THC is an isomer of CBD, and technically a CBD derivative when obtained via cyclization, some have argued that it should be protected under the AIA's 2018 amendment.[230] However, one could make the argument that Δ^8-THC is a synthetic cannabinoid since its natural abundance in cannabis is negligible compared to other cannabinoids, indicating that Δ^8-THC products are almost exclusively manufactured via the cyclization of CBD.[231] All synthetic cannabinoids are controlled by the Drug Enforcement Administration (DEA) within the US, so even if Δ^8-THC is legal at the state level under the AIA, it may still be considered illegal by federal law.

Despite the murky legal landscape surrounding Δ^8-THC, several products containing Δ^8-THC began appearing on the US market in 2019, stimulating public interest that was especially prominent in states where access to Δ^9-THC is restricted.[232] Because Δ^8-THC production is unregulated, the presence of by-products and impurities that are intrinsic to its synthesis poses an extreme risk to consumers. Ignoring the fact that Δ^8-THC consumption has not yet been deemed "safe" for human

consumption by government health agencies,[233,234] Δ^8-THC products have been found to contain novel cannabinoids with no known information on their bioactivity or safety.[235] Moreover, Δ^8-THC products obtained from the cyclization of CBD exhibit several impurities, including heavy metals that bioaccumulate within plants cultivated from contaminated soil.[236] To make matters worse, none of the twenty-seven products analyzed by Meehan-Atrash and Rahman reported accurate Δ^8-THC quantitates.[236] Until regulatory bodies approve Δ^8-THC for human consumption, there is an undeniable need for chemical separations that can distinguish Δ^8-THC and other adulterants within commercial products.

From an analytical standpoint, differentiating Δ^8-THC, Δ^9-THC, and CBD is rather complicated given that these cannabinoids are structural isomers. Cannabis also contains cannabichromene (CBC), another structural isomer of Δ^8-THC, Δ^9-THC, and CBD (**Figure 5.1** and **S5-1**).[237,238] Because structural isomers are isobaric, they cannot be distinguished using mass spectrometry (MS). Cannabinoids also cannot be distinguished by their fragment ions formed upon collision activation from either their protonated or deprotonated precursors,[239,240] so the introduction of orthogonal separation techniques such as liquid chromatography (LC) are necessary in quantitative workflows. Baseline separation of cannabinoids by LC typically requires 10 – 20 minute chromatographic runs and extensive sample preparation to ensure column longevity.[239–244] High throughput alternatives for cannabinoid separation include several electrochemical and colourimetric approaches,[245–248] although certain colourimetric methods lack specificity and can result in false positives if the sample contains other phenolic compounds.[249]

Alternative platforms that achieve the separation power afforded by LC, but without long elution times, include the various ion mobility spectrometry (IMS) techniques. Specifically, Hädener and coworkers developed a workflow for the separation of Δ^9-THC and CBD on a high-resolution drift-tube IMS (DTIMS) system.[250] Tose and coworkers coupled travelling wave IMS (TWIMS) with LC to separate Δ^9-THC, CBD, and their respective acidic forms found within the marijuana flower and in hashish.[251,252] Mashmoushi and coworkers used differential mobility spectrometry (DMS) to

separate Δ^9-THC, CBD, and CBC.[253] Unlike linear IMS technologies such as DTIMS and TWIMS, which separate ions based on their mobility at a set electric field strength below the low-field limit, DMS utilizes the non-linear dependence of an ion's mobility when field-strengths are increased above the low-field limit.[39–42] As ions pass through the DMS cell in a gas flow, an asymmetric waveform (separation voltage, SV; **Figure 5.2A**) causes them to migrate off-axis in a zig-zag trajectory. By applying a static compensation voltage (CV) offset to the SV such that the integral over a single SV duty-cycle is no longer zero, ions can be steered onto a stable trajectory that permits transmission through the DMS device (**Figure 5.2B**). The magnitude and sign (*i.e.,* positive or negative) of the CV needed to transmit ions through the DMS device is usually different for each analyte, and thus, creates a mechanism that spatially resolves ions based on their differential mobilities under high and low electric fields.

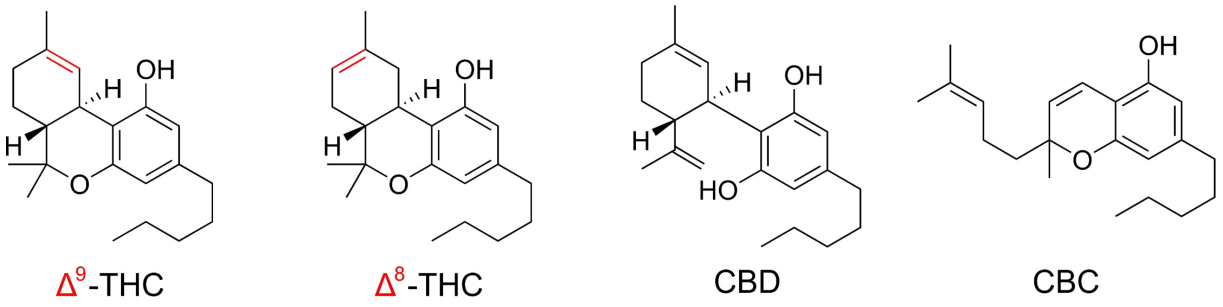

Figure 5.1. Structures of Δ^9-THC, Δ^8-THC, CBD, and CBC. Differences in double bond position between Δ^8/Δ^9-THC are highlighted in red.

The separation power afforded by DMS can be enhanced by doping the DMS carrier gas with solvent vapour.[45,254–256] The increase in separation power is a consequence of microsolvation, which increases the difference between the ion's high and low-field mobility and is usually ion-specific. This phenomenon is rooted in the heating/cooling cycles associated with field-induced temperature variations imparted by the SV, where the oscillating waveform drives analyte solvation/desolvation cycles as the ion transitions between the low-field to the high-field portion of the duty cycle.[64,257,258]

Mashmoushi *et al.* showed that optimal sensitivity and resolution was afforded by detecting the cannabinoids as deprotonated anions in a N_2 DMS environment that was seeded with 1.5 mol% of IPA.[253] However, our attempts to add Δ^8-THC to this workflow resulted in its coelution with CBD using various chemical modifiers (**Figures S5-1** and **S5-2**), indicating that an alternative separation strategy will be required. The successful separation of cannabinoids by flash chromatography employing Ag^+-impregnated silica implies that argentination could be a viable approach,[259] prompting us to investigate the potential of DMS to separate cannabinoids as $[M + Ag]^+$ adducts.

5.2 Experimental methods

The experimental apparatus consists of a planar SelexION DMS with a 1 mm gap-height (SCIEX, Canada), which was mounted in the atmospheric region between a Turbospray electrospray ionization (ESI) source and the sampling orifice of a QTRAP 5500 hybrid triple quadrupole linear ion trap mass spectrometer (*cf.* **Figure 1.1B** and **S5-4**).[39,41,42] Analytical standards of each cannabinoid were obtained as 1 mg mL^{-1} solutions in MeOH from Ceriliant (Texas, USA). Analytes were diluted to working concentrations of 100 – 500 ppb (100 – 500 ng mL^{-1}) in MeOH and subsequently infused into the ESI source at 10 µL min^{-1}. For data acquisition in negative mode, the ESI solvent was doped with 0.5% NH_4OH. Formation of Ag^+ adducts of the cannabinoids was afforded by adding 5 ppm (*i.e.,* 5 µg mL^{-1}) of AgOAc to the ESI solvent and monitoring ion transmission in positive mode.

The nascent ions generated by ESI were carried through the DMS region by the curtain gas (CUR; *ca.* 1 atm) towards the sampling orifice of the mass spectrometer. DMS-MS measurements consisted of generating an ionogram, in which MRM transitions of the deprotonated or argentinated ions were monitored at a fixed separation voltage (SV) while the compensation voltage (CV) was ramped from 0 V to 20 V in 0.1 V increments. MRM transitions of the deprotonated and

argentinated cannabinoids are provided in **Tables S5-1** and **S5-2**, respectively. SVs were selected to give the best possible separation in the respective DMS environment. In this case, the best separation was observed at the maximum SV accessible by our instrument (4500 V). N_2 was used as source gas, the curtain gas in the DMS cell (CUR; 20 psi), the collision gas for tandem-MS experiments (*ca.* 7 mTorr), and as the DMS resolving gas (DR; 0 – 50 psi). The temperature within the DMS cell was controlled using the on-board heater, which heats the ceramic casing that encompasses that DMS electrodes and CUR gas line. Solvent vapour was seeded into the CUR gas by cutting the gas line and then affixing the free ends with a Swagelok Tee. Liquid solvent was infused into the open end of the Tee connector using an Agilent 1100 LC pump at a flow rate that produces the desired mole fraction of solvent vapour within the CUR gas (*i.e.,* 1.5 mol%). All additional instrumental parameters are provided in **Table S5-3**.

5.3 Computational methods

Quantum-chemical calculations were performed to assess the affinity of each cannabinoid for argentination. Briefly, candidate geometries for the neutral and argentinated form of Δ^8-THC, Δ^9-THC, CBD, CBC, cannabinol (CBN), cannabigerol (CBG), and *exo*-THC were generated manually. Each candidate structure was used as an input for the Conformer-Rotamer Ensemble Sampling Tool (CREST),[260,261] which generated a series of low-energy structures using the GFN2-xTB semiempirical tight-binding model.[262] For each neutral and argentinated cannabinoid, all structures generated by CREST that were within 25 kJ mol^{-1} of the lowest energy conformer were extracted and additionally sorted by cosine similarity,[72] yielding 5 – 30 representative conformers. Each of the unique conformers was carried forward for optimization at the ωB97X-D3/Def2-TZVPP level of theory, which employed the RIJcosX approximation and the Def2/J auxiliary basis set.[263–268] Normal mode analyses were conducted to ensure that each structure corresponded to a true minimum (*i.e.,* no imaginary frequencies) and to calculate thermochemical corrections. Electronic energies of the optimized structures were refined with single-point energy calculations conducted at the DLPNO-

CCSD(T)/Def2-TZVPP level of theory, which used the Def2/C auxiliary basis set.[91–93,269] Thermochemical quantities were determined by combining DLPNO-CCSD(T) single point electronic energies with ωB97X-D3 thermochemistry, which we report as DLPNO-CCSD(T)/Def2-TZVPP//ωB97X-D3/Def2-TZVPP. All *ab initio* and density functional theory (DFT) calculations were performed using the ORCA computational package (version 5.0.3).[87,90,270,271] Results of the quantum-chemical calculations are provided in the ioChem-BD database entry associated with this manuscript (**https://doi.org/10.19061/iochem-bd-6-225**).[272] For the convenience of the reader, the structures of the lowest energy configuration of each argentinated and neutral cannabinoid are provided in **Supplementary Section S5-1**, alongside details concerning quantum-chemical calculations used to rationalize the fragmentation behaviour of each argentinated cannabinoids (**Supplementary Sections S5-2** and **S5-3**).

The affinity of each cannabinoid for argentination is determined by the Gibbs energy of association (ΔG_{ass}; **Eq. 5.1**) , where G_{Ag^+}, G_M, and $G_{[M+Ag]^+}$ are the Gibbs energies of the silver cation, neutral cannabinoid, and argentinated cannabinoid, respectively. Calculation of ΔG_{ass} uses weighted Gibbs energies, where the population ρ of the n^{th} isomer in the ensemble is determined by its Gibbs corrected electronic energy, G_n, (**Eq. 5.2**; $T = 298$ K). The Gibbs energy of the ensemble, G, is given by the product of the n^{th} isomer's population and Gibbs energy, summed over all n isomers (**Eq. 5.3**).

$$\Delta G_{ass} = G_{Ag^+} + G_M - G_{[M+Ag]^+} \qquad \textbf{Eq. 5.1}$$

$$\rho_n = \frac{exp\left(\frac{G_n}{(RT)}\right)}{\sum_n exp\left(\frac{G_n}{(RT)}\right)} \qquad \textbf{Eq. 5.2}$$

$$G = \sum_n (\rho_n)(G_n) \qquad \textbf{Eq. 5.3}$$

5.4 MS² analysis of argentinated cannabinoids

Since Δ^8/Δ^9-THC, CBD, and CBC are isobaric species with an accurate mass of 314.2246 Da, their argentinated forms are also isobaric, albeit with major isotopologues of m/z 421.1297 and 423.1293 associated with the ^{107}Ag (52 %) and ^{109}Ag (48 %) isotopes. This characteristic makes argentination susceptible to reductions in sensitivity due to isotope dilution. To address this issue, the transmission window of Q1 on the QTRAP 5500 was modified to allow all ions within a 3 Da window centered at 422 Da to be transmitted (*i.e.,* 422 ± 1.5 Da), enabling simultaneous transmission of the m/z 421 and 423 isotopologues. During the subsequent characterization of each argentinated cannabinoid by tandem-MS, we found that each argentinated isotopologue generated the same product ions (owing to loss of Ag-containing neutrals), and that major product ions originating from each cannabinoid were distinct. For example, the major product ion upon subjecting both [Δ^9-THC + ^{107}Ag]$^+$ and [Δ^9-THC + ^{109}Ag]$^+$ to CID is m/z 313, which corresponds to the loss of ^{107}AgH/^{109}AgH (**Figure 5.2A**). Conversely, CID of [Δ^8-THC + ^{107}Ag]$^+$ and [Δ^8-THC + ^{109}Ag]$^+$ both generate a fragment with a m/z of 245, which corresponds to the loss of $^{107}AgC_5H_9$/$^{109}AgC_5H_9$ (**Figure 5.2B**). CID of both CBC and CBD yielded a fragment of m/z 231 as their main product ion through the elimination of $^{107}AgC_6H_{11}$/$^{109}AgC_6H_{11}$ (**Figure 5.2C** and **Figure 5.2D**). However, MS^3 indicates that CBD yielded a product of m/z 231 from a silver-containing fragment with an isotopic distribution of 355/357 (arising from the loss of C_5H_8 from the parent ion), whereas CBC produces m/z 231 directly from the argentinated precursor. **Figure 5.3** provides a summary of the product ions observed via CID.

Considering the inability of MS² to distinguish Δ^8/Δ^9-THC, CBD, and CBC as protonated or deprotonated species (*i.e.,* [M + H]$^+$ or [M – H]$^-$),[239,240] it is unclear why argentination promotes unique fragmentation mechanisms for each cannabinoid. One possible explanation is related to the tendency of argentinated ions to fragment via the loss of AgH or other organo-silver species, which have significantly lower energy barriers of formation compared to the corresponding fragments that would be generated from their protonated/deprotonated analogues (*i.e.*, loss of a hydrogen, methyl,

or alkyl radical).[49,273,274] Another possibility is that the distinctive fragmentation behaviour of each argentinated cannabinoid is linked to the stability of the cation formed upon dissociation of the silver-containing fragment. Plausible mechanisms that explain how each argentinated cannabinoid fragments during CID are proposed in **Figure 5.3**. The MS^2 spectrum of Δ^9-THC indicates that the molecular ion decomposes into one major product via the loss of AgH (m/z 313). MS^3 experiments indicate that two fragments with a m/z of 231 and 217 are produced from the m/z 313 product ion, alongside several other minor fragments (**Figures S5-5** and **S5-6**). Based on this observation, it is likely that the initial loss of AgH, which yields m/z 313, entails the elimination of the hydrogen at the bicyclic interface as this particular fragmentation generates an exceptionally stable, conjugated cation. Only at sufficiently high collision energies does the m/z 313 fragment decompose further via ring contraction to expel 1-heptyne, yielding the m/z 217 species.

Interestingly, the intensity of the m/z 313 product ion that originates from $[\Delta^8\text{-THC} + \text{Ag}]^+$ is only a fraction of the intensity of the analogous species produced from $[\Delta^9\text{-THC} + \text{Ag}]^+$. It stands to reason that the loss of AgH from Δ^8-THC does not result in a particularly stable product ion owing to the position of the alkene, which does not afford extension of the conjugated network. Instead, AgH elimination from Δ^8-THC occurs concurrently with a retro Diels-Alder decomposition that produces isoprene and a vinyl cation with a m/z of 245. This cation is likely to exist in equilibrium with its cyclized form owing to the proximity of the oxygen lone pair and vacant, coplanar sp^2 orbital. Several other minor fragments ions originate from $[\Delta^8\text{-THC} + \text{Ag}]^+$, such as m/z 271, which fragments to m/z 231 via an intramolecular elimination that is reminiscent of the β-hydride abstraction of certain benzylpyridinium ions (**Figures S5-7** and **S5-8**).[275] This is contrary to the product ion spectrum of $[\text{CBC} + \text{Ag}]^+$, where the m/z 231 species dominates, indicating that it must be more stable relative to the m/z 231 fragment produced from $[\Delta^8/\Delta^9\text{-THC} + \text{Ag}]^+$, and thus, must exhibit a different structure.

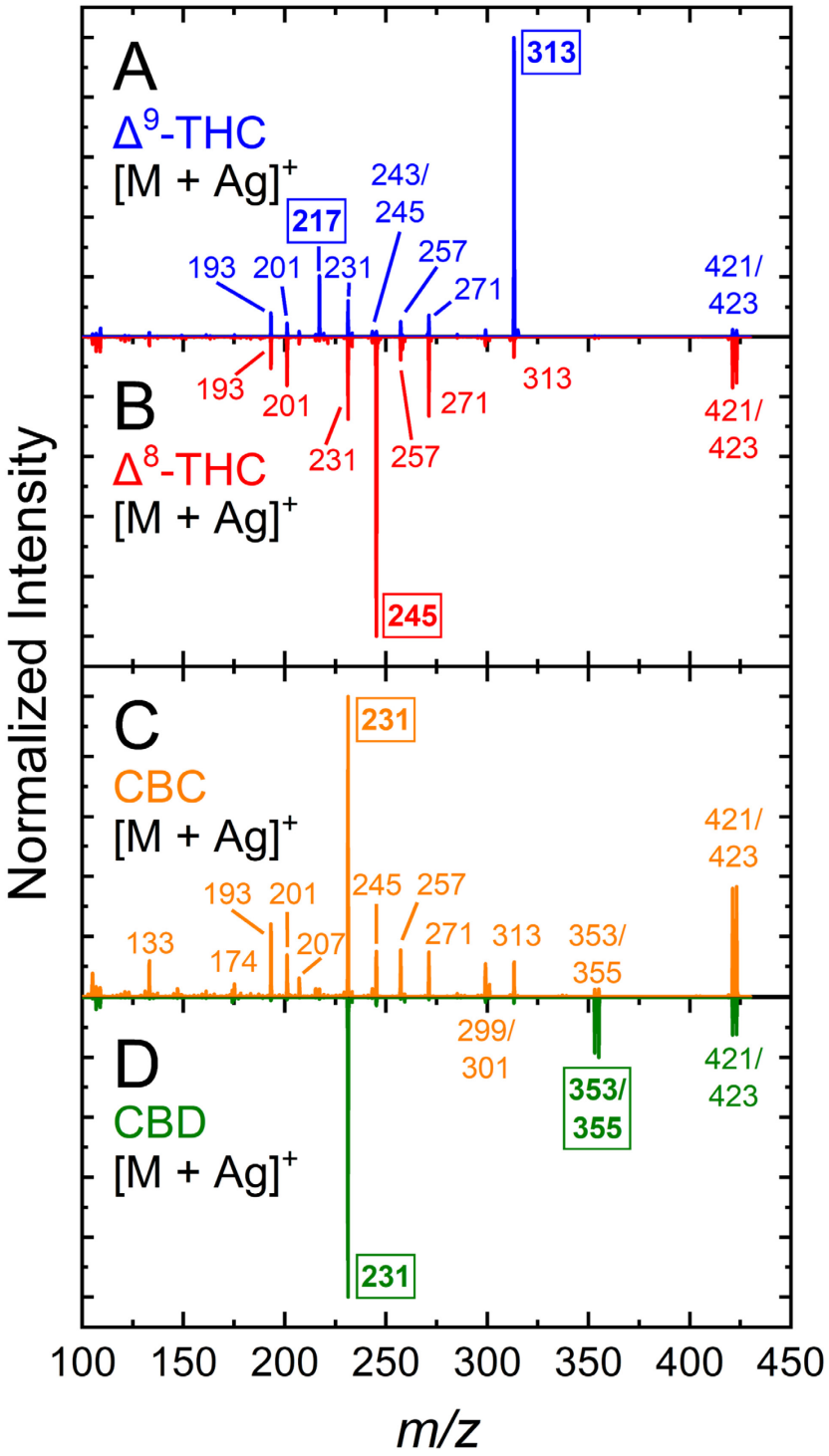

Figure 5.2. Product ion spectra of (**A**) $[\Delta^9\text{-THC} + \text{Ag}]^+$, (**B**) $[\Delta^8\text{-THC} + \text{Ag}]^+$, (**C**) $[\text{CBC} + \text{Ag}]^+$, and (**D**) $[\text{CBD} + \text{Ag}]^+$, as measured at CE = 35 V. Note that Q1 was modified to transmit both m/z 421 and 423 isotopologues of each argentinated cannabinoid. The m/z of major fragments are highlighted by boxes.

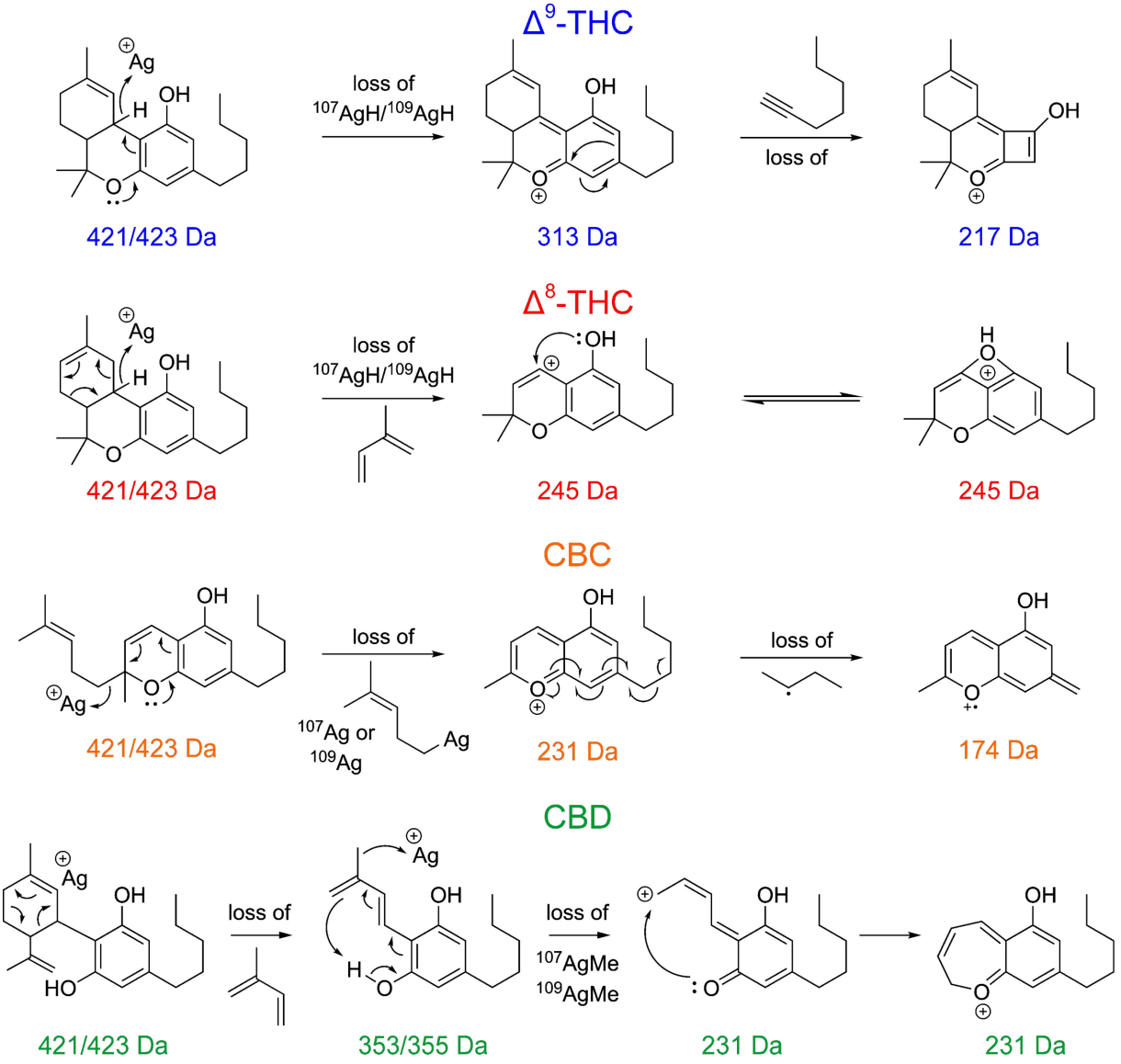

Figure 5.3. Proposed mechanisms of formation for the major product ions observed in the MS^2 spectra of $[\Delta^9\text{-THC} + Ag]^+$ (blue), $[\Delta^8\text{-THC} + Ag]^+$ (red), $[CBC + Ag]^+$ (orange), and $[CBD + Ag]^+$ (green).

The product ion spectrum of $[CBC + Ag]^+$ also contains a plethora of minor fragments (**Figures S5-9** and **S5-10**), the diversity of which is related to its structure. Instead of the tricyclic motif adopted by Δ^8/Δ^9-THC, CBC is a bicyclic system with an open chain that contains a single element of unsaturation. Experimental and computational validation of how the structural differences between cannabinoids impact their fragmentation mechanisms would be an interesting

follow-up study. Until such studies can be completed, we hypothesize that the "free arm" of CBC precludes decomposition via the retro Diels-Alder processes that were observed for Δ^8/Δ^9-THC. Instead, m/z 353/355 forms directly from $[\text{CBC} + \text{Ag}]^+$ via the loss of an isoprenyl radical. Further breakdown results in the formation of an aromatic diol with a m/z of 193 (**Figure S5-10**), or a hydroxylated methylchromene with a m/z of 174.

Compared to the diverse array of product ions observed for $[\text{CBC} + \text{Ag}]^+$, and to some extent with $[\Delta^8/\Delta^9\text{-THC} + \text{Ag}]^+$, $[\text{CBD} + \text{Ag}]^+$ exhibits a much simpler MS^2 spectrum. Only three ions with a m/z of 355, 353, and 231 are observed, with m/z 231 being the most intense feature in the product ion spectrum. All three fragments appear to be extremely stable, with the m/z 231 species being the most stable as per its intensity relative to the m/z 355 and 353 signals. Additionally, the ~52:48 ratio of the intensity for the m/z 353 and 355 species suggests that these product ions contain silver, differing by the isotopic composition of ^{107}Ag and ^{109}Ag. This was confirmed by performing MS^3 experiments on the m/z 353 and 355 species, both of which produce m/z 231 (**Figure S5-11**). It is likely that the m/z 353 and 355 fragment ions are produced from m/z 421 and 423, respectively, via a retro Diels-Alder decomposition that expels isoprene. This fragmentation is similar to the one incurred for $[\Delta^8\text{-THC} + \text{Ag}]^+$, although in this case, silver is retained within the product ion. The retention of silver suggests that CBD has a higher affinity for Ag^+ relative to Δ^8-THC, which is reflected in quantum-chemical calculations of the ΔG_{ass} for cannabinoid argentination (**Table 5.1**).

Table 5.1. Calculated ΔG_{ass} for each cannabinoid upon argentination. Calculations are performed at the DLPNO-CCSD(T)/Def2-TZVPP//ωB97X-D3/Def2-TZVPP level of theory.

Cannabinoid	ΔG_{ass} / kJ mol^{-1}
CBN	200.6
Δ^8-THC	205.6
exo-THC	210.3
Δ^9-THC	220.3
CBD	262.2
CBC	266.3
CBG	290.4

Although the argentinated cannabinoid isobars exhibit distinct fragmentation patterns when subjected to CID, several cannabinoids produce minor amounts of a fragment that is isobaric with the major fragment generated by another cannabinoid. For example, m/z 313 is the major fragment formed from $[\Delta^9\text{-THC} + \text{Ag}]^+$, but is also formed in small quantities by $[\Delta^8\text{-THC} + \text{Ag}]^+$, $[\text{CBC} + \text{Ag}]^+$, and $[\text{CBD} + \text{Ag}]^+$. Consequently, quantitation of Δ^9-THC solely by MS^2 would require subtraction of the contribution of Δ^8-THC, CBC, and CBD to the m/z 313 fragmentation channel. This deconvolution would be challenging, and ultimately precludes the use of tandem-mass spectrometry to *quantitatively* differentiate cannabinoid isobars. Zuilhof and coworkers have shown that tandem-MS can be used to *semi*-quantitatively distinguish cannabinoids as argentinated adducts, but this is only applicable when samples contain exclusively Δ^9-THC and CBD.[276] To accurately quantitate samples that contain additional cannabinoids, a secondary separation technique is needed.

5.5 DMS-MS^2 analysis of the argentinated cannabinoids

Guided by the prior success of separating Δ^9-THC, CBD, and CBC as deprotonated species, we hypothesized that separation of the argentinated forms of each cannabinoid could be achieved in a DMS environment seeded with 1.5 mol% of IPA vapour.[253] However, when infusing the cannabinoids via ESI (1 ppm in MeOH with 5 ppm of AgOAc) in the presence of 1.5 mol% of IPA, the signals corresponding $[\Delta^8\text{-THC} + \text{Ag}]^+$ and $[\Delta^9\text{-THC} + \text{Ag}]^+$ were not observed. Operation of the DMS in transmission mode (*i.e.,* SV = 0 V, CV = 0 V) while conducting Q1 scans indicated that IPA adducts of the argentinated cannabinoids dominate the gas phase population in the IPA-modified environment (**Figure S5-12**). This inability to observe the bare $[\Delta^8/\Delta^9\text{-THC} + \text{Ag}]^+$ species came as somewhat of a surprise, especially because other argentinated species have been detected as $[\text{M} + \text{Ag}]^+$ adducts under analogous conditions.[277] Quantum-chemical calculations of $[\Delta^8/\Delta^9\text{-THC} + \text{Ag}]^+$ show that Ag^+ is relatively exposed compared to the analytes described in reference 277 (*cf.* **Figure S5-4**). It stands to reason that introducing these species to an IPA-modified DMS

environment favours ion-solvent cluster formation irrespective of the affinity of the modifier for Ag^+. Previous studies using the trapped ion mobility platform have demonstrated that Δ^9-THC is particularly vulnerable to adduct formation, thus providing additional evidence that ion-solvent clustering adversely impacts the $[\Delta^8/\Delta^9\text{-THC} + Ag]^+$ signal.[278]

Because the susceptibility of $[\Delta^8/\Delta^9\text{-THC} + Ag]^+$ to adduct formation impedes the use of chemical modifiers in the DMS workflow, we assessed the potential of separating argentinated cannabinoids in a pure N_2 DMS environment. The separation efficacy was initially evaluated at the maximum SV achievable by the instrument (4500 V), at a DMS heater (DT) setting of 150 °C, and a declustering potential (DP) setting of 100 V. The ionograms measured under these conditions for $[\Delta^9\text{-THC} + Ag]^+$ and for $[\Delta^8\text{-THC} + Ag]^+$ are depicted in **Figure 5.4**. Curiously, the ionogram of $[\Delta^9\text{-THC} + Ag]^+$ exhibited two features: a minor peak at CV = 15 V and a major peak at CV = 18 V. Selecting each peak in the ionogram of $[\Delta^9\text{-THC} + Ag]^+$ and conducting precursor ion scans revealed that the entities eluting within the CV = 15 V window are clusters of the form $[\Delta^9\text{-THC} + Ag + AcOH]^+$ and $[\Delta^9\text{-THC} + Ag + AcOH + MeOH]^+$. The detection of clustered species by MRM suggests that these ions remain intact while passing through the DMS cell, and then dissociate in the atmospheric pressure region between the DMS cell and the orifice that leads to the mass spectrometer, or within the QJet/Q0 regions preceding Q1.[46] Because the DT and DP settings regulate collisional activation within these regions of the instrument, minimizing these settings should mitigate the post-DMS fragmentation of the AcOH-containing clusters. Indeed, minimizing the DT to 50 °C and the DP to 0 V prevented the dissociation of Δ^9-THC adducts, and resulted in an ionogram with a single peak for each cannabinoid with minimal loses to sensitivity (**Figure 5.4C** and **S5-13**).

After devising a technique that minimizes the dissociation of solvent adducts following DMS separation, we generated an ionogram for a mixture of argentinated cannabinoids containing Δ^8-THC, Δ^9-THC, CBD, and CBC. Resolving gas (*i.e.,* DR gas) was introduced to enhance separation of the peaks corresponding to Δ^9-THC and CBD (see TIC trace, **Figure 5.5A**; N_2,

DR = 40 psi). Introducing DR gas throttles the flow of the carrier gas that transports ions through the DMS device. As a result, ions spend a longer time in the DMS cell and experience more SV duty cycles. Greater exposure to the SV enhances differences in the off-axis migration of the different cannabinoid ions, which in turn improves the separation power of the instrument at the cost of sensitivity. **Figure 5.5B** – **Figure 5.5E** show the ionograms obtained when monitoring specific MRM channels. For example, **Figure 5.5B** shows the m/z 421/423 → m/z 313 channel, which yields an ionogram that is dominated by the feature associated with [Δ^9-THC + Ag]$^+$, but shows minor contributions from the Δ^8-THC, CBD, and CBC analogues. Achieving comparable peak areas for each argentinated cannabinoid requires that the Δ^8/Δ^9-THC content in the ESI solution to be 5-fold greater than the concentration of CBD and CBC. This coincides with the enhanced affinity of Ag^+ for CBD and CBC gleaned from quantum-chemical calculations; ΔG_{ass} for the argentination of CBD and CBC (262.2 and 266.3 kJ mol^{-1}, respectively) are significantly higher than for Δ^8-THC and Δ^9-THC (205.6 and 220.3 kJ mol^{-1}, respectively). Nevertheless, argentination resulted in excellent sensitivity within each MRM channel, and, based on the high signal to noise ratio observed, should be suitable for quantitation by standard addition.

To determine the linear response range for quantification, we monitored each analyte by their most prominent MRM transition: 421/423 → 313 for [Δ^9-THC + Ag]$^+$, 421/423 → 245 for [Δ^8-THC + Ag]$^+$, 421/423 → 353/355 for [CBD + Ag]$^+$, and 421/423 → 231 for [CBC + Ag]$^+$. Triplicate measurements of analyte responses were taken for cannabinoid concentrations within the 50 – 1000 ppb range, all of which were prepared in MeOH with 5 ppm of AgOAc and 200 ppb of CBD-A as an internal standard (m/z 465/467 → 231). The response for each cannabinoid in the 50 – 1000 ppb range is shown in **Figure S5-14** ($R^2 > 0.99$), although it should be noted that this assessment does not consider matrix effects. Because the separation strategy involves detection of the analyte as [M + Ag]$^+$, any matrix component that can bind Ag^+ can induce analyte suppression, and thus, interfere with quantitation. To ensure that the linear response is not compromised by matrix effects, the same standard addition approach was used to quantify cannabinoids within a commercial cannabis extract. The "Full Spectrum Delta-8 THC Oil" produced by RedPill, which

contains Δ^8- and Δ^9-THC at concentrations of 19 and 3.8 mg mL^{-1}, respectively, was selected for this purpose because its matrix includes several terpenes suspended in medium chain triglycerides, all of which can bind Ag^+ and lead to suppression of the analyte.

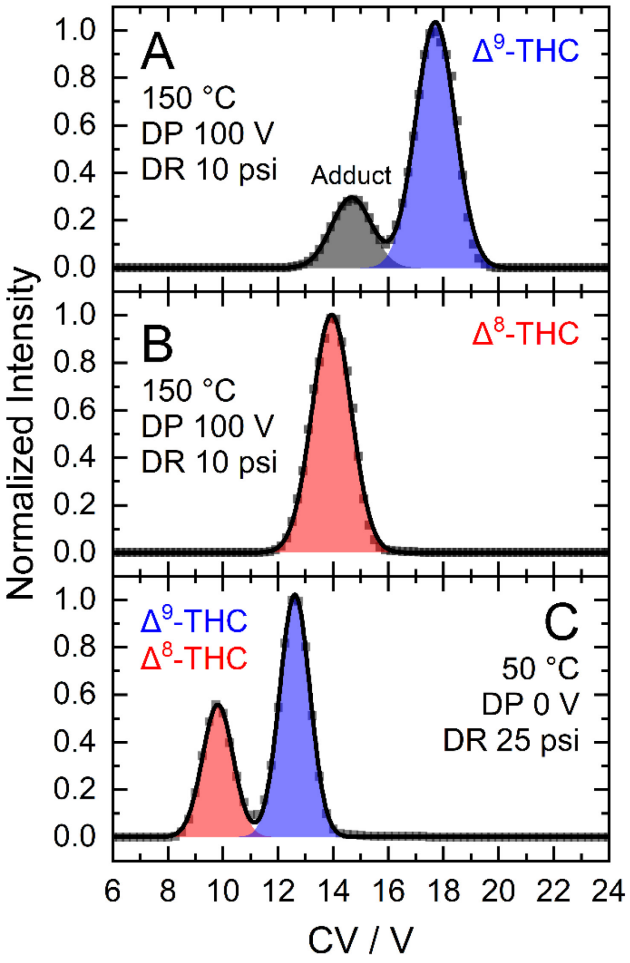

Figure 5.4. Ionograms of (**A**) $[\Delta^9\text{-THC} + Ag]^+$ and (**B**) $[\Delta^8\text{-THC} + Ag]^+$ in a pure N_2 environment at SV = 4500 V, DT = 150 °C, DP = 100 V, and DR = 10 psi. Ag^+ adducts of Δ^8/Δ^9-THC (1 ppm) were produced via ESI from 50:50 MeOH/H_2O containing 0.1% formic acid and 5 ppm of AgOAc. In panel (**A**), ion-solvent clusters of the form $[\Delta^9\text{-THC} + Ag + AcOH]^+$ and $[\Delta^9\text{-THC} + Ag + AcOH + MeOH]^+$ dissociate in the post DMS region, resulting in an additional ionogram peak when gating on the $[\Delta^9\text{-THC} + Ag]^+$ MRM transition. (**C**) Minimizing the DP and DT settings to 0 V and 50 °C, respectively, at SV = 4500 V prevents cluster dissociation and affords separation of a 1:1 mixture of Δ^8/Δ^9-THC (1 ppm each).

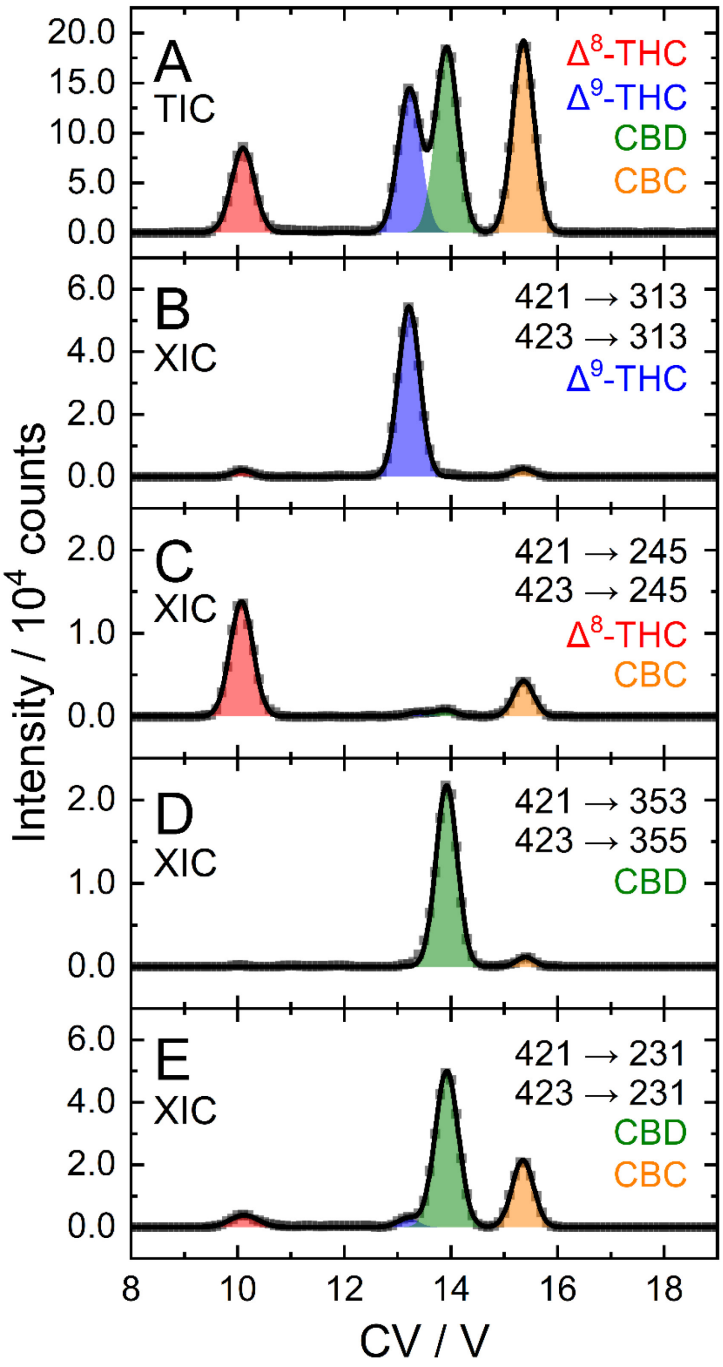

Figure 5.5. (**A**) Total ion chromatogram and (**B** – **E**) extracted ion chromatograms from specific MRM transitions for the separation of argentinated Δ^8-THC (red), Δ^9-THC (blue), CBC (orange), and CBD (green) by DMS-MS. Major contributions to each MRM channel are shown on the right of each panel. Ionograms were obtained in a pure N_2 environment at SV = 4500 V, DP = 0 V, and DT = 50 °C from a mixture containing Δ^8-THC (500 ppb), Δ^9-THC (500 ppb), CBD (100 ppb), CBC (100 ppb), and AgOAc (5 ppm) in MeOH.

Quantitation of the RedPill extract was accomplished by a "dilute and shoot" approach, whereby a small aliquot of sample was diluted in MeOH by a factor of 50,000 prior to treatment with 5 ppm of AgOAc. Samples were then quantified by standard additions of Δ^8-THC, Δ^9-THC (50 – 750 ppb) with CBD-A (200 ppb) as the internal standard. Each respective standard addition was performed in triplicate, with the limit of detection (LOD) and limit of quantitation (LOQ) being determined from the slope (S) and standard deviation (σ) of the calibration curve (**Eq. 5.4** and **Eq. 5.5**, respectively).[34] In addition to matrix effects, we also considered that cannabinoids exhibiting a high ΔG_{ass} for argentination can supress analytes with a comparatively low ΔG_{ass}. To account for this, we included standard additions of CBC and CBD (50 – 150 ppb) to the quantitation workflow. Linear response of each argentinated cannabinoid was not impacted by matrix components or high concentrations of CBC and CBD, as shown by the calibration curves in **Figure S5-15** ($R^2 > 0.99$). Moreover, LODs and LOQs associated with the argentination approach are comparable to those associated with DMS-based quantitation of cannabinoids as anions in an IPA modified environment (LOD ~ 20 ppb; see **Tables S4** and **S7** in ref. 253). Multiplication of the X-intercept determined from linear regression by the dilution factor yields concentrations of Δ^8/Δ^9-THC that align with those stated by the manufacturer (**Table 5.2**). Without knowledge of how the concentration of each cannabinoid was determined by the manufacturer, we cannot verify the accuracy of our results, although the agreement between the values supports the validity of the argentination approach for cannabinoid quantitation.

Table 5.2. Quantitation of the Full Spectrum Δ^8-THC Oil (RedPill). Quantitation was performed using standard additions ($n = 3$) of each cannabinoid with CBD-A (200 ppb) as the internal standard.

Cannabinoid	Manufacturer stated initial concentration / mg mL^{-1}	Measured Concentration /mg mL^{-1}	LOD / ppb	LOQ / ppb
Δ^8-THC	19	18.6 ± 0.5	19	57
Δ^9-THC	3.8	4.3 ± 0.3	15	45
CBD	< 1	0.3 ± 0.1	6	18
CBC	Not stated	0.1 ± 0.03	2	6

$$LOD = \left(\frac{10}{3}\right)\left(\frac{\sigma}{S}\right) \quad \textbf{Eq. 5.4}$$

$$LOQ = 10\left(\frac{\sigma}{S}\right) \quad \textbf{Eq. 5.5}$$

5.6 Extending the DMS-MS workflow to other argentinated cannabinoids

The success of the argentination approach described above prompted us to investigate whether other cannabinoids could be separated and quantified by DMS. Cannabigerol (CBG), the non-psychoactive precursor of other cannabinoids, is growing in popularity as a CBD alternative owing to the clinical evidence that supports its potential in treating neurodegenerative disorders.[279,280] Similarly, cannabinol (CBN), a non-biogenic but psychoactive cannabinoid, forms upon exposure of Δ^9-THC to air and light.[281] These compounds can be found within commercial extracts as either intended components or inadvertent adulterants, the latter of which may arise from non-specific extraction protocols of hemp that has been harvested prematurely or stored improperly. Although CBG and CBN are protected by the 2018 AIA interpretation, their low relative abundance within the cannabis plant indicates that products containing these compounds are likely sourced from non-compliant precursors or synthetic cannabinoids.[282] One of the hallmarks indicative of cannabinoid synthesis, particularly from the acid-catalyzed isomerization of CBD,[222–225,283] is *exo*-THC (*i.e.,* $\Delta^{9,11}$-THC),[284] a psychoactive cannabinoid exhibiting a similar potency to Δ^8-THC. It is reasonable to assume that DMS can be used to separate the argentinated forms of CBG, CBN, and *exo*-THC in tandem with Δ^9-THC, Δ^8-THC, CBD, and CBN, but before doing so, it is necessary to discern their fragmentation patterns such that analytes can be detected via MRM (**Figure 5.6**).

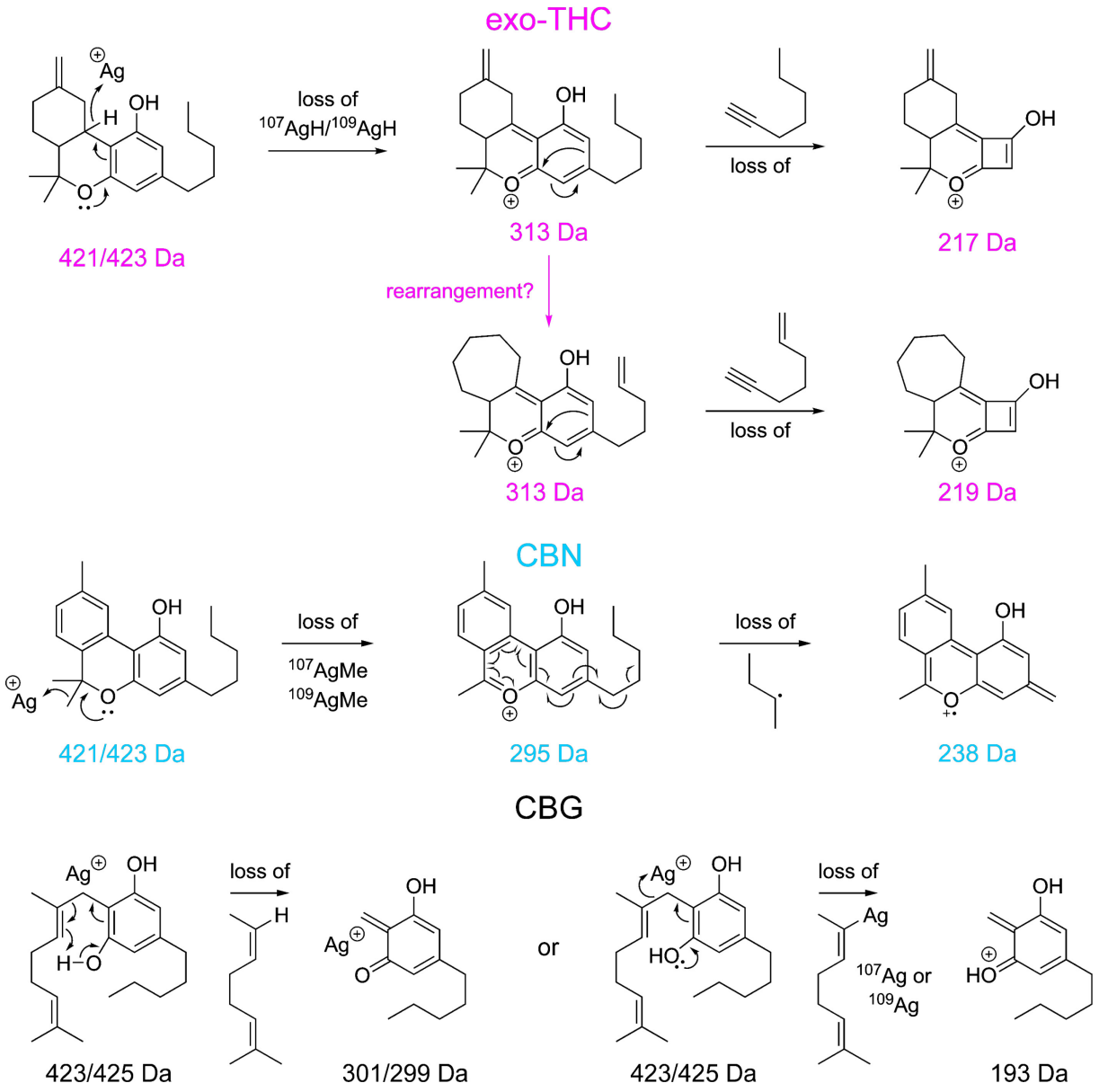

Figure 5.6. Proposed fragmentation mechanisms corresponding to the fragments observed in the MS^2 spectra of argentinated *exo*-THC (magenta), CBN (cyan), and CBG (black).

Exo-THC exhibits product ions identical to those produced by Δ^8/Δ^9-THC, although, interestingly, *exo*-THC generates significant quantities of fragment ion pairs that differ by 2 Da. For example, m/z 217/219 and 231/233 are generated from the m/z 313 product that arises from the loss of $^{107}AgH/^{109}AgH$ from [*exo*-THC + Ag]$^+$ (**Figure S5-16**). The ~1:3 ratio of the fragment

pairs does not coincide with the isotopic distribution of silver, so it is likely that these fragments are similar in structure to the 217 and 231 species observed during fragmentation of Δ^8/Δ^9-THC, albeit with one less element of unsaturation. This hypothesis is supported by performing MS^3 experiments on the m/z 217/219 and m/z 231/233 pairs, whereupon each pair produces fragments that also differ by 2 Da. It is unclear why changing the position of the double bond to the exocyclic position creates the additional m/z 219 and 233 fragment ions, or from where exactly the unsaturation element is removed. One possibility, stemming from the instability of exocyclic double bonds,[91] is that the methylenecyclohexane moiety undergoes concurrent hydrogenation and ring expansion, yielding a cycloheptane moiety through a variation of the well-known benzylium to tropylium rearrangement.[285,286]

The argentinated form of CBN (m/z 417 and 419) can be distinguished from the other cannabinoids solely by the m/z of the parent ion. However, aromatization of its cyclohexyl moiety raises the question of how the structural change will impact its fragmentation pattern during CID. MS^2 studies indicate that CBN readily loses ^{107}AgMe/^{109}AgMe, yielding a fragment with m/z 295 that dominates the product ion spectrum (**Figure S5-17**). This behaviour is likely a consequence of the relatively low ΔG_{ass} of CBN for argentination (200.6 kJ mol^{-1}) and the exceptional stability of the m/z 295 fragment, where the loss of ^{107}AgMe/^{109}AgMe extends conjugation throughout the tricyclic system. Only at sufficiently high collision energies does the m/z 295 species decompose via loss of a butyl radical, yielding the m/z 238 species. Conversely, CBG exhibits the highest ΔG_{ass} for argentination (290.4 kJ mol^{-1}), and thus requires the highest collision energies to induce fragmentation (**Figure S5-18**). The exceptionally high ΔG_{ass} of CBG is associated with the conformational flexibility of the sidechain that features the 1,5-diene motif, resulting in stronger coordination of Ag^+ relative to CBD and CBC whose 1,5-diene functionalities exist within their cyclic framework. Accordingly, $[CBG + Ag]^+$ exhibits several fragments ions that retain silver in addition to two primary fragmentation channels, one that retains silver (m/z 299/301) and one that involves the loss of silver to produce the protonated form of its phenolic core (m/z 193).

Although CBG has a mass that is distinct from the other cannabinoids studied, its ^{107}Ag-adduct (m/z 423) overlaps with the ^{109}Ag adducts of $\Delta^8/\Delta^9/exo$-THC, CBD, and CBC (m/z 423). This overlap can be avoided by gating exclusively on the ^{109}Ag isotopologue (m/z 425), but would result in a 52 % reduction in sensitivity (*i.e.,* the relative abundance of ^{107}Ag). Therefore, quantifying CBG requires monitoring a unique MRM transition that is distinct from the other argentinated cannabinoids. Although the product ions of $[\text{CBG} + \text{Ag}]^+$ are the same as those of other cannabinoids, the collision energy required to induce their formation is far greater. This is evident in **Figure 5.7** and **S5-19**, which demonstrates not only that DMS can resolve seven cannabinoids as argentinated adducts via MRM, but that the differing affinity of Ag^+ for each cannabinoid impacts their intensity in the corresponding ionogram. In other words, compounds exhibiting a greater ΔG_{ass} for argentination exhibit greater intensity during DMS analysis.

As described in **Chapter 5.5**, the quantitation of the RedPill extract demonstrated that the argentination strategy is insensitive to matrix effects and competition for Ag^+ coordination. However, the latter condition was only demonstrated for CBC and CBD. Among the set of cannabinoids studied, CBG exhibits the largest ΔG_{ass} for argentination (290.4 kJ mol^{-1}), and so has the greatest potential to supress cannabinoids exhibiting a lower ΔG_{ass}, and thereby interfering with quantitation. To assess the impact of CBG on analyte suppression, we quantified the cannabinoids present in the Full Spectrum Hemp Multicannabinoid Oil extract produced by NuLeaf Naturals. This extract contains five cannabinoids, namely CBN, Δ^9-THC, CBG, CBD, and CBC in a hemp seed oil matrix. However, it should be noted that the actual cannabinoid concentrations given on the product packaging are contradictory; the packaging states that CBN, Δ^9-THC, CBG, CBD, and CBC are present at 12 mg mL^{-1}, but also states that the concentration of Δ^9-THC is 13.6 mg mL^{-1} (**Figure S5-20**). The packaging also reports concentration as w/w, which is 14.2 mg g^{-1} for Δ^9-THC and 12.6 mg g^{-1} for the other cannabinoids. It is unclear from the packaging which concentrations are correct, especially since quantitation by standard addition indicates that the CBD and CBC concentrations reported by the manufacturer are inaccurate.

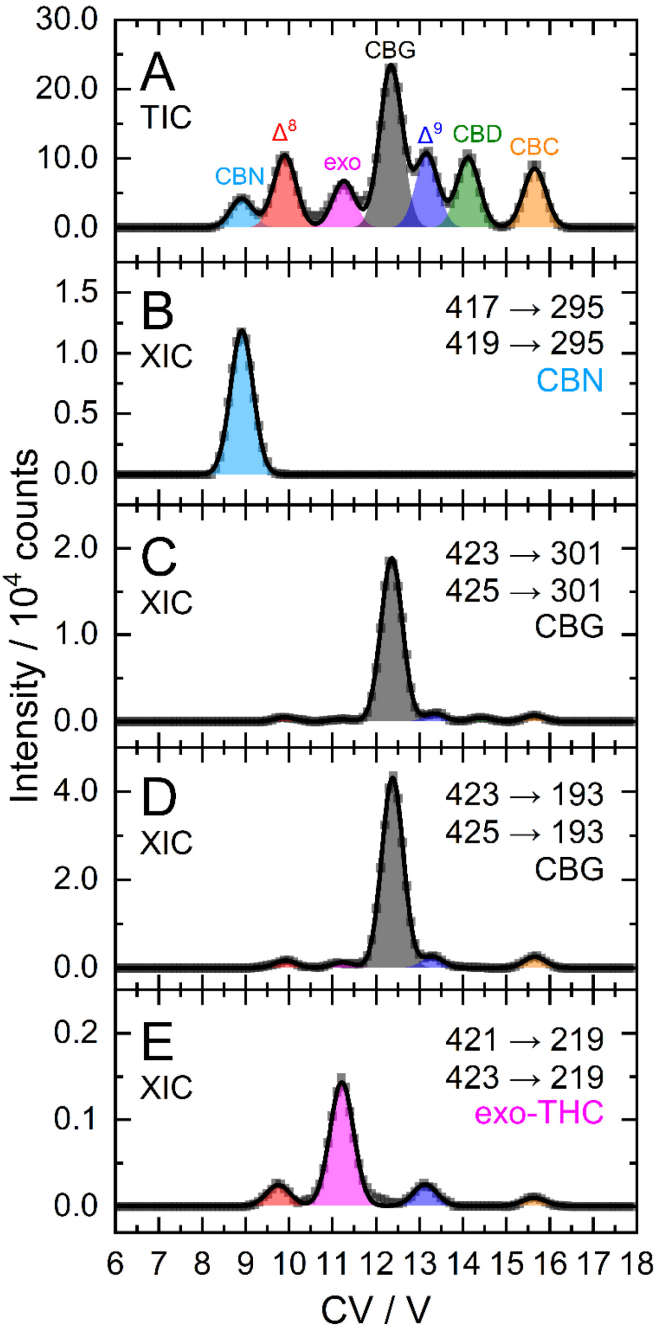

Figure 5.7. (**A**) Total ion chromatogram (TIC) and (**B** – **E**) extracted ion chromatograms (XIC) from a specific MRM transition for the separation of argentinated Δ^8-THC (red), Δ^9-THC (blue), CBC (orange), CBD (green), *exo*-THC (magenta), CBN (cyan), and CBG (black) by DMS-MS. Ionograms were obtained in a pure N_2 environment at SV = 4500 V, DP = 0 V, and DT = 50 °C from a mixture containing Δ^8-THC (500 ppb), Δ^9-THC (500 ppb), CBD (100 ppb), CBC (100 ppb), *exo*-THC (500 ppb), CBN (500 ppb), CBG (100 ppb), and AgOAc (10 ppm) in MeOH.

Extrapolation of the X-intercept via linear regression ($R^2 > 0.99$) and multiplication by the dilution factor indicates that the CBD and CBC concentrations are 17.8 ± 1.3 mg mL^{-1} and 2.1 ± 0.6 mg mL^{-1}, respectively (**Table 5.3**). The measured concentrations of CBN, Δ^9-THC, CBG in the extract align with those reported by the manufacturer, so it is unlikely that matrix effects or CBG suppression caused the inconsistency between the stated CBC and CBD concentrations and our findings. Were the inconsistencies due to isobaric interferences, both CBC and CBD would be uniformly affected, but we measure CBD at a higher concentration than the manufacturer's reported amount and CBC at a lower concentration. Alternatively, if matrix components or CBG resulted in suppression of CBC and CBD, then the concentration of all cannabinoids would be underestimated, especially those exhibiting low ΔG_{ass} for argentination (*i.e.,* CBN). Compared to the RedPill extract, the NuLeaf extract exhibited slightly higher LOD/LOQs for cannabinoids, which is indicative of *some* suppression, likely by CBG. Consequently, replicate measurements exhibit slightly increased standard deviations, although **Figure S5-21** indicates that linear response and quantitation via standard addition are unaffected ($R^2 > 0.99$). Because CBG is present in only small amounts in many cannabis products, it is expected to have only a minor impact in most cases when measuring cannabinoids via argentination.

Table 5.3. Results of the cannabinoid quantitation in the NuLeaf Naturals Full Spectrum Hemp Multicannabinoid Oil. Quantitation was performed using standard additions ($n = 3$) of each cannabinoid with CBD-A (300 ppb) as the internal standard.

Cannabinoid	Manufacturer stated initial concentration / mg mL^{-1}	Measured Concentration / mg mL^{-1}	LOD / ppb	LOQ / ppb
Δ^9-THC	13.6	14.5 ± 0.8	14	42
CBD	12.0	17.8 ± 1.3	17	51
CBN	12.0	12.4 ± 1.0	20	60
CBG	12.0	13.2 ± 0.8	12	36
CBC	12.0	2.1 ± 0.6	14	42

5.7 Conclusions

The separation of seven cannabinoids (Δ^8-THC, Δ^9-THC, CBD, CBC, *exo*-THC, CBN, and CBG), five of which are isobaric, was achieved by DMS in a pure N_2 environment when the analytes were detected as argentinated species (*i.e.,* $[M + Ag]^+$). Upon optimization of the MRM workflow to monitor analyte transmission through the DMS cell, it was discovered that the argentinated cannabinoids exhibit distinct fragmentation pathways. This finding was unexpected, as prior work suggested that the protonated and deprotonated forms of cannabinoids generate indistinguishable product ions from CID.[239,240] It seems that the disparate fragmentation behaviour for the argentinated precursors is driven by formation of stable product ions via the loss of AgH, AgMe, or other silver-containing neutral product. Additionally, ΔG_{ass}, a measure of the propensity of each cannabinoid for argentination, impacts fragmentation behaviour, where cannabinoids exhibiting a high ΔG_{ass} tend to produce fragment ions that retain silver, whereas those with a comparatively lower ΔG_{ass} release silver more easily.

Loss of silver-containing fragments were observed in all cannabinoids, providing an opportunity to mitigate sensitivity losses from isotope dilution (*i.e.,* 52 % ^{107}Ag / 48 % ^{109}Ag). For example, the ^{107}Ag and ^{109}Ag isotopologues of Δ^9-THC have a m/z of 421 and 423 Da, respectively, both of which produce a prominent fragment ion with a m/z of 313. Adjusting the transmission window of the first quadrupole mass filter to 3 Da and setting the precursor ion mass to 422 Da (*i.e.,* m/z 422 ± 1.5 Da) allows both isotopologues to be simultaneously detected by MRM (421/423 → 313) transition. Mitigation of isotope dilution could also be afforded by monitoring two MRM transitions for each argentinated precursor for Δ^9-THC (*i.e.,* 421 → 313 and 423 → 313), although this adds a layer of complexity to data processing. It is unfortunate that some cannabinoids produce small amounts of a fragment ion that has the same mass as a major fragment generated by another isobaric cannabinoid, as this negates the possibility of accurate quantitation solely by tandem-MS.

Incorporating DMS into the tandem-MS workflow enabled the (near)-baseline separation of Δ^8-THC, Δ^9-THC, CBD, CBC, *exo*-THC, CBN, and CBG, and thus, facilitated the determination of each cannabinoid's specific contribution to a particular MRM channel. To validate the effectiveness of the DMS-based separation, cannabinoid content was measured in two commercial extracts using standard additions with CBD-A as the internal standard. Linear response was observed across the 50 – 1000 ppb (ng/mL) range ($R^2 > 0.99$), and the limits of detection ranged from 10-20 ppb depending on the cannabinoid. The measured cannabinoid concentrations aligned with those reported by the manufacturer without any sample workup, which is especially impressive given that the matrix contained several additional components that are capable of binding Ag^+ and can potentially supress cannabinoid argentination. Interestingly, the stated quantities of CBD and CBC provided by Nuleaf Naturals did not agree with our quantitative results. Measurements of other commercial products have demonstrated that cannabinoid amounts stated by the manufacturer can differ by up to 40 % from their true quantity,[236] indicating poor testing capabilities. These findings underscore the necessity for analytical techniques that can accurately measure cannabinoid concentrations, in which the argentination + DMS-MS^2 approach described here holds promise in this regard.

Chapter 6

Development of tools to calculate ion mobility at arbitrary field strengths

This chapter contains supplementary material that can be found within **Appendix E**.

6.1 Introduction

The use of ion mobility spectrometry (IMS) as a standalone technique or when coupled to mass spectrometry (MS) continues to gain traction within the analytical and biophysical communities. This trend stems from the ability of IMS to separate analytes and probe their geometric structure. Several groups have shown that IMS-MS, which encompasses several variants,[56,287,288] can solve challenging analytical problems as either the sole separation dimension or when coupled to liquid chromatography (LC).[289,290] Each IMS technique uses electric fields to accelerate ions through the mobility region, with instrument variations being predominantly associated with the nature of the field (*i.e.,* oscillating or static) and its magnitude. When analytes enter the mobility region, which is filled with an inert gas (typically N_2), ion-neutral collisions create drag, countering field-induced acceleration. These opposing effects determines the velocity with which the analyte travels through the mobility cell and ultimately facilitates analyte separation. For each unique analyte, these interactions lead to a constant drift velocity for the analyte's ensemble (v_D) that is proportional to the applied electric field (*E;* **Eq. 6.1**):

$$v_D = KE \qquad \textbf{Eq. 6.1}$$

The proportionality factor, K, is colloquially known as the ion mobility coefficient, although it is far more common for practitioners to report the reduced mobility coefficient (K_0; **Eq. 6.2**),

$$K_0 = (K)\left(\frac{N}{N_0}\right) \qquad \textbf{Eq. 6.2}$$

where N is the particle density (molecules m^{-3}) within the IMS device, and N_0 is the particle density at 273.15 K and 1 atm (2.6868×10^{25} molecules m^{-3}), which is also called the Loschmidt constant. Rewriting **Eq. 6.1** using the reduced mobility coefficient yields **Eq. 6.3**, showing definitively that collision dynamics are influenced by the field strength and particle density, as represented by the reduced field strength term *E/N*. The *E/N* term is typically expressed in Townsend (Td), where 1 Td = 10^{-21} V m^2. Simply put, **Eq. 6.3** indicates that increasing the field strength induces greater acceleration of the ion, whereas increasing the particle density (*i.e.*, the pressure) increases the collision frequency such that the time for acceleration becomes shorter. Ultimately, this interdependency indicates that the reduced field strength is directly proportional to the mean collision energy of any ion-neutral collision.[36]

$$v_D = K_0 N_0 \frac{E}{N} \qquad \textbf{Eq. 6.3}$$

Within the low-field regime, an ion's velocity responds linearly to changes in the reduced field strength, and thus, enables relation of an ion's low-field mobility coefficient, $K(0)$, to its collision cross section (CCS) via the Mason-Schamp equation (**Eq. 6.4**),[36] whose derivation dates back to the early work on ion mobility by Langevin.[291]

$$K(0) = \frac{3}{16}\left(\frac{2\pi}{\mu k_B T}\right)^{1/2} \frac{q}{N\Omega(T)} \qquad \textbf{Eq. 6.4}$$

We note that **Eq. 6.4** is identical to **Eq. 1.2** (presented in **Chapter 1.1**), albeit in a different form. Here, μ is the reduced mass of the ion-neutral pair, q is the absolute charge of the ion, k_B is the Boltzmann constant, T is the absolute temperature of the bath gas, and Ω is the ion-neutral CCS, which is temperature dependent. The CCS represents the orientally-averaged collision area of the analyte with the buffer gas that fills the mobility cell, and as such, is intrinsically related to the 3D structure of the ion. The ability of IMS to discern molecular geometric structure from an ion's CCS depends on two crucial factors: 1) the precise measurement of ion mobility under strictly controlled experimental conditions (*i.e.,* temperature and pressure within the mobility region),[35,292] and 2) the meticulous modeling of CCS/ion mobility from the computed geometry of the analyte. Owing to

the significant role CCSs play in chemical separations, modelling CCS has become an integral component of IMS research. Calculating an ion's CCS *in silico* often mitigates ambiguity in IMS-based structural assignments and provides valuable insight into the nature of the IMS-based separation mechanism. When modeling ion mobility, practitioners are primarily concerned with capturing the dynamics of a collision event between an ion and a gas particle, as collisions strongly depend on the electric field, pressure, and temperature. To express this relationship, the ion mobility is adjusted by the alpha function, which is usually expressed as a Taylor series composed of even-ordered alpha coefficients (**Eq. 6.5** and **Eq. 6.6**, respectively).[293]

$$K\left(\frac{E}{N}\right) = K(0)\left[1 + \alpha\left(\frac{E}{N}\right)\right] \qquad \textbf{Eq. 6.5}$$

$$\alpha\left(\frac{E}{N}\right) = \alpha_2\left(\frac{E}{N}\right)^2 + \alpha_4\left(\frac{E}{N}\right)^4 + \alpha_6\left(\frac{E}{N}\right)^6 + \cdots \qquad \textbf{Eq. 6.6}$$

The alpha function is approximately zero if the reduced field strength is within the so-called low-field limit (*ca.* 0 – 10 Td), which is why low-field IMS techniques such as drift-tube IMS (DTIMS) can be used as a tool for both structural elucidation and analytical separations. Structural elucidation is typically performed within the low-field limit, where an ion's velocity distribution is characterized by a Maxwell-Boltzmann distribution at the temperature of the bath gas (T), and hence, renders the Mason-Schamp relation valid. While advances in instrumentation have enabled high-throughput measurements of CCS on many low-field IMS platforms,[100,105,106,134,294] development of computational frameworks for relating an ion's structure to its CCS has progressed at a much slower pace. Several methods (and software that implements these methods) have been published over the years to calculate CCSs, a summary of which is provided in **Supplementary Section 6-1** and in reference 160. However, most of the common CCS packages are limited to calculating thermal CCSs and/or low-field mobilities, and unfortunately are falling behind the surge in popularity of IMS techniques that operate at high field strengths.[39,295] Both MobCal-MPI[64] and IMoS[296,297] are notable exceptions, as they have been modified to allow calculations of ion mobility at arbitrary field strengths. The calculation of mobilities above the low-field limit is based on the

work of Kihara,[298] Mason and Schamp,[299] and Viehland and Mason,[300,301] the latter of whom devised two-temperature theory (2TT) to account for the non-negligible acceleration of ions in electric fields that surpass the low-field limit. Viehland and Mason define an effective temperature (T_{eff}) that is composed of thermal and field-induced contributions that describe the relative velocity distribution of the ion-neutral pair, which, when incorporated into **Eq. 6.5** and **Eq. 6.6**, generates **Eq. 6.7**.[300,301]

$$K = \frac{3}{16}\left(\sqrt{\frac{2\pi}{\mu k_B T_{eff}}}\right)\left(\frac{q(1+\alpha)}{N\left(\Omega(T_{eff})\right)}\right) \qquad \textbf{Eq. 6.7}$$

Note that T_{eff} can be expressed in terms of the drift velocity (**Eq. 6.8**), mobility coefficient (**Eq. 6.9**), or reduced mobility coefficient (**Eq. 6.10**), where M represents the molecular mass of the bath gas particle (*i.e.,* 28 Da for N_2).

$$T_{eff} = T + \left(\frac{M}{3k_B}\right)(v_D)^2(1+\beta) \qquad \textbf{Eq. 6.8}$$

$$T_{eff} = T + \left(\frac{M}{3k_B}\right)(KE)^2(1+\beta) \qquad \textbf{Eq. 6.9}$$

$$T_{eff} = T + \left(\frac{M}{3k_B}\right)\left(K_0 N_0 \frac{E}{N}\right)^2(1+\beta) \qquad \textbf{Eq. 6.10}$$

Eq. 6.7 – **Eq. 6.10** feature two correction factors, α and β, the former of which is distinct from the alpha function shown in **Eq. 6.5** and **Eq. 6.6**. These correction factors are non-zero when higher order approximations of 2TT are implemented but always result in an ion's T_{eff} being greater than T for any field strength greater than 0 Td. However, for low-field conditions (*ca.* < 10 Td), the contribution of the electric field to an ion's drift velocity is negligible, resulting in a relative velocity distribution of the ion-neutral pair that resembles its thermal velocity. Consequently, under low-field conditions T_{eff} and T are equal, and **Eq. 6.7** simplifies to **Eq. 6.4**.

Despite our group's prior success in implementing the 2TT approach in modelling mobilities above the low-field limit,[64] we have yet to formalize our approach within the IMS literature. Here, we report on an update to the parallelized CCS calculation suite MobCal-MPI, which is now capable of accurate ion mobility calculations at arbitrary field strengths. This update also optimizes the

treatment of ion-neutral collisions with N_2, where evaluating the ion-neutral interaction potential from both nitrogen atoms of N_2 instead of its centre of mass results in more accurate CCS calculations. By coupling the updated treatment of ion-neutral collisions with an empirically corrected 2TT implementation, MobCal-MPI 2.0 enables precise and efficient calculations of high-field mobilities that accurately reproduce ion behaviour on high-field IMS platforms.

6.2 Modelling and ion's 3D structure and atomic partial charges

Similar to its predecessor, MobCal-MPI 2.0 computes CCSs based on the ion's geometric structure (given as *xyz*-coordinates), partial charges, and atom classes defined by the MMFF94 force field.[71] In order to evaluate the accuracy and efficiency of CCS calculations, we employ four different test sets: the *calibration set* ($N = 162$), *validation set* ($N = 50$), *high-field validation set* ($N = 132$), and *peptide set* ($N = 12$). The *calibration* and *validation sets* are composed of analytes with known CCSs (obtained from references [100,106,107,109,111,302–306]), which encompass each atom type defined by the MMFF94 forcefield. Multiple conformers are considered for each analyte, which were obtained using the protocol outlined in the original MobCal-MPI publication.[110] The *high-field validation set* is composed of small, rigid analytes (with a maximum of five conformers), for which our group has previously measured their high-field mobilities.[64,95,307] Finally, structures in the *peptide set* were generated from the lowest energy structure determined from their amino acid sequence using the I-TASSER suite,[308,309] and are used exclusively for benchmarking. The *peptide set* contains 12 species ranging in length from 9 to 22 amino acid residues. To remove ambiguity in charge site assignment, the N-terminus and all basic residues (*i.e.,* His, Lys, and Arg) of each peptide were protonated, leading to charge states ranging from +2 to +5.

All structures in the *calibration*, *validation*, and *high-field validation sets* were reoptimized using DFT at the ωB97X-D3/def2-TZVPP level of theory.[166,263,266–268] Subsequent calculation of partition functions (via computation of vibrational frequencies and rotational constants) at the same level of

theory enables Boltzmann weighting of different conformers for each ion. Atomic partial charges were computed via the CHELPG partition scheme using a grid composed of points spaced apart by 0.1 Å, where each grid point is at most 3.0 Å away from any atom in the molecule.[310] Due to the size of the molecules within the *peptide set*, calculations were conducted using the faster TPSS-D3/def2-TZVPP level of theory[311] and a coarser grid for partial charges (0.3 Å spacing, 2.8 Å cut-off). DFT optimization of the structures obtained from I-TASSER was not necessary as the *peptide set* merely served for benchmarking. All DFT calculations were conducted with the ORCA 5.0.3 program suite[87,90] and were uploaded to the ioChem-BD database[272] (see https://iochem-bd.bsc.es/browse/review-collection/100/285126/7ae31bce0ab75f49f8043e51). Subsequent determination of the MMFF94 force field atom types was undertaken using OpenBabel.[312]

It should be noted that the level of theory (*i.e.,* the DFT functional and basis set size) can impact the accuracy of the subsequent CCS calculations. This influence arises from the accuracy in determining ion structure, including bond lengths, angles, atomic partial charges, and thermochemistry, the latter of which is especially important when a Boltzmann weighting of conformers is used. Previous investigations using MobCal-MPI have systematically explored the performance of various basis sets and functionals.[115] These studies revealed comparable performance among different hybrid functionals when combined with double or triple zeta basis sets that include polarization basis functions. With the introduction of MobCal-MPI 2.0, it is anticipated that this tool can be utilized for structures determined using multiple model chemistries. However, for the sake of consistency, users are recommended to perform geometry optimizations and assess thermochemistry using the methods employed for the calibration and validation sets (wB97X-D3/Def2-TZVPP).

6.3 Evaluating ion mobility through the simulation of ion-neutral collisions

There are several free CCS calculation packages that are available to academic users.[108,110,313–315] These software packages typically "shoot" a molecule of buffer gas towards an analyte from multiple points of origin, analyzing each collision event to determine scattering angles. Depending on the CCS package used, ion-neutral collisions are modelled using one of three methods (see **Figure** 6.1**A**). The simplest of the three is the projection approximation (PA), which ignores all interactions between the ion and collision gas and does not require any evaluation of the incident gas trajectories.[292,316] The PA calculates the CCS by defining the rotationally averaged area from buffer gas molecules that "strike" the ion. Although this method can evaluate an ion's CCS exceptionally fast, its utility is limited to large, globular species – the PA is not suitable for small molecules or microsolvated clusters because CCSs are determined exclusively from the ion's size, and not by ion-neutral interactions.

The elastic hard-sphere scattering (EHSS) improves on the PA by evaluating CCSs from the deflection angle of a gas molecule following its collision with the static analyte.[317] However, the EHSS method does not consider long-range interactions and treats all collisions as hard-sphere, specular scattering events. CCSs evaluated using the EHSS method tend to be inaccurate for small molecules where long-range interactions (*e.g.,* charge/induced-dipole) are important.[316,318,319] For example, the CCS of acetic acid in its neutral (CH_3COOH) and deprotonated (CH_3COO^-) forms are 41.82 Å^2 and 41.39 Å^2, respectively, when calculated by the PA method and 42.56 Å^2 and 41.11 Å^2, respectively, when calculated by the EHSS method. In contrast, the TM method computes values of 54.71 Å^2 and 105.34 Å^2, respectively. For systems where the long-range interactions become less crucial (*e.g.*, proteins), PA and EHSS methods produce relatively accurate CCSs in a fraction of the time required by the trajectory method (TM).[320,321] The increased calculation time of the TM stems from modelling collision events with a soft ion-neutral interaction potential that includes short- and long-range components. TM calculations require van der Waals (vdW), ion-induced dipole (IID),

and ion-quadrupole (IQ) components to describe what happens to a polarizable gas molecule upon interaction with a charged analyte. The vdW component accounts for Pauli repulsion at short distances and attractive dispersion forces at longer distances, whereas the IID and IQ terms account for the polarizability of the collision partner, which becomes more important at distances close to the minimum on the vdW potential. The functional forms of the vdW, IID, and IQ components are discussed in **Chapter 6.7**, which, when parameterized, yields CCSs of 55.5 Å^2 and 116.4 Å^2 for the CCSs of acetic acid and the acetate anion, respectively.

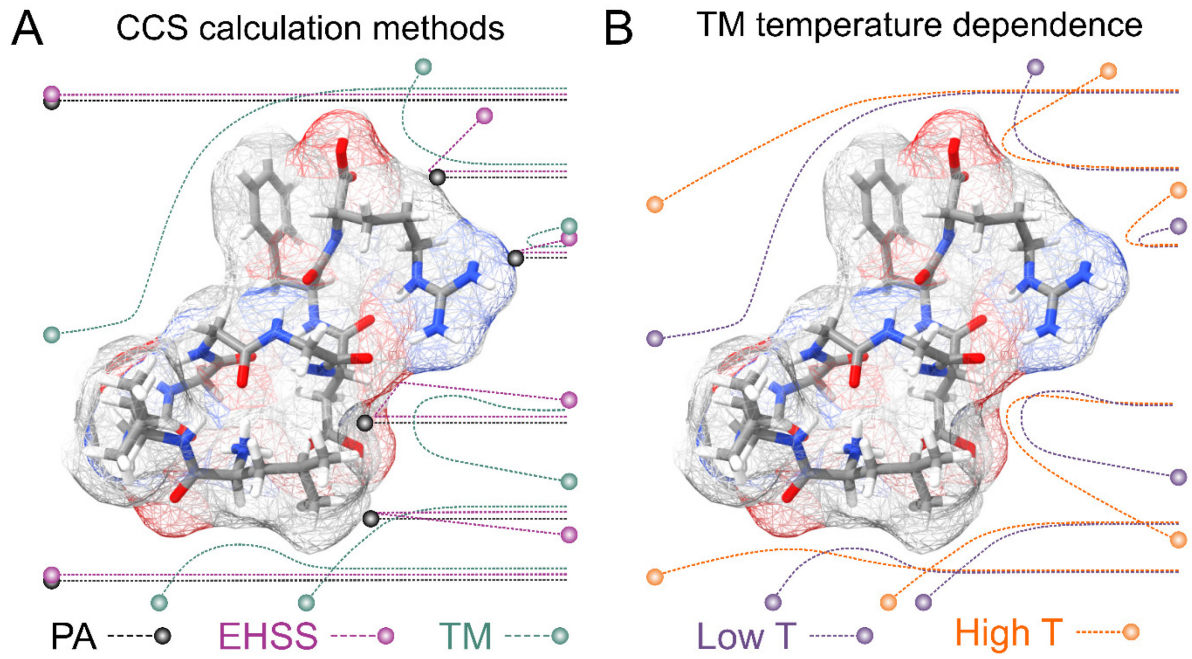

Figure 6.1. (**A**) Summary of the main CCS calculation routines represented through collision trajectories. The projection approximation (PA; black trace) and elastic hard sphere scattering (EHSS; light purple trace) only consider direct contact between the ion and collision gas. The trajectory method (TM; green trace) evaluates the neutral trajectory as per the ion-neutral interaction potential, which is influenced by the charge density of the analyte. Areas of high partial positive charge (blue) and high partial negative charge (red) are mapped onto the ion total electron density cloud. (**B**) The buffer gas trajectories depend on their incident velocity, which depends on the temperature of the TM simulation. Higher temperature simulations (orange) decrease the momentum transfer between the ion and buffer gas relative to lower temperature simulations (purple).

The TM determines an ion's CCS from the momentum transfer integrals that describe a collision event; these are averaged over several thousand iterations that sample multiple velocities and geometries of the ion and collision partner (see **Eq. 6.11**).[317] In **Eq. 6.11**, θ, φ, and γ define the relative orientation of the ion with respect to its collision partner, g is the relative velocity of the ion-neutral pair, b is the impact parameter, and χ is the scattering angle at which buffer gas is deflected upon interaction with the ion. Except for χ, all parameters are determined at the beginning of the CCS calculation. Evaluation of χ requires simulation of the trajectory that the buffer gas takes upon colliding with the analyte, which is governed by the interaction potential. After remission of the gas molecule, χ is calculated as the angle between the initial and final vectors that define the trajectory of the buffer gas.

$$\Omega_{avg}(T_{eff}) = \left(\frac{1}{8\pi^2}\right)\int_0^{2\pi} d\theta \int_0^{\pi} sin\,\varphi\, d\varphi \int_0^{2\pi} \frac{\pi}{8}\left(\frac{\mu}{k_b T_{eff}}\right)^3 d\gamma \int_0^{\infty} (g^5) exp\left(-\frac{\mu g^2}{2k_b T_{eff}}\right) dg \int_0^{\infty} 2b(1 - cos\,\chi(\theta,\varphi,\gamma,g,b))\, db \qquad \textbf{Eq. 6.11}$$

Of the available CCS calculation methods, the trajectory method (TM) provides the most physically realistic approach to modelling CCS without performing large scale stochastic simulations of the ion travelling through the mobility device.[322,323] This accuracy stems from the explicit consideration of the long-range component of the interaction potential, which will influence buffer gas trajectories. The velocity of the incoming buffer depends on the collision temperature (*i.e.,* T_{eff}), meaning that an increase in T_{eff} corresponds to an increase in the average velocity of the ion and the buffer gas. Since g describes the velocity of the buffer gas *relative to* the ion, one can simplify the evaluation of the collision event by assuming that the ion is static relative to the buffer gas. This indicates that increasing T_{eff} shifts the Maxwell-Boltzmann distribution that defines the incident buffer gas velocities to higher values. Increased gas velocities will result in the collision partner feeling less of the long-range component of the ion-neutral interaction potential.

Consequently, the momentum transfer between the buffer gas and analyte will decrease, which decreases the CCS.

The diminishing momentum transfer as T_{eff} increases is somewhat counterintuitive – one might expect that increasingly energetic collisions between the ion and buffer gas should yield a greater degree of momentum transfer. However, this is only true for *striking* collisions. Most collisions sampled during a TM calculation are *glancing* collisions, which deflect the collision partner to a lesser extent at high T_{eff}. This is best visualized by comparing collision events at low and high T_{eff} (see **Figure 6.1B**), where the scattering angle χ is *higher* for striking collisions compared to glancing collisions at high T_{eff}. Since momentum transfer is proportional to $(1-\cos\chi)$,[36] glancing collisions bring this term closer to zero [*i.e.*, for $\chi < 90°$; $(1-\cos\chi) < 1$] whereas striking collisions increase this term because head-on collisions reflect the buffer gas molecule (*i.e.*, $\chi > 90°$; $(1-\cos\chi) > 1$). The likelihood of a striking collision occurring between N_2 and a molecule with a CCS of 160 Å^2 is about 25% at 298 K. We can determine this quantity by assuming x% of collisions will be striking and $(1-x)$% of collisions will be glancing. As the ion's T_{eff} approaches infinity, its CCS approaches the hard-sphere limit, which means that the only feasible collision events are those in which N_2 strikes the ion. Thus, the probability that any collision will be striking can be estimated as the ratio between an ion's CCS at the hard-sphere limit (*i.e.,* as T_{eff} approaches infinity) and at the temperature of interest. By association, the probability that any collision will be glancing diminishes with increasing T_{eff} because the effective area in which an ion can deflect an incoming molecule of N_2 decreases. Moreover, momentum transfer becomes less efficient as incident N_2 velocities increase, meaning that any glancing collisions will be deflected to a lesser extent. So, what does this mean in terms of calculating an ion's CCS accurately? Given that the PA and EHSS methods do not incorporate a long-range component in their treatment of a collision event, they cannot accurately evaluate CCSs at different temperatures. Consequently, the PA and EHSS methods will not be useful when modelling an ion's mobility wherein its effective

temperature changes dynamically with the electric field. To evaluate an ion's CCS (and hence its mobility) at arbitrary field strengths, the temperature dependent TM must be used.

6.4 Sampling collision events using the trajectory method

Figure 6.2 shows a schematic depicting the general methodology of the trajectory method to compute collision integrals. Importantly, the collision dynamics must be sampled to evaluate χ, which depends on g, b, and the orientation of the ion relative to the starting position of the collision partner (N_2). Evaluation of χ thus requires simulation of the trajectory that the buffer gas takes upon colliding with the analyte. Depending on the initial conditions (*i.e.,* g, b, and ion-neutral orientation), substantially different collision behaviour can be observed. For example, N_2 will be scattered to a much greater extent for collisions defined by a small impact parameter (striking collision) compared to a large impact parameter (glancing collision). In terms of the relative velocity of the ion-neutral pair, which is determined by the effective temperature, the degree of scattering diminishes for glancing collisions with increasing g. In contrast, the relative velocity has a significantly smaller impact on χ for striking collisions (see **Supplementary Section S6-2**). After remission of the gas molecule, χ is calculated as the angle between the initial and final vectors that define the trajectory of the buffer gas, the magnitude of which are equal because MobCal-MPI 2.0 treats collisions elastically. With χ in hand for all starting conditions sampled, the CCS can be obtained via integration. For simplicity, we report the form of the $\Omega^{(l,s)}$ only for spherically symmetric ion-neutral interaction potentials in **Eq. 6.12** – **Eq. 6.14**, where the l and s indices denote the order of the collision integral. For further details on evaluating higher order collision integrals, please see **Supplementary Section S6-3** and **S6-4**.

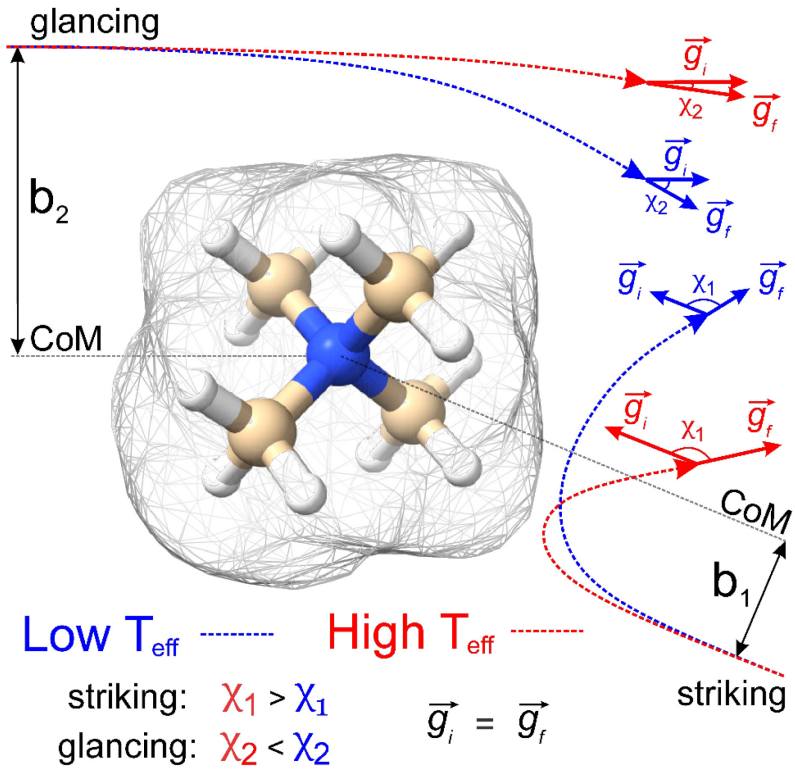

Figure 6.2. Schematic representation of how the trajectory method is employed for CCS calculations, using NMe_4^+ as an example. Two collision events are shown (striking vs. glancing) that exhibit different impact parameters ($b_{striking} < b_{glancing}$) and relative velocities ($g_{blue} < g_{red}$), the latter of which corresponds to differing effective temperatures (higher T_{eff} is associated with higher g). The scattering angle, χ, is calculated from the angle between the initial and final velocity vectors. Note that ion-neutral collisions are treated elastically, so the remission velocity (g_f) is equivalent to the incident velocity (g_i). Isosurfaces correspond to the vdW radii of the atoms contained within the molecule.

$$\Omega^{(l,s)}(T_{eff}) = \int_0^\infty Q^{(l)}(g)\omega^{(s)}(g, T_{eff})\ dg \qquad \textbf{Eq. 6.12}$$

$$\omega^{(s)}(g, T_{eff}) = \frac{1}{2^{s+1}(s+1)!}\left(\frac{\mu}{k_B T_{eff}}\right)^{s+2}\left(g^{2s+3}\, exp\left(-\frac{\mu g^2}{2k_B T_{eff}}\right)\right) \qquad \textbf{Eq. 6.13}$$

$$Q^{(l)}(g) = 2\pi\left[1 - \frac{1+(-1)^l}{2(1+l)}\right]^{-1}\int_0^\infty [1 - cos^l(\chi)]b\ db \qquad \textbf{Eq. 6.14}$$

Within **Eq. 6.14**, integration over b and the orientation of the ion is accomplished using Monte-Carlo (MC) sampling. In other words, the ion is randomly rotated in space and an impact parameter

is randomly chosen between 0 and an initially derived b_{max} (see **Supplementary Section S6-2** for details). The sample size of this MC integration is termed *imp* in MobCal-MPI. In contrast, the integration over the relative velocity of the ion-neutral pair is sampled on fixed grid points, which are denoted *inp*. In the previous implementation of MobCal-MPI, a weighted grid was used to efficiently integrate over velocity space.[110,317,319] However, changing the temperature that defines the velocity distribution requires the weighted grid to be modified for every collision integral because the weighting functions ($\omega^{(s)}$) depend on s and T_{eff} (as per **Eq. 6.13**). Since our goal is to efficiently calculate multiple collision integrals (up to $\Omega^{(2,4)}$) over the range defined by the temperature of the bath gas (T) and the highest effective temperature desired by the user ($T_{eff,max}$), we implemented a linear grid of velocity points defined by the temperature range. Because the linear grid of velocities is shared between all CCS integrations, only one set of N_2 scattering trajectories is required to evaluate all collision integrals. In other words, using a linear grid to sample collision events between T and $T_{eff,max}$ enables the simultaneous evaluation of the ion's mobility and CCS at any temperature within this range.

6.5 Statistical analysis of the sampled collision events

The integration over the MC sampled trajectories for a fixed relative velocity (g) yields the momentum transfer integrals ($Q^{(l)}$) for that particular velocity. To estimate the statistical uncertainties associated with the sampling, the integration is repeated *itn* times (yielding $Q_i^{(l)}(g)$ for i = 1, 2, …, *itn*, which in turn produces an average (**Eq. 6.15**), standard deviation (**Eq. 6.16**), and confidence interval (CI; **Eq. 6.17**).

$$\overline{Q^{(l)}}(g) = \sum_{i=1}^{itn} Q_i^{(l)}(g) \qquad \textbf{Eq. 6.15}$$

$$\sigma\left(Q^{(l)}(g)\right) = \sqrt{\sum_{i=1}^{itn} \frac{\left(\overline{Q^{(l)}}(g) - Q_i^{(l)}(g)\right)^2}{itn - 1}} \qquad \textbf{Eq. 6.16}$$

$$\sigma_{CI}\left(Q^{(l)}(g)\right) = \frac{t(99\%)}{\sqrt{itn}}\ \sigma\left(Q^{(l)}(g)\right) \qquad \textbf{Eq. 6.17}$$

Here, $t(99\%) = 2.57$ is the two-sided, 99 % quantile of the standard normal distribution. Increasing the amount of MC sampling points (imp) will lower the variances of the $Q_i^{(l)}(g)$, and increasing the number of repetitions (itn) will increase confidence in the average. Consequently, both values affect the uncertainty, which is represented by the 99 % confidence interval.

The above analysis is performed for each point within the velocity grid, which has a size of inp. The momentum transfer integrals are then integrated over these velocity grid points to yield the collision integrals (*cf.* **Eq. 6.12**). This integration can also be viewed as taking a weighted average of the $Q^{(l)}(g)$, whereby $\omega^{(s)}(g)$ reflects the weighting function. Thus, the uncertainties associated with each $Q^{(l)}(g)$ can be propagated according to **Eq. 6.18**, where Δg is the spacing of the velocity grid. Increasing inp decreases Δg, and hence, decreases the uncertainty of the calculated CCS. Given that $\Omega^{(1,1)}$ is the primary contributor to the mobility for all field strengths, and that other $\Omega^{(l,s)}$ provide only small corrections, we consider only $\sigma_{CI}(\Omega^{(1,1)})$ when evaluating the uncertainty of the mobility coefficient K. It is worth noting that **Eq. 6.18** does not require an additional normalization factor, as $\sum \omega^{(s)}(g_i)\Delta g$ equates to unity.

$$\sigma_{CI}(\Omega^{(l,s)}) = \sqrt{\sum_{i=1}^{inp}\left[\sigma_{CI}\left(Q^{(l)}(g_i)\right)\omega^{(s)}(g_i)\Delta g\right]^2} \qquad \textbf{Eq. 6.18}$$

6.6 Evaluating high-field mobilities via 2TT

To calculate high-field mobilities within MobCal-MPI 2.0, the user is prompted to give a range of effective temperatures, whereby the lowest temperature (T) is equivalent to the bath gas temperature of their IMS instrument, and the highest temperature ($T_{eff,max}$) denotes the maximum effective temperature for which they wish to compute mobilities. The velocity grid is set up accordingly, and the momentum transfer integrals are computed for each velocity grid point. Then, for a given $T_{eff,i}$, all required collision integrals $\Omega^{(l,s)}$ and matrix elements $a_{rs}(l)$ are computed. Next, the truncation-iteration procedure from 2TT theory is used to calculate the required quantities

using the 2^{nd} order approximation (see **Supplementary Section S6-3**).[64,301] From this, the drift velocity and the reduced field strength are obtained, whose ratio yields the ion mobility coefficient as per **Eq. 6.3**. Due to the quadratic relationship between T_{eff} and E/N (*cf.* **Eq. 6.8** – **Eq. 6.10**), the distribution of E/N values obtained from the linear grid of effective temperatures is non-uniform, with a greater density of grid points at higher field strengths. Fortunately, the ion mobility coefficient exhibits larger changes as the field strength increases, so the denser sampling of points at higher E/N enables more accurate reproduction of its behaviour.

6.7 Optimizing the accuracy of CCS calculations

In MobCal-MPI 2.0, we retain the form of the ion-neutral interaction potential (V_{total}; **Eq. 6.19**) from its predecessor, which consists of a van der Waals (vdW) term composed of a modified Buckingham potential (Exp-6) derived from the MM3 forcefield (V_{vdW}; **Eq. 6.20**),[324] an ion-induced dipole term (V_{IID}; **Eq. 6.21**),[318] and an ion-quadrupole term (V_{IQ}; **Eq. 6.22**).[318] With increasing buffer gas polarizability, the V_{IID} term plays an increasingly significant role in the ion-neutral potential. If the buffer gas possesses a quadrupole moment (*e.g.*, N_2), the addition of an ion-quadrupole potential is crucial for the evaluation of accurate scattering trajectories.[318,325] To mimic the quadrupole moment of molecular nitrogen ($4.65 \pm 0.08 \times 10^{-40}$ C cm^2),[326] partial charges of -0.4825 e are assigned to each nitrogen atom and balanced by a point charge of $+0.965$ e at its centre of mass. This simplifies the calculation of the ion-quadrupole potential, where the atomic partial charges on the analyte (q_i) are iterated over their distance to each pseudo-charge site of N_2.

$$V_{total} = V_{vdw} + V_{IID} + V_{IQ} \qquad \textbf{Eq. 6.19}$$

$$V_{vdW} = \sum_{i=1}^{\mathcal{N}} \varepsilon_i \left(1.84 \times 10^5 \, exp\left(\frac{12 r_i}{r_i^*}\right) - 2.25 \left(\frac{r_i^*}{r_i}\right)^6 \right) \qquad \textbf{Eq. 6.20}$$

$$V_{IID} = -\frac{\alpha e^2}{2} \left[\left(\sum_{i=1}^{\mathcal{N}} \frac{q_i x_i}{r_i^3} \right)^2 + \left(\sum_{i=1}^{\mathcal{N}} \frac{q_i y_i}{r_i^3} \right)^2 + \left(\sum_{i=1}^{\mathcal{N}} \frac{q_i z_i}{r_i^3} \right)^2 \right] \qquad \textbf{Eq. 6.21}$$

$$V_{IQ} = \frac{1}{4\pi\epsilon_0} \sum_{i=1}^{\mathcal{N}} \sum_{j=1}^{3} \frac{q_i q_j e^2}{r_{ij}} \qquad \textbf{Eq. 6.22}$$

In the original MobCal-MPI publication,[110] the ε_i and r_i^* parameters were based on the implementation from the Kim group,[302] who combined atomic parameters from the MMFF94 force field for the ion with parameters for molecular N_2.[71] The enhanced accuracy of this approach can be attributed to distinction of atom types within the MMFF94 framework (*e.g., sp*^{3} *versus sp*^{2} hybridized carbon centres have different ε_i and r_i^*), allowing for the more accurate evaluations of the vdW component of the ion-neutral interaction potential. Because the MMFF94 parameters derived for N_2 describe a molecular entity (*i.e.,* diatomic nitrogen), the distance term in the V_{vdW} pairwise interactions (r_i) can be evaluated in two ways (**Figure 6.3**). In the first case, N_2 can be treated as pseudo-atomic entity, whereby pairwise interactions are calculated with respect to its center of mass (CoM). Alternatively, ion-neutral interaction potentials can be evaluated by considering the pairwise interaction between each atom in the analyte and each nitrogen atom in N_2, and then averaging the result (Avg-N_2). The latter case (intuitively) seems to be more reasonable, especially at short ion-neutral distances where the orientation of the N_2 molecule significantly impacts the repulsive portion of the interaction potential (see **Supplementary Section S6-5**).

Owing to the inherent parameterization of vdW terms within the MMFF94 forcefield, linear scaling parameters (ρ_{dist} and ρ_{ener}) could be applied uniformly to the ε_i and r_i^* corresponding to each atom type, greatly simplifying their optimization (**Eq. 6.23** and **Eq. 6.24**, respectively). This suggests that the same optimization methodology for ρ_{dist} and ρ_{ener} can be applied to either the CoM or Avg-N_2 version of the potential.

$$\varepsilon_i' = \rho_{ener} \cdot \varepsilon_i \qquad \textbf{Eq. 6.23}$$

$$r_i^{*\prime} = \rho_{dist} \cdot r_i^* \qquad \textbf{Eq. 6.24}$$

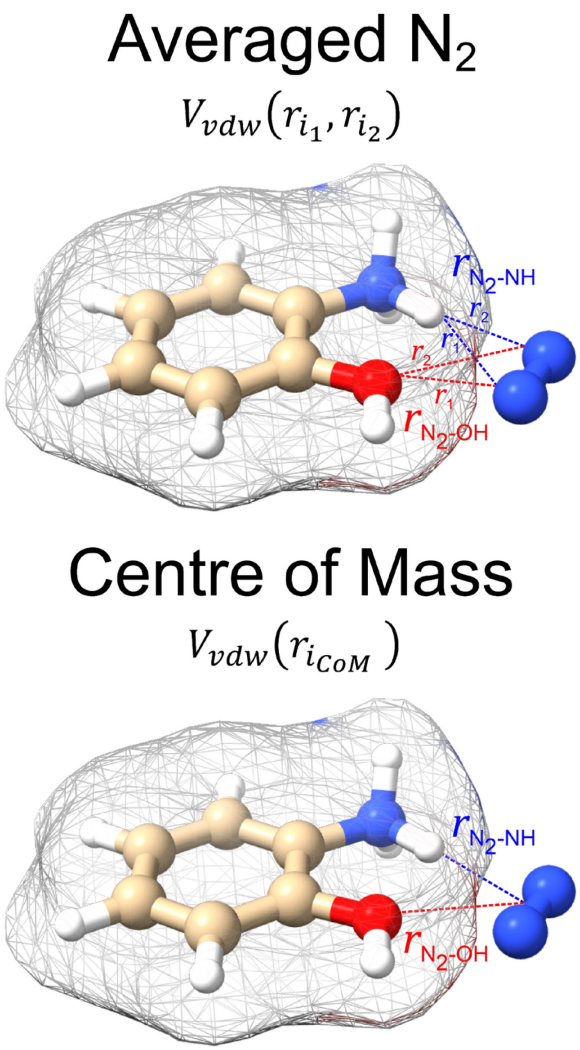

Figure 6.3. The two variations of calculating interaction potentials with N_2 depicted for *N*-protonated 2-aminophenol. In the averaged N_2 version, the potential is calculated from each atom of the ion to both atoms of N_2, and subsequently averaged. In the centre of mass version, the potential is calculated from each atom of the ion to the centre of mass of the N_2. Isosurfaces correspond to the vdW radii of the atoms contained within the molecule.

To assess the accuracy of both the CoM and Avg-N_2 approaches, we calculated the CCS of the 162 compounds in the *calibration set* using various combinations of ρ_{dist} and ρ_{ener}, and compared the results with their experimentally measured CCSs. **Figure 6.4A** and **Figure 6.4B** show the root mean square errors (RMSE) between the calculated and measured CCSs as contour plots for

the Avg-N_2 and CoM approaches, respectively. Similar to the previous version of MobCal-MPI, there is no single set of scaling parameters that performs best for MobCal-MPI 2.0, but rather a range of values that yield RMSEs of < 2.5 %. Interestingly, the CoM and Avg-N_2 methods exhibit comparable accuracies despite the Avg-N_2 approach being more physically realistic. It is possible that the similar accuracies observed for both approaches stem from the flexibility of the optimization of ρ_{dist} and ρ_{ener} when only considering a finite set of test molecules. To validate the accuracy of both approaches, we selected a set of scaling parameters that performed well for the CoM ($\rho_{dist} = 1.000$ and $\rho_{ener} = 0.580$) and Avg-N_2 approaches ($\rho_{dist} = 0.825$ and $\rho_{ener} = 1.275$), and assessed their accuracy using a separate set of 50 molecules (validation set; **Figure 6.4C** and **Figure 6.4D**, respectively).

By examining the differences between the experimentally determined and calculated CCSs of the *validation* set, it can be concluded that the Avg-N_2 and CoM methods both produce accurate results. We were surprised to find that the RMSE of the CoM version (2.27 %) is only slightly larger than the RMSE of the Avg-N_2 approach (2.16 %). The reason for their similarity is likely due to the prevalence of glancing collisions at 298 K, which account for approximately 75 % of all collisions for a molecule with a CCS of 160 $Å^2$.[64,257] The CoM approach, which does not accurately capture the repulsive portion of the interaction potential, still produces accurate CCSs at room temperature because the repulsive portion is only important when evaluating striking collisions. However, usage of the CoM rather than the Avg-N_2 approach is not justified at high reduced field strengths because an inaccurate treatment of ion-neutral repulsion will result in erroneous CCSs under conditions where striking collisions dominate (*i.e.,* at high T_{eff}). For this reason, we implemented the Avg-N_2 approach in MobCal-MPI 2.0 to ensure greater internal consistency of the code when adding collision gases, for which an explicit treatment of all atoms will also be important (*e.g.*, CO_2, SF_6).

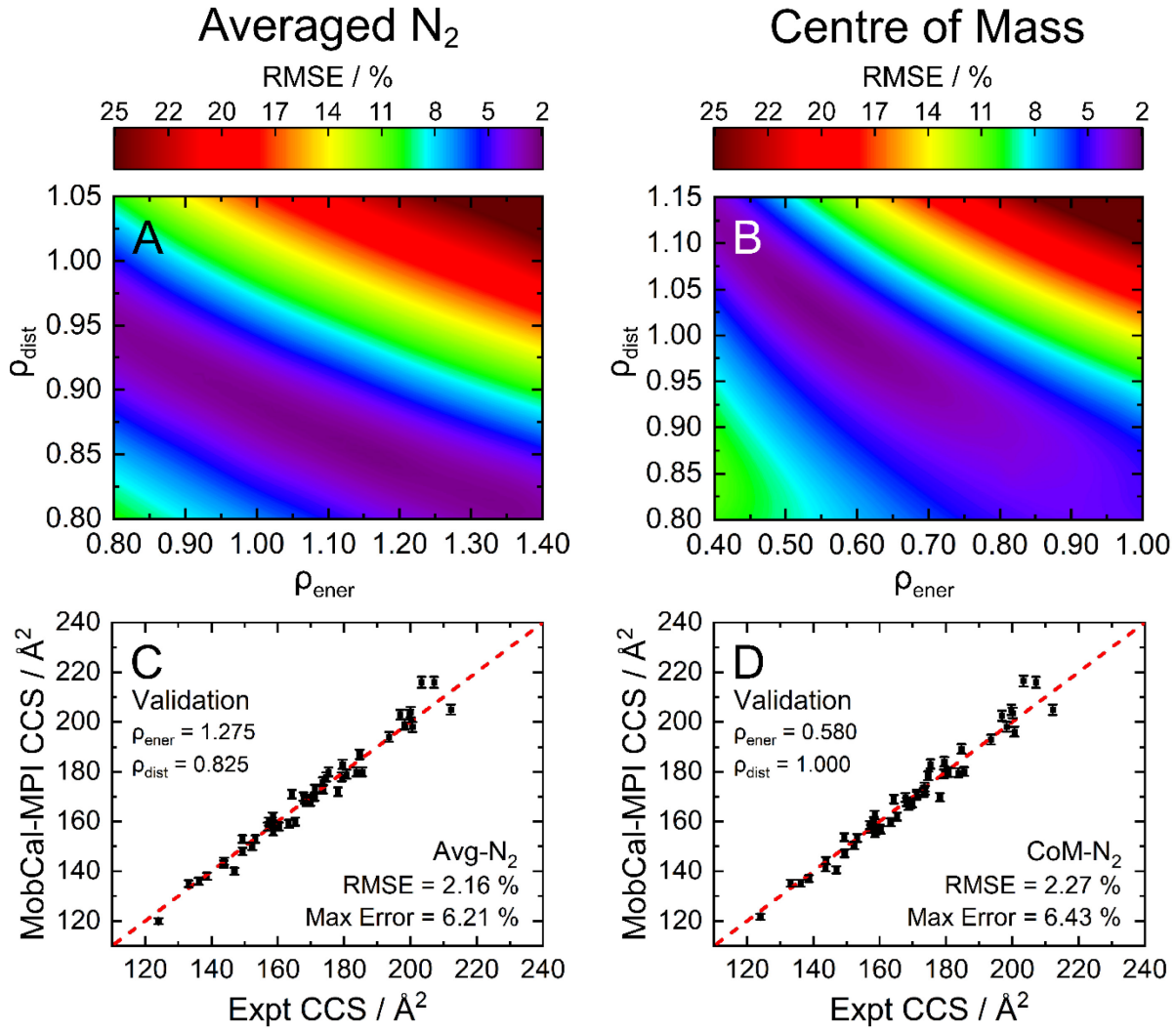

Figure 6.4. The RMSE, shown as a contour plot, for the optimization of ρ_{dist} and ρ_{ener} using the (**A**) Avg-N_2 or (**B**) CoM approach for the *calibration set* (162 molecules). To validate the accuracy of (**C**) Avg-N_2 or (**D**) CoM approaches, we employed the values of ρ_{dist} and ρ_{ener} yielding the lowest RMSE to calculate the CCS of 50 distinct molecules that were not present in the *calibration set* (*validation set*). All CCS calculations were performed at 298 K with $itn = 5$, $inp = 104$, and $imp = 512$.

6.8 Assessing CCS calculation uncertainty via the statistical analysis of collision events

After optimizing the scaling parameters for the Avg-N_2 approach, we assessed the ability of our new method to propagate statistical uncertainties that determine the final uncertainty of the CCS

calculation. In the previous version of MobCal-MPI, the uncertainty in a CCS calculation was determined by the standard deviation in the CCS measured during each *itn* cycle. While this methodology does assess uncertainty in a reasonable manner, it does not explicitly consider the effects of *all* integration parameters on the final uncertainty (*i.e., itn*, *imp*, and *inp*). Our new methodology for treating uncertainty is depicted in **Figure 6.5** using protonated caffeine as example. Here, the standard deviation in the calculated momentum transfer cross sections ($Q^{(l)}$; panel A) and the integrand for the CCS ($Q^{(l)}\omega^{(s)}$; panel B) are shown as a function of the relative velocity (g). Because we only sample a finite number (*imp*) of randomized trajectories per velocity point, the individual $Q_i^{(l)}(g)$ for each *itn* will be slightly different, the standard deviation of which is shown by the shaded areas in **Figure 6.5A**. The confidence interval describes that the value of $Q^{(l)}(g)$ upon infinite sampling of trajectories (*i.e.,* the statistically "true" value) lies within $\overline{Q^{(l)}}(g) \pm \sigma_{CI}\left(Q^{(l)}(g)\right)$ with 99 % confidence (*cf.* **Eq. 6.17**); this value is reported in the output of MobCal-MPI 2.0. Thus, increasing the number of trajectories sampled (*imp*) reduces the standard deviation, while increasing the number of iteration cycles (*itn*) reduces the uncertainty with respect to the "true value". Further, increasing the number of velocity points (*inp*) yields a finer grid along the x-axis, which in turn increases the accuracy of the numerical integration, and leads to a decrease in the final uncertainty of the collision integrals, $\sigma_{CI}(\Omega^{(l,s)})$.

In this statistical analysis, we observe a general trend where collision integrals of higher order or at higher temperatures always exhibit smaller uncertainties. For example, **Figure 6.5A** shows that the degree of momentum transfer decreases as the relative velocity between collision gas and ion increases. This decrease occurs because the contribution of glancing collisions to the total momentum transfer continually decreases with g until all collision events are striking.[327] Consequently, the standard deviations $\sigma(Q^{(l)})$ also decrease with g, leading to differing uncertainties for the two collision integrals shown in **Figure 6.5B** (2.0 Å^2 *vs.* 0.7 Å^2). This disparity is a consequence of the respective weight functions ($\omega^{(s)}$), which are centred at different relative

velocities owing to their evaluation at distinct values of s and T_{eff}. Note that the functional dependency of $Q^{(l)}$ on g is influenced by the various terms in the interaction potential.[328]

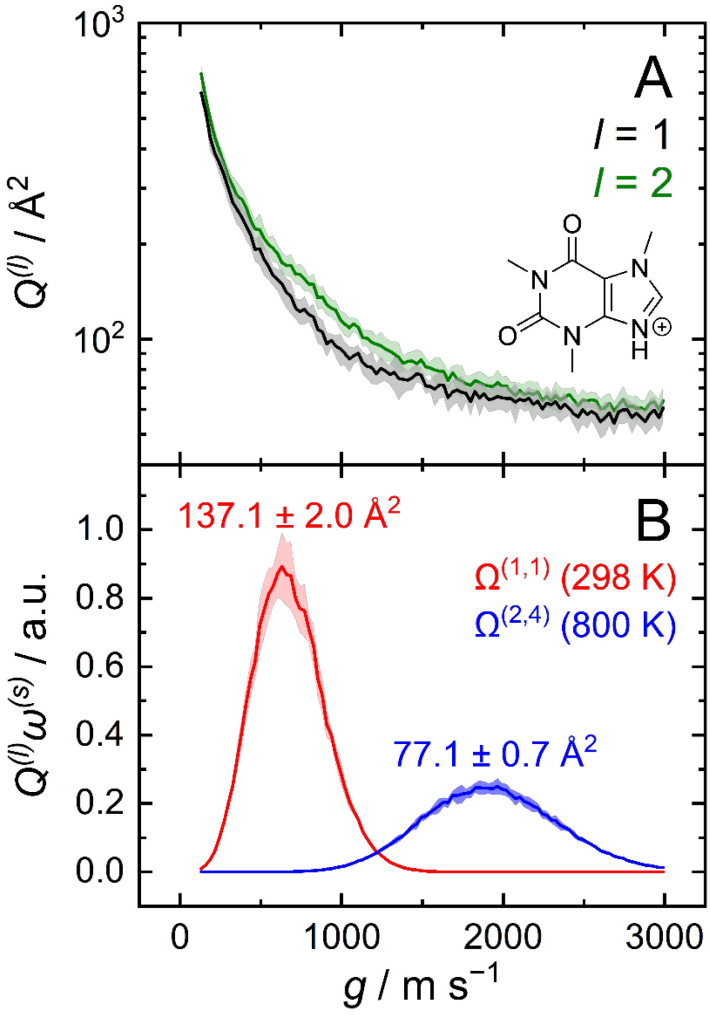

Figure 6.5. (**A**) Momentum transfer integrals and (**B**) CCS integrands of protonated caffeine. The standard deviations from **Eq. 6.16** are shown as shaded areas, and the final uncertainty for $\Omega^{(l,s)}$ corresponds to that from **Eq. 6.18**. CCS calculations were performed using $itn = 10$, $inp = 104$, $imp = 512$ and $T = 298$ K (panel B; red) for $\Omega^{(1,1)}$, and $T_{eff,max} = 800$ K for $\Omega^{(2,4)}$ (panel B; blue).

Although the decrease in CCS uncertainty with increasing temperature cannot be avoided unless a weighted grid for g is used, our implementation of the linear grid enables the near-instantaneous

evaluation of an ion's CCS for any temperature within a user-specified range once the $Q^{(l)}$ are determined. This occurs because an ion's CCS is determined from the area under the curve of $Q^{(l)}\omega^{(s)}$, the calculation time for which is practically instantaneous compared to the time required to evaluate N_2 scattering trajectories from $\sim 10^6$ collision events. However, accurate numerical integration necessitates that $Q^{(l)}\omega^{(s)}$ goes to zero as it approaches the integration limits. To ensure this condition is met, we establish boundary conditions that encompass the relative velocities that contribute to collision integrals at a given T_{eff}. **Figure 6.5B** illustrates this process, where the lowest order collision integral, $\Omega^{(1,1)}$, evaluated at the lowest temperature specified by the user (*i.e.,* T) determines the lower velocity integration limit. Similarly, the highest-order collision integral, $\Omega^{(2,4)}$, evaluated at the highest user-specified effective temperature (*i.e.,* $T_{eff,max}$) establishes the upper velocity integration limit. The exact method for determining integration limits using $Q^{(1)}\omega^{(1)}$ and $Q^{(2)}\omega^{(4)}$ is provided in **Supplementary Section S6-4**. Since the upper and lower limits of the effective temperature determine the range of relative velocities sampled, assessing trajectories on a common velocity grid produces internally consistent $Q^{(l)}$. This enables the use of the same trajectories to evaluate $Q^{(l)}\omega^{(s)}$ at any temperature between T and $T_{eff,max}$, thereby enabling straightforward determination of any CCS within the temperature range via numerical integration. By implementing the linear grid, MobCal-MPI 2.0 offers significantly faster CCS calculations for multiple temperatures compared to its predecessor, where collision integrals had to be recalculated for each user-specified temperature. In other words, if a user wants to compute CCSs at n effective temperatures, calculation via the original MobCal-MPI code takes n-times longer than MobCal-MPI 2.0.

6.9 An in-depth analysis of the uncertainty in CCS calculations

Owing to the impact of the size of *inp* and *imp* on the final uncertainty of calculated CCSs, a comprehensive analysis is required to understand their exact effect. This was accomplished by calculating the CCSs ($T = 298\ K$) of the *validation set* using discrete sampling sizes for the impact

parameter (*imp*; 256, 512, 768, and 1024) and the relative velocity of the ion-neutral pair (*inp*; 56, 104, 152, and 200). For optimal CCS calculation efficiency within the parallelized framework of MobCal-MPI 2.0, sampling sizes for *inp* and *imp* were chosen to be divisible by the number of cores used for the CCS calculation (here, $N_{cores} = 8$). The distribution of final relative uncertainties ($\sigma_{CI}(\Omega^{(1,1)})/\Omega^{(1,1)}$) is shown as a violin plot for each (*imp,inp*) combination, with the mean relative uncertainty noted in blue (**Figure 6.6**). As expected, the relative uncertainty decreases as the number of sampling points in either the *imp* or *inp* dimension increases. The average computing time also increases with increasing *imp* and *inp* because the number of trajectories sampled during one *itn* cycle is given by the product of *imp* and *inp*.

Our statistical analysis of uncertainty indicates the presence of a partial invariance along the diagonals of **Figure 6.6**. For example, the mean relative uncertainty and calculation time for (*inp,imp*) = (104,768) is similar to that observed from the (*inp,imp*) = (152,512). Using these relatively large *inp* grid sizes was necessary because of the changes implemented to MobCal-MPI 2.0, whereby velocities are sampled using a linear grid. Compared to the predecessors of MobCal-MPI,[317,319] which used a weighted velocity grid that confined the velocity distribution to values populated at the temperature of the CCS calculation, only 48 *inp* points were required to achieve a mean relative uncertainty of 0.95 %.[110] However, since the linear grid does not confine the velocity distribution to values populated at the effective temperature of the CCS calculation, additional velocity points are necessary to achieve an equivalent level of precision. Consequently, users should choose a set of (*imp,inp*) such that: 1) the statistical uncertainty of MobCal-MPI 2.0 parallels that of its predecessor, and 2) the statistical uncertainty does not exceed the RMSE between calculated and experimental CCS (2.16 %; *cf.* **Figure 6.4B**). We recommend settings of $imp = 512$ and $inp = 104$ for most CCS evaluations, as this offers a balance between high precision and calculation time. However, if a higher level of precision is required, such as distinguishing between two isomers or protomers with very similar CCS values, we recommend using $imp = 768$ or $imp = 1024$ along with an *inp* setting of 200 (**Table 6.1**).

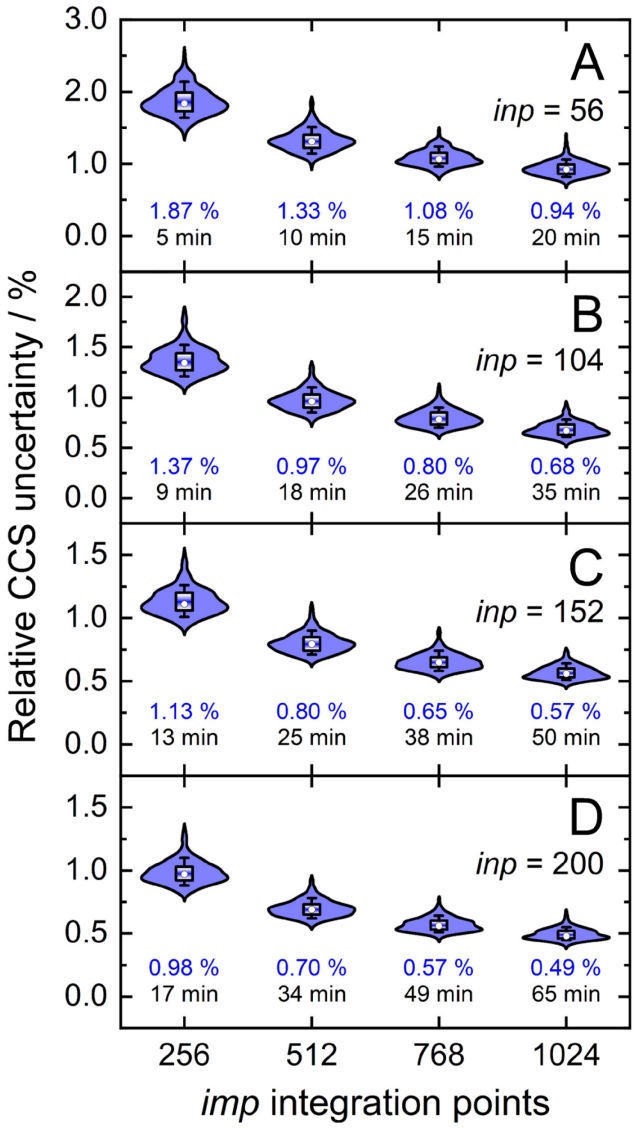

Figure 6.6. Distributions of relative CCS uncertainties, $\sigma_{CI}(\Omega^{(1,1)})/\Omega^{(1,1)}$, for the validation set ($N = 50$) for different combinations of velocity sample points (*inp*) and orientation/impact parameter sample points (*imp*). Blue numbers below each distribution correspond to mean relative CCS uncertainties and black numbers to average computing time.

Table 6.1. Recommended settings for CCS calculations in MobCal-MPI 2.0 under low-field conditions.

Calculation Type	*itn* setting	*inp* setting	*imp* setting
Routine	10	104	512
High-precision	10	200	768 or 1024

We would like to remind readers that the uncertainties shown in **Figure 6.6** are not reflective of the deviation between an experimentally measured and calculated CCS, but rather pertain to the uncertainties in the statistical sampling of collisions and how this uncertainty is propagated within the computational workflow. Moreover, the statistical uncertainties of the CCSs depend on the range of effective temperatures used in the calculation. **Figure 6.5B** illustrates that, for a considerable fraction of the velocity grid points, $Q^{(l)}\omega^{(s)}$ values become negligible when the upper end of the velocity grid is defined by a relatively high effective temperature (*i.e.,* $T_{eff,max} \gg T$), thereby negating their contribution to the CCS integrand at high T_{eff}. To evaluate the effect of grid sizes on CCS calculations performed for a range of effective temperatures, we undertook an analysis akin to that of **Figure 6.6**. In this case, the relative uncertainty for CCSs when evaluated between $T = 298$ K and $T_{eff,max} = 800$ K are approximately 30 % larger than those for a CCS calculation performed solely at $T = 298$ K (1.26 % *vs.* 0.97 %; see **Supplementary Section S6-6**). Because this comparison was made for the suggested sampling sizes of $inp = 104$ and $imp = 512$, we recommend that users seeking CCSs at various effective temperatures employ the high-precision sampling sizes. For $T = 298$ K and $T_{eff,max} = 800$ K, $inp = 200$ and $imp = 1024$ yields a mean relative uncertainty of 0.64 % for $\Omega^{(1,1)}$ at $T = 298$ K, which decreases further for the higher temperatures. Despite the high-precision settings being more computationally expensive, the linear grid significantly decreases the computing time because the trajectories determining the $Q^{(l)}$ need be evaluated only once. Thus, the added computational expense is offset, making this drawback relatively minor in terms of the efficiency of MobCal-MPI 2.0.

6.10 Implementing 2TT within MobCal-MPI 2.0 for mobility calculations at arbitrary fields

In the MobCal-MPI 2.0 interface, users are prompted to input the bath gas temperature and an upper limit for the ion effective temperature (*i.e.,* T and $T_{eff,max}$, respectively). Specifying a

temperature range calls the 2TT module, which initiates calculation of the ion's CCS and reduced mobility at reduced field strengths that fall within the given temperature range. Users can also specify a grid size for the temperature range such that CCSs and reduced mobilities are printed at desired increments of T_{eff}.

Table 6.2 shows an example output from MobCal-MPI 2.0, where the CCS and reduced mobility of protonated amoxapine in N_2 was calculated between $T = 373$ K and an arbitrary choice of $T_{eff,max} = 700$ K on a temperature grid composed of 8 points. $T = 373$ K corresponds to the bath gas temperature, which yields a CCS and reduced mobility in the zero-field limit (*i.e.,* $E/N = 0$). Because all collision integrals are evaluated on the same linear velocity grid, users can increase the number of points sampled within the temperature range up to $T_{eff,max}$ without incurring an increase in calculation time.

Table 6.2. Example output data from MobCal-MPI 2.0 for protonated amoxapine, showing relevant mobility data in N_2 for a range of effective temperatures ($T = 373$ K and $T_{eff,max} = 700$ K).

T_{eff} / K	E / N / Td	K_0 / cm^2 V^{-1} s^{-1}	CCS / Å^2	CCS uncertainty / %
373.0	0.0	1.2250	154.27	0.64%
402.7	50.0	1.2162	150.08	0.63%
449.0	81.3	1.2028	144.50	0.62%
501.8	107.9	1.1878	139.19	0.61%
551.4	129.1	1.1742	135.02	0.61%
600.9	148.2	1.1609	131.44	0.60%
650.5	166.1	1.1479	128.34	0.59%
700.0	183.0	1.1353	125.63	0.58%

Notably, the CCS and its uncertainty decreases at higher effective temperatures, which is a consequence of the decreased efficiency in momentum transfer with increasing relative velocity (*cf.* **Figure 6.5**).[64,257,327,328] The inverse relationship between CCS and mobility leads one to expect that K_0 should increase with T_{eff}, but this is not the case. The decrease of K_0 with T_{eff} is a consequence of the kinetic theory of gases, which states that the apparent viscosity of the collision gas increases

with T_{eff}.[61] This underscores the fact that the ion mobility is not a constant, but rather a function of the field strength. Since the reduced field strength computed by MobCal-MPI 2.0 is determined by the effective temperature of the ion, the alpha function can be readily obtained from the calculated mobility data using **Eq. 6.25** and may be subsequently fit to an even order polynomial of the form given by **Eq. 6.6** to determine the alpha coefficients. Employing this workflow for protonated amoxapine results in $\alpha_2 = -2.935 \times 10^{-6}$ Td^{-2}, $\alpha_4 = 3.080 \times 10^{-11}$ Td^{-4}, and $\alpha_6 = -2.553 \times 10^{-16}$ Td^{-6}.

$$\alpha\left(\frac{E}{N}\right) = \frac{K_0(E/N)}{K_0(0)} - 1 \qquad \textbf{Eq. 6.25}$$

To assess the accuracy of 2TT in calculating high field mobilities, one can compare the alpha curves obtained through experimentation and computation. This comparison is shown in **Figure 6.7A** for protonated amoxapine (blue trace), whose experimental alpha curve (black trace) was determined using the protocol outlined in **Supplementary Section S6-7**. MobCal-MPI 2.0 captures the general trend of amoxapine's alpha curve, which adopts increasingly negative values as the reduced field strength increases. However, the computed alpha curve exhibits more negative values than the experimental curve, indicating that calculated mobility coefficient decreases faster with field strength compared to the actual measurement. This finding aligns with the observations made by Siems *et al.*,[329] who reported that the 2TT approach yields accurate mobilities at low and medium field strengths, but underestimates mobilities at high field strengths. Consequently, alpha curves evaluated using 2TT will almost always exhibit a systematic, negative deviation, especially at high field strengths.

To address the systematic deviation between the computed and measured alpha functions, we introduced an empirical correction to 2TT, inspired by the dependence of the deviations on field strength found by Siems *et al.* (see **Supplementary Section S6-8** for details).[329] Briefly, a field-dependent correction factor (f_{corr}) is used to adjust the mobilities calculated from 2TT (K_{2TT}) using **Eq. 6.26** and **Eq. 6.27**.

$$K_{corr} = f_{corr} \cdot K_{2TT} \quad \textbf{Eq. 6.26}$$

$$f_{corr}\left(\frac{E}{N}\right) = 1 + A\,exp\left(-\frac{B}{E/N}\right) \quad \textbf{Eq. 6.27}$$

The parameters A and B, which represent the maximum deviation at infinitely high field strengths and the field strength at which deviations become significant, respectively, can be tuned for a specific ion such that the deviation between the computed and measured alpha curves is minimized. For protonated amoxapine, optimizing A and B leads to almost perfect alignment of the computed and experimental alpha curves (**Figure 6.7A**; red trace). Moreover, the value obtained for A (4.4 %) is consistent with the range reported by Siems *et al.* (5 – 7 %), and the value of $B = 132$ Td indicates that the correction becomes most significant at high field strengths.

To investigate the general performance of the empirical correction, we assessed its ability to correct high-field mobilities for a large set of compounds. An efficient means of obtaining a dataset of high-field mobilities is via DMS, which is also known as field-asymmetric ion mobility spectrometry (FAIMS).[39,293,330] In DMS, the ions are subjected to an asymmetric waveform (separation voltage; SV) that consists of high-field and low-field components. The SV induces the off-axis displacement of the ion by an amount proportional to its alpha function. The application of a species-specific compensation voltage (CV) to the SV enables ions to traverse the DMS device. For a given SV, each analyte is transmitted at a distinct CV that is intrinsically linked to the ion's alpha function. By monitoring the dependence of the CV required for analyte transmission at different strengths of the SV field, the corresponding SV *vs.* CV relationship (*i.e.,* a dispersion plot) can be employed to derive the alpha function using the method described in **Supplementary Section S6-7**.

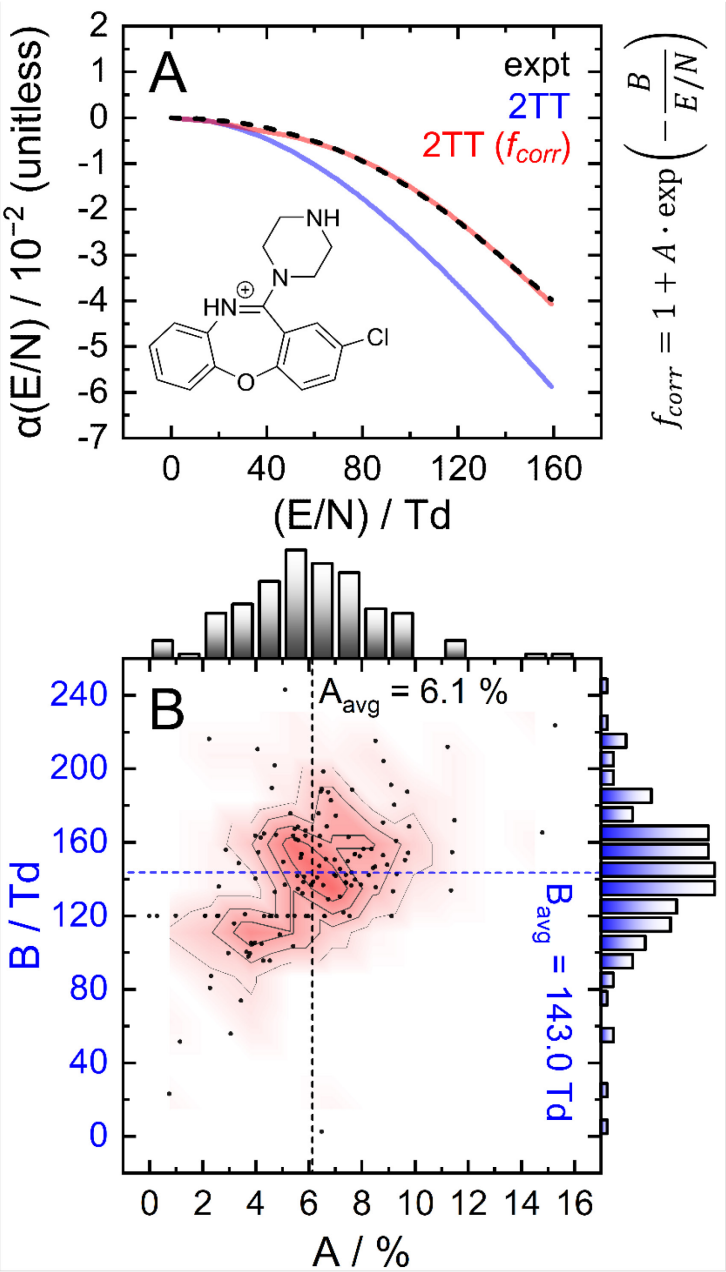

Figure 6.7. Investigation of the empirical correction to 2TT. (**A**) Comparison of experimental and calculated alpha functions for protonated amoxapine. Optimized parameters are $A = 4.4$ % and $B = 132$ Td. (**B**) 2D distribution of optimized A and B parameters of the empirical correction, f_{corr}, for each of the 132 compounds is the *high-field validation set*.

Dispersion plots for 132 compounds were procured from previously published datasets from our group to generate the *high-field validation* set.[64,95,307] Each analyte's dispersion plot was recorded on

the SelexION DMS platform (SCIEX; 1 mm gap and $T = 373$ K) in a pure N_2 environment between SV = 0 – 4000 V. In theory, each analyte's dispersion curve can be converted to the corresponding alpha curve. However, because our goal is to reproduce experimentally measured quantities, Haack and Hopkins employed an iterative method previously published by our group to calculate dispersion plots from the mobility data generated by the 2TT implementation within MobCal-MPI 2.0.[258] In general, the calculated dispersion plots displayed positive compensation voltage (CV) shifts relative to those determined experimentally (**Figure 6.8A**). Positive CV shifts indicate that the systematic underestimation of mobility that was observed for protonated amoxapine is also observed for most compounds in the *high-field validation set*.

Since the empirical correction to 2TT could be employed to replicate the alpha curve of amoxapine, it is reasonable to assume that the same approach can be employed to address the systematic CV shift observed in the dispersion plots. To this end, A and B were optimized such that the deviation between the calculated and experimental dispersion curves were minimized (for select examples, see **Supplementary Section S6-8**). **Figure 6.7B** shows the distributions of the A and B parameters obtained for each compound in the *high-field validation set*, the majority of which align with the results found by Siems *et al.* (5 – 7 % for A and 100 – 200 Td for B).[329] The parameters exhibit unimodal distributions when considered independently or together, the latter of which is best visualized in the contour plot. The data also suggests little to no correlation between the two parameters, although it is worth noting that B becomes undefined as A approaches zero.

Expanding the applicability of the empirical correction to various chemical systems necessitates knowledge of the values for A and B *a priori* such that they can be applied to a broad range high-field mobilities predicted by 2TT. Because these parameters are uniformly distributed about their respective means and are seemingly uncorrelated with properties relevant to collision theory (see **Supplementary Section S6-8**), we chose to use the average values of A (6.1 %) and B (143.0 Td) to test the accuracy of this approach. A_{avg} and B_{avg} were hard-coded into MobCal-MPI 2.0, enabling the calculation of high-field mobility data using a uniform set of correction factors. The

deviations between calculated and experimental dispersion plots that either employ or exclude the empirical correction to 2TT are shown in **Figure 6.8B**. As previously mentioned, exclusion of the empirical correction results in a systematic overestimation of the CV values for all 132 species, especially at high field strength. Using the empirical correction with A_{avg} and B_{avg} removes the systematic deviation, shifting the error in CV towards zero for all SVs sampled in the dispersion plot. **Figure 6.8C** shows the distribution of CV deviations at $SV_{pp} = 4000$ V. When applying the empirical correction, over 88 % of the data falls within a ± 4 V range of the experimental value. The mean deviation between calculated and experimental CV is – 0.4 V at $SV_{pp} = 4000$ V, equivalent to a relative deviation of approximately 4 %. The full width at half maximum (FWHM) of this distribution is 5.7 V, which is comparable to the experimental FWHM at this separation field amplitude (≈ 3 V).[39] It is worth mentioning that the variances are virtually unaffected by the empirical correction, meaning that this approach strictly corrects the deviations of 2TT in determining high-field mobilities, but does not impact uncertainties specific to individual analytes.

Although we derived the empirical correction based on fundamental deviations of 2TT at high fields,[329] it is not possible to deconvolute the error incurred from breakdown of 2TT at high-field strengths from other sources of error. For example, MobCal-MPI 2.0 treats all collisions elastically,[110,317,319] and as such, ignores the inherent inelasticity of ion-neutral collisions with molecular entities such as N_2. Specifically, collision events do not consider the deposition of energy into the ion's rotational and vibrational degrees of freedom, both of which will influence the ion's mobility, especially at high field strengths due to species-to-species differences in momentum transfer,[331] vibrational broadening,[77] and increased rotation of the ion during the collision event.[332] The complexity of these problems currently preclude the development of a computational framework that can model these effects, as simulating these effects requires exact knowledge of how internal energy is exchanged between the collision gas and the ion's rovibrational states. As advances are made in treating the inelasticity problem, we expect that the width of the distributions shown in **Figure 6.8C** will decrease.

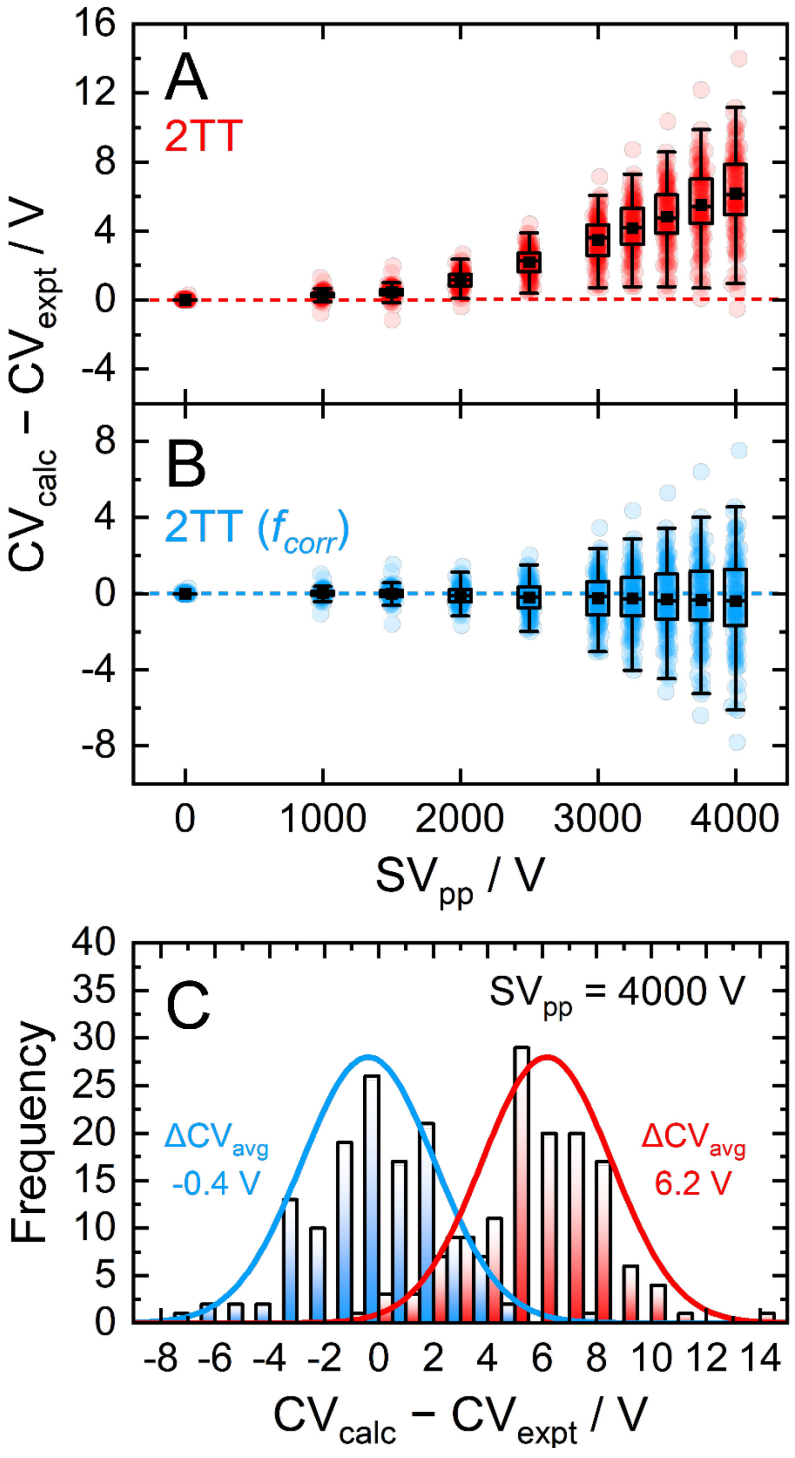

Figure 6.8. Comparison of measured vs. calculated dispersion plots over a range of separation field amplitudes as box plots for (**A**) uncorrected 2TT and (**B**) 2TT including the empirical correction employing A_{avg} and B_{avg}. Panel (**C**) shows the distribution of CV deviations using the uncorrected and empirically correct 2TT at the highest SV_{pp} (4000 V).

It is worth mentioning that the enhancements made to MobCal-MPI 2.0 that allow calculation of ion mobility at arbitrary field strengths are also applicable to TWIMS and TIMS instrumentation. Analysis of survival yields for a range of thermometer ions with a m/z between 200 – 300 Da resulted in significant fragmentation and/or isomerization on both platforms, indicating substantial increases to the ion's T_{eff} despite operating within the low-field limit.[143,147,333] For example, when employing "soft" conditions on commercial TWIMS and TIMS systems, the measured T_{eff} for a specific chemical thermometer, the *p*-methoxybenzylpyridinium ion, exceeded 500 K. This finding could potentially explain the class-specific CCS calibration challenges inherent to TWIMS and TIMS,[35] where the elevated T_{eff} causes the experimentally relevant CCS value to deviate from the DTIMS CCS value from which they are fit to (T_{eff} = 298 K). Consequently, it would be reasonable to compare CCS measurements obtained via TWIMS/TIMS with MobCal-MPI 2.0 calculations conducted at various field strengths within the low-field limit to assess the degree in which an ion's CCS evolves with T_{eff}.

6.11 Benchmarking the performance of MobCal-MPI 2.0

Having demonstrated the accuracy and precision with which MobCal-MPI 2.0 can model mobility data at arbitrary field strengths, we sought to benchmark code performance on parallelized, high-performance computing (HPC) architecture. Proper benchmarking requires the explicit consideration of parameters that affect CCS calculation times, which include the number of atoms within an analyte molecule and the number of HPC cores used. This was accomplished by monitoring the time taken to calculate the CCS for each conformer of the 50 species in the *validation set* (N = 238 unique conformers). Since TM-based CCS calculations are often used for short and medium length peptides, we opted to supplement the *validation set* with the *peptide set*, which comprises 12 peptides ranging in length from 9 to 22 amino acid residues that can adopt charge states between +2 to +5. Combining the *validation* and *peptide* sets yields 250 conformers that

range in size from 16 to 374 atoms. The time required to calculate the CCS for each conformer at $T = 298$ K was measured using 4, 8, 16, and 32 cores in parallel with $itn = 10$, $inp = 96$, and $imp = 512$. The benchmarking process uses a different value for the inp parameter than the recommended setting of 104, as MobCal-MPI 2.0 requires inp (and imp) to be divisible by the number of cores utilized for parallel computing. Because 104 is not evenly divisible by 16 or 32, we chose the nearest integer that is evenly divisible by 4, 8, 16, and 32, which is 96. Additionally, it is important to consider that the random seed number used to determine the starting orientation of N_2 relative to the ion influences the runtimes. Because certain starting conditions may lead to "lost" trajectories (*i.e.,* those where the N_2 gets captured by the ion) calculation times can be artificially inflated. To account for this effect during benchmarking, we conduct CCS calculations using three random seeds and then averaged the respective runtimes. This approach ensures that any increase in calculation time caused by lost trajectories from one seed will be averaged out.

The averaged runtimes for the 250 conformers of the *validation set* are presented in **Figure 6.9A**. As expected, runtimes increase with the number of atoms in the ion owing to the iterative nature with which the ion-neutral interaction potential is evaluated. Calculation times increase linearly with the number of atoms in the ion when the *validation set* and the *peptide set* are considered independently ($\mathcal{O}(N)$; see **Supplementary Section S6-9**). However, extrapolation of the line of best fit determined from linear regression of the *validation set* indicates that the peptides do not conform to the same trend line, requiring slightly longer runtimes to complete. The increased runtimes for the peptides are likely a consequence of their greater charge, which can induce the capture of N_2 molecules at low relative velocities. In other words, N_2 trajectories with small relative velocities are more susceptible to becoming "lost," and thus artificially increase the runtime. It is hard to gauge the exact behaviour of how runtimes might evolve for systems larger than those studied here, but we expect that the scaling of these times will always outperform $\mathcal{O}(N^2)$, where N is the number of atoms.

Linear regression of the averaged runtimes for the validation set with respect to the number of atoms yields slopes that follow an inverse relationship with the number of cores. This indicates efficient code parallelization, where doubling the number of cores approximately halves the runtime. This trend can also be observed in **Figure 6.9B**, where the distributions of the individual speedup factors for all conformers in the *validation* and *peptide set* are shown as violin plots. The averages of these distributions reflect the aforementioned speed increase, which is to be expected as the total number of collision events sampled is evenly distributed among all cores (*i.e.,* $itn \times inp \times imp$). Only for 32 cores do we observe a slightly lower average speedup than the expected value of 8 (as compared to runtime for 4 cores), suggesting the presence of a small parallel execution overhead. Naturally, the absolute runtimes heavily depend on the computing system used, so the runtimes reported here, which were assessed using 2nd generation AMD EPYC processers (AMD Rome 7532 @ 2.40 GHz), will vary from other systems. Nevertheless, calculation of "routine" small molecules (*i.e.,* those containing less than 70 atoms) complete in less than 30 minutes on 8 cores, highlighting the efficiency with which MobCal-MPI 2.0 can compute accurate CCSs to complement experimental results.

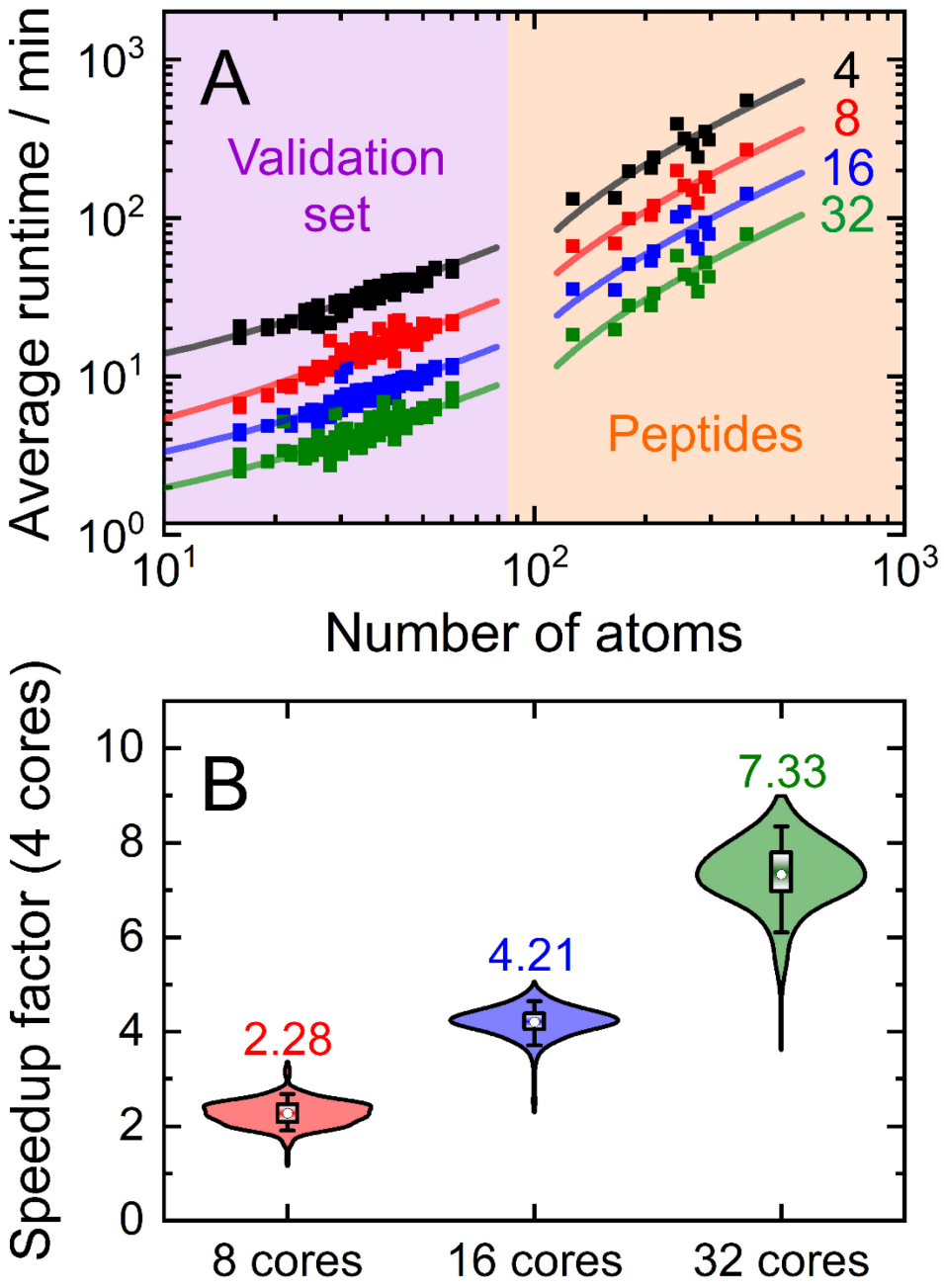

Figure 6.9. (**A**) MobCal-MPI 2.0 runtimes for CCS calculations ($T = 298$ K) of the validation set and 12 peptides as a function of the number of atoms. Calculations used 4 (black), 8 (red), 16 (blue), or 32 (green) cores in parallel. Linear regression is performed on the validation set, the lines for which are extrapolated to the peptides. (**B**) Violin plot showing the distribution of speedup factors from using 8, 16, or 32 cores compared to 4 cores. All runtimes are reported as the average from three CCS evaluations that employ different seed numbers on the same grid size (*itn* = 10, *inp* = 96, and *imp* = *512*).

6.12 Conclusions

This chapter reports on the latest version of the parallelized CCS calculation suite MobCal-MPI 2.0, which significantly improves the handling of collision dynamics with N_2. Owing to the diatomic nature of molecular N_2, the vdW component of the ion-neutral interaction potential can be evaluated in two ways. In the first approach, N_2 can be treated as pseudo-atomic entity, whereby the pairwise interactions that determine the vdW component of the ion-neutral interaction potential are calculated with respect to its centre of mass (CoM). The CoM approach was shown to be erroneous at short ion-neutral distances, where the repulsive portion of the interaction potential is strongly affected by the orientation of N_2 relative to the molecule. Consequently, the methodology to evaluate the vdW component was modified to a second approach that considers the averaged, pairwise interaction between each atom in the molecule and each nitrogen atom in the N_2 collision partner (Avg-N_2). By optimizing the vdW parameters for both the CoM and Avg-N_2 methods and evaluating the RMSE between computed and experimental CCSs, it was determined that the Avg-N_2 approach slightly outperforms the CoM in terms of calculating CCSs at $T = 298$ K. Specifically, the Avg-N_2 approach exhibits a RMSE of 2.16 %, whereas the CoM approach exhibits a RMSE of 2.27 % for a diverse set of 50 molecules that were not used to optimize the vdW parameters (*i.e.*, the *validation set*). This increased accuracy will provide practitioners with greater confidence in assigning experimental mobility data to analyte structures.

Because the calculation of CCSs is based on a finite number of collision events, there are inherent statistical uncertainties associated with the computed values. We have made modifications to the workflow to evaluate these uncertainties accurately. In MobCal-MPI 2.0, uncertainties in CCS calculations emerge from the choice of the three sampling parameters, namely: 1) the number of cycles in which collision events are sampled (*itn*), 2) the number of relative velocities of the ion-neutral pair that are sampled (*inp*), and 3) the number of impact parameter and ion-neutral orientations (*imp*). For routine CCS and low-field mobility calculations, we find that settings of $itn = 10$, $inp = 104$, and $imp = 512$ yield an uncertainty of 0.97 %. For higher precision, we

recommend settings of $itn = 10$, $inp = 200$, and $imp = 768$ or 1024, which reduces the uncertainty in the calculated CCS and low-field mobilities to 0.57 %.

To meet the growing demand for evaluation of ion mobility at high field strengths, the second-order approximation of 2TT was implemented in MobCal-MPI 2.0 alongside an empirical correction. This addition allows for the evaluation of CCS and ion mobility at multiple field strengths that are defined by a range of effective temperatures. When augmented with the empirical correction to 2TT, which corrects for the underestimation of ion mobilities at high field strengths,[329] MobCal-MPI 2.0 accurately predicts the high-field mobilities of a set of 132 analytes. Specifically, the high-field mobility data generated by MobCal-MPI 2.0 was used to reproduce the DMS dispersion plots of the 132 analytes, yielding an average error of only -0.4 V in compensation voltage at the highest separation voltage sampled (4000 V). This deviation translates to a relative error of less than 4 % in the capability of MobCal-MPI 2.0 to compute high-field DMS data at 136 Td (with an electrode spacing of 1 mm, $T = 373$ K, and $p = 1$ atm).

Another notable change of MobCal-MPI 2.0 compared to its predecessor is the modification of the velocity grid (*inp*) from a weighted approach (*i.e.,* greater density of points at the maximum of the distribution of velocities at T_{eff}) to a linear grid spacing. Implementing the linear spacing for the *inp* grid enables the evaluation of collision integrals using a single set of trajectories. In contrast, the non-linear spacing of the weighted *inp* grid in the previous version of MobCal-MPI required the revaluation of collision integrals for each temperature desired by the user. The introduction of the linear grid in MobCal-MPI 2.0 results in considerably faster CCS computations compared to the previous version; if a user requires CCSs at n effective temperatures, MobCal-MPI 2.0 can accomplish the task n times faster than MobCal-MPI.

Further benchmarking of MobCal-MPI 2.0 reveals its ability to compute low- and high-field mobility data with exceptional efficiency. For example, the CCS of an ion composed of 50 atoms can be obtained in approximately 20 minutes when using 8 cores in parallel. We also find that the decrease in calculation times scales roughly linearly with the number of cores employed; a small

parallel execution overhead is observed only when 32 cores are used. We believe that MobCal-MPI 2.0 will be a valuable tool for the IMS community, who can use this code to support their experimental findings with accurate models of an ion's mobility/CCS. Although no CCS calculation method is free of systematic biases, the *calibration*, *validation*, and *high-field validation sets* were meticulously selected to encompass a diverse range of functional groups that span the molecular space defined by the MMFF94 forcefield. However, our datasets do not contain anionic or metal adducted species, begging the question of whether the accuracy of MobCal-MPI 2.0 extends to these analytes. As we continue to broaden our collection of low- and high-field mobility data, we plan to evaluate the capability of MobCal-MPI 2.0 to model the mobilities of anionic and metal-adducted species, and to investigate the impact of inelasticity and vibrational broadening on computed mobilities.

Chapter 7

Conclusions

7.1 Concluding remarks and future outlook

DMS has emerged as a powerful analytical tool with diverse applications in various scientific disciplines. The utility of DMS extends far beyond its separation capabilities, as performing DMS experiments in microsolvating environments samples intermolecular interactions that are likely to resemble those that occur in the condensed phase. This, in turn, facilitates the prediction of important molecular attributes that are routinely screened for during the early stages of drug design. Moreover, if one knows the nature of the intermolecular interactions that occur between an analyte and its collision environment *a priori*, then it becomes possible to predict the parameters needed to transmit a particular analyte through the DMS cell. Such predictive capabilities open new avenues for understanding complex chemical systems and hold promise for advancing fields ranging from drug discovery and environmental analysis to proteomics and metabolomics.

The ability to predict an analyte's DMS behaviour from first-principles or an ML-assisted approach would greatly assist with environmental analyses and other quantitative workflows. Targeted approaches, in which the identity of the analyte is known, will benefit the most from these models of DMS behaviour since the ability to set a specific SV/CV pair for a desired analyte will reduce the time required for analytical method development and mitigate redundant data acquisition. For untargeted approaches, it would be fruitful to utilize the dispersion plot as an additional metric for compound identification. For example, an ion's CCS, as inferred from its dispersion plot using ML modelling, could provide additional information when identifying an unknown analyte. Furthermore, the correlation of an ion's DMS behaviour with its physicochemical properties suggests that DMS might also find application as a property measurements tool for drug design or for developing transport models of environmental contaminants. The first hurdle to overcome *en route* to creating these predictive models is the acquisition of suitably sized data sets

that contain representative molecules. For example, the data set that we have assembled to date contains small positively charged organic molecules, so we expect that property predictions for large biological molecules, metal-containing species, and anions would be inaccurate. It will be interesting to explore how many molecules of a particular type are required in the training set to yield accurate properties predictions, and which other molecular properties correlate with DMS clustering behaviour.

Aside from property prediction, there are many interesting directions yet to be explored with respect to dynamic clustering and its impact on differential mobility. Some work has been conducted to explore how modifier mixtures impact differential mobility,[156,334,335] notably in the context of preferential microsolvation,[155] but the literature on this topic is still relatively sparse. Given that solvation by different modifiers can alter the relative stability of different charge sites and different analyte conformations,[30–32,63,154,186,187,336,337] modifying DMS collision environments with solvent mixtures could offer an additional degree of tunability with respect to ion structure. One can extend this logic to include non-polar modifier species (*e.g.*, cyclohexane and toluene),[156,334] which would interact weakly via charge-induced dipole and charge-quadrupole interactions, but which might affect analyte structure and stability, and therefore induce interesting DMS behaviour. This could be especially useful in preserving native-like ion configurations of peptides/proteins under the extreme conditions of a DMS device without modifying the charge distribution.[68,177]

Another point of interest is that DMS measurements have traditionally been conducted on small, organic cations despite the plethora of other compound classes that are commercially available. DMS-MS experiments on chemically diverse species might reveal interesting new phenomena. For example, do anionic species, which are generally more polarizable and subject to electron detachment, exhibit subtly different DMS behaviour to cations? What happens when large biological species are introduced to the DMS given that they can adopt zwitterionic configurations in the gas phase, undergo dipole alignment with the electric field, and exhibit asymmetric microsolvation at multiple different sites simultaneously? There is also evidence that electrospray ionization generates

"molecular asteroids" – relatively large, highly-charged droplets comprised of the analyte and the ESI solvent – which survive transit through the DMS cell and pass into the mass spectrometer.[338,339] Could these molecular asteroids be used to study a "fully solvated" ion using gas phase techniques? Readers who are interested in these fields are directed to work of Benter, Cooper, Donald, Glover, Shvartsburg, and Smith for additional information.[162,173,174,201,340–345]

Regarding the ability to model an ion's high-field mobility on the DMS platform, it is important to identify areas that could introduce differences between our model and experiment. With respect to the DMS instrumentation, systematic deviations could be introduced if the carrier gas is not completely dry, although this is not expected to be an issue given that the DMS carrier gas should be dried before its introduction to the mobility cell. A more likely source of error could stem from the known bath gas temperature gradient along the transmission axis and the axis of the separation field (see **Figure 35** in reference 39). Non-uniform gas dynamics and electrode heating induces a position-dependent bath gas temperature, which has been shown to impact ion trajectories as they pass through the DMS cell.[346] It is also possible that molecular dipoles could experience some degree of alignment with the applied electric field – a topic that Shvartsburg has covered in detail using proteins as model analytes.[340,341,345,347,348] Should alignment occur, the 3D orientationally-averaged CCSs that we employ for modelling purposes would not be correct. However, we expect that molecular alignment is not a significant contributor to model error given the relatively low dipole moments for the small molecules that we have studied to date. It is much more likely that discrepancies between measured and computed dispersion curves are associated with inaccuracies in the underlying chemical theory. We highlight five areas that, moving forward, are worth considering in more detail in the context of modelling both ion mobility and differential mobility:

i. *The accuracy of quantum chemical calculations* is of paramount importance. Differential mobility simulations rely on computed CCSs, which in turn rely on computed molecular geometries, partial charges, and relative energies. This interdependence means that any errors associated with the computational method will be propagated through the model for differential mobility. To this

end, we conducted a preliminary survey of the choice of DFT method on CCS calculation accuracy, which indicated that MobCal-MPI outputs are relatively consistent across model chemistries.[115] However, the impact of relative isomer and cluster energies and the effect of anharmonicity on predicted thermochemistry in the context of DMS simulations has not been well researched. Preliminary work that we have conducted suggests that introducing anharmonic corrections to computed vibrational frequencies impacts the predicted DMS behaviour, although the agreement between simulation and experiment is still qualitative. Our work in this regard is ongoing.

ii. The impact of *molecular inelasticity* on *in silico* DMS modelling has yet to be explored thoroughly. Clearly, inelastic collisions must be considered in an accurate model of differential mobility given that ion heating is observed in DMS. However, assessing energy redistribution following collision is non-trivial; the rate of energy exchange changes from one system to another, and it is likely to be field dependent (*i.e.,* varies with collision energy). Whether predictions of an ion's DMS behaviour will improve by calculating CCSs inelastically is still an open question.[38,314]

iii. *2TT and its impact on field-dependent mobility* is an important consideration. Siems, Viehland, and Hill demonstrated that at the maximum field strengths commonly employed in DMS, CCSs are underestimated by 5-7% even when employing higher-order corrections to 2TT.[329] As a result, for a given CCS, the high-field mobility is underestimated *when empirical corrections are not employed*. This underestimation manifests as a shift to more positive CV values for non-clustering collision environments in our computed dispersion curves (see **Figure 6.7** and **Figure 6.8A**).

iv. *The accuracy of CCS calculation methods at high temperatures* is not well established. CCS calculation packages rely on parameters that are scaled to reproduce experimentally determined low-temperature CCS values. Testing the ability of these codes to compute temperature-dependent CCSs accurately first requires the measurement of CCSs for many analytes across a wide range of bath gas temperatures. The temperature and pressure control needed for these

measurements are especially challenging at the upper limit of effective temperature in DMS devices (*ca.* 1000 K).

v. The assumption that the *analytes respond instantaneously to changes in electric field* is most likely valid for rigid ions in a non-clustering environment,[349] but becomes unnecessary if one adopts a *kinetic* description. Modelling DMS behaviour with a kinetic approach will be important for large, flexible ions in a microsolvating environment where changes in cluster size may not respond instantaneously to changes in the electric field strength.

A different topic requiring a considerable amount of investigation, and one which our group is actively engaged in, is the observation that many *pure* analytes exhibit multiple features in a DMS ionogram. These sub-populations can be associated with different conformers or tautomers,[44,47,50,201,344,350] diastereomers,[43,45,49,351] or with post-DMS fragmentation of an aggregate species (*e.g.*, solvent clusters and proton-bound analyte dimers).[46,352] Although the identity of each feature can be deduced by, for example, collision-induced dissociation,[50] hydrogen-deuterium exchange,[197,353] and/or trapped ion spectroscopy, [18,354–359] there is no simple *a priori* method to determine whether a particular analyte will exhibit multiple features in a DMS ionogram. This complicates the use of DMS in an analytical setting – if an analyte exhibits multiple populations that vary with DMS conditions, but the device is set to select only one sub-population, one runs the risk of underestimating analyte concentration in quantitative workflows. Consequently, practitioners must be careful to calibrate and conduct experiments under identical conditions, and explicitly state those conditions in subsequent reports.[35] In the context of DMS-based predictions of condensed phase properties, the presence of multiple DMS peaks can also confuse efforts to create predictive ML models. Which ionogram peak(s) should be selected as features for model building? Does the analyte exhibit the same geometric structure in different solvent-modified environments and, if not, does this impact ML model accuracy? These are all open-ended questions, and I look forward to seeing how the community drives progress in this field.

References

(1) Kulmala, M. Dynamical Atmospheric Cluster Model. *Atmos Res* **2010**, *98* (2–4), 201–206. https://doi.org/10.1016/J.ATMOSRES.2010.03.022.

(2) Kulmala, M.; Kontkanen, J.; Junninen, H.; Lehtipalo, K.; Manninen, H. E.; Nieminen, T.; Petäjä, T.; Sipilä, M.; Schobesberger, S.; Rantala, P.; Franchin, A.; Jokinen, T.; Järvinen, E.; Äijälä, M.; Kangasluoma, J.; Hakala, J.; Aalto, P. P.; Paasonen, P.; Mikkilä, J.; Vanhanen, J.; Aalto, J.; Hakola, H.; Makkonen, U.; Ruuskanen, T.; Mauldin, R. L.; Duplissy, J.; Vehkamäki, H.; Bäck, J.; Kortelainen, A.; Riipinen, I.; Kurtén, T.; Johnston, M. V.; Smith, J. N.; Ehn, M.; Mentel, T. F.; Lehtinen, K. E. J.; Laaksonen, A.; Kerminen, V. M.; Worsnop, D. R. Direct Observations of Atmospheric Aerosol Nucleation. *Science (1979)* **2013**, *339* (6122), 943–946. https://doi.org/10.1126/science.1227385.

(3) MacTaylor, R. S.; Castleman, A. W. Cluster Ion Reactions: Insights into Processes of Atmospheric Significance. *Journal of Atmospheric Chemistry 2000 36:1* **2000**, *36* (1), 23–63. https://doi.org/10.1023/A:1006376914390.

(4) Yang, K.; Feng, L.; Shi, X.; Liu, Z. Nano-Graphene in Biomedicine: Theranostic Applications. *Chem Soc Rev* **2012**, *42* (2), 530–547. https://doi.org/10.1039/C2CS35342C.

(5) Zhang, Q.; Huang, J. Q.; Qian, W. Z.; Zhang, Y. Y.; Wei, F. The Road for Nanomaterials Industry: A Review of Carbon Nanotube Production, Post-Treatment, and Bulk Applications for Composites and Energy Storage. *Small* **2013**, *9* (8), 1237–1265. https://doi.org/10.1002/SMLL.201203252.

(6) Higaki, T.; Li, Y.; Zhao, S.; Li, Q.; Li, S.; Du, X. S.; Yang, S.; Chai, J.; Jin, R. Atomically Tailored Gold Nanoclusters for Catalytic Application. *Angewandte Chemie International Edition* **2019**, *58* (25), 8291–8302. https://doi.org/10.1002/ANIE.201814156.

(7) Tao, Y.; Li, M.; Ren, J.; Qu, X. Metal Nanoclusters: Novel Probes for Diagnostic and Therapeutic Applications. *Chem Soc Rev* **2015**, *44* (23), 8636–8663. https://doi.org/10.1039/C5CS00607D.

(8) Kwak, K.; Lee, D. Electrochemistry of Atomically Precise Metal Nanoclusters. *Acc Chem Res* **2019**, *52* (1), 12–22. https://doi.org/10.1021/acs.accounts.8b00379.

(9) Mizoguchi, A.; Ohshima, Y.; Endo, Y. The Study for the Incipient Solvation Process of NaCl in Water: The Observation of the NaCl–(H_2O)n (n = 1, 2, and 3) Complexes Using Fourier-Transform Microwave Spectroscopy. *J Chem Phys* **2011**, *135* (6), 064307. https://doi.org/10.1063/1.3616047.

(10) Fárník, M.; Fedor, J.; Kočišek, J.; Lengyel, J.; Pluhařová, E.; Poterya, V.; Pysanenko, A. Pickup and Reactions of Molecules on Clusters Relevant for Atmospheric and Interstellar Processes. *Physical Chemistry Chemical Physics* **2021**, *23* (5), 3195–3213. https://doi.org/10.1039/D0CP06127A.

(11) Atkins, C. G.; Banu, L.; Rowsell, M.; Blagojevic, V.; Bohme, D. K.; Fridgen, T. D. Structure of $[Pb(Gly\text{-}H)]^+$ and the Monosolvated Water and Methanol Solvated Species by Infrared Multiple-Photon Dissociation Spectroscopy, Energy-Resolved Collision-Induced Dissociation, and Electronic Structure Calculations. *Journal of Physical Chemistry B* **2009**, *113* (43), 14457–14464. https://doi.org/10.1021/jp905654v.

(12) Kapota, C.; Lemaire, J.; Maître, P.; Ohanessian, G. Vibrational Signature of Charge Solvation vs Salt Bridge Isomers of Sodiated Amino Acids in the Gas Phase. *J Am Chem Soc* **2004**, *126* (6), 1836–1842. https://doi.org/10.1021/ja036932v.

(13) Dopfer, O.; Patzer, A.; Chakraborty, S.; Alata, I.; Omidyan, R.; Broquier, M.; Dedonder, C.; Jouvet, C. Electronic and Vibrational Spectra of Protonated Benzaldehyde-Water Clusters, $[BZ\text{-}(H_2O)_{N\leq 5}]H^+$: Evidence for Ground-State Proton Transfer to Solvent for n ≥ 3. *J Chem Phys* **2014**, *140* (12), 124314. https://doi.org/10.1063/1.4869341.

(14) Polfer, N. C.; Oomens, J. Vibrational Spectroscopy of Bare and Solvated Ionic Complexes of Biological Relevance. *Mass Spectrom Rev* **2009**, *28* (3), 468–494. https://doi.org/10.1002/MAS.20215.

(15) Dunbar, R. C.; Martens, J.; Berden, G.; Oomens, J. Water Microsolvation Can Switch the Binding Mode of Ni(II) with Small Peptides. *Journal of Physical Chemistry Letters* **2017**, *8* (12), 2634–2638. https://doi.org/10.1021/acs.jpclett.7b00973.

(16) Chang, T. M.; Chakrabarty, S.; Williams, E. R. Hydration of Gaseous M-Aminobenzoic Acid: Ionic vs Neutral Hydrogen Bonding and Water Bridges. *J Am Chem Soc* **2014**, *136* (29), 10440–10449. https://doi.org/10.1021/jp402217g.

(17) Chang, T. M.; Prell, J. S.; Warrick, E. R.; Williams, E. R. Where's the Charge? Protonation Sites in Gaseous Ions Change with Hydration. *J. Am. Chem. Soc* **2012**, *12*, 46. https://doi.org/10.1021/ja304929h.

(18) Coughlan, N. J. A.; Stockett, M. H.; Kjær, C.; Ashworth, E. K.; Bulman Page, P. C.; Meech, S. R.; Brøndsted Nielsen, S.; Blancafort, L.; Hopkins, W. S.; Bull, J. N. Action Spectroscopy of the Isolated Red Kaede Fluorescent Protein Chromophore. *J Chem Phys* **2021**, *155* (12), 124304. https://doi.org/10.1063/5.0063258.

(19) Wang, X. bin; Yang, X.; Wang, L. S.; Nicholas, J. B. Photodetachment and Theoretical Study of Free and Water-Solvated Nitrate Anions, $NO_3^-(H_2O)n$ (N=0–6). *J Chem Phys* **2001**, *116* (2), 561. https://doi.org/10.1063/1.1427067.

(20) Hou, G. L.; Kong, X. T.; Valiev, M.; Jiang, L.; Wang, X. bin. Probing the Early Stages of Solvation of Cis-Pinate Dianions by Water, Acetonitrile, and Methanol: A Photoelectron Spectroscopy and Theoretical Study. *Physical Chemistry Chemical Physics* **2016**, *18* (5), 3628–3637. https://doi.org/10.1039/C5CP05974G.

(21) Fridgen, T. D.; McMahon, T. B.; Maître, P.; Lemaire, J. Experimental Infrared Spectra of Cl−(ROH) (R = H, CH_3, CH_3CH_2) Complexes in the Gas phase. *Physical Chemistry Chemical Physics* **2006**, *8* (21), 2483–2490. https://doi.org/10.1039/B603102A.

(22) Rajabi, K.; Gillis, E. A. L.; Fridgen, T. D. Structures of Alkali Metal Ion-Adenine Complexes and Hydrated Complexes by IRMPD Spectroscopy and Electronic Structure Calculations. *Journal of Physical Chemistry A* **2010**, *114* (10), 3449–3456. https://doi.org/10.1021/jp9098683.

(23) Power, A. A.; Ali, O. Y.; Burt, M. B.; Fridgen, T. D. IRMPD Spectroscopic and Computational Study of Gas Phase $[M(Ura\text{-}H)(Ura)]^+$ and $[M(Ura\text{-}H)(H_2O)_n]^+$ (M = Sr, Ba; n = 1, 2) Complexes. *Int J Mass Spectrom* **2012**, *330–332*, 233–240. https://doi.org/10.1016/J.IJMS.2012.08.020.

(24) Moghaddam, M. B.; Fridgen, T. D. IRMPD Spectroscopic Study of Microsolvated $[Na(GlyAla)]^+$ and $[Ca(GlyAla\text{-}H)]^+$ and the Blue Shifting of the Hydrogen-Bonded Amide Stretch with Each Water Addition. *Journal of Physical Chemistry B* **2013**, *117* (20), 6157–6164. https://doi.org/10.1021/jp402217g.

(25) Fischer, K. C.; Voss, J. M.; Zhou, J.; Garand, E. Probing Solvation-Induced Structural Changes in Conformationally Flexible Peptides: IR Spectroscopy of Gly_3H^+-(H_2O). *Journal of Physical Chemistry A* **2018**, *122* (41), 8213–8221. https://doi.org/10.1021/acs.jpca.8b07546.

(26) Servage, K. A.; Fort, K. L.; Silveira, J. A.; Shi, L.; Clemmer, D. E.; Russell, D. H. Unfolding of Hydrated Alkyl Diammonium Cations Revealed by Cryogenic Ion Mobility-Mass Spectrometry. *J Am Chem Soc* **2015**, *137* (28), 8916–8919. https://doi.org/10.1021/jacs.5b05448.

(27) Park, S. J.; Narvaez, W. A.; Schwartz, B. J. How Water-Ion Interactions Control the Formation of Hydrated Electron:Sodium Cation Contact Pairs. *Journal of Physical Chemistry B* **2021**, *125* (47), 13027–13040. https://doi.org/10.1021/acs.jpcb.1c08256.

(28) Brodbelt, J. S.; Morrison, L. J.; Santos, I. Ultraviolet Photodissociation Mass Spectrometry for Analysis of Biological Molecules. *Chem Rev* **2020**, *120* (7), 3328–3380. https://doi.org/10.1021/acs.chemrev.9b00440.

(29) Liu, F. C.; Ridgeway, M. E.; Park, M. A.; Bleiholder, C. Tandem-Trapped Ion Mobility Spectrometry/Mass Spectrometry (TTIMS/MS): A Promising Analytical Method for Investigating Heterogenous Samples. *Analyst* **2022**, *147*, 2317–2337. https://doi.org/10.1039/D2AN00335J.

(30) Warnke, S.; von Helden, G.; Pagel, K. Protein Structure in the Gas Phase: The Influence of Side-Chain Microsolvation. *J Am Chem Soc* **2013**, *135* (4), 1177–1180. https://doi.org/10.1021/ja308528d.

(31) Seo, J.; Hoffmann, W.; Warnke, S.; Bowers, M. T.; Pagel, K.; von Helden, G. Retention of Native Protein Structures in the Absence of Solvent: A Coupled Ion Mobility and Spectroscopic Study. *Angewandte Chemie International Edition* **2016**, *55* (45), 14173–14176. https://doi.org/10.1002/anie.201606029.

(32) Göth, M.; Lermyte, F.; Schmitt, X. J.; Warnke, S.; Von Helden, G.; Sobott, F.; Pagel, K. Gas phase Microsolvation of Ubiquitin: Investigation of Crown Ether Complexation Sites Using Ion Mobility-Mass Spectrometry. *Analyst* **2016**, *141* (19), 5502–5510. https://doi.org/10.1039/c6an01377e.

(33) Cumeras, R.; Figueras, E.; Davis, C. E.; Baumbach, J. I.; Gràcia, I. Review on Ion Mobility Spectrometry. Part 1: Current Instrumentation. *Analyst* **2015**, *140* (5), 1376–1390. https://doi.org/10.1039/c4an01100g.

(34) Cumeras, R.; Figueras, E.; Davis, C. E.; Baumbach, J. I.; Gràcia, I. Review on Ion Mobility Spectrometry. Part 2: Hyphenated Methods and Effects of Experimental Parameters. *Analyst* **2015**, *140* (5), 1391–1410. https://doi.org/10.1039/c4an01101e.

(35) Gabelica, V.; Shvartsburg, A. A.; Afonso, C.; Barran, P.; Benesch, J. L. P.; Bleiholder, C.; Bowers, M. T.; Bilbao, A.; Bush, M. F.; Campbell, J. L.; Campuzano, I. D. G.; Causon, T.; Clowers, B. H.; Creaser, C. S.; De Pauw, E.; Far, J.; Fernandez-Lima, F.; Fjeldsted, J. C.; Giles, K.; Groessl, M.; Hogan, C. J.; Hann, S.; Kim, H. I.; Kurulugama, R. T.; May, J. C.; McLean, J. A.; Pagel, K.; Richardson, K.; Ridgeway, M. E.; Rosu, F.; Sobott, F.; Thalassinos, K.; Valentine, S. J.; Wyttenbach, T. Recommendations for Reporting Ion Mobility Mass Spectrometry Measurements. *Mass Spectrom Rev* **2019**, *38* (3), 291–320. https://doi.org/10.1002/mas.21585.

(36) Mason, E. A.; McDaniel, E. W. *Transport Properties of Ions in Gases*; John Wiley and Sons: New York, 1988.

(37) Revercomb, H. E.; Mason, E. A. Theory of Plasma Chromatography/Gaseous Electrophoresis. A Review. *Anal Chem* **1975**, *47* (7), 970–983. https://doi.org/10.1021/ac60357a043.

(38) Larriba-Andaluz, C.; Prell, J. S. Fundamentals of Ion Mobility in the Free Molecular Regime. Interlacing the Past, Present and Future of Ion Mobility Calculations. *Int Rev Phys Chem* **2020**, *39* (4), 569–623. https://doi.org/10.1080/0144235X.2020.1826708.

(39) Schneider, B. B.; Nazarov, E. G.; Londry, F.; Vouros, P.; Covey, T. R. Differential Mobility Spectrometry/Mass Spectrometry History, Theory, Design Optimization, Simulations, and Applications. *Mass Spectrom Rev* **2016**, *35* (6), 687–737. https://doi.org/10.1002/mas.21453.

(40) Kolakowski, B. M.; Mester, Z. Review of Applications of High-Field Asymmetric Waveform Ion Mobility Spectrometry (FAIMS) and Differential Mobility Spectrometry (DMS). *Analyst* **2007**, *132* (9), 842–864. https://doi.org/10.1039/b706039d.

(41) Krylov, E. V.; Nazarov, E. G.; Miller, R. A. Differential Mobility Spectrometer: Model of Operation. *Int J Mass Spectrom* **2007**, *266* (1–3), 76–85. https://doi.org/10.1016/j.ijms.2007.07.003.

(42) Schneider, B. B.; Covey, T. R.; Coy, S. L.; Krylov, E. V.; Nazarov, E. G. Planar Differential Mobility Spectrometer as a Pre-Filter for Atmospheric Pressure Ionization Mass Spectrometry. *Int J Mass Spectrom* **2010**, *298* (1–3), 45–54. https://doi.org/10.1016/j.ijms.2010.01.006.

(43) Jin, W.; Jarvis, M.; Star-Weinstock, M.; Altemus, M. A Sensitive and Selective LC-Differential Mobility-Mass Spectrometric Analysis of Allopregnanolone and Pregnanolone in Human Plasma. *Anal Bioanal Chem* **2013**, *405* (29), 9497–9508. https://doi.org/10.1007/s00216-013-7391-2.

(44) Shvartsburg, A. A.; Creese, A. J.; Smith, R. D.; Cooper, H. J. Separation of Peptide Isomers with Variant Modified Sites by High-Resolution Differential Ion Mobility Spectrometry. *Anal Chem* **2010**, *82* (19), 8327–8334. https://doi.org/10.1021/ac101878a.

(45) Šala, M.; Lísa, M.; Campbell, J. L.; Holčapek, M. Determination of Triacylglycerol Regioisomers Using Differential Mobility Spectrometry. *Rapid Communications in Mass Spectrometry* **2016**, *30* (2), 256–264. https://doi.org/10.1002/rcm.7430.

(46) Anwar, A.; Psutka, J.; Walker, S. W. C.; Dieckmann, T.; Janizewski, J. S.; Larry Campbell, J.; Scott Hopkins, W. Separating and Probing Tautomers of Protonated Nucleobases Using Differential Mobility Spectrometry. *Int J Mass Spectrom* **2018**, *429*, 174–181. https://doi.org/10.1016/j.ijms.2017.08.008.

(47) Liu, C.; Gómez-Ríos, G. A.; Schneider, B. B.; le Blanc, J. C. Y.; Reyes-Garcés, N.; Arnold, D. W.; Covey, T. R.; Pawliszyn, J. Fast Quantitation of Opioid Isomers in Human Plasma by Differential Mobility Spectrometry/Mass Spectrometry via SPME/Open-Port Probe

Sampling Interface. *Anal Chim Acta* **2017**, *991*, 89–94. https://doi.org/10.1016/j.aca.2017.08.023.

(48) Cohen, A.; Ross, N. W.; Smith, P. M.; Fawcett, J. P. Analysis of 17β-Estradiol, Estriol and Estrone in American Eel (Anguilla Rostrata) Tissue Samples Using Liquid Chromatography Coupled to Electrospray Differential Ion Mobility Tandem Mass Spectrometry. *Rapid Communications in Mass Spectrometry* **2017**, *31* (10), 842–850. https://doi.org/10.1002/rcm.7853.

(49) Maccarone, A. T.; Duldig, J.; Mitchell, T. W.; Blanksby, S. J.; Duchoslav, E.; Campbell, J. L. Characterization of Acyl Chain Position in Unsaturated Phosphatidylcholines Using Differential Mobility-Mass Spectrometry. *J Lipid Res* **2014**, *55* (8), 1668–1677. https://doi.org/10.1194/jlr.M046995.

(50) Campbell, J. L.; Le Blanc, J. C. Y.; Schneider, B. B. Probing Electrospray Ionization Dynamics Using Differential Mobility Spectrometry: The Curious Case of 4-Aminobenzoic Acid. *Anal Chem* **2012**, *84* (18), 7857–7864. https://doi.org/10.1021/ac301529w.

(51) Liu, C.; Yves Le Blanc, J. C.; Schneider, B. B.; Shields, J.; Federico, J. J.; Zhang, H.; Stroh, J. G.; Kauffman, G. W.; Kung, D. W.; Ieritano, C.; Shepherdson, E.; Verbuyst, M.; Melo, L.; Hasan, M.; Naser, D.; Janiszewski, J. S.; Hopkins, W. S.; Campbell, J. L. Assessing Physicochemical Properties of Drug Molecules via Microsolvation Measurements with Differential Mobility Spectrometry. *ACS Cent Sci* **2017**, *3* (2), 101–109. https://doi.org/10.1021/acscentsci.6b00297.

(52) Liu, C.; le Blanc, J. C. Y.; Shields, J.; Janiszewski, J. S.; Ieritano, C.; Ye, G. F.; Hawes, G. F.; Hopkins, W. S.; Campbell, J. L. Using Differential Mobility Spectrometry to Measure Ion Solvation: An Examination of the Roles of Solvents and Ionic Structures in Separating Quinoline-Based Drugs. *Analyst* **2015**, *140* (20), 6897–6903. https://doi.org/10.1039/c5an00842e.

(53) Guevremont, R.; Purves, R. W.; Guevremont, R.; Purves, R. W. Atmospheric Pressure Ion Focusing in a High-Field Asymmetric Waveform Ion Mobility Spectrometer. *Review of Scientific Instruments* **1999**, *70* (2), 1370–1383. https://doi.org/10.1063/1.1149599.

(54) Isenberg, S. L.; Armistead, P. M.; Glish, G. L. Optimization of Peptide Separations by Differential Ion Mobility Spectrometry. *J Am Soc Mass Spectrom* **2014**, *25* (9), 1592–1599. https://doi.org/10.1007/s13361-014-0941-9.

(55) Kanu, A. B.; Dwivedi, P.; Tam, M.; Matz, L.; Hill Jr., H. H. Ion Mobility–Mass Spectrometry. *J Mass Spectrom* **2008**, *43* (7), 1–22. https://doi.org/10.1002/jms.

(56) Lanucara, F.; Holman, S. W.; Gray, C. J.; Eyers, C. E. The Power of Ion Mobility-Mass Spectrometry for Structural Characterization and the Study of Conformational Dynamics. *Nat Chem* **2014**, *6* (4), 281–294. https://doi.org/10.1038/nchem.1889.

(57) Larriba-Andaluz, C.; Carbone, F. The Size-Mobility Relationship of Ions, Aerosols, and Other Charged Particle Matter. *J Aerosol Sci* **2021**, *151*, 105659. https://doi.org/10.1016/j.jaerosci.2020.105659.

(58) Shvartsburg, A. A. *Differential Ion Mobility Spectrometry: Nonlinear Ion Transport and Fundamentals of FAIMS*; CRC Press: Boca Raton, 2008. https://doi.org/10.1201/9781420051070.

(59) Rees, J. A. *Transport Properties of Ions in Electro-Negative Gases*; John Wiley and Sons: New York, 1974; Vol. 24. https://doi.org/10.1016/0042-207X(74)90043-8.

(60) Shvartsburg, A. A.; Smith, R. D. Fundamentals of Traveling Wave Ion Mobility Spectrometry. *Anal Chem* **2008**, *80* (24), 9689–9699. https://doi.org/10.1021/ac8016295.

(61) Alberty, R. J. *Physical Chemistry*, 2nd ed.; Wiley: New York, 1996.

(62) Purves, R. W.; Guevremont, R. Electrospray Ionization High-Field Asymmetric Waveform Ion Mobility Spectrometry-Mass Spectrometry. *Anal Chem* **1999**, *71* (13), 2346–2357. https://doi.org/10.1021/ac981380y.

(63) Campbell, J. L.; Zhu, M.; Hopkins, W. S. Ion-Molecule Clustering in Differential Mobility Spectrometry: Lessons Learned from Tetraalkylammonium Cations and Their Isomers. *J Am Soc Mass Spectrom* **2014**, *25* (9), 1583–1591. https://doi.org/10.1007/s13361-014-0939-3.

(64) Haack, A.; Bissonnette, J. R.; Ieritano, C.; Hopkins, W. S. Improved First-Principles Model of Differential Mobility Using Higher Order Two-Temperature Theory. *J Am Soc Mass Spectrom* **2022**, *33* (3), 535–547. https://doi.org/10.1021/jasms.1c00354.

(65) Wales, D. J.; Doye, J. P. K. Global Optimization by Basin-Hopping and the Lowest Energy Structures of Lennard-Jones Clusters Containing up to 110 Atoms. *Journal of Physical Chemistry A* **1997**, *101* (28), 5111–5116. https://doi.org/10.1021/jp970984n.

(66) Hopkins, W. S.; Marta, R. A.; McMahon, T. B. Proton-Bound 3-Cyanophenylalanine Trimethylamine Clusters: Isomer-Specific Fragmentation Pathways and Evidence of Gas phase Zwitterions. *Journal of Physical Chemistry A* **2013**, *117* (41), 10714–10718. https://doi.org/10.1021/jp407766j.

(67) Hopkins, W. S.; Marta, R. A.; Steinmetz, V.; McMahon, T. B. Mode-Specific Fragmentation of Amino Acid-Containing Clusters. *Physical Chemistry Chemical Physics* **2015**, *17* (43), 28548–28555. https://doi.org/10.1039/c5cp03517a.

(68) Ieritano, C.; Rickert, D.; Featherstone, J.; Honek, J. F.; Campbell, J. L.; Blanc, J. C. Y. le; Schneider, B. B.; Hopkins, W. S. The Charge-State and Structural Stability of Peptides Conferred by Microsolvating Environments in Differential Mobility Spectrometry. *J Am Soc Mass Spectrom* **2021**, *32* (4), 956–968. https://doi.org/10.1021/jasms.0c00469.

(69) Wang, J.; Wolf, R. M.; Caldwell, J. W.; Kollman, P. A.; Case, D. A. Development and Testing of a General Amber Force Field. *J Comput Chem* **2004**, *25* (9), 1157–1174. https://doi.org/10.1002/jcc.20035.

(70) Rappé, A. K.; Casewit, C. J.; Colwell, K. S.; Goddard, W. A.; Skiff, W. M. UFF, a Full Periodic Table Force Field for Molecular Mechanics and Molecular Dynamics Simulations. *J Am Chem Soc* **1992**, *114* (25), 10024–10035. https://doi.org/10.1021/ja00051a040.

(71) Halgren, T. A. Merck Molecular Force Field. II. MMFF94 van Der Waals and Electrostatic Parameters for Intermolecular Interactions. *J Comput Chem* **1996**, *17* (5–6), 520–552. https://doi.org/10.1002/(SICI)1096-987X(199604)17:5/6<520::AID-JCC2>3.0.CO;2-W.

(72) Zhou, C.; Ieritano, C.; Hopkins, W. S. Augmenting Basin-Hopping With Techniques From Unsupervised Machine Learning: Applications in Spectroscopy and Ion Mobility. *Front Chem* **2019**, *7*, 519. https://doi.org/10.3389/fchem.2019.00519.

(73) Porezag, D.; Frauenheim, T.; Köhler, T.; Seifert, G.; Kaschner, R. Construction of Tight-Binding-like Potentials on the Basis of Density-Functional Theory: Application to Carbon. *Phys Rev B* **1995**, *51* (19), 12947–12957. https://doi.org/10.1103/PhysRevB.51.12947.

(74) Elstner, M.; Porezag, D.; Jungnickel, G.; Elsner, J.; Haugk, M.; Frauenheim, Th.; Suhai, S.; Seifert, G. Self-Consistent-Charge Density-Functional Tight-Binding Method for Simulations of Complex Materials Properties. *Phys Rev B* **1998**, *58* (11), 7260–7268. https://doi.org/10.1103/PhysRevB.58.7260.

(75) Throssel, K.; Frisch, M. J. Evaluation and Improvement of Semi-Empirical Methods I: PM7R8: A Variant of PM7 with Numerically Stable Hydrogen Bonding Corrections. *in prep.*

(76) Roothaan, C. C. J. New Developments in Molecular Orbital Theory. *Rev Mod Phys* **1951**, *23* (2), 69–89. https://doi.org/10.1103/RevModPhys.23.69.

(77) Haack, A.; Crouse, J.; Schlüter, F. J.; Benter, T.; Hopkins, W. S. A First Principle Model of Differential Ion Mobility: The Effect of Ion-Solvent Clustering. *J Am Soc Mass Spectrom* **2019**, *30* (12), 2711–2725. https://doi.org/10.1007/s13361-019-02340-1.

(78) Crouse, J.; Haack, A.; Benter, T.; Hopkins, W. S. Understanding Nontraditional Differential Mobility Behavior: A Case Study of the Tricarbastannatrane Cation, N(CH2CH2CH2)3Sn. *J Am Soc Mass Spectrom* **2020**, *31* (4), 796–802. https://doi.org/10.1021/jasms.9b00042.

(79) Klimeš, J.; Michaelides, A. Perspective: Advances and Challenges in Treating van Der Waals Dispersion Forces in Density Functional Theory. *Journal of Chemical Physics* **2013**, *137* (12), 1–15. https://doi.org/10.1063/1.4754130.

(80) Riley, K. E.; Piton, M. Stabilization and Structure Calculations for Noncovalent Interactions in Extended Molecular Systems Based on Wave Function and Density Functional Theories. *Chem. Rev.* **2010**, *110*, 5023–5063. https://doi.org/10.1021/cr1000173.

(81) Grimme, S. Supramolecular Binding Thermodynamics by Dispersion-Corrected Density Functional Theory. *Chemistry A European Journal* **2012**, *18* (32), 9955–9964. https://doi.org/10.1002/chem.201200497.

(82) Goerigk, L.; Grimme, S. A Thorough Benchmark of Density Functional Methods for General Main Group Thermochemistry, Kinetics, and Noncovalent Interactions. *Physical Chemistry Chemical Physics* **2011**, *13* (14), 6670–6688. https://doi.org/10.1039/c0cp02984j.

(83) Mardirossian, N.; Head-Gordon, M. Thirty Years of Density Functional Theory in Computational Chemistry: An Overview and Extensive Assessment of 200 Density Functionals. *Mol Phys* **2017**, *115* (19), 2315–2372. https://doi.org/10.1080/00268976.2017.1333644.

(84) Jordan, M. J. T.; Del Bene, J. E. Unraveling Environmental Effects on Hydrogen-Bonded Complexes: Matrix Effects on the Structures and Proton-Stretching Frequencies of Hydrogen-

Halide Complexes with Ammonia and Trimethylamine. *J Am Chem Soc* **2000**, *122* (9), 2101–2115. https://doi.org/10.1021/ja993981s.

(85) Bende, A.; Muntean, C. M. The Influence of Anharmonic and Solvent Effects on the Theoretical Vibrational Spectra of the Guanine-Cytosine Base Pairs in Watson-Crick and Hoogsteen Configurations. *J Mol Model* **2014**, *20* (3), 1–12. https://doi.org/10.1007/s00894-014-2113-z.

(86) Ieritano, C.; Featherstone, J.; Carr, P. J. J.; Marta, R. A.; Loire, E.; McMahon, T. B.; Hopkins, W. S. The Structures and Properties of Anionic Tryptophan Complexes. *Physical Chemistry Chemical Physics* **2018**, *20* (41), 26532–26541. https://doi.org/10.1039/c8cp04533j.

(87) Neese, F. The ORCA Program System. *WIREs Computational Molecular Science* **2012**, *2* (1), 73–78. https://doi.org/10.1002/wcms.81.

(88) Liakos, D. G.; Sparta, M.; Kesharwani, M. K.; Martin, J. M. L.; Neese, F. Exploring the Accuracy Limits of Local Pair Natural Orbital Coupled-Cluster Theory. *J Chem Theory Comput* **2015**, *11* (4), 1525–1539. https://doi.org/10.1021/ct501129s.

(89) Liakos, D. G.; Guo, Y.; Neese, F. Comprehensive Benchmark Results for the Domain Based Local Pair Natural Orbital Coupled Cluster Method (DLPNO-CCSD(T)) for Closed- And Open-Shell Systems. *Journal of Physical Chemistry A* **2020**, *124* (1), 90–100. https://doi.org/10.1021/acs.jpca.9b05734.

(90) Neese, F. Software Update: The ORCA Program System—Version 5.0. *WIREs Computational Molecular Science* **2022**, *12* (5), e1606. https://doi.org/10.1002/WCMS.1606.

(91) Riplinger, C.; Sandhoefer, B.; Hansen, A.; Neese, F. Natural Triple Excitations in Local Coupled Cluster Calculations with Pair Natural Orbitals. *Journal of Chemical Physics* **2013**, *139* (13), 134101. https://doi.org/10.1063/1.4821834.

(92) Riplinger, C.; Neese, F. An Efficient and near Linear Scaling Pair Natural Orbital Based Local Coupled Cluster Method. *Journal of Chemical Physics* **2013**, *138* (3), 34106. https://doi.org/10.1063/1.4773581.

(93) Riplinger, C.; Pinski, P.; Becker, U.; Valeev, E. F.; Neese, F. Sparse Maps - A Systematic Infrastructure for Reduced-Scaling Electronic Structure Methods. II. Linear Scaling Domain Based Pair Natural Orbital Coupled Cluster Theory. *Journal of Chemical Physics* **2016**, *144* (2), 24109. https://doi.org/10.1063/1.4939030.

(94) Hopkins, W. S. Determining the Properties of Gas phase Clusters. *Mol Phys* **2015**, *113* (21), 3151–3158. https://doi.org/10.1080/00268976.2015.1053545.

(95) Ieritano, C.; Lee, A.; Crouse, J.; Bowman, Z.; Mashmoushi, N.; Crossley, P. M.; Friebe, B. P.; Campbell, J. L.; Hopkins, W. S. Determining Collision Cross Sections from Differential Ion Mobility Spectrometry. *Anal Chem* **2021**, *93* (25), 8937–8944. https://doi.org/10.1021/acs.analchem.1c01420.

(96) Walker, S. W. C.; Anwar, A.; Psutka, J. M.; Crouse, J.; Liu, C.; le Blanc, J. C. Y.; Montgomery, J.; Goetz, G. H.; Janiszewski, J. S.; Campbell, J. L.; Hopkins, W. S. Determining Molecular Properties with Differential Mobility Spectrometry and Machine Learning. *Nat Commun* **2018**, *9* (1), 5096. https://doi.org/10.1038/s41467-018-07616-w.

(97) Di, L.; Whitney-Pickett, C.; Umland, J. P.; Zhang, H.; Zhang, X.; Gebhard, D. F.; Lai, Y.; Federico, J. J.; Davidson, R. E.; Smith, R.; Reyner, E. L.; Lee, C.; Feng, B.; Rotter, C.; Varma, M. v.; Kempshall, S.; Fenner, K.; El-kattan, A. F.; Liston, T. E.; Troutman, M. D. Development of a New Permeability Assay Using Low-efflux MDCKII Cells. *J Pharm Sci* **2011**, *100* (11), 4974–4985. https://doi.org/10.1002/JPS.22674.

(98) Navia, M. A.; Chaturvedi, P. R. Design Principles for Orally Bioavailable Drugs. *Drug Discov Today* **1996**, *1* (5), 179–189. https://doi.org/10.1016/1359-6446(96)10020-9.

(99) Chaturvedi, P. R.; Decker, C. J.; Odinecs, A. Prediction of Pharmacokinetic Properties Using Experimental Approaches during Early Drug Discovery. *Curr Opin Chem Biol* **2001**, *5* (4), 452–463. https://doi.org/10.1016/S1367-5931(00)00228-3.

(100) Zheng, X.; Aly, N. A.; Zhou, Y.; Dupuis, K. T.; Bilbao, A.; Paurus, V. L.; Orton, D. J.; Wilson, R.; Payne, S. H.; Smith, R. D.; Baker, E. S. A Structural Examination and Collision Cross Section Database for over 500 Metabolites and Xenobiotics Using Drift Tube Ion Mobility Spectrometry. *Chem Sci* **2017**, *8* (11), 7724–7736. https://doi.org/10.1039/c7sc03464d.

(101) Zhou, Z.; Tu, J.; Xiong, X.; Shen, X.; Zhu, Z. J. LipidCCS: Prediction of Collision Cross-Section Values for Lipids with High Precision to Support Ion Mobility-Mass Spectrometry-Based Lipidomics. *Anal Chem* **2017**, *89* (17), 9559–9566. https://doi.org/10.1021/acs.analchem.7b02625.

(102) Zhou, Z.; Shen, X.; Tu, J.; Zhu, Z. J. Large-Scale Prediction of Collision Cross-Section Values for Metabolites in Ion Mobility-Mass Spectrometry. *Anal Chem* **2016**, *88* (22), 11084–11091. https://doi.org/10.1021/acs.analchem.6b03091.

(103) Shah, A. R.; Agarwal, K.; Baker, E. S.; Singhal, M.; Mayampurath, A. M.; Ibrahim, Y. M.; Kangas, L. J.; Monroe, M. E.; Zhao, R.; Belov, M. E.; Anderson, G. A.; Smith, R. D. Machine Learning Based Prediction for Peptide Drift Times in Ion Mobility Spectrometry. *Bioinformatics* **2010**, *26* (13), 1601–1607. https://doi.org/10.1093/bioinformatics/btq245.

(104) Picache, J. A.; Rose, B. S.; Balinski, A.; Leaptrot, K. L.; Sherrod, S. D.; May, J. C.; McLean, J. A. Collision Cross Section Compendium to Annotate and Predict Multi-Omic Compound Identities. *Chem Sci* **2019**, *10* (4), 983–993. https://doi.org/10.1039/c8sc04396e.

(105) May, J. C.; Morris, C. B.; McLean, J. A. Ion Mobility Collision Cross Section Compendium. *Anal Chem* **2017**, *89* (2), 1032–1044. https://doi.org/10.1021/acs.analchem.6b04905.

(106) Hines, K. M.; Ross, D. H.; Davidson, K. L.; Bush, M. F.; Xu, L. Large-Scale Structural Characterization of Drug and Drug-Like Compounds by High-Throughput Ion Mobility-Mass Spectrometry. *Anal Chem* **2017**, *89* (17), 9023–9030. https://doi.org/10.1021/acs.analchem.7b01709.

(107) Paglia, G.; Williams, J. P.; Menikarachchi, L.; Thompson, J. W.; Tyldesley-Worster, R.; Halldórsson, S.; Rolfsson, O.; Moseley, A.; Grant, D.; Langridge, J.; Palsson, B. O.; Astarita, G. Ion Mobility Derived Collision Cross Sections to Support Metabolomics Applications. *Anal Chem* **2014**, *86* (8), 3985–3993. https://doi.org/10.1021/ac500405x.

(108) Ewing, S. A.; Donor, M. T.; Wilson, J. W.; Prell, J. S. Collidoscope: An Improved Tool for Computing Collisional Cross-Sections with the Trajectory Method. *J Am Soc Mass Spectrom* **2017**, *28* (4), 587–596. https://doi.org/10.1007/s13361-017-1594-2.

(109) Wu, T.; Derrick, J.; Nahin, M.; Chen, X.; Larriba-Andaluz, C. Optimization of Long Range Potential Interaction Parameters in Ion Mobility Spectrometry. *Journal of Chemical Physics* **2018**, *148* (7), 074102. https://doi.org/10.1063/1.5016170.

(110) Ieritano, C.; Crouse, J.; Campbell, J. L.; Hopkins, W. S. A Parallelized Molecular Collision Cross Section Package with Optimized Accuracy and Efficiency. *Analyst* **2019**, *144* (5), 1660–1670. https://doi.org/10.1039/c8an02150c.

(111) Regueiro, J.; Negreira, N.; Berntssen, M. H. G. Ion-Mobility-Derived Collision Cross Section as an Additional Identification Point for Multiresidue Screening of Pesticides in Fish Feed. *Anal Chem* **2016**, *88* (22), 11169–11177. https://doi.org/10.1021/acs.analchem.6b03381.

(112) Bowman, Z. A. Determining Molecular Physicochemical Properties Using Differential Mobility Spectrometry, University of Waterloo, 2019. https://doi.org/http://hdl.handle.net/10012/15173.

(113) Stow, S. M.; Causon, T. J.; Zheng, X.; Kurulugama, R. T.; Mairinger, T.; May, J. C.; Rennie, E. E.; Baker, E. S.; Smith, R. D.; McLean, J. A.; Hann, S.; Fjeldsted, J. C. An Interlaboratory

Evaluation of Drift Tube Ion Mobility-Mass Spectrometry Collision Cross Section Measurements. *Anal Chem* **2017**, *89* (17), 9048–9055. https://doi.org/10.1021/acs.analchem.7b01729.

(114) Hinnenkamp, V.; Klein, J.; Meckelmann, S. W.; Balsaa, P.; Schmidt, T. C.; Schmitz, O. J. Comparison of CCS Values Determined by Traveling Wave Ion Mobility Mass Spectrometry and Drift Tube Ion Mobility Mass Spectrometry. *Anal Chem* **2018**, *90* (20), 12042–12050. https://doi.org/10.1021/acs.analchem.8b02711.

(115) Ieritano, C.; Hopkins, W. S. Assessing Collision Cross Section Calculations Using MobCal-MPI with a Variety of Commonly Used Computational Methods. *Mater Today Commun* **2021**, *27*, 102226. https://doi.org/10.1016/j.mtcomm.2021.102226.

(116) Ieritano, C.; Featherstone, J.; Haack, A.; Guna, M.; Campbell, J. L.; Hopkins, W. S. How Hot Are Your Ions in Differential Mobility Spectrometry? *J Am Soc Mass Spectrom* **2020**, *31* (3), 582–593. https://doi.org/10.1021/jasms.9b00043.

(117) Frisch, M. J.; Trucks, G. W.; Schlegel, H. B.; Scuseria, G. E.; Robb, M. A.; Cheeseman, J. R.; Scalmani, G.; V. Barone, B.; Mennucci, G.; Petersson, A. Gaussian 09. Gaussian Incorporated: Wallingford, CT 2009.

(118) Wales, D. *Energy Landscapes*; Cambridge University Press, 2004. https://doi.org/10.1017/cbo9780511721724.

(119) Becke, A. D. Density-Functional Exchange-Energy Approximation with Correct Asymptotic Behavior. *Phys Rev A (Coll Park)* **1988**, *38* (6), 3098–3100. https://doi.org/10.1103/PhysRevA.38.3098.

(120) Lee, C.; Yang, W.; Parr, R. G. Development of the Colle-Salvetti Correlation-Energy Formula into a Functional of the Electron Density. *Phys Rev B* **1988**, *37* (2), 785–789. https://doi.org/10.1103/PhysRevB.37.785.

(121) Besler, B. H.; Merz, K. M.; Kollman, P. A. Atomic Charges Derived from Semiempirical Methods. *J Comput Chem* **1990**, *11* (4), 431–439. https://doi.org/10.1002/jcc.540110404.

(122) Singh, U. C.; Kollman, P. A. An Approach to Computing Electrostatic Charges for Molecules. *J Comput Chem* **1984**, *5* (2), 129–145. https://doi.org/10.1002/jcc.540050204.

(123) Stewart, J. J. P. Optimization of Parameters for Semiempirical Methods VI: More Modifications to the NDDO Approximations and Re-Optimization of Parameters. *J Mol Model* **2013**, *19* (1), 1–32. https://doi.org/10.1007/s00894-012-1667-x.

(124) Levin, D. S.; Miller, R. A.; Nazarov, E. G.; Vouros, P. Rapid Separation and Quantitative Analysis of Peptides Using a New Nanoelectrospray-Differential Mobility Spectrometer-Mass Spectrometer System. *Anal Chem* **2006**, *78* (15), 5443–5452. https://doi.org/10.1021/ac060003f.

(125) Breiman, L. Random Forests. *Mach Learn* **2001**, *45* (1), 5–32. https://doi.org/10.1023/A:1010933404324.

(126) Quinlan, J. R. Induction of Decision Trees. *Mach Learn* **1986**, *1* (1), 81–106. https://doi.org/10.1007/bf00116251.

(127) Paglia, G.; Astarita, G. Metabolomics and Lipidomics Using Traveling-Wave Ion Mobility Mass Spectrometry. *Nat Protoc* **2017**, *12* (4), 797–813. https://doi.org/10.1038/nprot.2017.013.

(128) Paglia, G.; Angel, P.; Williams, J. P.; Richardson, K.; Olivos, H. J.; Thompson, J. W.; Menikarachchi, L.; Lai, S.; Walsh, C.; Moseley, A.; Plumb, R. S.; Grant, D. F.; Palsson, B. O.; Langridge, J.; Geromanos, S.; Astarita, G. Ion Mobility-Derived Collision Cross Section as an Additional Measure for Lipid Fingerprinting and Identification. *Anal Chem* **2015**, *87* (2), 1137–1144. https://doi.org/10.1021/ac503715v.

(129) Stienstra, C. M. K.; Ieritano, C.; Haack, A.; Hopkins, W. S. Bridging the Gap between Differential Mobility, Log S , and Log P Using Machine Learning and SHAP Analysis . *Anal Chem* **2023**, *95*, 10309–10321. https://doi.org/10.1021/acs.analchem.3c00921.

(130) Mansouri, K.; Grulke, C. M.; Judson, R. S.; Williams, A. J. OPERA Models for Predicting Physicochemical Properties and Environmental Fate Endpoints. *J Cheminform* **2018**, *10* (1), 1–19. https://doi.org/10.1186/s13321-018-0263-1.

(131) Chouinard, C. D.; Beekman, C. R.; Kemperman, R. H. J.; King, H. M.; Yost, R. A. Ion Mobility-Mass Spectrometry Separation of Steroid Structural Isomers and Epimers. *International Journal for Ion Mobility Spectrometry* **2017**, *20* (1–2), 31–39. https://doi.org/10.1007/s12127-016-0213-4.

(132) Harris, R. A.; May, J. C.; Stinson, C. A.; Xia, Y.; McLean, J. A. Determining Double Bond Position in Lipids Using Online Ozonolysis Coupled to Liquid Chromatography and Ion Mobility-Mass Spectrometry. *Anal Chem* **2018**, *90* (3), 1915–1924. https://doi.org/10.1021/acs.analchem.7b04007.

(133) Shliaha, P. V.; Gorshkov, V.; Kovalchuk, S. I.; Schwämmle, V.; Baird, M. A.; Shvartsburg, A. A.; Jensen, O. N. Middle-Down Proteomic Analyses with Ion Mobility Separations of Endogenous Isomeric Proteoforms. *Anal Chem* **2020**, *92* (3), 2364–2368. https://doi.org/10.1021/acs.analchem.9b05011.

(134) Chen, T. C.; Ibrahim, Y. M.; Webb, I. K.; Garimella, S. V. B.; Zhang, X.; Hamid, A. M.; Deng, L.; Karnesky, W. E.; Prost, S. A.; Sandoval, J. A.; Norheim, R. V.; Anderson, G. A.; Tolmachev, A. V.; Baker, E. S.; Smith, R. D. Mobility-Selected Ion Trapping and Enrichment Using Structures for Lossless Ion Manipulations. *Anal Chem* **2016**, *88* (3), 1728–1733. https://doi.org/10.1021/acs.analchem.5b03910.

(135) Dwivedi, P.; Bendiak, B.; Clowers, B. H.; Hill, H. H. Rapid Resolution of Carbohydrate Isomers by Electrospray Ionization Ambient Pressure Ion Mobility Spectrometry-Time-of-

Flight Mass Spectrometry (ESI-APIMS-TOFMS). *J Am Soc Mass Spectrom* **2007**, *18* (7), 1163–1175. https://doi.org/10.1016/j.jasms.2007.04.007.

(136) Poltash, M. L.; McCabe, J. W.; Shirzadeh, M.; Laganowsky, A.; Russell, D. H. Native IM-Orbitrap MS: Resolving What Was Hidden. *TrAC - Trends in Analytical Chemistry* **2020**, *124*, 115533. https://doi.org/10.1016/j.trac.2019.05.035.

(137) Lyu, J.; Liu, Y.; McCabe, J. W.; Schrecke, S.; Fang, L.; Russell, D. H.; Laganowsky, A.; Laganowsky, A. Discovery of Potent Charge-Reducing Molecules for Native Ion Mobility Mass Spectrometry Studies. *Anal Chem* **2020**, *92* (16), 11242–11249. https://doi.org/10.1021/acs.analchem.0c01826.

(138) Gabelica, V.; Livet, S.; Rosu, F. Optimizing Native Ion Mobility Q-TOF in Helium and Nitrogen for Very Fragile Noncovalent Structures. *J Am Soc Mass Spectrom* **2018**, *29* (11), 2189–2198. https://doi.org/10.1007/s13361-018-2029-4.

(139) Liu, F. C.; Kirk, S. R.; Bleiholder, C. On the Structural Denaturation of Biological Analytes in Trapped Ion Mobility Spectrometry-Mass Spectrometry. *Analyst* **2016**, *141* (12), 3722–3730. https://doi.org/10.1039/c5an02399h.

(140) Harrison, J. A.; Kelso, C.; Pukala, T. L.; Beck, J. L. Conditions for Analysis of Native Protein Structures Using Uniform Field Drift Tube Ion Mobility Mass Spectrometry and Characterization of Stable Calibrants for TWIM-MS. *J Am Soc Mass Spectrom* **2019**, *30* (2), 256–267. https://doi.org/10.1007/s13361-018-2074-z.

(141) Allen, S. J.; Eaton, R. M.; Bush, M. F. Structural Dynamics of Native-Like Ions in the Gas Phase: Results from Tandem Ion Mobility of Cytochrome c. *Anal Chem* **2017**, *89* (14), 7527–7534. https://doi.org/10.1021/acs.analchem.7b01234.

(142) Allen, S. J.; Eaton, R. M.; Bush, M. F. Analysis of Native-Like Ions Using Structures for Lossless Ion Manipulations. *Anal Chem* **2016**, *88* (18), 9118–9126. https://doi.org/10.1021/acs.analchem.6b02089.

(143) Morsa, D.; Gabelica, V.; De Pauw, E. Fragmentation and Isomerization Due to Field Heating in Traveling Wave Ion Mobility Spectrometry. *J Am Soc Mass Spectrom* **2014**, *25* (8), 1384–1393. https://doi.org/10.1007/s13361-014-0909-9.

(144) Merenbloom, S. I.; Flick, T. G.; Williams, E. R. How Hot Are Your Ions in TWAVE Ion Mobility Spectrometry? *J Am Soc Mass Spectrom* **2012**, *23* (3), 553–562. https://doi.org/10.1007/s13361-011-0313-7.

(145) An, X.; Eiceman, G. A.; Stone, J. A. A Determination of the Effective Temperatures for the Dissociation of the Proton Bound Dimer of Dimethyl Methylphosphonate in a Planar Differential Mobility Spectrometer. *International Journal for Ion Mobility Spectrometry* **2010**, *13* (1), 25–36. https://doi.org/10.1007/s12127-010-0037-6.

(146) An, X.; Eiceman, G. A.; Räsänen, R. M.; Rodriguez, J. E.; Stone, J. A. Dissociation of Proton Bound Ketone Dimers in Asymmetric Electric Fields with Differential Mobility Spectrometry and in Uniform Electric Fields with Linear Ion Mobility Spectrometry. *Journal of Physical Chemistry A* **2013**, *117* (30), 6389–6401. https://doi.org/10.1021/jp401640t.

(147) Morsa, D.; Gabelica, V.; De Pauw, E. Effective Temperature of Ions in Traveling Wave Ion Mobility Spectrometry. *Anal Chem* **2011**, *83* (14), 5775–5782. https://doi.org/10.1021/ac201509p.

(148) Smith, D. P.; Knapman, T. W.; Campuzano, L.; Malham, R. W.; Berryman, J. T.; Radford, S. E.; Ashcroft, A. E. Deciphering Drift Time Measurements from Travelling Wave Ion Mobility Spectrometry- Mass Spectrometry Studies. *European Journal of Mass Spectrometry* **2009**, *15* (2), 113–130. https://doi.org/10.1255/ejms.947.

(149) Zhao, Y.; Yang, J. Y.; Thieker, D. F.; Xu, Y.; Zong, C.; Boons, G. J.; Liu, J.; Woods, R. J.; Moremen, K. W.; Amster, I. J. A Traveling Wave Ion Mobility Spectrometry (TWIMS) Study of the Robo1-Heparan Sulfate Interaction. *J Am Soc Mass Spectrom* **2018**, *29* (6), 1153–1165. https://doi.org/10.1007/s13361-018-1903-4.

(150) Hale, O. J.; Sisley, E. K.; Griffiths, R. L.; Styles, I. B.; Cooper, H. J. Native LESA TWIMS-MSI: Spatial, Conformational, and Mass Analysis of Proteins and Protein Complexes. *J Am Soc Mass Spectrom* **2020**, *31* (4), 873–879. https://doi.org/10.1021/jasms.9b00122.

(151) Devine, P. W. A.; Fisher, H. C.; Calabrese, A. N.; Whelan, F.; Higazi, D. R.; Potts, J. R.; Lowe, D. C.; Radford, S. E.; Ashcroft, A. E. Investigating the Structural Compaction of Biomolecules Upon Transition to the Gas phase Using ESI-TWIMS-MS. *J Am Soc Mass Spectrom* **2017**, *28* (9), 1855–1862. https://doi.org/10.1007/s13361-017-1689-9.

(152) Scarff, C. A.; Thalassinos, K.; Hilton, G. R.; Scrivens, J. H. Travelling Wave Ion Mobility Mass Spectrometry Studies of Protein Structure: Biological Significance and Comparison with X-Ray Crystallography and Nuclear Magnetic Resonance Spectroscopy Measurements. *Rapid Communications in Mass Spectrometry* **2008**, *22* (20), 3297–3304. https://doi.org/10.1002/rcm.3737.

(153) Eldrid, C.; Ujma, J.; Kalfas, S.; Tomczyk, N.; Giles, K.; Morris, M.; Thalassinos, K. Gas Phase Stability of Protein Ions in a Cyclic Ion Mobility Spectrometry Traveling Wave Device. *Anal Chem* **2019**, *91* (12), 7554–7561. https://doi.org/10.1021/acs.analchem.8b05641.

(154) Schneider, B. B.; Covey, T. R.; Coy, S. L.; Krylov, E. v.; Nazarov, E. G. Chemical Effects in the Separation Process of a Differential Mobility/Mass Spectrometer System. *Anal Chem* **2010**, *82* (5), 1867–1880. https://doi.org/10.1021/ac902571u.

(155) Coughlan, N. J. A.; Liu, C.; Lecours, M. J.; Campbell, J. L.; Hopkins, W. S. Preferential Ion Microsolvation in Mixed-Modifier Environments Observed Using Differential Mobility Spectrometry. *J Am Soc Mass Spectrom* **2019**, *30* (11), 2222–2227. https://doi.org/10.1007/s13361-019-02332-1.

(156) Ruskic, D.; Hopfgartner, G. Modifier Selectivity Effect on Differential Ion Mobility Resolution of Isomeric Drugs and Multidimensional Liquid Chromatography Ion Mobility Analysis. *Anal Chem* **2019**, *91* (18), 11670–11677. https://doi.org/10.1021/acs.analchem.9b02212.

(157) Campbell, J. L.; Kafle, A.; Bowman, Z.; Blanc, J. C. Y. Le; Liu, C.; Hopkins, W. S. Separating Chiral Isomers of Amphetamine and Methamphetamine Using Chemical Derivatization and Differential Mobility Spectrometry. *Analytical Science Advances* **2020**, *1* (4), 233–244. https://doi.org/10.1002/ansa.202000066.

(158) Marchese, R.; Grandori, R.; Carloni, P.; Raugei, S. A Computational Model for Protein Ionization by Electrospray Based on Gas phase Basicity. *J Am Soc Mass Spectrom* **2012**, *23* (11), 1903–1910. https://doi.org/10.1007/s13361-012-0449-0.

(159) Konermann, L.; Ahadi, E.; Rodriguez, A. D.; Vahidi, S. Unraveling the Mechanism of Electrospray Ionization. *Anal Chem* **2013**, *85* (1), 2–9. https://doi.org/10.1021/ac302789c.

(160) Rolland, A. D.; Prell, J. S. Computational Insights into Compaction of Gas phase Protein and Protein Complex Ions in Native Ion Mobility-Mass Spectrometry. *TrAC - Trends in Analytical Chemistry* **2019**, *116*, 282–291. https://doi.org/10.1016/j.trac.2019.04.023.

(161) Guevremont, R. High-Field Asymmetric Waveform Ion Mobility Spectrometry: A New Tool for Mass Spectrometry. *J Chromatogr A* **2004**, *1058* (1–2), 3–19. https://doi.org/10.1016/j.chroma.2004.08.119.

(162) Cooper, H. J. To What Extent Is FAIMS Beneficial in the Analysis of Proteins? *J Am Soc Mass Spectrom* **2016**, *27* (4), 566–577. https://doi.org/10.1007/s13361-015-1326-4.

(163) Hale, O. J.; Illes-Toth, E.; Mize, T. H.; Cooper, H. J. High-Field Asymmetric Waveform Ion Mobility Spectrometry and Native Mass Spectrometry: Analysis of Intact Protein Assemblies and Protein Complexes. *Anal Chem* **2020**, *92* (10), 6811–6816. https://doi.org/10.1021/acs.analchem.0c00649.

(164) Sisley, E. K.; Illes-Toth, E.; Cooper, H. J. In Situ Analysis of Intact Proteins by Ion Mobility Mass Spectrometry. *TrAC - Trends in Analytical Chemistry* **2020**, *124*, 115534. https://doi.org/10.1016/j.trac.2019.05.036.

(165) Dos Santos Cabrera, M. P.; Costa, S. T. B.; De Souza, B. M.; Palma, M. S.; Ruggiero, J. R.; Ruggiero Neto, J. Selectivity in the Mechanism of Action of Antimicrobial Mastoparan Peptide Polybia-MP1. *European Biophysics Journal* **2008**, *37* (6), 879–891. https://doi.org/10.1007/s00249-008-0299-7.

(166) Chai, J. Da; Head-Gordon, M. Long-Range Corrected Hybrid Density Functionals with Damped Atom-Atom Dispersion Corrections. *Physical Chemistry Chemical Physics* **2008**, *10* (44), 6615–6620. https://doi.org/10.1039/b810189b.

(167) Goddard, T. D.; Huang, C. C.; Meng, E. C.; Pettersen, E. F.; Couch, G. S.; Morris, J. H.; Ferrin, T. E. UCSF ChimeraX: Meeting Modern Challenges in Visualization and Analysis. *Protein Science* **2018**, *27* (1), 14–25. https://doi.org/10.1002/pro.3235.

(168) Maziejuk, M.; Puton, J.; Szyposzyńska, M.; Witkiewicz, Z. Fragmentation of Molecular Ions in Differential Mobility Spectrometry as a Method for Identification of Chemical Warfare Agents. *Talanta* **2015**, *144*, 1201–1206. https://doi.org/10.1016/j.talanta.2015.07.039.

(169) Santiago, B. G.; Campbell, M. T.; Glish, G. L. Variables Affecting the Internal Energy of Peptide Ions During Separation by Differential Ion Mobility Spectrometry. *J Am Soc Mass Spectrom* **2017**, *28* (10), 2160–2169. https://doi.org/10.1007/s13361-017-1726-8.

(170) Bohme, D. K. Proton Transport in the Catalyzed Gas phase Isomerization of Protonated Molecules. *Int J Mass Spectrom Ion Process* **1992**, *115* (2–3), 95–110. https://doi.org/10.1016/0168-1176(92)85035-X.

(171) Blagojevic, V.; Chramow, A.; Schneider, B. B.; Covey, T. R.; Bohme, D. K. Differential Mobility Spectrometry of Isomeric Protonated Dipeptides: Modifier and Field Effects on Ion Mobility and Stability. *Anal Chem* **2011**, *83* (9), 3470–3476. https://doi.org/10.1021/ac200100s.

(172) Creese, A. J.; Shimwell, N. J.; Larkins, K. P. B.; Heath, J. K.; Cooper, H. J. Probing the Complementarity of FAIMS and Strong Cation Exchange Chromatography in Shotgun

Proteomics. *J Am Soc Mass Spectrom* **2013**, *24* (3), 431–443. https://doi.org/10.1007/s13361-012-0544-2.

(173) Rosting, C.; Yu, J.; Cooper, H. J. High Field Asymmetric Waveform Ion Mobility Spectrometry in Nontargeted Bottom-up Proteomics of Dried Blood Spots. *J Proteome Res* **2018**, *17* (6), 1997–2004. https://doi.org/10.1021/acs.jproteome.7b00746.

(174) Zhao, H.; Creese, A. J.; Cooper, H. J. Online LC-FAIMS-MS/MS for the Analysis of Phosphorylation in Proteins. *Methods in Molecular Biology* **2016**, *1355*, 241–250. https://doi.org/10.1007/978-1-4939-3049-4_16.

(175) Fang, P.; Liu, M.; Xue, Y.; Yao, J.; Zhang, Y.; Shen, H.; Yang, P. Controlling Nonspecific Trypsin Cleavages in LC-MS/MS-Based Shotgun Proteomics Using Optimized Experimental Conditions. *Analyst* **2015**, *140* (22), 7613–7621. https://doi.org/10.1039/c5an01505g.

(176) Xu, Y. F.; Lu, W.; Rabinowitz, J. D. Avoiding Misannotation of In-Source Fragmentation Products as Cellular Metabolites in Liquid Chromatography-Mass Spectrometry-Based Metabolomics. *Anal Chem* **2015**, *87* (4), 2273–2281. https://doi.org/10.1021/ac504118y.

(177) Seale, B.; Schneider, B. B.; le Blanc, J. C. Y. Enhancing Signal and Mitigating Up-Front Peptide Fragmentation Using Controlled Clustering by Gas phase Modifiers. *Anal Bioanal Chem* **2019**, *411* (24), 6365–6376. https://doi.org/10.1007/s00216-019-02036-1.

(178) Malloum, A.; Fifen, J. J.; Conradie, J. Solvation Energies of the Proton in Methanol Revisited and Temperature Effects. *Physical Chemistry Chemical Physics* **2018**, *20* (46), 29184–29206. https://doi.org/10.1039/c8cp05823g.

(179) Malloum, A.; Malloum, A.; Fifen, J. J.; Conradie, J. Exploration of the Potential Energy Surfaces of Small Ethanol Clusters. *Physical Chemistry Chemical Physics* **2020**, *22* (23), 13201–13213. https://doi.org/10.1039/d0cp01393e.

(180) Knochenmuss, R.; Cheshnovsky, O.; Leutwyler, S. Proton Transfer Reactions in Neutral Gas phase Clusters: 1-Naphthol with H2O, D2O, CH3OH, NH3 and Piperidine. *Chem Phys Lett* **1988**, *144* (4), 317–323. https://doi.org/10.1016/0009-2614(88)87121-5.

(181) Boyd, S. L.; Boyd, R. J. A Density Functional Study of Methanol Clusters. *J Chem Theory Comput* **2007**, *3* (1), 54–61. https://doi.org/10.1021/ct6002912.

(182) Bagal, D.; Kitova, E. N.; Liu, L.; El-Hawiet, A.; Schnier, P. D.; Klassen, J. S. Gas Phase Stabilization of Noncovalent Protein Complexes Formed by Electrospray Ionization. *Anal Chem* **2009**, *81* (18), 7801–7806. https://doi.org/10.1021/ac900611a.

(183) Catalina, M. I.; Van Den Heuvel, R. H. H.; Van Duijn, E.; Heck, A. J. R. Decharging of Globular Proteins and Protein Complexes in Electrospray. *Chemistry - A European Journal* **2005**, *11* (3), 960–968. https://doi.org/10.1002/chem.200400395.

(184) Sterling, H. J.; Prell, J. S.; Cassou, C. A.; Williams, E. R. Protein Conformation and Supercharging with DMSO from Aqueous Solution. *J Am Soc Mass Spectrom* **2011**, *22* (7), 1178–1186. https://doi.org/10.1007/s13361-011-0116-x.

(185) Kaldmäe, M.; Österlund, N.; Lianoudaki, D.; Sahin, C.; Bergman, P.; Nyman, T.; Kronqvist, N.; Ilag, L. L.; Allison, T. M.; Marklund, E. G.; Landreh, M. Gas phase Collisions with Trimethylamine-N-Oxide Enable Activation-Controlled Protein Ion Charge Reduction. *J Am Soc Mass Spectrom* **2019**, *30* (8), 1385–1388. https://doi.org/10.1007/s13361-019-02177-8.

(186) Thinius, M.; Polaczek, C.; Langner, M.; Bräkling, S.; Haack, A.; Kersten, H.; Benter, T. Charge Retention/Charge Depletion in ESI-MS: Experimental Evidence. *J Am Soc Mass Spectrom* **2020**, *31* (4), 773–784. https://doi.org/10.1021/jasms.9b00044.

(187) Haack, A.; Polaczek, C.; Tsolakis, M.; Thinius, M.; Kersten, H.; Benter, T. Charge Retention/Charge Depletion in ESI-MS: Theoretical Rationale. *J Am Soc Mass Spectrom* **2020**, *31* (4), 785–795. https://doi.org/10.1021/jasms.9b00044.

(188) Hunter, E. P. L.; Lias, S. G. Evaluated Gas Phase Basicities and Proton Affinities of Molecules: An Update. *J Phys Chem Ref Data* **1998**, *27* (3), 413–656. https://doi.org/10.1063/1.556018.

(189) Robinson, E. W.; Shvartsburg, A. A.; Tang, K.; Smith, R. D. Control of Ion Distortion in Field Asymmetric Waveform Ion Mobility Spectrometry via Variation of Dispersion Field and Gas Temperature. *Anal Chem* **2008**, *80* (19), 7508–7515. https://doi.org/10.1021/ac800655d.

(190) Krylov, E. v.; Nazarov, E. G. Electric Field Dependence of the Ion Mobility. *Int J Mass Spectrom* **2009**, *285* (3), 149–156. https://doi.org/10.1016/j.ijms.2009.05.009.

(191) Ayodeji, I.; Vazquez, T.; Bailey, R.; Evans-Nguyen, T. Rapid Pre-Filtering of Amphetamine and Derivatives by Direct Analysis in Real Time (DART)-Differential Mobility Spectrometry (DMS). *Analytical Methods* **2017**, *9* (34), 5044–5051. https://doi.org/10.1039/c7ay00892a.

(192) Blackburn, M. A.; Kapron, J.; Mackie, J.; Firth, J.; Harrison, M.; McDougall, S. Identification and Subsequent Removal of an Interference by FAIMS in the Bioanalysis of Dianicline in Animal Plasma. *Bioanalysis* **2011**, *3* (18), 2119–2127. https://doi.org/10.4155/bio.11.194.

(193) Manicke, N. E.; Belford, M. Separation of Opiate Isomers Using Electrospray Ionization and Paper Spray Coupled to High-Field Asymmetric Waveform Ion Mobility Spectrometry. *J Am Soc Mass Spectrom* **2015**, *26* (5), 701–705. https://doi.org/10.1007/s13361-015-1096-z.

(194) Grimes, N.; Vuppala, S.; Ayodeji, I.; Donovan, J.; Evans-Nguyen, T. Enabling Field Asymmetric Ion Mobility Spectrometry Separation of Fentanyl-Related Compounds Using Controlled Humidity. *Anal Chem* **2020**, *92* (4), 2917–2921. https://doi.org/10.1021/acs.analchem.9b02997.

(195) Qi, Y.; Geib, T.; Schorr, P.; Meier, F.; Volmer, D. A. On the Isobaric Space of 25-Hydroxyvitamin D in Human Serum: Potential for Interferences in Liquid Chromatography/Tandem Mass Spectrometry, Systematic Errors and Accuracy Issues.

Rapid Communications in Mass Spectrometry **2015**, *29*, 1–9. https://doi.org/10.1002/rcm.7075.

(196) Ray, J. A.; Kushnir, M. M.; Yost, R. A.; Rockwood, A. L.; Wayne Meikle, A. Performance Enhancement in the Measurement of 5 Endogenous Steroids by LC-MS/MS Combined with Differential Ion Mobility Spectrometry. *Clinica Chimica Acta* **2014**, *438*, 330–336. https://doi.org/10.1016/j.cca.2014.07.036.

(197) Lam, K. H. B.; Le Blanc, J. C. Y.; Campbell, J. L. Separating Isomers, Conformers, and Analogues of Cyclosporin Using Differential Mobility Spectroscopy, Mass Spectrometry, and Hydrogen-Deuterium Exchange. *Anal Chem* **2020**, *92* (16), 11053–11061.

(198) Zhang, J. D.; Kabir, K. M. M.; Donald, W. A. Metal-Ion Free Chiral Analysis of Amino Acids as Small as Proline Using High-Definition Differential Ion Mobility Mass Spectrometry. *Anal Chim Acta* **2018**, *1036*, 172–178. https://doi.org/10.1016/j.aca.2018.06.026.

(199) Mie, A.; Jörntén-Karlsson, M.; Axelsson, B. O.; Ray, A.; Reimann, C. T. Enantiomer Separation of Amino Acids by Complexation with Chiral Reference Compounds and High-Field Asymmetric Waveform Ion Mobility Spectrometry: Preliminary Results and Possible Limitations. *Anal Chem* **2007**, *79* (7), 2850–2858. https://doi.org/10.1021/ac0618627.

(200) Mie, A.; Ray, A.; Axelsson, B. O.; Jörnten-Karlsson, M.; Reimann, C. T. Terbutaline Enantiomer Separation and Quantification by Complexation and Field Asymmetric Ion Mobility Spectrometry-Tandem Mass Spectrometry. *Anal Chem* **2008**, *80* (11), 4133–4140. https://doi.org/10.1021/ac702262k.

(201) Zhang, J. D.; Donor, M. T.; Rolland, A. D.; Leeming, M. G.; Wang, H.; Trevitt, A. J.; Kabir, K. M. M.; Prell, J. S.; Donald, W. A. Protonation Isomers of Highly Charged Protein Ions Can Be Separated in FAIMS-MS. *Int J Mass Spectrom* **2020**, *457*, 116425. https://doi.org/10.1016/j.ijms.2020.116425.

(202) Marlton, S. J. P.; Mckinnon, B. I.; Ucur, B.; Bezzina, J. P.; Blanksby, S. J.; Trevitt, A. J. Discrimination between Protonation Isomers of Quinazoline by Ion Mobility and UV-Photodissociation Action Spectroscopy. **2020**. https://doi.org/10.1021/acs.jpclett.0c01009.

(203) Rauk, A.; Allen, L. C.; Mislow, K. Pyramidal Inversion. *Angewandte Chemie International Edition in English* **1970**, *9* (6), 400–414. https://doi.org/10.1002/anie.197004001.

(204) Belostotskii, A. M.; Gottlieb, H. E.; Shokhen, M. Nitrogen Inversion in Cyclic Amines and the Bicyclic Effect. *Journal of Organic Chemistry* **2002**, *67* (26), 9257–9266. https://doi.org/10.1021/jo020221i.

(205) Daly, S.; Rosu, F.; Gabelica, V. Mass-Resolved Electronic Circular Dichroism Ion Spectroscopy. *Science (1979)* **2020**, *368* (6498), 1465–1468. https://doi.org/10.1126/science.abb1822.

(206) Wojcik, R.; Nagy, G.; Attah, I. K.; Webb, I. K.; Garimella, S. V. B.; Weitz, K. K.; Hollerbach, A.; Monroe, M. E.; Ligare, M. R.; Nielson, F. F.; Norheim, R. V.; Renslow, R. S.; Metz, T. O.; Ibrahim, Y. M.; Smith, R. D. SLIM Ultrahigh Resolution Ion Mobility Spectrometry Separations of Isotopologues and Isotopomers Reveal Mobility Shifts Due to Mass Distribution Changes. *Anal Chem* **2019**, *91* (18), 11952–11962. https://doi.org/10.1021/acs.analchem.9b02808.

(207) Li, G.; DeLaney, K.; Li, L. Molecular Basis for Chirality-Regulated Aβ Self-Assembly and Receptor Recognition Revealed by Ion Mobility-Mass Spectrometry. *Nat Commun* **2019**, *10*, 5038. https://doi.org/10.1038/s41467-019-12346-8.

(208) Zhou, Z.; Luo, M.; Chen, X.; Yin, Y.; Xiong, X.; Wang, R.; Zhu, Z. J. Ion Mobility Collision Cross-Section Atlas for Known and Unknown Metabolite Annotation in Untargeted Metabolomics. *Nat Commun* **2020**, *11*, 4334. https://doi.org/10.1038/s41467-020-18171-8.

(209) Perlman, A. I.; McLeod, H. M.; Ventresca, E. C.; Salinas, M. G.; Post, P. J.; Schuh, M. J.; Abu Dabrh, A. M. Medical Cannabis State and Federal Regulations: Implications for United

States Health Care Entities. *Mayo Clin Proc* **2021**, *96* (10), 2671–2681. https://doi.org/10.1016/J.MAYOCP.2021.05.005.

(210) Kruger, D. J.; Korach, N. J.; Kruger, J. S. Requirements for Cannabis Product Labeling by U.S. State. *Cannabis Cannabinoid Res* **2022**, *7* (2), 156–160. https://doi.org/10.1089/can.2020.0079.

(211) Leos-Toro, C.; Fong, G. T.; Meyer, S. B.; Hammond, D. Cannabis Labelling and Consumer Understanding of THC Levels and Serving Sizes. *Drug Alcohol Depend* **2020**, *208*, 107843. https://doi.org/10.1016/J.DRUGALCDEP.2020.107843.

(212) Pertwee, R. G. The Diverse CB1 and CB2 Receptor Pharmacology of Three Plant Cannabinoids: Δ9-Tetrahydrocannabinol, Cannabidiol and Δ9-Tetrahydrocannabivarin. *Br J Pharmacol* **2008**, *153* (2), 199–215. https://doi.org/10.1038/SJ.BJP.0707442.

(213) Huestis, M. A. Human Cannabinoid Pharmacokinetics. *Chem Biodivers* **2007**, *4* (8), 1770–1804. https://doi.org/10.1002/CBDV.200790152.

(214) Martin, B. R.; Mechoulam, R.; Razdan, R. K. Discovery and Characterization of Endogenous Cannabinoids. *Life Sci* **1999**, *65* (6–7), 573–595. https://doi.org/10.1016/S0024-3205(99)00281-7.

(215) Laprairie, R. B.; Bagher, A. M.; Kelly, M. E. M.; Denovan-Wright, E. M. Cannabidiol Is a Negative Allosteric Modulator of the Cannabinoid CB1 Receptor. *Br J Pharmacol* **2015**, *172* (20), 4790–4805. https://doi.org/10.1111/BPH.13250.

(216) Black, N.; Stockings, E.; Campbell, G.; Tran, L. T.; Zagic, D.; Hall, W. D.; Farrell, M.; Degenhardt, L. Cannabinoids for the Treatment of Mental Disorders and Symptoms of Mental Disorders: A Systematic Review and Meta-Analysis. *Lancet Psychiatry* **2019**, *6* (12), 995–1010. https://doi.org/10.1016/S2215-0366(19)30401-8.

(217) Hoch, E.; Niemann, D.; von Keller, R.; Schneider, M.; Friemel, C. M.; Preuss, U. W.; Hasan, A.; Pogarell, O. How Effective and Safe Is Medical Cannabis as a Treatment of Mental

Disorders? A Systematic Review. *Eur Arch Psychiatry Clin Neurosci* **2019**, *269* (1), 87–105. https://doi.org/10.1007/s00406-019-00984-4.

(218) Rep. Conaway, K. M. [R-T.-11]. *H.R.2 - 115th Congress (2017-2018): Agriculture Improvement Act of 2018*. https://www.congress.gov/bill/115th-congress/house-bill/2?q=%7B%22sea%20rch%22%3A%5B%22hr2+115%E2%80%93334%22%2C%22hr2%22%2C%22115%E2%80%93334%%2022%5D%7D&s=4&r=1 (accessed 2023-03-11).

(219) Malone, T.; Gomez, K. Hemp in the United States: A Case Study of Regulatory Path Dependence. *Appl Econ Perspect Policy* **2019**, *41* (2), 199–214. https://doi.org/10.1093/AEPP/PPZ001.

(220) Kumar, N.; Puljević, C.; Ferris, J.; Winstock, A.; Barratt, M. J. Cannabis Use Patterns at the Dawn of US Cannabis Reform. *J Cannabis Res* **2019**, *1* (1), 1–6. https://doi.org/10.1186/s42238-019-0003-z.

(221) Hinckley, J. D.; Hopfer, C. Marijuana Legalization in Colorado: Increasing Potency, Changing Risk Perceptions, and Emerging Public Health Concerns for Youth. *Adolesc Psychiatry* **2021**, *11* (2), 95–116. https://doi.org/10.2174/2210676611666210616163340.

(222) Webster, G. R. B.; Sarna, L. P.; Mechoulam, R. Conversion of CBD to Δ8-THC and Δ9-THC. US 2004/0143126 A1, 2004.

(223) Kiselak, T. D.; Koerber, R.; Verbeck, G. F. Synthetic Route Sourcing of Illicit at Home Cannabidiol (CBD) Isomerization to Psychoactive Cannabinoids Using Ion Mobility-Coupled-LC–MS/MS. *Forensic Sci Int* **2020**, *308*, 110173. https://doi.org/10.1016/J.FORSCIINT.2020.110173.

(224) Marzullo, P.; Foschi, F.; Coppini, D. A.; Fanchini, F.; Magnani, L.; Rusconi, S.; Luzzani, M.; Passarella, D. Cannabidiol as the Substrate in Acid-Catalyzed Intramolecular Cyclization. *J Nat Prod* **2020**, *83* (10), 2894–2901. https://doi.org/10.1021/acs.jnatprod.0c00436.

(225) Franco, C.; Protti, S.; Porta, A.; Pollastro, F.; Profumo, A.; Mannucci, B.; Merli, D. Stability of Cannabidiol (CBD) in Solvents and Formulations: A GC–MS Approach. *Results Chem* **2022**, *4*, 100465. https://doi.org/10.1016/J.RECHEM.2022.100465.

(226) Tagen, M.; Klumpers, L. E. Review of Delta-8-Tetrahydrocannabinol (Δ8-THC): Comparative Pharmacology with Δ9-THC. *Br J Pharmacol* **2022**, *179* (15), 3915–3933. https://doi.org/10.1111/bph.15865.

(227) Adams, R.; Pease, D. C.; Cain, C. K.; Clark, J. H. Structure of Cannabidiol. VI. Isomerization of Cannabidiol to Tetrahydrocannabinol, a Physiologically Active Product. Conversion of Cannabidiol to Cannabinol. *J Am Chem Soc* **1940**, *62* (9), 2402–2405. https://doi.org/10.1021/ja01866a040.

(228) Gaoni, Y.; Mechoulam, R. Hashish—VII : The Isomerization of Cannabidiol to Tetrahydrocannabinols. *Tetrahedron* **1966**, *22* (4), 1481–1488. https://doi.org/10.1016/S0040-4020(01)99446-3.

(229) Golombek, P.; Müller, M.; Barthlott, I.; Sproll, C.; Lachenmeier, D. W. Conversion of Cannabidiol (CBD) into Psychotropic Cannabinoids Including Tetrahydrocannabinol (THC): A Controversy in the Scientific Literature. *Toxics 2020, Vol. 8, Page 41* **2020**, *8* (2), 41. https://doi.org/10.3390/TOXICS8020041.

(230) UNITED STATES COURT OF APPEALS FOR THE NINTH CIRCUIT - Opinion by Judge Fisher. *AK FUTURES LLC, Plaintiff-Appellee v. BOYD STREET DISTRO, LLC, a California Limited Liability Company, Defendant-Appellant*; 2022. https://mjbizdaily.com/wp-content/uploads/2022/05/AK-Futures.pdf (accessed 2023-03-14).

(231) Wang, Y. H.; Avula, B.; Elsohly, M. A.; Radwan, M. M.; Wang, M.; Wanas, A. S.; Mehmedic, Z.; Khan, I. A. Quantitative Determination of Δ9-THC, CBG, CBD, Their Acid Precursors

and Five Other Neutral Cannabinoids by UHPLC-UV-MS. *Planta Med* **2018**, *84* (4), 260–266. https://doi.org/10.1055/s-0043-124873.

(232) Leas, E. C.; Nobles, A. L.; Shi, Y.; Hendrickson, E. Public Interest in ∆8-Tetrahydrocannabinol (Delta-8-THC) Increased in US States That Restricted ∆9-Tetrahydrocannabinol (Delta-9-THC) Use. *International Journal of Drug Policy* **2022**, *101*, 103557. https://doi.org/10.1016/J.DRUGPO.2021.103557.

(233) *FDA Issues Warning Letters to Companies Illegally Selling CBD and Delta-8 THC Products / FDA*. https://www.fda.gov/news-events/press-announcements/fda-issues-warning-letters-companies-illegally-selling-cbd-and-delta-8-thc-products (accessed 2023-03-11).

(234) *5 Things to Know about Delta-8 Tetrahydrocannabinol – Delta-8 THC / FDA*. https://www.fda.gov/consumers/consumer-updates/5-things-know-about-delta-8-tetrahydrocannabinol-delta-8-thc (accessed 2023-03-11).

(235) Radwan, M. M.; Wanas, A. S.; Gul, W.; Ibrahim, E. A.; Elsohly, M. A. Isolation and Characterization of Impurities in Commercially Marketed Δ8-THC Products. **2022**. https://doi.org/10.1021/acs.jnatprod.2c01008.

(236) Meehan-Atrash, J.; Rahman, I. Novel Δ8-Tetrahydrocannabinol Vaporizers Contain Unlabeled Adulterants, Unintended Byproducts of Chemical Synthesis, and Heavy Metals. *Chem Res Toxicol* **2022**, *35* (1), 73–76. https://doi.org/10.1021/acs.chemrestox.1c00388.

(237) Turner, S. E.; Williams, C. M.; Iversen, L.; Whalley, B. J. Molecular Pharmacology of Phytocannabinoids. *Prog Chem Org Nat Prod* **2017**, *103*, 61–101. https://doi.org/10.1007/978-3-319-45541-9_3.

(238) Brown, N. K.; Harvey, D. J. In Vitro Metabolism of Cannabichromene in Seven Common Laboratory Animals. *Drug Metabolism and Disposition* **1990**, *18* (6).

(239) Citti, C.; Linciano, P.; Panseri, S.; Vezzalini, F.; Forni, F.; Vandelli, M. A.; Cannazza, G. Cannabinoid Profiling of Hemp Seed Oil by Liquid Chromatography Coupled to High-

Resolution Mass Spectrometry. *Front Plant Sci* **2019**, *10* (February), 1–17. https://doi.org/10.3389/fpls.2019.00120.

(240) Lelario, F.; Pascale, R.; Bianco, G.; Scrano, L.; Bufo, S. A. Hemp Chemotype Definition by Cannabinoids Characterization Using LC-ESI(+)-LTQ-FTICR MS and Infrared Multiphoton Dissociation. *Separations* **2021**, *8* (12). https://doi.org/10.3390/separations8120245.

(241) Shah, I.; Al-Dabbagh, B.; Salem, A. E.; Hamid, S. A. A.; Muhammad, N.; Naughton, D. P. A Review of Bioanalytical Techniques for Evaluation of Cannabis (Marijuana, Weed, Hashish) in Human Hair. *BMC Chemistry 2019 13:1* **2019**, *13* (1), 1–20. https://doi.org/10.1186/S13065-019-0627-2.

(242) Calvi, L.; Pentimalli, D.; Panseri, S.; Giupponi, L.; Gelmini, F.; Beretta, G.; Vitali, D.; Bruno, M.; Zilio, E.; Pavlovic, R.; Giorgi, A. Comprehensive Quality Evaluation of Medical Cannabis Sativa L. Inflorescence and Macerated Oils Based on HS-SPME Coupled to GC–MS and LC-HRMS (q-Exactive Orbitrap®) Approach. *J Pharm Biomed Anal* **2018**, *150*, 208–219. https://doi.org/10.1016/J.JPBA.2017.11.073.

(243) Delgado-Povedano, M. M.; Sánchez-Carnerero Callado, C.; Priego-Capote, F.; Ferreiro-Vera, C. Untargeted Characterization of Extracts from Cannabis Sativa L. Cultivars by Gas and Liquid Chromatography Coupled to Mass Spectrometry in High Resolution Mode. *Talanta* **2020**, *208*, 120384. https://doi.org/10.1016/J.TALANTA.2019.120384.

(244) McRae, G.; Melanson, J. E. Quantitative Determination and Validation of 17 Cannabinoids in Cannabis and Hemp Using Liquid Chromatography-Tandem Mass Spectrometry. *Anal Bioanal Chem* **2020**, *412* (27), 7381–7393. https://doi.org/10.1007/S00216-020-02862-8.

(245) dos Santos, N. A.; Souza, L. M.; Domingos, E.; França, H. S.; Lacerda, V.; Beatriz, A.; Vaz, B. G.; Rodrigues, R. R. T.; Carvalho, V. V.; Merlo, B. B.; Kuster, R. M.; Romão, W. Evaluating the Selectivity of Colorimetric Test (Fast Blue BB Salt) for the Cannabinoids Identification in Marijuana Street Samples by UV–Vis, TLC, ESI(+)FT-ICR MS and

ESI(+)MS/MS. *Forensic Chemistry* **2016**, *1*, 13–21. https://doi.org/10.1016/J.FORC.2016.07.001.

(246) Amini, K.; Sepehrifard, A.; Valinasabpouri, A.; Safruk, J.; Angelone, D.; De, T.; Lourenco, C. Recent Advances in Electrochemical Sensor Technologies for THC Detection—a Narrative Review. *Journal of Cannabis Research 2022 4:1* **2022**, *4* (1), 1–7. https://doi.org/10.1186/S42238-022-00122-3.

(247) Stevenson, H.; Bacon, A.; Joseph, K. M.; Gwandaru, W. R. W.; Bhide, A.; Sankhala, D.; Dhamu, V. N.; Prasad, S. A Rapid Response Electrochemical Biosensor for Detecting Thc In Saliva. *Scientific Reports 2019 9:1* **2019**, *9* (1), 1–11. https://doi.org/10.1038/s41598-019-49185-y.

(248) Comeau, Z. J.; Boileau, N. T.; Lee, T.; Melville, O. A.; Rice, N. A.; Troung, Y.; Harris, C. S.; Lessard, B. H.; Shuhendler, A. J. On-the-Spot Detection and Speciation of Cannabinoids Using Organic Thin-Film Transistors. *ACS Sens* **2019**, *4* (10), 2706–2715. https://doi.org/10.1021/acssensors.9b01150.

(249) França, H. S.; Acosta, A.; Jamal, A.; Romao, W.; Mulloor, J.; Almirall, J. R. Experimental and Ab Initio Investigation of the Products of Reaction from Δ9-Tetrahydrocannabinol (Δ9-THC) and the Fast Blue BB Spot Reagent in Presumptive Drug Tests for Cannabinoids. *Forensic Chemistry* **2020**, *17*, 100212. https://doi.org/10.1016/J.FORC.2019.100212.

(250) Hädener, M.; Kamrath, M. Z.; Weinmann, W.; Groessl, M. High-Resolution Ion Mobility Spectrometry for Rapid Cannabis Potency Testing. *Anal Chem* **2018**, *90* (15), 8764–8768. https://doi.org/10.1021/acs.analchem.8b02180.

(251) Tose, L. V; Santos, N. A.; Rodrigues, R. R. T.; Murgu, M.; Gomes, A. F.; Vasconcelos, G. A.; Souza, P. C. T.; Vaz, B. G.; Romão, W. Isomeric Separation of Cannabinoids by UPLC Combined with Ionic Mobility Mass Spectrometry (TWIM-MS)-Part I. *Int J Mass Spectrom* **2017**, *418*, 112–121. https://doi.org/10.1016/j.ijms.2016.10.018.

(252) Santos, N. A. Dos; Tose, L. V; Da Silva, S. R. C.; Murgu, M.; Kuster, R. M.; Ortiz, R. S.; Camargo, F. A. O.; Vaz, B. G.; Lacerda, V. *; Romão, W. Analysis of Isomeric Cannabinoid Standards and Cannabis Products by UPLC-ESI-TWIM-MS: A Comparison with GC-MS and GC × GC-QMS. *Article J. Braz. Chem. Soc* **2019**, *30* (1), 60–70. https://doi.org/10.21577/0103-5053.20180152.

(253) Mashmoushi, N.; Larry Campbell, J.; di Lorenzo, R.; Scott Hopkins, W. Rapid Separation of Cannabinoid Isomer Sets Using Differential Mobility Spectrometry and Mass Spectrometry. *Analyst* **2022**, *147* (10), 2198–2206. https://doi.org/10.1039/D1AN02327F.

(254) Schneider, B. B.; Covey, T. R.; Nazarov, E. G. DMS-MS Separations with Different Transport Gas Modifiers. *International Journal for Ion Mobility Spectrometry* **2013**, *16* (3), 207–216. https://doi.org/10.1007/s12127-013-0130-8.

(255) Chen, P. S.; Chen, S. H.; Chen, J. H.; Haung, W. Y.; Liu, H. T.; Kong, P. H.; Yang, O. H. Y. Modifier-Assisted Differential Mobility–Tandem Mass Spectrometry Method for Detection and Quantification of Amphetamine-Type Stimulants in Urine. *Anal Chim Acta* **2016**, *946*, 1–8. https://doi.org/10.1016/j.aca.2016.09.027.

(256) Wei, M. S.; Kemperman, R. H. J.; Yost, R. A. Effects of Solvent Vapor Modifiers for the Separation of Opioid Isomers in Micromachined FAIMS-MS. *J Am Soc Mass Spectrom* **2019**, *30* (5), 731–742. https://doi.org/10.1007/s13361-019-02175-w.

(257) Ieritano, C.; Hopkins, W. S. The Hitchhiker's Guide to Dynamic Ion-Solvent Clustering: Applications in Differential Ion Mobility Spectrometry. *Physical Chemistry Chemical Physics* **2022**, *24* (35), 20594–20615. https://doi.org/10.1039/d2cp02540j.

(258) Haack, A.; Hopkins, W. S. Kinetics in DMS: Modeling Clustering and Declustering Reactions. *J Am Soc Mass Spectrom* **2022**, *33*, 2250–2262. https://doi.org/10.1021/jasms.2c00224.

(259) Huang, S.; Qiu, R.; Fang, Z.; Min, K.; Van Beek, T. A.; Ma, M.; Chen, B.; Zuilhof, H.; Salentijn, G. I. Semiquantitative Screening of THC Analogues by Silica Gel TLC with an

Ag(I) Retention Zone and Chromogenic Smartphone Detection. **2022**. https://doi.org/10.1021/acs.analchem.2c01627.

(260) Grimme, S. Exploration of Chemical Compound, Conformer, and Reaction Space with Meta-Dynamics Simulations Based on Tight-Binding Quantum Chemical Calculations. *J Chem Theory Comput* **2019**, *15* (5), 2847–2862. https://doi.org/10.1021/acs.jctc.9b00143.

(261) Pracht, P.; Bohle, F.; Grimme, S. Automated Exploration of the Low-Energy Chemical Space with Fast Quantum Chemical Methods. *Physical Chemistry Chemical Physics* **2020**, *22* (14), 7169–7192. https://doi.org/10.1039/C9CP06869D.

(262) Bannwarth, C.; Ehlert, S.; Grimme, S. GFN2-XTB - An Accurate and Broadly Parametrized Self-Consistent Tight-Binding Quantum Chemical Method with Multipole Electrostatics and Density-Dependent Dispersion Contributions. *J Chem Theory Comput* **2019**, *15* (3), 1652–1671. https://doi.org/10.1021/acs.jctc.8b01176.

(263) Grimme, S.; Antony, J.; Ehrlich, S.; Krieg, H. A Consistent and Accurate Ab Initio Parametrization of Density Functional Dispersion Correction (DFT-D) for the 94 Elements H-Pu. *Journal of Chemical Physics* **2010**, *132* (15), 154104. https://doi.org/10.1063/1.3382344.

(264) Ekström, U.; Visscher, L.; Bast, R.; Thorvaldsen, A. J.; Ruud, K. Arbitrary-Order Density Functional Response Theory from Automatic Differentiation. *J Chem Theory Comput* **2010**, *6* (7), 1971–1980. https://doi.org/10.1021/ct100117s.

(265) Andrae, D.; Häußermann, U.; Dolg, M.; Stoll, H.; Preuß, H. Energy-Adjusted Ab Initio Pseudopotentials for the Second and Third Row Transition Elements. *Theor Chim Acta* **1990**, *77* (2), 123–141. https://doi.org/10.1007/BF01114537.

(266) Weigend, F. Accurate Coulomb-Fitting Basis Sets for H to Rn. *Physical Chemistry Chemical Physics* **2006**, *8* (9), 1057–1065. https://doi.org/10.1039/b515623h.

(267) Weigend, F.; Ahlrichs, R. Balanced Basis Sets of Split Valence, Triple Zeta Valence and Quadruple Zeta Valence Quality for H to Rn: Design and Assessment of Accuracy. *Physical Chemistry Chemical Physics* **2005**, *7* (18), 3297–3305. https://doi.org/10.1039/b508541a.

(268) Lin, Y. S.; Li, G. de; Mao, S. P.; Chai, J. da. Long-Range Corrected Hybrid Density Functionals with Improved Dispersion Corrections. *J Chem Theory Comput* **2013**, *9* (1), 263–272. https://doi.org/10.1021/ct300715s.

(269) Hellweg, A.; Hättig, C.; Höfener, S.; Klopper, W. Optimized Accurate Auxiliary Basis Sets for RI-MP2 and RI-CC2 Calculations for the Atoms Rb to Rn. *Theor Chem Acc* **2007**, *117* (4), 587–597. https://doi.org/10.1007/s00214-007-0250-5.

(270) Valeev, E. F. *Libint: A library for the evaluation of molecular integrals of many-body operators over Gaussian functions, Version 2.6.0*. http://libint.valeyev.net/.

(271) Lehtola, S.; Steigemann, C.; Oliveira, M. J. T.; Marques, M. A. L. Recent Developments in LIBXC — A Comprehensive Library of Functionals for Density Functional Theory. *SoftwareX* **2018**, *7*, 1–5. https://doi.org/10.1016/j.softx.2017.11.002.

(272) Álvarez-Moreno, M.; De Graaf, C.; López, N.; Maseras, F.; Poblet, J. M.; Bo, C. Managing the Computational Chemistry Big Data Problem: The IoChem-BD Platform. *J Chem Inf Model* **2015**, *55* (1), 95–103. https://doi.org/10.1021/ci500593j.

(273) Shoeib, T.; Zhao, J.; Aribi, H. E.; Hopkinson, A. C.; Michael Siu, K. W. Dissociations of Complexes between Monovalent Metal Ions and Aromatic Amino Acid or Histidine. *J Am Soc Mass Spectrom* **2013**, *24* (1), 38–48. https://doi.org/10.1007/s13361-012-0511-y.

(274) Sigsworth, S. W.; Castleman, A. W. Rates of Hydride Abstraction from Amines via Reactions with Ground-State Ag+ and Cu+. *J Am Chem Soc* **1989**, *111* (10), 3566–3569. https://doi.org/10.1021/ja00192a012.

(275) Ieritano, C.; Hopkins, W. S. "Thermometer" Ions Can Fragment Through an Unexpected Intramolecular Elimination: These Are Not the Fragments You Are Looking For. *J Phys Chem Lett* **2021**, 5994–5999. https://doi.org/10.1021/acs.jpclett.1c01538.

(276) Zuilhof, H.; Salentijn, G. I. J.; Huang, S.; Claassen, F. W.; van Beek, T. A.; Chen, B.; Zeng, J. Rapid Distinction and Semiquantitative Analysis of THC and CBD by Silver-Impregnated Paper Spray Mass Spectrometry. *Anal Chem* **2021**, *93* (8), 3794–3802. https://doi.org/10.1021/acs.analchem.0c04270.

(277) Ieritano, C.; Campbell, J. L.; Hopkins, W. S. Unravelling the Factors That Drive Separation in Differential Mobility Spectrometry: A Case Study of Regioisomeric Phosphatidylcholine Adducts. *Int J Mass Spectrom* **2019**, *444*. https://doi.org/10.1016/j.ijms.2019.116182.

(278) Zietek, B. M.; Mengerink, Y.; Jordens, J.; Somsen, G. W.; Kool, J.; Honing, M. Adduct-Ion Formation in Trapped Ion Mobility Spectrometry as a Potential Tool for Studying Molecular Structures and Conformations. *International Journal for Ion Mobility Spectrometry* **2018**, *21* (1–2), 19–32. https://doi.org/10.1007/s12127-017-0227-6.

(279) Nachnani, R.; Raup-Konsavage, W. M.; Vrana, K. E. The Pharmacological Case for Cannabigerol. *Journal of Pharmacology and Experimental Therapeutics* **2021**, *376* (2), 204–212. https://doi.org/10.1124/JPET.120.000340.

(280) Cascio, M. G.; Gauson, L. A.; Stevenson, L. A.; Ross, R. A.; Pertwee, R. G. Evidence That the Plant Cannabinoid Cannabigerol Is a Highly Potent A2-Adrenoceptor Agonist and Moderately Potent 5HT1A Receptor Antagonist. *Br J Pharmacol* **2010**, *159* (1), 129–141. https://doi.org/10.1111/J.1476-5381.2009.00515.X.

(281) Sampson, P. B. Phytocannabinoid Pharmacology: Medicinal Properties of Cannabis Sativa Constituents Aside from the "Big Two." *J Nat Prod* **2021**, *84* (1), 142–160. https://doi.org/10.1021/acs.jnatprod.0c00965.

(282) Bloemendal, V. R. L. J.; Van Hest, J. C. M.; Rutjes, F. P. J. T. Organic & Biomolecular Chemistry Synthetic Pathways to Tetrahydrocannabinol (THC): An Overview. *Org. Biomol. Chem* **2020**, *18*, 3203. https://doi.org/10.1039/d0ob00464b.

(283) Banerjee, A.; Hayward, J. J.; Trant, J. F. "Breaking Bud": The Effect of Direct Chemical Modifications of Phytocannabinoids on Their Bioavailability, Physiological Effects, and Therapeutic Potential. *Org Biomol Chem* **2023**. https://doi.org/10.1039/D3OB00068K.

(284) Roman, M. G.; Cheng, Y. C.; Kerrigan, S.; Houston, R. Evaluation of Tetrahydrocannabinolic Acid (THCA) Synthase Polymorphisms for Distinguishing between Marijuana and Hemp. *J Forensic Sci* **2022**, *67* (4), 1370–1381. https://doi.org/10.1111/1556-4029.15045.

(285) Fridgen, T. D.; Troe, J.; Viggiano, A. A.; Midey, A. J.; Williams, S.; McMahon, T. B. Experimental and Theoretical Studies of the Benzylium +/ Tropylium + Ratios after Charge Transfer to Ethylbenzene. *Journal of Physical Chemistry A* **2004**, *108* (26), 5600–5609. https://doi.org/10.1021/jp031328s.

(286) Jusko, P.; Simon, A.; Banhatti, S.; Brünken, S.; Joblin, C. Direct Evidence of the Benzylium and Tropylium Cations as the Two Long-Lived Isomers of C7H7+. *ChemPhysChem* **2018**, *19* (23), 3182–3185. https://doi.org/10.1002/CPHC.201800744.

(287) May, J. C.; McLean, J. A. Ion Mobility-Mass Spectrometry: Time-Dispersive Instrumentation. *Anal Chem* **2015**, *87* (3), 1422–1436. https://doi.org/10.1021/ac504720m.

(288) Dodds, J. N.; Baker, E. S. Ion Mobility Spectrometry: Fundamental Concepts, Instrumentation, Applications, and the Road Ahead. *J Am Soc Mass Spectrom* **2019**, *30* (11), 2185–2195. https://doi.org/10.1007/s13361-019-02288-2.

(289) Baker, E. S.; Livesay, E. A.; Orton, D. J.; Moore, R. J.; Danielson, W. F.; Prior, D. C.; Ibrahim, Y. M.; LaMarche, B. L.; Mayampurath, A. M.; Schepmoes, A. A.; Hopkins, D. F.; Tang, K.; Smith, R. D.; Belov, M. E. An LC-IMS-MS Platform Providing Increased Dynamic

Range for High-Throughput Proteomic Studies. *J Proteome Res* **2010**, *9* (2), 997–1006. https://doi.org/10.1021/pr900888b.

(290) Rister, A. L.; Dodds, E. D. Liquid Chromatography-Ion Mobility Spectrometry-Mass Spectrometry Analysis of Multiple Classes of Steroid Hormone Isomers in a Mixture. *Journal of Chromatography B* **2020**, *1137*, 121941. https://doi.org/10.1016/j.jchromb.2019.121941.

(291) Langevin, P. Une Formule Fondamentale de Théorie Cinétique. *Annales de Chimie et de Physique* **1905**, *5*, 245–288.

(292) Gabelica, V.; Marklund, E. Fundamentals of Ion Mobility Spectrometry. *Curr Opin Chem Biol* **2018**, *42*, 51–59. https://doi.org/10.1016/J.CBPA.2017.10.022.

(293) Buryakov, I. A.; Krylov, E. V.; Nazarov, E. G.; Rasulev, U. K. A New Method of Separation of Multi-Atomic Ions by Mobility at Atmospheric Pressure Using a High-Frequency Amplitude-Asymmetric Strong Electric Field. *Int J Mass Spectrom Ion Process* **1993**, *128* (3), 143–148. https://doi.org/10.1016/0168-1176(93)87062-W.

(294) Chouinard, C. D.; Nagy, G.; Webb, I. K.; Shi, T.; Baker, E. S.; Prost, S. A.; Liu, T.; Ibrahim, Y. M.; Smith, R. D. Improved Sensitivity and Separations for Phosphopeptides Using Online Liquid Chromotography Coupled with Structures for Lossless Ion Manipulations Ion Mobility–Mass Spectrometry. *Anal Chem* **2018**, *90* (18), 10889–10896. https://doi.org/10.1021/acs.analchem.8b02397.

(295) Kirk, A. T.; Grube, D.; Kobelt, T.; Wendt, C.; Zimmermann, S. High-Resolution High Kinetic Energy Ion Mobility Spectrometer Based on a Low-Discrimination Tristate Ion Shutter. *Anal Chem* **2018**, *90* (9), 5603–5611. https://doi.org/10.1021/acs.analchem.7b04586.

(296) Gandhi, V. D.; Larriba-Andaluz, C. Predicting Ion Mobility as a Function of the Electric Field for Small Ions in Light Gases. *Anal Chim Acta* **2021**, *1184*, 339019. https://doi.org/10.1016/j.aca.2021.339019.

(297) Gandhi, V. D.; Short, K.; Hua, L.; Rodríguez, I.; Larriba-Andaluz, C. A Numerical Tool to Calculate Ion Mobility at Arbitrary Fields from All-Atom Models. *J Aerosol Sci* **2023**, *169*, 106122. https://doi.org/10.1016/j.jaerosci.2022.106122.

(298) Kihara, T. The Mathematical Theory of Electrical Discharges in Gases. B. Velocity-Distribution of Positive Ions in a Static Field. *Rev Mod Phys* **1953**, *25* (4), 844–852. https://doi.org/10.1103/RevModPhys.25.844.

(299) Mason, E. A.; Schamp, H. W. Mobility of Gaseous Ions in Weak Electric Fields. *Ann Phys (N Y)* **1958**, *4* (3), 233–270. https://doi.org/10.1016/0003-4916(58)90049-6.

(300) Viehland, L. A.; Mason, E. A. Gaseous Lon Mobility in Electric Fields of Arbitrary Strength. *Ann Phys (N Y)* **1975**, *91* (2), 499–533. https://doi.org/10.1016/0003-4916(75)90233-X.

(301) Viehland, L. A.; Mason, E. A. Gaseous Ion Mobility and Diffusion in Electric Fields of Arbitrary Strength. *Ann Phys (N Y)* **1978**, *110* (2), 287–328. https://doi.org/10.1016/0003-4916(78)90034-9.

(302) Lee, J. W.; Lee, H. H. L.; Davidson, K. L.; Bush, M. F.; Kim, H. I. Structural Characterization of Small Molecular Ions by Ion Mobility Mass Spectrometry in Nitrogen Drift Gas: Improving the Accuracy of Trajectory Method Calculations. *Analyst* **2018**, *143* (8), 1786–1796. https://doi.org/10.1039/C8AN00270C.

(303) Righetti, L.; Bergmann, A.; Galaverna, G.; Rolfsson, O.; Paglia, G.; Dall'Asta, C. Ion Mobility-Derived Collision Cross Section Database: Application to Mycotoxin Analysis. *Anal Chim Acta* **2018**, *1014*, 50–57. https://doi.org/10.1016/j.aca.2018.01.047.

(304) Bijlsma, L.; Bade, R.; Celma, A.; Mullin, L.; Cleland, G.; Stead, S.; Hernandez, F.; Sancho, J. V. Prediction of Collision Cross-Section Values for Small Molecules: Application to Pesticide Residue Analysis. *Anal Chem* **2017**, *89* (12), 6583–6589. https://doi.org/10.1021/acs.analchem.7b00741.

(305) Bauer, A.; Kuballa, J.; Rohn, S.; Jantzen, E.; Luetjohann, J. Evaluation and Validation of an Ion Mobility Quadrupole Time-of-Flight Mass Spectrometry Pesticide Screening Approach. *J Sep Sci* **2018**, *41* (10), 2178–2187. https://doi.org/10.1002/jssc.201701059.

(306) Campuzano, I.; Bush, M. F.; Robinson, C. V.; Beaumont, C.; Richardson, K.; Kim, H. H. I.; Kim, H. H. I. Structural Characterization of Drug-like Compounds by Ion Mobility Mass Spectrometry: Comparison of Theoretical and Experimentally Derived Nitrogen Collision Cross Sections. *Anal Chem* **2012**, *84* (2), 1026–1033. https://doi.org/10.1021/ac202625t.

(307) Ieritano, C.; Campbell, J. L.; Hopkins, W. S. Predicting Differential Ion Mobility Behaviour in Silico Using Machine Learning. *Analyst* **2021**, *146* (15), 4737–4743. https://doi.org/10.1039/D1AN00557J.

(308) Yang, J.; Zhang, Y. I-TASSER Server: New Development for Protein Structure and Function Predictions. *Nucleic Acids Res* **2015**, *43* (W1), W174–W181. https://doi.org/10.1093/nar/gkv342.

(309) Zheng, W.; Zhang, C.; Li, Y.; Pearce, R.; Bell, E. W.; Zhang, Y. Folding Non-Homologous Proteins by Coupling Deep-Learning Contact Maps with I-TASSER Assembly Simulations. *Cell Reports Methods* **2021**, *1* (3), 100014. https://doi.org/10.1016/j.crmeth.2021.100014.

(310) Breneman, C. M.; Wiberg, K. B. Determining Atom-Centered Monopoles from Molecular Electrostatic Potentials. The Need for High Sampling Density in Formamide Conformational Analysis. *J Comput Chem* **1990**, *11* (3), 361–373. https://doi.org/10.1002/jcc.540110311.

(311) Tao, J.; Perdew, J. P.; Staroverov, V. N.; Scuseria, G. E. Climbing the Density Functional Ladder: Nonempirical Meta–Generalized Gradient Approximation Designed for Molecules and Solids. *Phys Rev Lett* **2003**, *91* (14), 146401. https://doi.org/10.1103/PhysRevLett.91.146401.

(312) O'Boyle, N. M.; Banck, M.; James, C. A.; Morley, C.; Vandermeersch, T.; Hutchison, G. R. Open Babel: An Open Chemical Toolbox. *J Cheminform* **2011**, *3* (1), 33. https://doi.org/10.1186/1758-2946-3-33.

(313) Zanotto, L.; Heerdt, G.; Souza, P. C. T.; Araujo, G.; Skaf, M. S. High Performance Collision Cross Section Calculation-HPCCS. *J Comput Chem* **2018**, *39*, 1675–1681. https://doi.org/10.1002/jcc.25199.

(314) Larriba, C.; Hogan, C. J. Ion Mobilities in Diatomic Gases: Measurement versus Prediction with Non-Specular Scattering Models. *Journal of Physical Chemistry A* **2013**, *117* (19), 3887–3901. https://doi.org/10.1021/jp312432z.

(315) Larriba, C.; Hogan, C. J. Free Molecular Collision Cross Section Calculation Methods for Nanoparticles and Complex Ions with Energy Accommodation. *J Comput Phys* **2013**, *251*, 344–363. https://doi.org/10.1016/j.jcp.2013.05.038.

(316) Wyttenbach, T.; Von Helden, G.; Batka, J. J.; Carlat, D.; Bowers, M. T. Effect of the Long-Range Potential on Ion Mobility Measurements. *J Am Soc Mass Spectrom* **1997**, *8* (3), 275–282. https://doi.org/10.1016/S1044-0305(96)00236-X.

(317) Shvartsburg, A. A.; Jarrold, M. F. An Exact Hard-Spheres Scattering Model for the Mobilities of Polyatomic Ions. *Chem Phys Lett* **1996**, *261* (1–2), 86–91. https://doi.org/10.1016/0009-2614(96)00941-4.

(318) Kim, H.; Kim, H. I.; Johnson, P. v.; Beegle, L. W.; Beauchamp, J. L.; Goddard, W. A.; Kanik, I. Experimental and Theoretical Investigation into the Correlation between Mass and Ion Mobility for Choline and Other Ammonium Cations in N2. *Anal Chem* **2008**, *80* (6), 1928–1936. https://doi.org/10.1021/ac701888e.

(319) Mesleh, M. F.; Hunter, J. M.; Shvartsburg, A. A.; Schatz, G. C.; Jarrold, M. F. Structural Information from Ion Mobility Measurements: Effects of the Long-Range Potential. *Journal of Physical Chemistry* **1996**, *100* (40), 16082–16086. https://doi.org/10.1021/JP961623V.

(320) Shvartsburg, A. A.; Mashkevich, S. V.; Baker, E. S.; Smith, R. D. Optimization of Algorithms for Ion Mobility Calculations. *Journal of Physical Chemistry A* **2007**, *111* (10), 2002–2010. https://doi.org/10.1021/jp066953m.

(321) Marklund, E. G.; Degiacomi, M. T.; Robinson, C. V.; Baldwin, A. J.; Benesch, J. L. P. Collision Cross Sections for Structural Proteomics. *Structure* **2015**, *23* (4), 791–799. https://doi.org/10.1016/j.str.2015.02.010.

(322) Lai, R.; Dodds, E. D.; Li, H. Molecular Dynamics Simulation of Ion Mobility in Gases. *J Chem Phys* **2018**, *148* (6), 064109. https://doi.org/10.1063/1.4998955.

(323) Larriba-Andaluz, C. A Perspective on the Theoretical and Numerical Aspects of Ion Mobility Spectrometry. *Int J Mass Spectrom* **2021**, *470*, 116719. https://doi.org/10.1016/J.IJMS.2021.116719.

(324) Lii, J. H.; Allinger, N. L. Molecular Mechanics. The MM3 Force Field for Hydrocarbons. 3. The van Der Waals' Potentials and Crystal Data for Aliphatic and Aromatic Hydrocarbons. *J Am Chem Soc* **1989**, *111* (23), 8576–8582. https://doi.org/10.1021/ja00205a003.

(325) Kim, H. I.; Kim, H.; Pang, E. S.; Ryu, E. K.; Beegle, L. W.; Loo, J. A.; Goddard, W. A.; Kanik, I. Structural Characterization of Unsaturated Phosphatidylcholines Using Traveling Wave Ion Mobility Spectrometry. *Anal Chem* **2009**, *81* (20), 8289–8297. https://doi.org/10.1021/ac900672a.

(326) Graham, C.; Imrie, D. A.; Raab, R. E. Measurement of the Electric Quadrupole Moments of CO2 , CO, N2 , Cl2 and BF3. *Mol Phys* **1998**, *93* (1), 49–56. https://doi.org/10.1080/002689798169429.

(327) Hirschfelder, J. O.; Curtiss, C. F.; Bird, R. B. *Molecular Theory of Gases and Liquids*, Corrected.; John Wiley \& Sons, Inc.: New York, NY, USA, 1964.

(328) Hahn, H.-S.; Mason, E. A. Random-Phase Approximation for Transport Cross Sections. *Chem Phys Lett* **1971**, *9* (6), 633–635. https://doi.org/10.1016/0009-2614(71)85149-7.

(329) Siems, W. F.; Viehland, L. A.; Hill, H. H. Correcting the Fundamental Ion Mobility Equation for Field Effects. *Analyst* **2016**, *141* (23), 6396–6407. https://doi.org/10.1039/c6an01353h.

(330) Krylov, E.; Nazarov, E. G.; Miller, R. A.; Tadjikov, B.; Eiceman, G. A. Field Dependence of Mobilities for Gas phase-Protonated Monomers and Proton-Bound Dimers of Ketones by Planar Field Asymmetric Waveform Ion Mobility Spectrometer (PFAIMS). *J Phys Chem A* **2002**, *106* (22), 5437–5444. https://doi.org/10.1021/jp020009i.

(331) Viehland, L. A.; Lin, S. L.; Mason, E. A. Kinetic Theory of Drift-Tube Experiments with Polyatomic Species. *Chem Phys* **1981**, *54* (3), 341–364. https://doi.org/10.1016/0301-0104(81)85111-7.

(332) Shvartsburg, A. A.; Mashkevich, S. V; Siu, K. W. M. Incorporation of Thermal Rotation of Drifting Ions into Mobility Calculations: Drastic Effect for Heavier Buffer Gases. *J Phys Chem A* **2000**, *104* (42), 9448–9453. https://doi.org/10.1021/jp001753a.

(333) Morsa, D.; Hanozin, E.; Eppe, G.; Quinton, L.; Gabelica, V.; Pauw, E. De. Effective Temperature and Structural Rearrangement in Trapped Ion Mobility Spectrometry. *Anal Chem* **2020**, *92* (6), 4573–4582. https://doi.org/10.1021/acs.analchem.9b05850.

(334) Ruskic, D.; Klont, F.; Hopfgartner, G. Clustering and Nonclustering Modifier Mixtures in Differential Mobility Spectrometry for Multidimensional Liquid Chromatography Ion Mobility-Mass Spectrometry Analysis. *Anal Chem* **2021**, *93* (17), 6638–6645. https://doi.org/10.1021/acs.analchem.0c04889.

(335) Blagojevic, V.; Koyanagi, G. K.; Bohme, D. K. Multi-Component Ion Modifiers and Arcing Suppressants to Enhance Differential Mobility Spectrometry for Separation of Peptides and Drug Molecules. *J Am Soc Mass Spectrom* **2014**, *25* (3), 490–497. https://doi.org/10.1007/s13361-013-0800-0.

(336) Seo, J.; Warnke, S.; Gewinner, S.; Schöllkopf, W.; Bowers, M. T.; Pagel, K.; von Helden, G. The Impact of Environment and Resonance Effects on the Site of Protonation of

Aminobenzoic Acid Derivatives. *Physical Chemistry Chemical Physics* **2016**, *18* (36), 25474–25482. https://doi.org/10.1039/C6CP04941A.

(337) Levin, D. S.; Vouros, P.; Miller, R. A.; Nazarov, E. G.; Morris, J. C. Characterization of Gas phase Molecular Interactions on Differential Mobility Ion Behavior Utilizing an Electrospray Ionization-Differential Mobility-Mass Spectrometer System. *Anal Chem* **2006**, *78* (1), 96–106. https://doi.org/10.1021/ac051217k.

(338) Kang, Y.; Schneider, B. B.; Covey, T. R. On the Nature of Mass Spectrometer Analyzer Contamination. *J Am Soc Mass Spectrom* **2017**, *28* (11), 2384–2392. https://doi.org/10.1007/s13361-017-1747-3.

(339) Markert, C.; Thinius, M.; Lehmann, L.; Heintz, C.; Stappert, F.; Wissdorf, W.; Kersten, H.; Benter, T.; Schneider, B. B.; Covey, T. R. Observation of Charged Droplets from Electrospray Ionization (ESI) Plumes in API Mass Spectrometers. *Anal Bioanal Chem* **2021**, *413* (22), 5587–5600. https://doi.org/10.1007/s00216-021-03452-y.

(340) Shvartsburg, A. A.; Bryskiewicz, T.; Purves, R. W.; Tang, K.; Guevremont, R.; Smith, R. D. Field Asymmetric Waveform Ion Mobility Spectrometry Studies of Proteins: Dipole Alignment in Ion Mobility Spectrometry? *Journal of Physical Chemistry B* **2006**, *110* (43), 21966–21980. https://doi.org/10.1021/jp062573p.

(341) Pathak, P.; Shvartsburg, A. A. Assessing the Dipole Moments and Directional Cross Sections of Proteins and Complexes by Differential Ion Mobility Spectrometry. *Anal Chem* **2022**, *94* (19), 7041–7049. https://doi.org/10.1021/acs.analchem.2c00343.

(342) Shvartsburg, A. A.; Smith, R. D. Separation of Protein Conformers by Differential Ion Mobility in Hydrogen-Rich Gases. *Anal Chem* **2013**, *85* (14), 6967–6973. https://doi.org/10.1021/ac4015963.

(343) Creese, A. J.; Cooper, H. J. Separation and Identification of Isomeric Glycopeptides by High Field Asymmetric Waveform Ion Mobility Spectrometry. *Anal Chem* **2012**, *84* (5), 2597–2601. https://doi.org/10.1021/ac203321y.

(344) Shvartsburg, A. A.; Creese, A. J.; Smith, R. D.; Cooper, H. J. Separation of a Set of Peptide Sequence Isomers Using Differential Ion Mobility Spectrometry. *Anal Chem* **2011**, *83* (18), 6918–6923. https://doi.org/10.1021/ac201640d.

(345) Shvartsburg, A. A. Ultrahigh-Resolution Differential Ion Mobility Separations of Conformers for Proteins above 10 KDa: Onset of Dipole Alignment? *Anal Chem* **2014**, *86* (21), 10608–10615. https://doi.org/10.1021/ac502389a.

(346) Erdogdu, D.; Wissdorf, W.; Stappert, F.; Kersten, H.; Benter, T.; Kirk, A. T.; Allers, M.; Zimmermann, S.; Schneider, B. B.; Covey, T. WP 467: Chemical Kinetic and Ion Transport Simulations: Temperature Dependence of Ion Mobility and Its Impact on Cluster Equilibria. In *Proceedings of the 66th ASMS Conference on Mass Spectrometry and Allied Topics*; San Diego, 2018.

(347) Pathak, P.; Shvartsburg, A. A. Low-Field Differential Ion Mobility Spectrometry of Dipole-Aligned Macromolecules. *Anal Chem* **2020**, *92* (20), 13855–13863. https://doi.org/10.1021/acs.analchem.0c02551.

(348) Shvartsburg, A. A.; Andrzejewski, R.; Entwistle, A.; Giles, R. Ion Mobility Spectrometry of Macromolecules with Dipole Alignment Switchable by Varying the Gas Pressure. *Anal Chem* **2019**, *91* (13), 8176–8183. https://doi.org/10.1021/acs.analchem.9b00525.

(349) Wissdorf, W.; Seifert, L.; Derpmann, V.; Klee, S.; Vautz, W.; Benter, T. Monte Carlo Simulation of Ion Trajectories of Reacting Chemical Systems: Mobility of Small Water Clusters in Ion Mobility Spectrometry. *Journal of The American Society for Mass Spectrometry 2013 24:4* **2013**, *24* (4), 632–641. https://doi.org/10.1007/S13361-012-0553-1.

(350) Shvartsburg, A. A.; Zheng, Y.; Smith, R. D.; Kelleher, N. L. Separation of Variant Methylated Histone Tails by Differential Ion Mobility. *Anal Chem* **2012**, *84* (15), 6317–6320. https://doi.org/10.1021/ac301541r.

(351) Ieritano, C.; Yves Le Blanc, J. C.; Schneider, B. B.; Bissonnette, J. R.; Haack, A.; Hopkins, W. S. Protonation-Induced Chirality Drives Separation by Differential Ion Mobility Spectrometry. *Angewandte Chemie - International Edition* **2022**, *61* (9), e202116794. https://doi.org/10.1002/anie.202116794.

(352) Campbell, M. T.; Glish, G. L. Fragmentation in the Ion Transfer Optics after Differential Ion Mobility Spectrometry Produces Multiple Artifact Monomer Peaks. *Int J Mass Spectrom* **2018**, *425*, 47–54. https://doi.org/10.1016/j.ijms.2018.01.007.

(353) Zhu, S.; Campbell, J. L.; Chernushevich, I.; le Blanc, J. C. Y.; Wilson, D. J. Differential Mobility Spectrometry-Hydrogen Deuterium Exchange (DMS-HDX) as a Probe of Protein Conformation in Solution. *J Am Soc Mass Spectrom* **2016**, *27* (6), 991–999. https://doi.org/10.1007/s13361-016-1364-6.

(354) Wang, Y.; Alhajji, E.; Rieul, B.; Berthias, F.; Maître, P. Infrared Isomer-Specific Fragmentation for the Identification of Aminobutyric Acid Isomers Separated by Differential Mobility Spectrometry. *Int J Mass Spectrom* **2019**, *443*, 16–21. https://doi.org/10.1016/J.IJMS.2019.05.014.

(355) Berthias, F.; Maatoug, B.; Glish, G. L.; Moussa, F.; Maitre, P. Resolution and Assignment of Differential Ion Mobility Spectra of Sarcosine and Isomers. *J Am Soc Mass Spectrom* **2018**, *29* (4), 752–760. https://doi.org/10.1007/s13361-018-1902-5.

(356) Cruz-Ortiz, A. F.; Rossa, M.; Berthias, F.; Berdakin, M.; Maitre, P.; Pino, G. A. Fingerprints of Both Watson-Crick and Hoogsteen Isomers of the Isolated (Cytosine-Guanine)H+ Pair. *Journal of Physical Chemistry Letters* **2017**, *8* (22), 5501–5506. https://doi.org/10.1021/acs.jpclett.7b02140.

(357) Coughlan, N. J. A.; Carr, P. J. J.; Walker, S. C.; Zhou, C.; Guna, M.; Campbell, J. L.; Hopkins, W. S. Measuring Electronic Spectra of Differential Mobility-Selected Ions in the Gas Phase. *J Am Soc Mass Spectrom* **2020**, *31* (2), 405–410. https://doi.org/10.1021/jasms.9b00039.

(358) Mashmoushi, N.; Juhász, D. R.; Coughlan, N. J. A.; Schneider, B. B.; Le Blanc, J. C. Y.; Guna, M.; Ziegler, B. E.; Campbell, J. L.; Hopkins, W. S. UVPD Spectroscopy of Differential Mobility-Selected Prototropic Isomers of Rivaroxaban. *Journal of Physical Chemistry A* **2021**, *125*, 8195. https://doi.org/10.1021/acs.jpca.1c05564.

(359) Heldmaier, F. V.; Coughlan, N. J. A.; Haack, A.; Huard, R.; Guna, M.; Schneider, B. B.; Le Blanc, J. C. Y.; Campbell, J. L.; Nooijen, M.; Hopkins, W. S. UVPD Spectroscopy of Differential Mobility-Selected Prototropic Isomers of Protonated Adenine. *Physical Chemistry Chemical Physics* **2021**, *23* (35), 19892–19900. https://doi.org/10.1039/D1CP02688G.

Appendix A

Publications in reverse chronological order

Note that each numeric index is hyperlinked to the article's landing page.

(27) Ashworth, E. K., Dezalay, J., Ryan, C. R. M., Ieritano, C., Hopkins, W. S., Chambrier, I., Cammidge, A. N., Stockett, M. H., Noble, J. A., & Bull, J. N. (2023). Protomers of the green and cyan fluorescent protein chromophores investigated using action spectroscopy. *Physical Chemistry Chemical Physics*. *Accepted manuscript.*

(26) Haack, A.,* Ieritano, C.,* Hopkins, W. S. MobCal-MPI 2.0: An Accurate and Parallelized Package for Calculating Field-Dependent Collision Cross Sections and Ion Mobilities. *Analyst.* **2023**, 148, 3257 – 3273. *Equal contribution.

(25) Steinstra, C. M. K., Ieritano, C., Haack, A., Hopkins, W. S. Bridging the Gap between Differential Mobility, Log S, and Log P Using Machine Learning and SHAP Analysis. *Anal. Chem.* **2023**, 95 (27), 10309 – 10321.

(24) Ieritano, C., Haack, A., Hopkins, W. S. Chemical Transformations can Occur during DMS Separations: Lessons Learned from Beer's Bittering Compounds. *J. Am. Soc. Mass Spectrom.* **2023**, 34 (7), 1315 – 1329.

(23) Ieritano, C., Thomas, P., Hopkins, W. S. Argentination: A Silver Bullet for Cannabinoid Analysis by Differential Mobiltiy Spectrometry. *Anal. Chem.* **2023**, 95 (22), 8668 – 8678.

(22) Bissonnette, J. R., Ryan, C. R., Haack, A., Ieritano, C., Hopkins, W. S. First-Principles Modeling of Preferential Solvation in Mixed-Modifier Differential Mobility Spectrometry. *J. Am. Soc. Mass Spectrom.* **2023**, 34 (7), 1417 – 1427.

(21) Ieritano, C., Hopkins, W. S. The hitchhiker's guide to dynamic ion–solvent clustering: applications in differential ion mobility spectrometry. *Phys. Chem. Chem. Phys.* **2022**, 24, 20594 – 20615.

(20) Haack, A., Bissonnette, J. R., Ieritano, C., Hopkins, W. S. Improved First-Principles Model of Differential Mobility Using Higher Order Two-Temperature Theory. *J. Am. Soc. Mass Spectrom.* **2022**, 33 (3), 535 – 547.

(19) Ieritano, C., Le Blanc, J. C. Y., Schneider, B. B., Bissonnette, J. R., Haack, A., Hopkins, W. S. Protonation-Induced Chirality Drives Separation by Differential Ion Mobility Spectrometry. *Angew. Chem. Int. Ed.* **2022**, 61 (9), e202116794. *Frontispiece*.

(18) Ieritano, C., Campbell, J. L., Hopkins, W. S. Predicting Differential Ion Mobility Behaviour *in silico* using Machine Learning. *Analyst.* **2021**, 146 (*15*), 4737 – 4743.

(17) Ieritano, C., Lee, A., Crouse, J., Bowman, Z., Mashmoushi, N., Crossley, P. M., Friebe, B. P., Campbell, J. L., Hopkins, W. S. Determining Collision Cross Sections from Differential Ion Mobility. *Anal. Chem.* **2021**, 93 (*25*), 8937 – 8944.

(16) Ieritano, C., Hopkins, W. S. "Thermometer" Ions Can Fragment Through an Unexpected Intramolecular Elimination: These Are Not the Fragments You Are Looking For. *J. Phys. Chem. Lett.* **2021**, *12* (25), 5994 – 5999.

(15) Ieritano, C., Rickert, D., Featherstone, J., Honek, J. F., Campbell, J. L., Le Blanc, J. C. Y., Schneider, B. B., Hopkins, W. S. The Charge-State and Structural Stability of Peptides Conferred by Microsolvating Environments in Differential Mobility Spectrometry. *J. Am. Soc. Mass Spectrom.* **2021**, 32 (*4*), 956 – 968. ***Cover Article.***

(14) Ieritano, C., Hopkins, W. S. Assessing collision cross section calculations using MobCal-MPI with a variety of commonly used computational methods. *Mat. Today Comm.* **2021**, 27, 102226.

(13) Ieritano, C., Montgomery, C. A., Goll, J. M., Chan, H. Y. Some Like It Hot: Experimentally determining $\Delta\Delta H^{\ddagger}$, $\Delta\Delta S^{\ddagger}$, and $\Delta\Delta G^{\ddagger}$ between Kinetic and Thermodynamic Diels-Alder Pathways using Microwave-Assisted Synthesis. *J. Chem. Ed.* **2021**, 98 (*2*), 577 – 586.

(12) Ieritano, C. Featherstone, J., Haack, A., Guna, M., Campbell, J. L., Hopkins, W. S. How Hot are your Ions in Differential Mobility Spectrometry? *J. Am. Soc. Mass Spectrom.* **2020**, *31 (3)*, 582–593.

(11) Ieritano, C., Crouse, J., Campbell, J. L., Hopkins, W. S. A Parallelized Molecular Collision Cross Section Package with Optimized Accuracy and Efficiency. *Analyst* **2019**, *144* (5), 1660–1670.

(10) Zhou, C., Ieritano, C., Hopkins, W. S. Augmenting Basin-Hopping With Techniques From Unsupervised Machine Learning : Applications in Spectroscopy and Ion Mobility. *Front. Chem.* **2019**, *7*, 519.

(9) Ieritano, C., Campbell, J. L., Hopkins, W. S. Unravelling the Factors That Drive Separation in Differential Mobility Spectrometry: A Case Study of Regioisomeric Phosphatidylcholine Adducts. *Int. J. Mass Spectrom.* **2019**, *444*, 116182.

(8) Ieritano, C., Featherstone, J., Carr, P. J. J., Marta, R. A., Loire, E., McMahon, T. B., Hopkins, W. S. The Structures and Properties of Anionic Tryptophan Complexes. *Phys. Chem. Chem. Phys.* **2018**, *20* (41), 26532–26541.

(7) Gao, F., Ieritano, C., Chen, K. T., Dias, G. M., Rousseau, J., Bénard, F., Seimbille, Y. Two Bifunctional Desferrioxamine Chelators for Bioorthogonal Labeling of Biovectors with Zirconium-89. *Org. Biomol. Chem.* **2018**, *16* (28), 5102–5106.

(6) Chen, K. T., Ieritano, C., Seimbille, Y. Early-Stage Incorporation Strategy for Regioselective Labeling of Peptides Using the 2-Cyanobenzothiazole/ 1,2-Aminothiol Bioorthogonal Click Reaction. *ChemistryOpen* **2018**, *7* (3), 256–261. ***Cover Article.***

(5) Chen, K. T., Nguyen, K., Ieritano, C., Gao, F., Seimbille, Y. A Flexible Synthesis of 68Ga-Labeled Carbonic Anhydrase IX (CAIX)-Targeted Molecules via CBT/1,2-Aminothiol Click Reaction. *Molecules* **2018**, *24* (1), 23.

(4) Liu, C., Le Blanc, J. C. Y., Schneider, B. B., Shields, J., Federico, J. J., Zhang, H., Stroh, J. G., Kauffman, G. W., Kung, D. W., Ieritano, C., et al. Assessing Physicochemical Properties of Drug Molecules via Microsolvation Measurements with Differential Mobility Spectrometry. *ACS Cent. Sci.* **2017**, *3* (2), 101–109. ***Cover Article.***

(3) Fillion, E., Kavoosi, A., Nguyen, K., Ieritano, C. $B(C_6F_5)_3$-Catalyzed Transfer 1,4-Hydrostannylation of α,β-Unsaturated Carbonyls Using *i*Pr-Tricarbastannatrane. *Chem. Commun.* **2016**, *52*, 12813–12816.

(2) Ieritano, C., Carr, P. J. J., Hasan, M., Burt, M., Marta, R. A., Steinmetz, V., Fillion, E., Mcmahon, T. B., Hopkins, W. S. The Structures and Properties of Proton- and Alkali-Bound Cysteine Dimers. *Phys. Chem. Chem. Phys.* **2016**, *18*, 4704–4710.

(1) Liu, C., Le Blanc, J. C. Y., Shields, J., Janiszewski, J. S., Ieritano, C., Ye, G. F., Hawes, G. F., Hopkins, W. S., Campbell, J. L. Using Differential Mobility Spectrometry to Measure Ion Solvation: An Examination of the Roles of Solvents and Ionic Structures in Separating Quinoline-Based Drugs. *Analyst* **2015**, *140*, 6897–6903. ***Cover Article.***

Appendix B

Supplementary information for Chapter 3: Experimental consequences of dynamic ion solvation

This appendix is a .pdf file of the Supporting Information of the following manuscript:

> Ieritano, C., Rickert, D., Featherstone, J., Honek, J. F., Campbell, J. L., Le Blanc, J. C. Y., Schneider, B. B., Hopkins, W. S. The Charge-State and Structural Stability of Peptides Conferred by Microsolvating Environments in Differential Mobility Spectrometry. *J. Am. Soc. Mass Spectrom.* **2021**. 32 (*4*), 956 – 968. ***Cover Article.***
>
> https://pubs.acs.org/doi/abs/10.1021/jasms.0c00469

The file name of this .pdf is "**Ieritano_Christian_AppendixB_Ch3.pdf**".

If you accessed this thesis from a source other than the University of Waterloo, you may not have access to this file. You may access it by searching for this thesis at **http://uwspace.uwaterloo.ca**.

Appendix C

Supplementary information for Chapter 4: Protonation-induced chirality drives separation by DMS

This appendix is a .pdf file of the Supporting Information of the following manuscript:

> Ieritano, C., Le Blanc, J. C. Y., Schneider, B. B., Bissonnette, J. R., Haack, A., Hopkins, W. S. Protonation-Induced Chirality Drives Separation by Differential Ion Mobility Spectrometry. *Angew. Chem. Int. Ed.* **2022**. 61 (9), e202116794. *Frontispiece*.
>
> https://onlinelibrary.wiley.com/doi/full/10.1002/anie.202116794

The file name of this .pdf is "**Ieritano_Christian_AppendixC_Ch4.pdf**".

Appendix D

Supplementary information for Chapter 5: Argentination: a silver bullet for cannabinoid analysis by DMS-MS^2

This appendix is a .pdf file of the Supporting Information of the following manuscript:

> Ieritano, C., Thomas, P., Hopkins, W. S. Argentination: A Silver Bullet for Cannabinoid Analysis by Differential Mobility Spectrometry. *Anal. Chem.* **2023**. 95 (22), 8668 – 8678.
>
> https://pubs.acs.org/doi/abs/10.1021/acs.analchem.3c01241

The file name of this .pdf is "**Ieritano_Chritian_AppendixD_Ch5.pdf**".

If you accessed this thesis from a source other than the University of Waterloo, you may not have access to this file. You may access it by searching for this thesis at **http://uwspace.uwaterloo.ca**.

Appendix E

Supplementary information for Chapter 6: Development of tools to calculate ion mobility at arbitrary field strengths

This appendix is a .pdf file of the Supporting Information of the following manuscript:

> Haack, A.,* Ieritano, C.,* Hopkins, W. S. MobCal-MPI 2.0: An Accurate and Parallelized Package for Calculating Field-Dependent Collision Cross Sections and Ion Mobilities. *Analyst.* **2023**, 148, 3257 – 3273. *Equal contribution.
>
> https://pubs.rsc.org/en/content/articlelanding/2023/AN/D3AN00545C

The file name of this .pdf is "**Ieritano__Chritian__AppendixE__Ch6.pdf**".

If you accessed this thesis from a source other than the University of Waterloo, you may not have access to this file. You may access it by searching for this thesis at **http://uwspace.uwaterloo.ca**.